Electrochemical sensing and immunosensing using metallophthalocyanines and biomolecular modified surfaces

A thesis submitted in fulfillment of the requirements for the degree of

Doctor of Philosophy

of

Rhodes University

by

Philani Nkosinathi Mashazi

Supervisor: Professor Tebello Nyokong

December 2011

DEDICATION

I dedicate this work to my sisters:

Sibonisiwe Mashazi (who passed-on when I was born – 'coward'☹) and

Nokuthula Mashazi (who passed on barely a month after I started my PhD programme).

"Gone but not forgotten and Your spirits lives on in our memories"

ACKNOWLEDGEMENTS

"I can do all things through Christ who strengthens me." Philippians 4:13.

First and foremost, I would like to thank my Heavenly Father, God, the Almighty for all the blessings and the gift of LIFE from which all things perceived are made possible.

My heartfelt and sincere gratitude goes to Prof. Tebello Nyokong for her unequalled guidance, supervision and encouragements through the years of my programme. I remain eternally grateful to you Prof. for your encouragements and assistance. To you a big "THANK YOU - Kealeboha". To S22, You guys are the best, ☺☺☺!

I would also like to thank my former and current bosses at Mintek, Dr. Daven Compton, Dr. Elma van der Lingen and Dr. Robert T. Tshikhudo, for the opportunity to pursue my studies. I would also like to thank my colleagues for interesting and intriguing discussions that we shared.

To my loving family; my father Mr. S. A. Mashazi and my mother Mrs. D. M. Mashazi, I thank you from the bottom of my heart for your unparalled support. To my siblings; Sizwe, Sandile and Nkululelo thank you guys for the support and all the motivation I got was through your success; "maThabane, maNsele, maZwelibanzi".

To the love of my life; Mayibongwe Xulu, thank you my love for your unwavering support through all the years of my programme. I thank you from the bottom of my heart for your unconditional support and encouragements. You're truly a godsent Angel☺☺. To my son, Samukelo, boy you are my strength and the captain of my chearing squad. I look in your eyes and all I see is me - yeay!!!! All the support I get from you makes me a proud Father in the whole wideworld – "Uyakuthanda ubaba ndodana,☺☺!"

ABSTRACT

The synthesis of cobalt and manganese phthalocyanine complexes bearing eight hexylthio and four amino substituents was carried out. The formation of thin films of these complexes using different modification methods was also studied. Hexylthio functionalized metallophthalocyanine complexes were immobilized onto gold electrode surfaces using the self-assembly techniques. Surface modifications using cobalt and manganese tetraamino phthalocyanine as polymers, monolayers (onto electrografted surfaces) and as carbon nanotube – metallophthalocyanine conjugates was also carried out. The new method of modifying gold electrodes with metal tetraamino phthalocyanine complexes was investigated. The modified electrode surfaces were studied for their electrocatalytic properties and as potential electrochemical sensors for the detection of hydrogen peroxide (H_2O_2). The limits of detection for the H_2O_2 were of the orders of ~10^{-7} M for all the modified electrodes. The modified electrodes gave very good analytical parameters; such as good sensitivity, linearity at studied concentration range and well-defined analytical peaks with increased current densities. The modification methods were reproducible, highly conducting thin films were formed and the modified electrodes were very stable.

The design of electrochemical immunosensors for the detection of measles-specific antibodies was also carried out. The modified surface with measles-antigen as sensing element was accomplished using covalent immobilization for an intimate connection of the measles-antigen as a sensing layer onto an electrode surface. Two methods of detecting measles-specific antibodies were investigated and these methods were based on electrochemical impedance, i.e. label-free detection, and voltammetric method using horse-radish peroxidase (HRP) labeled antibody as a reporter. The detection of measles-specific antibodies was accomplished using both these methods. The potential applications of the designed immunosensor were evaluated in real samples (human and newborn calf serum) and the electrodes could detect the antibodies in the complex sample matrix with ease.

TABLE OF CONTENTS

LIST OF ABBREVIATIONS

2-AET	2-aminoethanethiol
2-HEDS	2-hydroxytheyldisulfide
2-MESA	2-mercaptoethanesulfonic acid
4-NBD	4-Nitrobenzene diazonium salf
$(LuOAc)_2Pc_2$	1,3-bis-[hexahxylthio phthalocyanine] Lutetium acetate tetrabuytl calix-4-arene
$[HHexTPc]_2\ NO_2$	Bis-(hexahexylthiol)phthalocyanine) methoxy nitrate
AC	Alternating current
AEBD	2-Aminoethanebenzene diazonium salt
AET	Aminoethanethiol
AFM	Atomic force microscopy
Ag	Silver electrode
Au	Gold working electrode
AuCQC	Gold coated quartz crystal
BDCA	Benzene-1,4-dicarbaldehyde
BPPGE	Basal plane pyrolytic graphite electrode
CA	Cysteamine
CE	Counter electrode
OBTPc	Octabutylthiophthalocyanine
OcHexTc	Octahexylthiolphthalocyanine
Pc	Phthalocyanine
TAcETPc	Tetraacetoxyethylthiophthalocyanine
TAPc	Tetraamino phthalocyanine
TCAPc	Tetracarboxylic acid phthalocyanine
TCPc	Tetracarboxyphthalocyanine
TDEAETPc	Tetra(2-deethylaminoethanethiol)phthalocyanine
TDMPc	Tetra(dodecylmercapto)phthalocyanine
TPP	Tetraphenyl porphyrin
TPTPc	Tetrapenylthiophthalocyanine
TSPc	Tetra sulfonated phthalocyanine
CPE	Carbon paste electrode or Constant phase element
TOTPc	Tetraoctaylthiophthalocyanine
CV	Cyclic voltammetry
CV	Cyclic voltammogram
DC	Direct current
DEAET	Diethylaminoethanethiol
OAcTPPc	Octa(acetylthio)pentyl phthalocyanine
DWCNT	Double-walled carbon nanotube
EDS	Energy dispercive X-ray spectroscopy
EDX	Energy dispersive X-ray
EIS	Electrochemical impedance spectroscopy
ESCA	Electron spectroscopy for chemical analysis
dOMe	Dimethoxy
OMe	Methoxy

FTIR	Fourier transform infrared
GCE	Glassy carbon working electrode
HHexMOMePc	Hexeahexyl-22-(mercaptooctyl)-25-methyl phthalocyanine
HHexMPMePc	Hexeahexyl-22-(mercaptopropyl)-25-methyl phthalocyanine
HHexMSOMePc	Hexeahexyl-22-(methylsulfonyloxy)octyl-25-methyl phthalocyanine
TDHexDTDPDPc	Tetra-deca-kishexyl-(dithiodipropyl)diphthalocyanine
HOMO	Highest occupied molecular orbital
HOPG	Highly ordered pyrolytic graphite
HRP	Horse-radish peroxidase
HRSEM	High resolution scanning electron microscopy
HRTEM	High resolution transmission electron microscopy
HS	Human serum
ITO	Indium Tin Oxide
LCAO	Linear combination of the atomic orbitals
LCR	Linear concentration range
LMCT	Ligand-to-metal charge transfer
LoD	Limit of detection
Lu_2Pc_4	1,3-bis-[hexahxylthio phthalocyanine] Lutetium tetrabuytl calix-4-arene
LUMO	Lowest unoccupied molecular orbital
M	Metal
ME	Mercaptoethanol
MeEtTOOPPc	Methoxyethylthio octa(pentyl) phthalocyanine
MLCT	Metal-to-ligand charge transfer
MP	Metalloporphyrin
MPc	Metallophthalocyanine
MPc SAM	Metallophthalocyanine self-assembled monolayer
MPP	Metallo tetra phenyl porphyrin
MWCNT	Multi-walled carbon nanotube
NCS	Newborn calf serum
OPG	Ordered pyrolytic graphite
OTTLE	Optically transparent thin layer electrode
PA	Phenylamino
PBS	Phosphate buffer saline
dONCSPc	Dioxananocosanesulfonyl phthalocyanine
PEA	Phenylethylamino
polyCoTAPc	Polymer of cobalt tetraamino phthalocyanine
polyMnTAPc	Polymer of manganese tetraamino phthalocyanine
polyMTAPc	Polymer of metal tetraamino phthalocyanine
PON	Peroxynitrite
PPy	Polypyrrole
Pt	Platinum electrode
QCM	Quartz crystal microbalance
QCM-D	Quartz crystal microbalance with dissipation
RE	Reference electrode
RSH	Thiol derivatives

RSSR	Cystine
SAM	Self-assembled monolayer
SEM	Scanning electron microscopy
SERS	Surface-Enhanced Raman Spectroscopy
ODTPc	Octa(dodecylthio)phthalocyanine
SPAuE	Screen-printed gold electrode
SPCE	Screen-printed carbon electrode
SPE	Screen-printed electrode
SWCNT	Single-walled carbon nanotube
SWV	Square wave voltammetry
TBABF4	Tetrabytylammoniumtetrafluoroborate
TEAP	Tetraethyl ammonium perchlorate
TEM	Transmission electron microscopy
TMB	Tetramethylbenzidine
UV-vis	Ultraviolet visible spectroscopy
VCE	Vitreous carbon electrode
WE	Working electrode
WHO	World health organization
XPS	X-ray photoelectron spectroscopy

LIST OF SYMBOLS

A	Real or geometric surface area
C or c	Concentration
C_{dl}	Double-layer capacitance
D	Diffusion coefficient
E	Potential
$E_{1/2}$	Half-wave potential
E_{pa}	Anodic peak potential
E_{pc}	Cathodic peak potential
F	Faraday's constant
f	Frequency
Hz	Hertz
I	Current
I(t)	Sinusodial current
I_p	Peak current
I_{pa}	Anodic peak potential
I_{pc}	Cathodic peak potential
I_{SS}	Steady-state current
j	Complex number
K_{amp}	Amperometric selective coefficient
k_{app} or k^0	Apparent electron transfer constant
Med	Mediator
M_{red}	Metal reduction peak potential
n	Number of electron
Ox	Oxidized species
Q	Charge
Q_{SAM}	Total charge under reduction peak for SAM
Q_{bare}	Total charge under reduction peak for bare
r	Radius
R	Universal gas constant
R_{CT}	Charger-transfer resistance
R_S or R_e	Solution or electrolyte resistance
Red	Reduced species
T	Temperature
ν	Scan rate
V	Volt
V	Volume
V(t)	Sinusodial potential
Z	Impedance
Z′	Real component of impedance
Z″	Imaginary component of impedance
Zw	Warburg impedance
α	Rate of electron transfer or non-peripheral position
β	Peripheral position

λ_{max}	Maximum wavelength
θ	Phase angle
Γ_{MPc}	Surface coverage or concentration
Γ_{ibf}	Ion barrier factor
Ω	Ohm

LIST OF FIGURES

Figure 4.4 : The 3D AFM images of MOcHexTPc SAMs modified gold surfaces with MOcHexTPc-SAM in air non-contact or tapping mode.

Figure 4.5 : Evolution of the cyclic voltammograms of 1 mM (a) CoTAPc and (b) MnTAPc during the formation of polymers on gold electrode and (c) CoTAPc on ITO.

Figure 4.6 : Cyclic voltammograms of (a) GCE-polyCoTAPc, (b) Au-polyCoTAPc, (c) GCE-polyMnTAPc and (d) Au-polyMnTAPc films, DMF + 0.1 M $TBABF_4$ solution.

Figure 4.7 : Cyclic voltammograms of (i) bare or unmodified electrodes and (ii) polyCoTAPc and (iii) polyMnTAPc modified (a) gold and (b) glassy carbon electrodes.

Figure 4.8 : 2D and 3D AFM (1 x 1 μm) micrographs of (a) bare ITO and (b) $[polyCoTAPc]_{30}$ modified ITO at wide potential window (-1.20 to +1.00 V vs Ag|AgCl).

Figure 4.9 : AFM 2D and 3D (1 x 1 μm) micrographs for $[polyCoTAPc]_n$ formed at different scan numbers n = (a) 30 and (b) 50 . Scan range -200 to 900 mV on ITO surfaces.

Figure 4.10 : Nyquist and corresponding bode plots (i) bare electrodes, (ii) polyCoTAPc and (iii) polyMnTAPc modified Au electrodes in (1:1) 1 mM $K_4/K_3[Fe(CN)_6]$.

Figure 4.11 : Cyclic voltammograms of (a) SPAuE recorded for the fabrication of phenylnitro monolayer and (b) reduction of NO_2 to NH_2 in (1:9, ethanol: water).

Figure 4.12 : Cyclic voltammograms of SPAuE, SPAuE-PA and SPAuE-PA-MTAP in 0.10 M KOH and (c) SPAuE-PA-MTAPc in pH 7.4 PBS solution.

Figure 4.13 : Cyclic voltammograms of SPAuE, SPAuE-PA, SPAuE-PA-MTAPc, (a) 1.0 mM $NH_4Fe(SO_4)_2$ in 1.0 mM $HClO_4$ and (b) (1:1) 2.0 mM $K_4/K_3Fe(CN)_6$ in 0.10 M KCl.

Figure 4.14 : HRSEM images of bare gold coated quartz crystals (AuCQC) and screen-printed gold electrode (SPAuE).

Figure 4.15 : HRSEM images and their corresponding EDS spectra for (a) bare AuCQC, (b) AuCQC-PA, (c) AuCQC-PA-MnTAPc and (d) AuCQC-PA-CoTAPc surfaces.

Figure 4.16 : 2D and 3D AFM images images for (a) bare AuCQC, (b) AuCQC-PA, (c) AuCQC-PA-MnTAPc and (d) AuCQC-PA-CoTAPc.

Figure 4.17 : (a) Raman spectra for (i) MnTAPc and (ii) CoTAPc complexes in their powder form and (b) SPAuE surfaces modified with (i) PA, (ii) PA-MnTAPc and (iii) PA-CoTAPc.

Figure 4.18 : XPS analysis (a) survey spectra, (b) C1s high resolution region and (c) N1s high resolution region for the SPAuE surfaces modified with PA, PA-SWCNT-MTAPc.

LIST OF TABLES

LIST OF SCHEMES

Chapter 1:

Introduction and literature review

1 GENERAL INTRODUCTION AND LITERATURE REVIEW

1.1 Motivation and the aims of the dissertation

Motivation

The study of chemically modified electrode surfaces with catalytic materials and their use for the design of electrochemical sensors and biosensors is a subject of interest internationally. This is due to the fact that these catalytic materials will increase surface activity by enhancing catalytic currents and by lowering operating over potentials. The choice of the material will also enhance the selectivity and the sensitivity of the modified electrodes towards the analyte of interest. One of the factors that play an important role is the method by which these catalytic materials are immobilized onto the electrode surfaces. The electrochemical sensors or biosensors that are stable and may be applied for the detection of analytes in extreme environmental and chemical conditions are desirable. Reproducibility of the method is also important for repeatability and consistency. Furthermore, the construction technique determines the shelf life and the reliability of the designed electrochemical sensor and/or biosensor.

Electrochemistry as a method of choice is studied in detail in this work and has been chosen due to its simplicity, user-friendliness, cost effective, portability and offers faster analyte determination compared to other analytical methods. The other advantages of using electrochemistry for the design of electrochemical sensors or biosensors are that they: (i) offer both qualitative and quantitave results for the detected analyte within a single experimental run and (ii) can be miniaturized for ease of portability allowing for decentralization of measurements. The recent advances in the sensing field together with the emerging new fields of

nanotechnology and nanoscience have seen an increase in the use of nanomaterials in a wide variety of areas such as in analytical chemistry, clinical, medicinal, drug delivery, food and environment for monitoring. In electrochemical sensing, the nanomaterials are useful as they increase the surface area and the sensitivity of the electrode surface. This work explored the effect of nanomaterials (carbon nanotubes) on the detection of various biological analytes.

With the success of glucose biosensor for point-of-care and home-based monitoring; majority of the applications in the study of electrochemical systems have focused on the real-life applications of these systems. The surveillance of communicable and infectious diseases is a subject of international interest. In the recent past, there has been a worldwide outbreaks and spread of various communicable and infectious diseases such as influenza A (H1N1 virus). There is continuously a need to design and develop analytical tools for on-site monitoring of communicable diseases. The field of electrochemical biosensors design and development with relevance towards disease surveillance is known as immunosensing. This work investigated the design of electrochemical-based sensors for H_2O_2 detection and immunosensors for communicable disease surveillance and a model analyte of one disease (measles) was studied.

Aims of dissertation:

a) Investigate various methods of the immobilization of redox active metallo phthalocyanines (MPc) onto different electrode surfaces as electrocatalysts for the detection of hydrogen peroxide.

b) Study the effect nanomaterials (carbon nanotubes) conjugates will have on the electrocatalysis of MPc towards the detection of hydrogen peroxide.

c) Characterize the modified surfaces to confirm their modifications with biomolecules, electrocatalysts and nanomaterial conjugates using surface techniques (such as microscopy, spectroscopy and electrochemistry).

d) Study the design of sensitive and specific electrochemical immunosensors for an early detection of disease biomarkers such as antibodies or antigens in human blood or serum.

The work in this dissertation is presented in various chapters:

Chapter 1: Introduction

This chapter introduces various sensors and biosensors, metallophthalocyanine properties, nanostructured material (carbon nanotubes) properties, surface characterization techniques, electrode modification techniques, biomolecule reaction and the applications of these systems.

Chapter 2: Experimental

This chapter outlines the experimental processes and methods performed for the preparation of new metallo phthalocyanines, nanostructured materials, biomolecules and their immobilization on the electrode surfaces.

Chapter 3: Characterization of synthesized complexes.

This chapter is dedicated solely to the characterization of metallophthalocyanine complexes using electrochemistry and spectroelectrochemistry.

Chapter 4: Electrode surface fabrication and characterization

This chapter discusses various strategies utilized for the immobilization of different materials on the electrode surfaces. The characterization of various electrode modified surfaces using different surface techniques is discussed.

Chapter 5: Electrocatalysis and electroanalysis studies towards detection of H_2O_2

This chapter investigates the electrocatalytic and electroanalytical properties of the modified electrodes towards detection and monitoring of hydrogen peroxide using modified electrode surfaces.

Chapter 6: Detection of measles-specific antibodies on an antigen modified surface

This chapter investigates the electrochemical detection of measles antibodies onto an antigen modified electrode surfaces via label and label-free methods of immunosensor design.

Chapter 7: Conclusions

Chapter 8: References

1.2 Types of sensors

1.2.1 Electrochemical sensors

Numerous sensors have been or are being developed for the detection and monitoring of organics, inorganics, environmental and biological molecules [1,2]. Sensors that utilize or integrate biological molecules as recognition or sensing element are characterized as a class of sensor devices called biosensors. The use of biological molecules for sensing applications allows for their applicability in biochemistry, clinical analysis or medical diagnosis [3], environmental analysis [4-14], to name but a few.

The increase in biosensor applications has also been motivated by the recent availability of pure biologically active substances; such as microorganisms, proteins, cells, peptides, antibodies, antigens, DNA, aptamers, cells and tissues, which can be immobilized onto an electrode surface as recognition elements [11,15-17]. The recognition process is based on the lock-and-key principle where molecular recognition is identified by shape and/or size and allows for identification of one specific substance in the matrix containing many other substances. Biosensing technology owes its prominent demand to the pioneering success of glucose diabetes monitoring devices that are commercially and readily available world-wide [18,19].

The analytical methods currently used for detection and monitoring of viruses and disease infections, require bulk equipments for their operation. These analytical methods (i.e. chromatography, spectroscopy, microscopy and spectrometry) are laboratory centralized and require skilled personnel for operation, data analysis and interpretation. However, majority of these bulky techniques are currently utilized for diagnostic applications. The example of one such method that has established itself

in the diagnostic industry is the ELISA (Enzyme-Linked Immuno-Sorbent Assay). ELISA is used worldwide for the detection and monitoring of disease outbreaks, epidemiological viral screening, early disease detection and diagnosis and environmental monitoring [20]. There is a need for systems that can offer same sensitivity and specificity as ELISA but are not laboratory-based, simple to operate and with ease of data interpretation. The advantages of electrochemical methods, which are described above, make this a method of choice for the design of chemical and biological sensors and/or biosensors.

In electrochemical sensing, the systems are designed to incorporate two major components, i.e. recognition element and transducer element. To easily identifiy the concept and the material used to construct sensors or biosensors, these systems are named using their recognition elements [11,16,21] or output signal [22-25]. For an example, a biosensor constructed using antigen/antibody modified electrode with the electrical output signal for detection is called electrochemical immunosensor. Various other sensors may be constructed and their names derived from the output signal, transducer elements, or recognition elements and these components are shown in Figure 1.1.

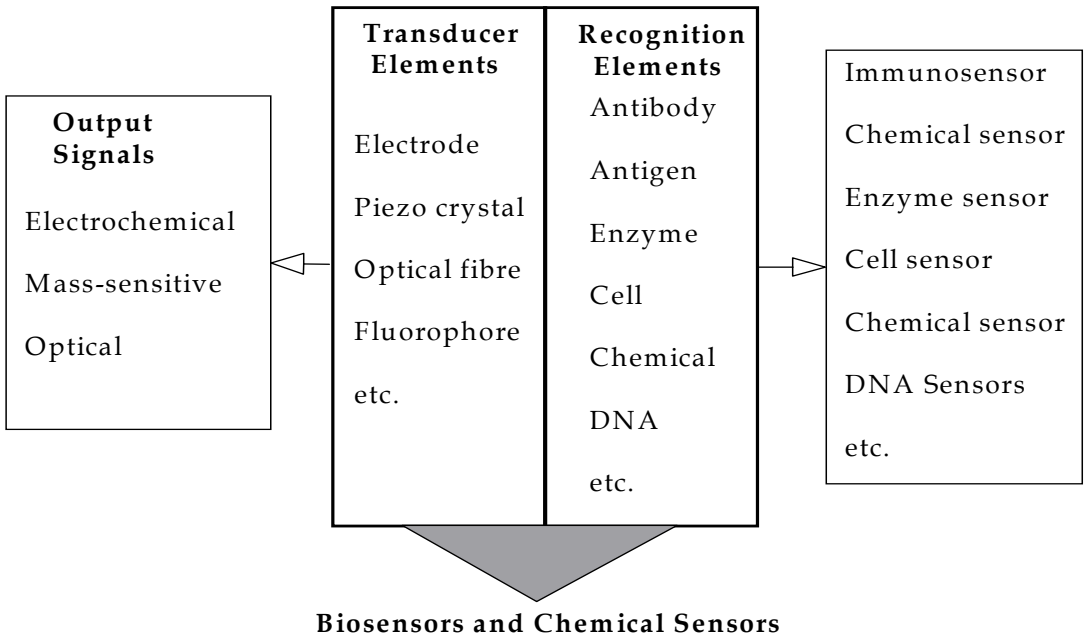

Figure 1.1: Sensor and biosensor names, transducer and recognition elements.

1.2.2 Mass-sensitive sensors

The mass-sensitive systems are based on the signal due to mass changes on the crystal surfaces or sensor-chips; i.e. quartz crystal microbalance (QCM) and surface plasmon resonance (SPR). QCM method is based on piezoelectric effect and detects the changes in mass by monitoring the intrinsic change in frequency of the quartz crystal chip [26-29]. The SPR method monitors the incident angle shift as the mass on the sensor-chip changes [30,31]. In both these systems, the output signal is obtained as a result of chemical or biological interactions taking place on the crystal or sensor surface. In this study, the quartz crystal microbalance with dissipation (QCM-D) was used for monitoring interaction and molecular recognition on the electrode surface. Using QCM-D may also give various parameters that are important during the research and development stages of sensors and biosensors.

1.2.3 Immunosensors

Immunosensors are biosensor systems that utilize the specificity and the selectivity of antigen-antibody immune or affinity reactions for their operations [21]. A stable immune complex is formed when the antibody recognizes the antigen and one antibody binds selectively to one antigen, and vise versa. The immune complex formation is a naturally occurring phenomenon that takes place within a biological microorganism. During the infection, the antigen enters the body which then signals the immune response to produce antibodies to fight the intruder (antigen). The reaction that happens between the antibody and antigen results in a formation of an immune complex and this complex is isolated from the body system through cellular endocytosis. Antigen is any molecule that the body recognizes as foreign, while the antibody is the immune system response to foreign molecules (antigens) that enters the body. There are five classes of antibodies (or immunoglobulins, Ig) and these are IgG, IgM, IgA, IgD and IgE [32]. The antibodies are distinguishable by their sizes and type of heavy chains found in the molecule, i.e. γ-chains (IgG, 90kDa), μ-chains (IgM, 900kDa), α-chains (IgA, 160kDa-320kDa), ε-chains (IgE, 200kDa) and δ-chains in IgD, 180kDa. The antibody has four polypeptide chains, i.e. two identical heavy chains and two light chains, held together by disulfide bridges to form a Y-shaped molecule as shown in Figure 1.2. The heavy and light chains contain constant and variable regions. The variable region containing the antigen binding site has high specificity and affinity towards the antigen. The antigen-antibody interactions occur through multiple non-covalent bonds such as hydrogen bonds, ionic bonds, hydrophobic bonds and van der Waals interactions, Figure 1.2. The stability of the immune complex that forms between the antibody and the antigen is achieved when many of these bonds act together, otherwise each of these bonds individually are usually weak.

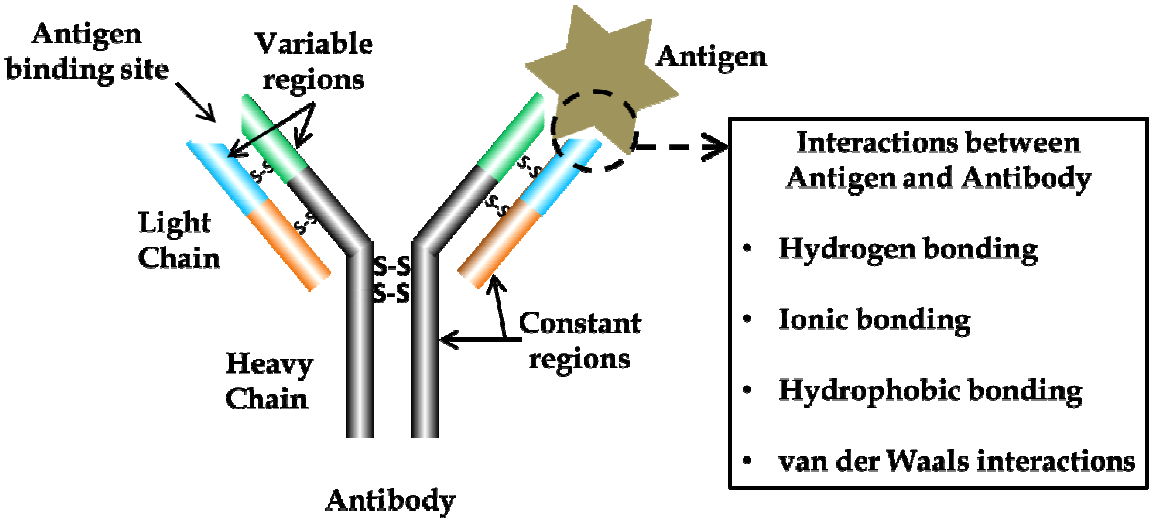

Figure 1.2: Simplified antibody (immunoglobulin) structure and its interactions with antigen.

These reactions provide us with the opportunity to detect diseases and virus infections. The most commonly used procedure for monitoring the antibody-antigen reactions is ELISA [33] discussed above. The enzyme labels are difficult and expensive to produce. Therefore, label-free detection systems are of interest. Electrochemical detection offers both label and label-free detection systems depending on the method used.

Label versus label-free immunosensor detection: The electrochemical immunosensors may operate as direct or indirect sensors [4]. The direct (label-free) immunosensor measures the changes during the interaction between the antigen-antibody binding reaction and this interaction results in the changes in properties that can be monitored and detected in real time. The indirect (labeled) immunosensors operate by incorporating an additional step as a secondary reaction requiring the use of enzyme-label to produce a property to be measured. Figure 1.3 shows the schematic representation for the comparison of the (a) labeled detection and (b) label-free detection of an antibody on an antigen-bound surface. The output signals are shown

as (a) increase in current with increasing antibody concentration [34] and (b) increase in the electrochemical impedance Nyquist plot semi-circle with the increasing antibody concentration [35,36]. In this study, the design of electrochemical immunosensors for the detection of measles-specific antibodies is investigated. To the candidate's knowledge the detection of measles-specific antibodies will be reported here for the first time.

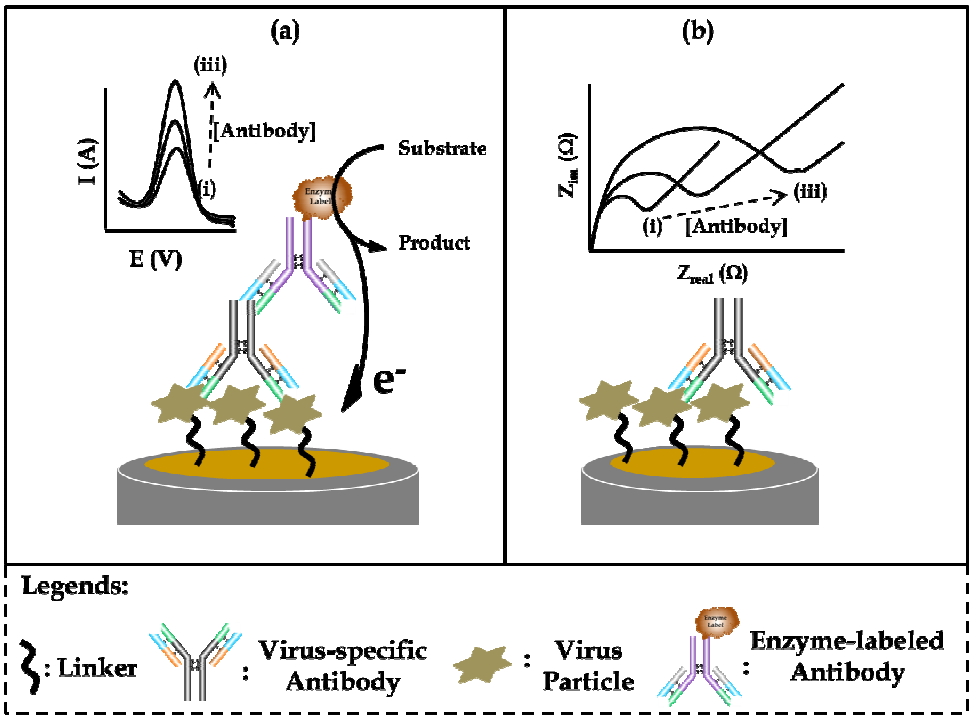

Figure 1.3: Schematic representation of (a) labelled detection and (b) label-free detection of antibodies onto an antigen-bound electrode surface and respective signal output at each detection (a) current [34] and (b) impedance [35,36] increases.

The utilization of antibodies and/or antigens in electrochemical immunosensing has not been successful and this is due to the absence of sensitive electrical signal generating mechanism thus leading to the use of indirect electrochemical detection [37-40].

Electrochemical immunosensors are built to mimic the ELISA method and may utilize the labeled antibody that binds to the analyte in order to detect its concentration. The detection antibodies are coupled to the enzymes and the most commonly used enzymes are alkaline phosphatase, β-galactosidase, horseradish peroxidase, laccase, catalase, urease and glucose oxidase [4,41-51] and this allows for the quantitative measurement of the bound analyte by monitoring the electrical signal generated by the enzymatic reactions.

Aims of this study:

- The design of electrochemical immunosensors for the detection of measles-specific antibodies was investigated.

- Two methods of detecting measles-specific antibodies were investigated, i.e. label and label-free immusonensors using cyclic voltammetry and impedance spectroscopy, respectively.

The study of metallophthalocyanine complexes forms the majority of the materials investigated in this thesis, hence their properties are discussed next.

1.3 Metallophthalocyanines and their applications

The study of metallophthalocyanine (MPc) complexes commenced after their serendipitous discovery in the early 1900s and they have been found to be useful in various applications. The majority of the early applications of MPc complexes were as blue-green pigments [52,53]. MPc applications have since grown tremendously and one of their pioneering applications to date is in the medical field as photosensitizer drugs in the treatment of cancer using photodynamic therapy [54-57]. In the past few decades, MPc applications have been extended and these applications now include their use as thin films on electrode surfaces for the design of chemical sensors [58,59].

MPcs are highly conjugated, planar and aromatic macrocycle complexes with 18-π electron system [60]. They contain four isoindole groups linked by four nitrogen groups, Figure 1.4 (a). They have similar core structure to the natural occurring metalloporphyrin (MPP) complexes, Figure 1.4 (b), but have an extended conjugation of benzene rings. Majority of the application for the MPc complexes requires their solubility in organic and aqueous solutions. To improve the solubility of the MPc complexes, the introduction of substituents is crucial. The substitution in MPc complexes can be achieved either on the central metal ion (axial ligation) or on the ring system. The substituents on the ring can be attached either on the peripheral (β) positions (2,3,9,10,16,17,23,24) or at non-peripheral (α) positions (1,4,8,11,15,18,22,25) as shown in Figure 1.4 (a).

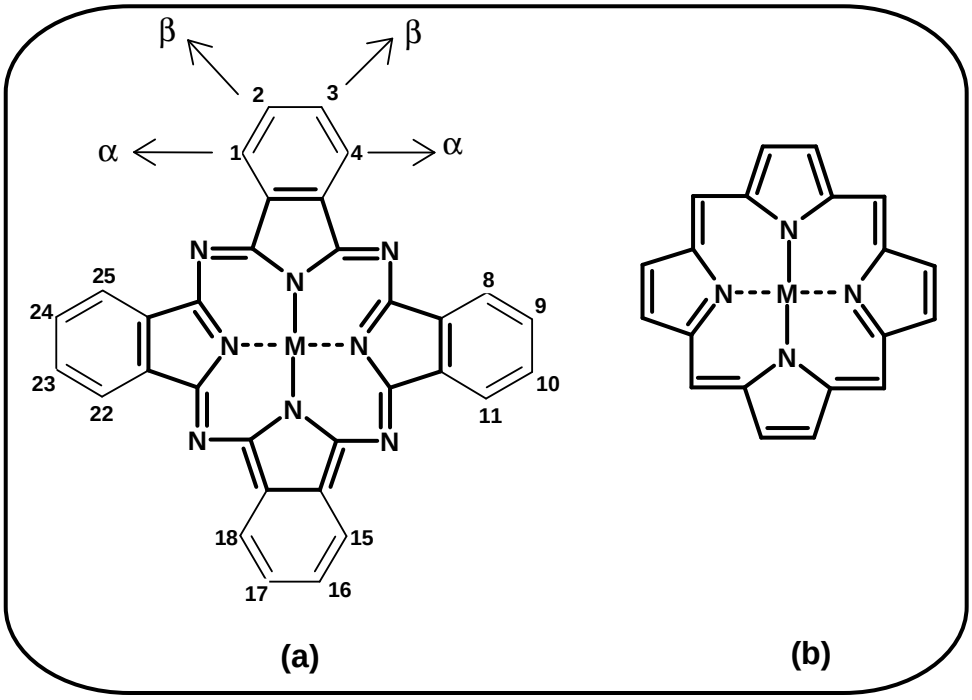

Figure 1.4: Molecular structure of (a) metallo-phthalocyanine (MPc) and (b) metallo-porphyrin (MPP) complexes with numbering.

The synthesis of MPc complexes, especially substituted MPc complexes with various groups, can be achieved by cyclotetramerization of substituted 4,5-dicyanobenzene compounds (**1**) and (**2**), shown in Scheme 1.1. Various other starting materials are used for the synthesis of phthalocyanine complexes and these are phthalic anhydrides and phthalimides (substituted or un-substituted). The 1,2-substituted-4,5-dicyanobenzene (**1**) is used for the synthesis of peripherally substituted octa-(2,3,9,10, 16,17,23,24) phthalocyanine complexes (**3**) and (**4**) [61-64]. The 3,6- substituted-4,5-dicyanobenzene (**2**) is used for the preparation of non-peripherally substituted octa-(1,4,8,11,15,18,22,25) phthalocyanine complexes (**5**) and (**6**) [65,66]. Substituted-4,5-dicyano-benzene at position 4 or 5 are used for the synthesis of tetra substituted constitutional isomers with different geometries 3,10,17,24-(C4h); 3,10,16,24-(Cs); 3,9,16,24-(C2v), 3,9,17,23-(D2v).

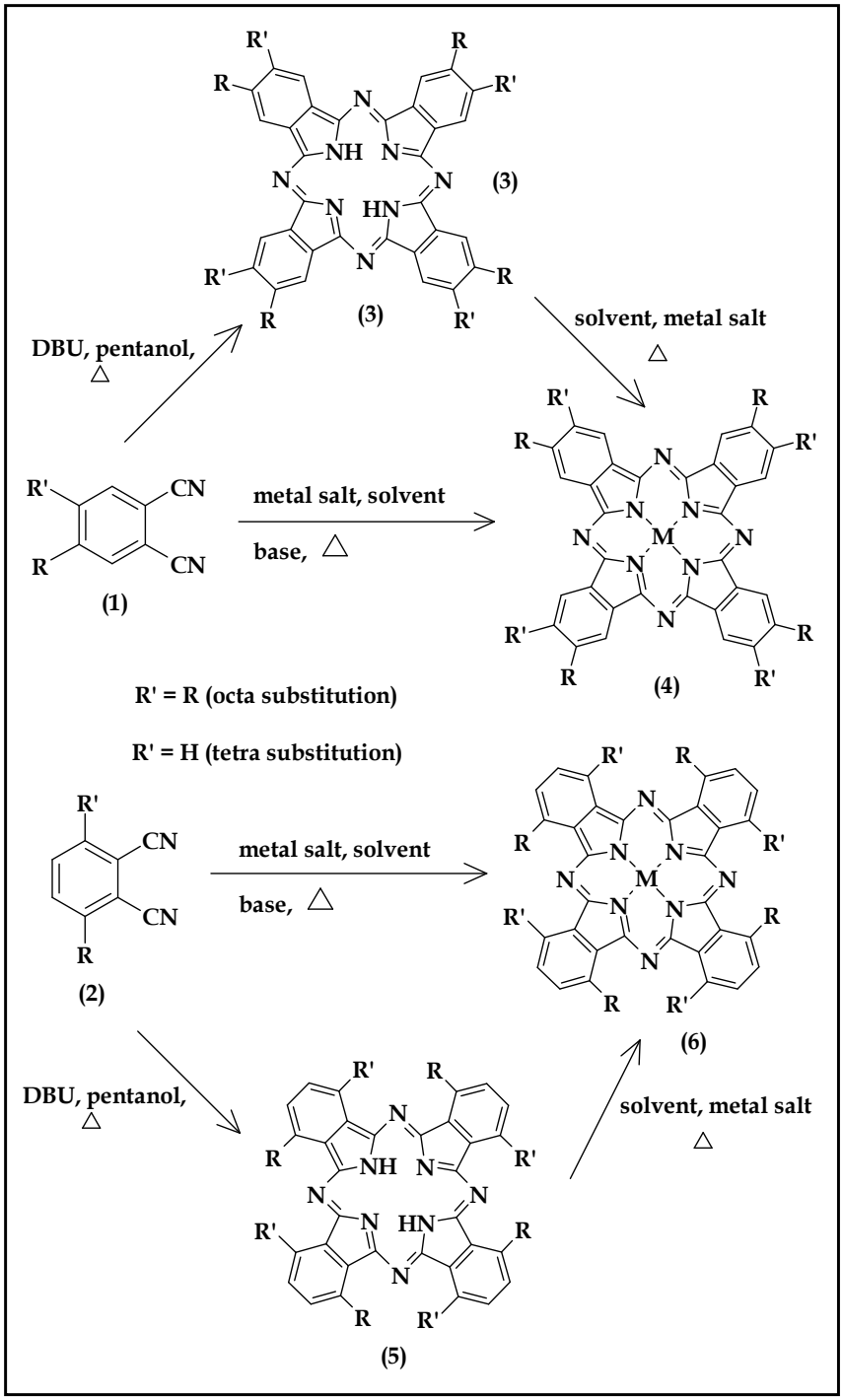

Scheme 1.1: Synthesis route for tetra-substituted and octa-substituted MPc complexes at (**4**) peripheral and (**6**) non-peripheral positions. R′ = H for tetra-substituted and R′ = R for octa-substituted MPc complexes.

Metallophthalocyanine complexes bearing hexylthio groups at the peripheral and non-peripheral positions (**12-15**) are employed in this work. They were synthesized following methods similar to those reported [61-66] and shown in Scheme 1.2. Complexes (**12**, **14** and **15**) are reported for the first time. The synthesis of complex (**13**) has been reported before but the electrochemical properties of **13** were not investigated, hence the interest in studying this complex and compared to their non-peripheral substituted complex **12**. These complexes (**12-15**) were further studied for their abilities to form SAMs onto gold electrode surfaces and their applications towards the detection of H_2O_2.

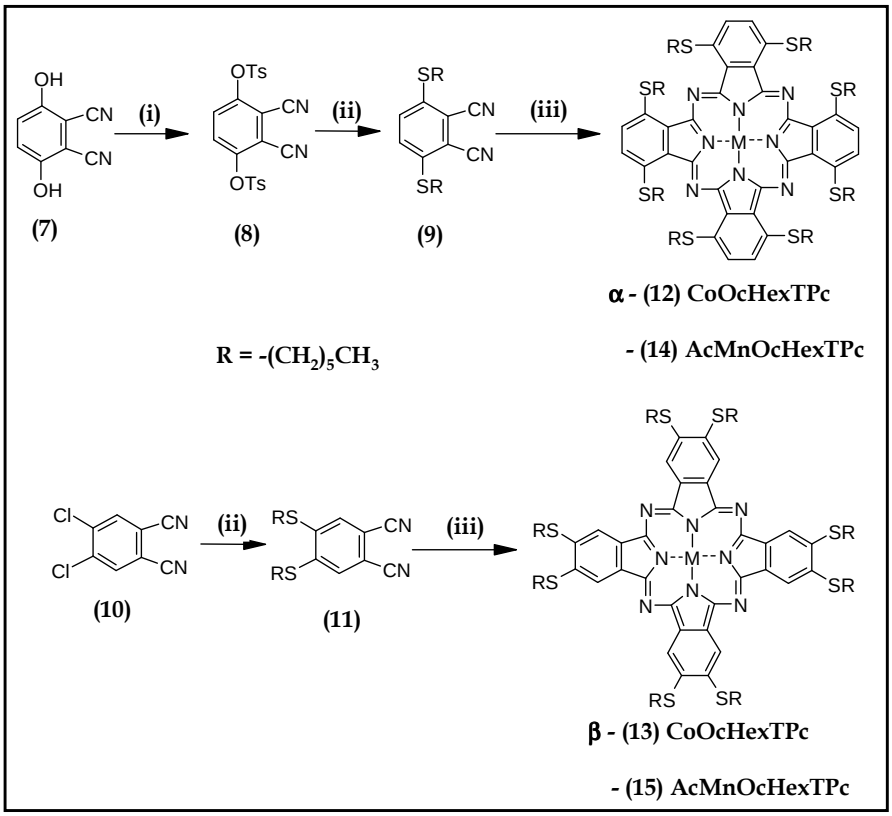

Scheme 1.2: Synthesis of manganese and cobalt octakis-hexylthiophthalocyanine substituted at non-peripheral (α-MOcHexTPc, **12** and **14**) and peripheral (β-MOcHexTPc, **13** and **15**) positions. Reagents: (i) TsCl, Acetone, K_2CO_3. (ii) 1-hexanethiol, K_2CO_3, DMSO. (iii) $CoCl_2$ or $Mn(Ac)_2$, 1-pentanol, DBU. Ac = acetate and TsCl = p-toluenesulfonyl chloride.

Metal tetra-amino phthalocyanine complexes with cobalt (CoTAPc, **16**) and manganese (MnTAPc, **17**) metal ions shown in Figure 1.5 were also employed. Though these complexes are not new, their applications and analysis in this work are new.

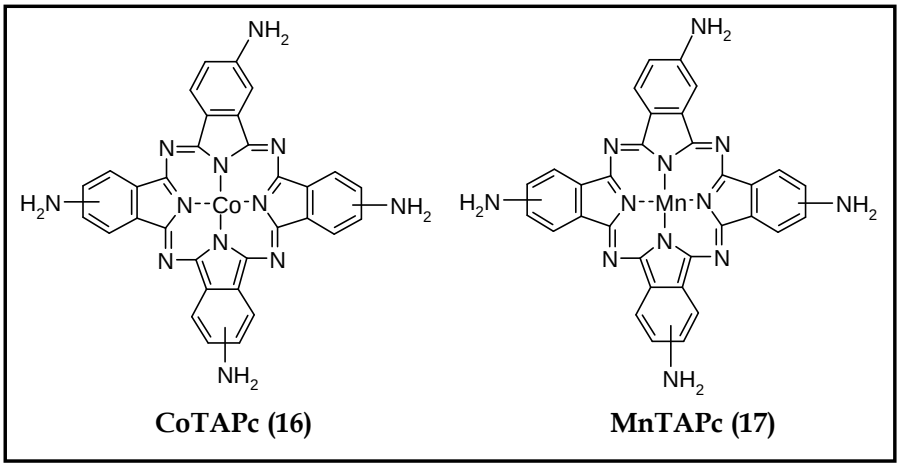

Figure 1.5: Shows the chemical structure of MTAPc (metal tetra-amino phthalocyanine) complexes (**17, 18**) used in this work.

Table 1.1 below shows the metal alkylthiophthalocyanines and the metal tetra-aminophthalocyanines complexes that have been reported in literature [67-116], their electrocatalytic properties towards different analytes and method of modification. From the Table 1.1, it is clear that a number of metal alkylthiolphthalocyanines have been synthesized and studied for their electrocatalytic studies towards the detection of various analytes. It is of interest to note that the detection of H_2O_2 (a biologically important molecule) has never been done on these various complexes. Therefore, in this study the detection of H_2O_2 onto electrode surfaces modified with newly synthesized hexylthio phthalocyanines as SAMs will be investigated. In addition to the studies of SAMs, metal tetra-amino phthalocyanine (MTAPc) complexes will also be investigated and they have not been used for H_2O_2 electrocatalysis, Table 1.1. Several methods of immobilizing MTAPc complexes will be investigated.

Table 1.1: Electrochemical data for the studies of octa-alkythiol and tetra-amino substituted phthalocyanines showing their method of modification, the analytes used for their detection and electrode material used.

MPc Complex	Electrode	Analyte	Method of modification	Ref.
Alkylthio-functionalized metallophthalocyanines				
CoOBTPc	Au	Cysteine	SAM	[67]
CoOBTPc	Au	Homocysteine	SAM	[68]
CoOBTPc	Au	Penicillamine	SAM	[68]
CoOBTPc	Au	Thiocyanate	SAM	[68]
CoOBTPc	Au	--	SAM	[69]
FeOBTPc	Au	Cysteine	SAM	[70]
FeOBTPc	Au	Homocysteine	SAM	[68]
FeOBTPc	Au	Penicillamine	SAM	[68]
FeOBTPc	Au	Thiocyanate	SAM	[68]
CoOHETPc	Au	Cysteine	SAM	[68]
CoOHETPc	Au	Homocysteine	SAM	[68]
CoOHETPc	Au	Penicillamine	SAM	[68]
CoOHETPc	Au	Thiocyanate	SAM	[68]
FeOHETPc	Au	Cysteine	SAM	[68]
FeOHETPc	Au	Homocysteine	SAM	[68]
FeOHETPc	Au	Penicillamine	SAM	[68]
FeOHETPc	Au	Thiocyanate	SAM	[68]
NiTAcETPc	GCE	H_2	Electrodeposition	[71]
CoTAcETPc	GCE	H_2	Electrodeposition	[71]
$[ZnHHexTPc]_2$ NO_2	Au-Glass	VOC	Spin-coat	[72]
$[CoHHexTPc]_2$ NO_2	Au-Glass	VOC	Spin-coat	[72]
Lu_2Pc_4	Au-Glass	VOC	Spin-coat	[73]
$(LuOAc)_2Pc_2$	Au-Glass	VOC	Spin-coat	[73]
PddONCSPc	Au-Si	--	Spin-coat	[74]
MnOPTPc	Au	Cysteine	SAM	[75]
TiOPTPc	Au	Cysteine	SAM	[75]
VOPTPC	Au	Cysteine	SAM	[75]
TiTPTPc	Au	Cysteine	SAM	[75]
MnTPTPc	Au	Cysteine	SAM	[75]
FeTDEAETPc	Au	Carbofuran	SAM	[76]
CoTDEAETPc	Au	Carbofuran	SAM	[76]
MnTDEAETPc	Au	Carbofuran	SAM	[76]
SnTDTPc	Au	--	SAM	[77]
SnODTPc	Au	--	SAM	[77]

Table 1.1 Continued.

NiTDMPc	Au	Chlorophenols	polymer	[78]
NiTDMPc	Au	--	SAM	[79]
dOMeSiOAcTPPc	Au	--	SAM	[80]
MeEtTOSiOPPc	Au	--	SAM	[80]
H_2HHexMPMePc	Au	--	SAM	[81]
H_2HHexMOMePc	Au	--	SAM	[81]
H_2HHexMSOMePc	Au	--	SAM	[81]
NiTDMPc	Au	Nitrite	polymer	[82]
NiTDMPc	Au	Sulphite	polymer	[83]
CoTDMPc	Au	--	SAM	[79]
CoTDMPc	Au	Nitrite	polymer	[84]
CoTDMPc	Au	Sulphite	polymer	[83]
FeTDMPc	Au	--	SAM	[79]
FeTDMPc	Au	Nitrite	polymer	[84]
FeTDMPc	Au	Sulphite	polymer	[83]
ZnTDMPc	Au	--	SAM	[79]
MnTDMPc	Au	--	SAM	[85]
MnTDMPc	Au	Nitrite	polymer	[84]
MnTDMPc	Au	Sulphite	polymer	[83]
CuTOTPc	Pt-Glass	Nitrite	Spin-coat	[86]
NiTOTPc	Pt-Glass	Nitrite	Spin-coat	[86]
CuOOTPc	Pt-Glass	Nitrite	Spin-coat	[86]
NiOOTPc	Pt-Glass	Nitrite	Spin-coat	[86]
H_2TDHexDTDPDPc	Au	--	SAM	[87]
H_2TDHexDTDPDPc	Au	--	Spin-coat	[87]
Amino-functionalized phthalocyanines				
CoTAPc	OPG	2-AET	Adsorbed	[88]
CoTAPc	VCE	2-ME	Adsorbed	[89]
CoTAPc	VCE	2-MESA	Adsorbed	[89]
CoTAPc	VCE	Cysteine	Adsorbed	[89]
CoTAPc	VCE	Glutathion	Adsorbed	[89]
CoTAPc	VCE	2-ME	Polymer	[89-91]
CoTAPc	VCE	2-ME	Adsorbed	[91]
CoTAPc	VCE	2-MESA	Polymer	[89]
CoTAPc	VCE	Cysteine	Polymer	[89]
CoTAPc	VCE	Glutathion	Polymer	[89]
CoTAPc	VCE	2-ME	Drop-dry	[90]
NiTAPc	VCE	Dopamine	Polymer	[92]
MnTAPc	Pt	PON	Polymer	[93]
CoTAPc	GCE	Sulfide	Polymer	[94]

Table 1.1 Continued.

CoTAPc	GCE	2-ME	Polymer	[94]
CoTAPc	HOPG	Sulfide	Polymer	[94]
CoTAPc	HOPG	2-ME	Polymer	[94]
CoTAPc	Au	O_2	SAM	[95]
CoTAPc	Ag	O_2	SAM	[95]
MnTAPc	ITO	--	Spin-coated	[96]
NiTAPc	BPPGE-SWCNT	NO	Polymer	[97]
NiTAPc	BPPGE	NO	Polymer	[97]
CuTAPc	Pt	Cysteine	Polymer	[98]
FeTAPc	GCE	Hydrazine	Polymer	[99]
FeTAPc	GCE	Hydrazine	Adsorbed	[99]
CoTAPc	GCE	Hydrazine	Polymer	[100,101]
CoTAPc	SnO_2:F Glass	Hydrazine	Polymer	[100]
H_2TAPc	GCE	Hydrazine	Polymer	[100]
H_2TAPc	SnO_2:F Glass	Hydrazine	Polymer	[100]
CoTAPc	GCE	--	Polymer	[102]
CoTAPc	ITO	--	Polymer	[102]
ZnTAPc	GCE	--	Polymer	[102]
ZnTAPc	ITO	--	Polymer	[102]
CoTAPc	Au-DTSP	--	SAM	[103]
CoTAPc	VCE-RDE	O_2	Polymer	[104]
CoTAPc	VCE-RDE	O_2	Adsorbed	[104]
MnTAPc	GCE/ITO	Glycine	Polymer	[105]
CrTAPc	ITO/GCE	Nitrite	Polymer	[106]
MnTAPc	GCE	Nitrite	Polymer	[107]
TiTAPc	GCE	Nitrite	Polymer	[107]
CoTAPc	Graphite	Glucose	Adsorbed	[108]
CoTAPc	OPG	2-ME	Adsorbed	[109]
CoTAPc	OPG	2-HEDS	Adsorbed	[110]
CoTAPc	OPG	2-MESA	Polymer	[111]
CoTAPc	VCE	2-MESA	Polymer	[111]
CoTAPc	OPG	2-MESA	Adsorbed	[111]
CoTAPc	VCE	2-MESA	Adsorbed	[111]
CuTAPc	GCE	--	Polymer	[112]
CuTAPc	ITO	--	Polymer	[112]
CuTAPc	Au	O_2	SAM	[113]
CuTAPc	Ag	O_2	SAM	[113]
FeTAPc	Au	O_2	SAM	[113]
FeTAPc	Ag	O_2	SAM	[113]
CoTAPC	Au-AET-SWCNT	Dopamine	SAM	[114]
CoTAPc	BPPGE	DEAET	Adsorbed	[115]

CoTAPc	BPPGE-SWCNT	DEAET	Adsorbed	[115]
CoTAPc	BPPGE	Asulum	Polymer	[116]
CoTAPc	BPPGE-MWCNT	Asulum	Polymer	[116]

OBTPc – octabutylthiophthalocyanine, OHETPc – octahydroxythiophthalocyanine, TAcETPc – tetraacetoxyethylthiophthalocyanine, [HHexTPc]2NO2 – bis hexahexylthiophthalocyanine methoxynitrate, OPTPc – octaphenylthiophthalocyanine, TPTPc – tetraphenylthiophthalocyanine, TDEAETPc – tetradiethylaminoethylthiophthalocyanine, TDTPc – tetradodecylthio phthalocyanine, ODTPc – octadodecylthiophthalocyanine, dONCSPc – dioxananocosane sulfonylphthalocyanine, TDMPc – tetradodecylmercaptophthalocyanine, TOTPc – tetraoctyl thiophthalocyanine, OOTPc – octaoctylthiophthalocyanine, TDHHexDTDPDPc – tetradecakishexyldithio-dipropyl-diphthalocyanine, HHexMPMePc – hexahexyl-22-mercaptopropyl-25-methylphthalocyanine, HHexMOMePc – hexahexyl-22-mercaptooctyl-25-methyl phthalocyanine, HHexMSOMePc – hexahexyl-22-mercaptosulfonyloxyoctyl-25-methyl phthalocyanine, dOMeOAcTPPc – dimethoxy-octaacetylthio-tetrapentylphthalocyanine, MeEtTOOPPc – methoxyethylthiooctapentylphthalocyanine, TAPc – tetraaminophthalocyanine, VOC – volatile organic compounds, SAM – self-assembled monolayer, VCE – vitreous carbon electrode, 2-ME – 2-mercaptoethanol, 2-MESA – 2-mercaptoethanesulfonic acid, 2-AET – 2-aminoethanethiol, PON – peroxynitrite, 2-HEDS – 2-hydroxyethyldisulfide, (H)OPG – highly ordered pyrollitic graphite, BPPGE – Basal plane pyrollitic graphite and DEAET – diethylaminoethanethiol.

1.3.1 Spectroscopic characterization of MPc

The absorption spectrum of MPc complexes exhibit two bands referred to as Soret or B band between 300 – 450 nm (blue region) and an intense Q band between 600 – 800 nm (red region). These absorption bands are a result of π-π^* transitions from a conjugated system. Figure 1.6 shows (a) a typical absorption spectrum of MPc and (b) Gouterman's four orbital model for the origins of the Q and B bands. The Q band according to Gouterman's model is observed as a result of the electron transition

from the a_{1u} (HOMO orbital) to e_g (LUMO orbital) while the B bands are observed as a result of the electron transition from a_{2u} or b_{2u} of HOMO orbitals to e_g of the LUMO orbital.

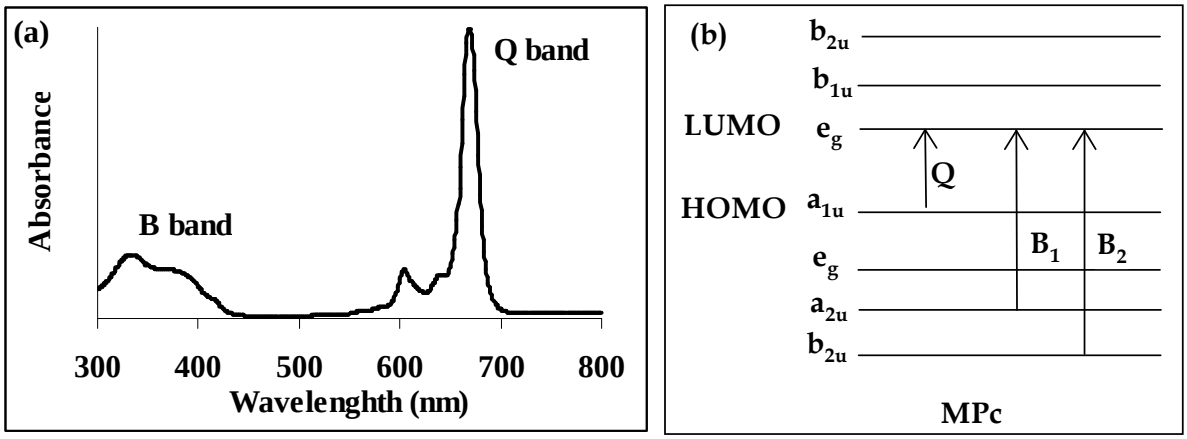

Figure 1.6: (a) Typical absorption spectrum of metallophthalocyanines and (b) Gouterman's four orbital model showing electron transitions and the origins of the Q and B band. HOMO (highest occupied molecular orbital) and LUMO (lowest unoccupied molecular orbital).

The nature and the position of the substituents on the ring of MPc will affect the position of the Q band. The electron-donating substituents will shift the Q band maxima due to a decrease in HOMO-LUMO energy gap causing the bathochromic (red) shift. The electron-withdrawing substituents have the opposite effect, i.e. they increase the HOMO-LUMO energy gap, thus leading to hypsochromic (blue) shift of a Q band [117,118]. The position, i.e. peripherally versus non-peripheral, of the substituents also affects the shift of a Q band maxima. Non-peripheral substitution causes the red-shift in the phthalocyanine Q band maxima [60,119-121], due to perturbation of the HOMO (i.e. raising its energy). Oxidation states of the metal ions within the phthalocyanine cavity also have been found to influence the position of the Q band. The metal ion with the oxidation state (+2) of the neutral MPc complex have the Q band maxima at lower wavelengths when compared to metal ions with

+3 oxidation state of neutral MPc. The solvent used for acquiring the absorption spectra also influences the Q band absorption maxima of phthalocyanines and this could be attributed to coordinating and disaggregation properties of the solvent. For an example, solvents that can coordinate to the central metal ion can result in the Q band shift to higher wavelengths [122]. In the absorption spectra there are other absorption bands that may be observed between 450 – 650 nm region and these bands are attributed to charge-transfer transitions from metal to phthalocyanine ligand (MLCT) or from the phthalocyanine ligand to metal (LMCT) [60].

1.3.2 Electrochemical properties of MPc

Phthalocyanines are electron rich and they exhibit several electrochemical redox processes due to the fact that they can accept and donate electrons. The metal free phthalocyanine ligand shows electrochemical activity occurring at the conjugated ring system. The oxidation of the ring involves successive removal of electrons from the HOMO and the reduction involves successive addition of electrons from the LUMO orbitals. The phthalocyanine exists as a dianion, Pc(-2), at its neutral state. The oxidation of the Pc(-2) leads to the removal of the two electrons from the HOMO (a_{1u}) and the formation of Pc(-1) and Pc(0) π-cation species [123]. The reduction of the Pc(-2) which is the addition of electrons in the e_g (LUMO) results in the formation Pc(-3), Pc(-4), Pc(-5) and Pc(-6) π-anion species [124,125]. The e_g orbital is doubly-degenerate and therefore can accommodate four electrons for possible reduction of Pc(-2). The band gap between the first oxidation redox peak and the first reduction redox peak of the metal-free phthalocyanine ring is ~1.6 V [126] and the substituents on the ring systems determine how big or small this band gab. When the electroactive metal ion is included into the phthalocyanine ring cavity, the redox processes due to the central metal are observed in between the phthalocyanine ring

processes [127]. Similar to the absorption spectrum, electrochemical properties of the phthalocyanines are affected by several conditions, i.e. solvent used, nature of the molecule and the substituents on the phthalocyanine ligand [128,129]. Spectroelectrochemistry technique which combines the use of UV-vis spectroscopy with electrochemical perturbation at various applied potentials is used to assign the observed electrochemical properties of the phthalocyanines redox processes [130,131]. Ring-based redox processes due to either oxidation (forming π-cation radicals) or reduction (forming π-anion radicals) results in the disappearance of the Q band and the formation of new bands at 500 – 600 nm [132-135]. During the spectroelectrochemical measurement, the solution within the reaction cell changes colour [132,136]. If the redox processes during spectroelectro-chemical experiment are metal-based, the shift in the Q band occurs and the intensity of the Q band is not affected [132]. In the cases where the complex has charge-transfer bands (MLCT or LMCT) these may either be formed or lost during the spectroelectrochemistry experiment.

Spectroelectrochemistry, UV-vis and electrochemistry methods are used for the characterization of new phthalocyanine complexes in this thesis.

1.3.3 Electrocatalytic applications of MPcs

This study will investigate the electrocatalysis of H_2O_2 electrochemical reactions using MPc complexes and their conjugates as electrode modifiers. Electrocatalysis, by definition, is an increase of rate of electron transfer of electrochemical reactions by using a catalyst (electrocatalyst). The electrocatalysts used in this work are MPc complexes. The use of MPc complexes as electrocatalysts and for electrocatalytic studies requires their immobilization onto electrode surfaces. At bare surfaces some

reactions occur slowly (i.e. at high overpotentials) or do not occur. MPc complexes, if used as electrocatalysts on the electrode surfaces, promote or facilitate these reactions and reduce their overpotentials. The examples of such reactions are thiol oxidation [137,138], hydrogen peroxide oxidation or reduction [139,140] and oxygen reduction [141,142] as shown in Table 1.1 (above). The interest in the study of H_2O_2 electrocatalysis is due to the potential that these systems possess in the study of enzymatic-based reactions. There are a few reports on MPc-based H_2O_2 electrocatalysis [139,140] and very few of these are on gold electrode surfaces [143]. The gold surface is an inert material and offers variable methods for their surface modifications, e.g. SAMs and grafting, electropolymerization, to name but a few. The applications of MPc complexes also results in the reduction of overpotential of analyte oxidation or reduction reactions and also increase current densities [53,144,145]. Figure 1.7 shows a schematic representation of electrocatalytic reaction and the effect of the presence of the mediator between the electrode and the substrate.

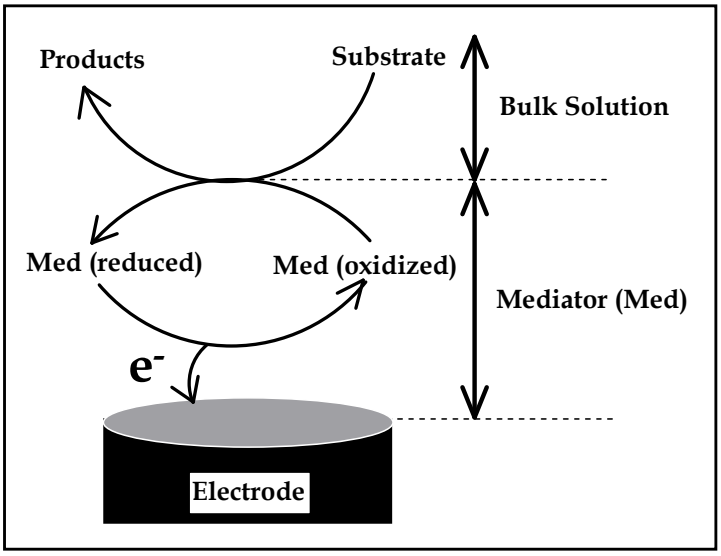

Figure 1.7: Schematic representation of electrocatalytic reaction with the mediator between the electrode and the substrate.

The MPc complexes which contain cobalt, iron and manganese as electroactive central metal ions possess good electroactivity towards various analytes. The electrocatalysis processes generally occur at potentials close to where metal ion redox process takes place or on the ring system. The example of the MPc electrocatalyzed mechanism is the thiol (RSH) oxidation [137], equations 1.1 – 1.3. First, the central metal ion, if $M^{II}Pc^{-2}$ is employed, undergoes oxidation from $M^{II}Pc^{-2}$ to $M^{III}Pc^{-2}$, equation 1.1. The thiol (RSH) is oxidized by the $M^{III}Pc^{-2}$ to form a radical ($RS^{\cdot}$), equation 1.2. During the oxidation of RSH the radical $RS^{\cdot}$ forms and the electrocatalyst is regenerated to $M^{II}Pc^{-2}$, equation 1.3. Two $RS^{\cdot}$ radicals combine to form a disulphide product (RSSR) [146]. Equations 1.4 – 1.6 show ring-based mediated electrocatalytic oxidation of thiol [137,147].

$$M^{II}Pc^{-2} \longrightarrow [M^{III}Pc^{-2}]^{+} + e^{-} \quad (1.1)$$

$$[M^{III}Pc^{-2}]^{+} + RSH \longrightarrow M^{II}Pc^{-2} + RS^{\bullet} + H^{+} \quad (1.2)$$

$$2RS^{\bullet} \longrightarrow RSSR \quad (1.3)$$

$$M^{II}Pc^{-2} \longrightarrow [M^{II}Pc^{-1}]^{+} + e^{-} \quad (1.4)$$

$$2[M^{II}Pc^{-1}]^{+} \longrightarrow ([M^{II}Pc^{-1}]^{+})_2 \quad (1.5)$$

$$[M^{II}Pc^{-1}]^{+} + RS^{-} \longrightarrow M^{II}Pc^{-2} + RSSR \quad (1.6)$$

1.3.4 Electrode modification

The choice of the working electrode materials is governed mainly by their useful potential range in a particular environment (solvent, electrolyte) for the reactions to be studied. Several electrode materials used as working electrodes range from noble metal electrodes (gold and platinum), carbon electrodes (glassy carbon, carbon paste

and pyrolytic graphite) and glassy indium tin oxide (ITO). The emergence and use of screen-printed electrodes (SPE) has also introduced several working electrode materials since inks (and their different compositions) can be printed on ceramic or plastic sheets. In this study, conventional electrodes (gold, glassy carbon electrode and indium tin oxide) and screen-printed gold electrodes have been used. Table 1.1 shows which electrodes have been employed with thiol-functionalized MPc or tetra-amino MPc complexes, the analytes detected and the method used for the electrodes modification. SPEs have not been thoroughly used for the MPc studies, hence their use in this work. The method of modifying these electrodes with MTAPc complexes is new and reported for the first time here.

The studies conducted on conventional electrode surfaces are aimed at using these systems as a preliminary step before being adapted onto screen-printed electrodes. On the conventional electrodes, the surface modification and pre-treatment can be achieved by first polishing and regeneration to expose new surfaces. The conventional electrode pre-treatment steps is a tedious and time consuming step; hence the use of SPEs. For SPEs, different surface materials can be printed onto ceramic substrates [148,149] or flexible polymeric materials [150-155]. The SPEs are highly miniaturized when compared to the conventional electrodes and they are more applicable in biological systems where their small size enables facile maneuvering [156,157]. In addition to their ability to be miniaturized, SPEs also allows for small volume applications and avoid electrolyte leakage problems [156,158]. The SPE method of preparation is amendable to mass production at low cost with high reproducibility. The other advantage of using screen-printed electrodes is that they are disposable and highly reproducible.

There are several reported methods for modifying electrodes with electrocatalytic materials and these depend on (i) the electrode material, (ii) properties of the

electrocatalytic materials, (iii) analytes to be detected and (iv) the reaction type to be studied. In this study, MPc as electrode modifiers will be used and their thin film forming properties and methods are discussed.

The modification of electrode surfaces with MPc complexes has been studied and the methods used include Langmuir-Blodgetts (LB) films [137,159-162], electropolymerization [104,112,163,164], drop dry [137,165,166], self-assembly [67] and covalent immobilization [167]. Several other methods are described in Table 1.1. Each method has its own advantages and disadvantages. The purpose of investigating the methods of forming MPc thin films is aimed at finding a simpler, cost effective, stable and reproducible method with good control of the MPc orientation and surface functionality. Amongst several different ways of modifying electrodes self-assembly, electropolymerization and electrochemical grafting are the methods used in this study for the immobilization of electroactive MPc complexes and biomolecules, hence are discussed below.

1.3.4.1 Electropolymerization

Electropolymerization is the method used for the electrosynthesis of polymeric materials onto electrode surfaces. This method involves the repetitive cycling (using cyclic voltammetry) of a monomer containing solution to an activated form that will polymerize to form a polymer film. In electrochemistry, it is of importance that the polymers form good electron conducting films and this further promotes the formation of the polymers. During the formation of the polymer, less pinholes are formed since polymerization at exposed (pinholes) sites on the electrode surface is accentuated. The formation of the insulating polymeric film will lead to the passivation of the electrode [168]. During the polymer growth the increase in peak

current and/or formation of new peaks are indicative of the formation of the polymer as shown in Figure 1.8. The advantages of electropolymerization are that precise film thickness and rate of film deposition can be maintained by (i) varying the potential/current conditions of the working electrode and (ii) limiting the number of cycles during the electropolymerization.

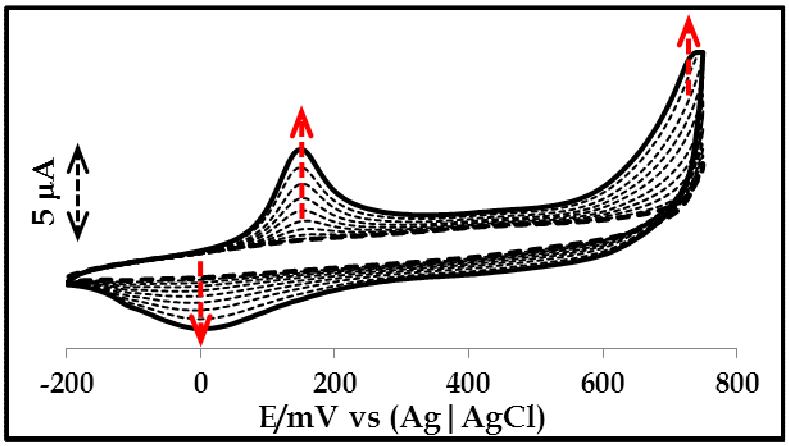

Figure 1.8: Repeated cyclic voltammograms showing the electropolymerization and formation of polyaniline onto gold electrode (unpublished work). Scan rate = 0.05 V/s.

The several functional groups which may be attached to Pc ring and known to undergo polymerization include phenols [169], arylamines or amines [170,171], and pyrrole [172-175]. Scheme 1.3 shows the polymerization mechanism of tetra-aminophthalocyanine complexes upon the oxidation of the amino group of the monomer.

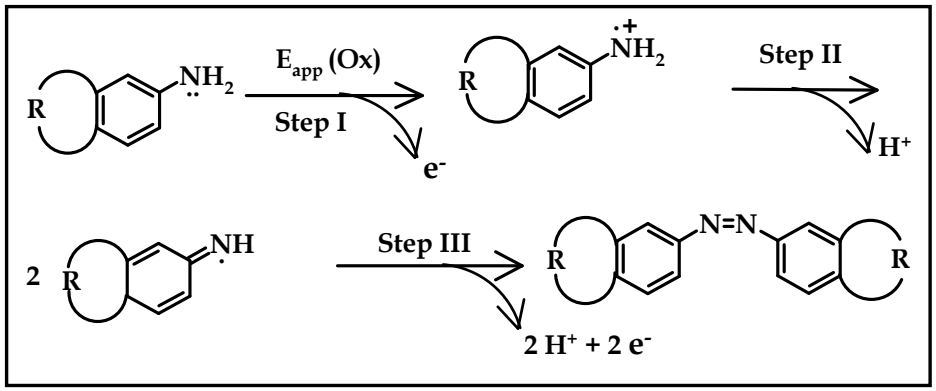

Scheme 1.3: Schematic diagram of electropolymerization of metal tetra-amino phthalocyanine monomer. R represents the rest of the Pc molecule [112].

Step I (in Scheme 1.3), is the oxidation of the NH_2 group, step II - the loss of a proton from the radical cation and step III - the N=N oxidative coupling of the phthalocyanine monomers. The driving force to the stability and hence the formation of oligomers and polymers from the radicals is the desire to return to aromaticity.

The following experimental variables govern the polymer growth mechanism [176]:

i) The nature of monomer employed, in particular its solubility,
ii) Nature of the counter ion employed,
iii) The polymerization solvent. The monomer should have an oxidation potential which is accessible via a suitable solvent system,
iv) The nature and size of electrode,
v) The electrochemical conditions: i.e. monomer must produce radical cations which react more quickly with other monomer radicals to form the polymer.
vi) The monomer should produce a polymer with a lower oxidation potential if the material is to be produced in a state that has a higher conductivity.

The motivations for studying polymers of metal tetra-aminophthalocyanine (polyMTAPc) complexes are as follows:

(i) They form good conducting layers on electrode surfaces and reported here is their polymer formation on gold electrode surfaces.
(ii) The electrocatalytic properties of polyMTAPc onto gold and carbon electrode will be studied for their potential for H_2O_2 electrocatalysis and this (to the candidate's knowledge) will be for the first time is done.
(iii) The immobilization of the polyMTAPc on different electrode surfaces will be studied to ascertain the effect of electrode surface material (carbon, gold and ITO) on the polymer material that forms.

1.3.4.2 Self-assembled monolayers (SAMs)

Molecular self-assembly is the method of immobilizing amine or sulfur-containing molecules onto coinage metal surfaces (gold, silver and copper) forming a monolayer thin film [177-181]. The self-assembly method by definition is the spontaneous adsorption of an appropriate molecule from its solution directly onto the surface of an appropriate substrate (coinage metal surfaces) thus forming an ultrathin film of monolayer thickness [177,180,181]. The formation of SAMs onto metal surfaces results in the controlled immobilization of molecular assemblies due to chemisorption with a strong covalent thiolate (Au-S) bond [179] in the case of gold. This phenomenon was first demonstrated by Nuzzo and Allara in 1983 when they showed the adsorption of sulfur-containing compounds onto gold surfaces forming self-assembled monolayer (SAMs) [182]. A few years later in 1987-1988, several groups published numerous papers [183-191] on SAMs and these were believed to have increased the interest of self-assembly method. The formation of SAMs is via chemisorption which is an irreversible adsorption of electroactive substances on

electrode surfaces through a covalent bond interaction [192-196]. SAMs of alkanethiol derivatives and thiol substituted phthalocyanines [197-199] form organic layers on gold and their properties are mostly controlled by the end groups (in alkane thiols) or the electroactive nature of the MPc complex. The use of SAM's method for the immobilization of thiol-derivatized MPc complexes is summarized in Table 1.1.

SAMs have been used for studying the theory of heterogeneous electron transfer [200,201], design of chemical and electrochemical sensors [178,202,203], in non-linear optics [202] and biosensors [204-214]. SAMs are especially relevant to electrochemical phenomenon in corrosion, electroanalysis and electrocatalysis. The use of SAMs has also been demonstrated in the stabilization of metal nanoparticles with hydrophilic ligands bearing –SH and several other functional groups, such as OH, CO_2H and NH_2 and their possible use in biomedical and pharmaceutical [215-218].

There are currently three methods for forming MPc-SAMs onto gold electrode surfaces. The first approach involves the synthesis of MPcs bearing sulphur or thiol substituents and followed by their immobilization as thin films onto gold electrode surface [67-70,197], Figure 1.9(a). The second strategy involves pre-modification of the electrode surface with a SAMs that allows for axial ligation with the metal ion within an MPc complex [219], Figure 1.9(b). The third strategy involves the use of a ring-based covalent attachment of the MPc molecule with complimentary functional groups to the terminal functional group of a pre-formed SAM [103,220,221], Figure 1.9(c). Alternatively, the vertically oriented MPc SAM can form when MPc complexes have a single thiol substituent in-contact with the surface [80,87], Figure 1.9(d). These strategies result in the attachment of MPcs as SAMs onto the gold electrode surfaces via the sulphur groups and also lead to three types of MPc SAM orientation on the gold electrode surface; Figure 1.9(a) octopus, Figure 1.9(b) umbrella and Figure 1.9(c and d) vertical orientations.

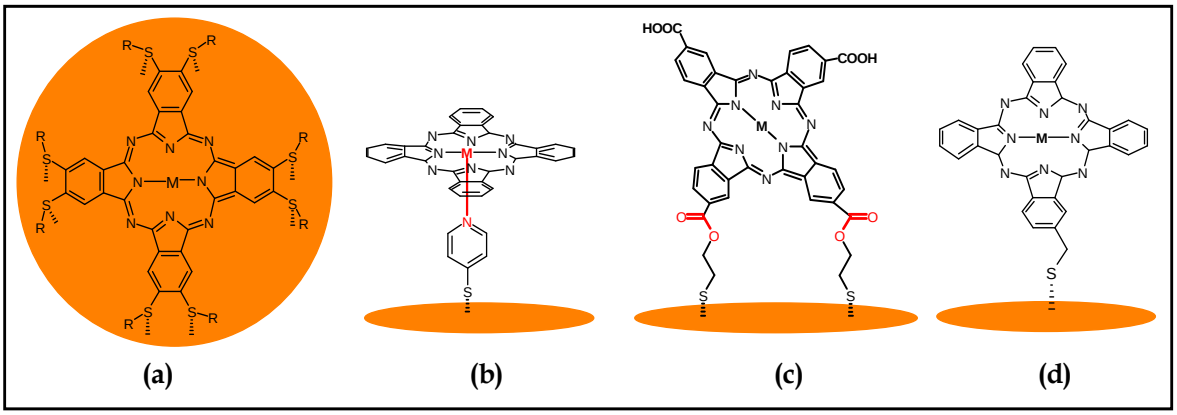

Figure 1.9: Diagram showing the different immobilization strategies and orientations of MPc-SAMs on gold electrodes.

The orientations of MPc-SAMs in Figure 1.9 are governed by the number and the position of thiol substituents on the MPc molecule. The formation of closely-packed monolayer is time dependent, i.e. the longer the deposition time the more compact, well-ordered and defect-free is the SAMs. The difficulty and multistep reactions involved in the synthesis of thiol substituted MPcs has resulted in rather limited number of reports on their fabrications as SAMs.

This study investigates the synthesis of cobalt and manganese phthalocyanine complexes bearing hexylthio substituents at peripheral and non-peripheral positions. The thiol substituted MPc complexes are now well known (Table 1.1) and most of these complexes contain different metal ions and different functional groups. There are a few numbers of these complexes containing manganese as the central metal ion. Also most of the complexes are substituted at the peripheral position instead of the sterically hindered non-peripheral position of the Pc ring, which may affect the redox activity. The interest in MnPc complexes is due to their complex electrochemistry. For example the products formed on reduction of $Mn^{II}Pc$ complexes are not clearly understood, with some reports suggesting the formation of $Mn^{II}Pc^{-3}$ (ring based

reduction) and others $Mn^{I}Pc^{-2}$ (metal-based reduction) [60,222]. Thus the study of new MnPc complexes is of importance in elucidating the electrochemistry of these complexes and contributing to this interesting field of study. The interest in CoPc derivatives that are easily oxidized is of importance, since the oxidation of analytes may occur at lower oxidation potentials. The effect of peripheral versus non-peripheral substitution is also important for the design of phthalocyanines and studying their electrocatalytic properties. The ability of the MOcHexTPc (metal octahexylthio phthalocyanine) complexes (**12-14**) to form self-assembled monolayers on the gold electrode surface is reported.

The characterization of SAMs can be achieved using several surface techniques such as FT-Raman and infrared spectroscopy, X-ray photoelectron spectroscopy, electrochemistry and scanning-probe microscopy. Electrochemical techniques, particularly cyclic voltammetry have been employed to investigate the integrity of SAMs on gold electrodes. Since the chemisorbed species in SAMs are surface confined, the redox centers are close to the electrode surface and therefore surface properties can be studied. The peak current (I_p) of surface confined species is directly proportional to the scan rate defined by the equation 1.7:[180,181]

$$I_p = \frac{n^2F^2A\Gamma\nu}{4RT} \qquad (1.7)$$

where A = surface area of the electrode, n is the number of electrons, F is Faraday's constant (96,485 Coulombs.mol^{-1}), T is temperature (K), R is universal gas constant and Γ = total surface coverage by electroactive species defined by equation 1.8.

$$\Gamma = \frac{Q}{nFA} \qquad (1.8)$$

Q is the charge under the redox active peak (Coulombs) and other symbols are as described for equation 1.7. In strong alkaline solution, SAMs may undergo oxidative (equation 1.9) or reductive (equation 1.10) desorption. The charge (Q) under

desorption peaks may be used to calculate surface concentration (Γ) of the SAMs. The theoretical relationship in accordance to equation 1.8, above [177,180,181] is used.

$$\text{Au-SR} + 4OH^- \longrightarrow \text{Au} + RSO_2^- + 2H_2O + 3e^- \qquad (1.9)$$

$$\text{Au-SR} + e^- \longrightarrow \text{Au} + RS^- \qquad (1.10)$$

The formation of a closely-packed pinhole-free SAMs is usually shown by the inhibition of gold surface oxidation, probably by the exclusion of water [180,181]. The area (Q_{Bare}) under the reduction or stripping peak is a true measure of the total pinhole area available for an undisturbed penetration of ions present in the working solution. After the SAMs have formed on the electrode surface, (Q_{SAM}) gives the "ion barrier factor" (designated herein as Γ_{ibf}), equation 1.11:

$$\Gamma_{ibf} = 1 - \frac{Q_{SAM}}{Q_{Bare}} \qquad (1.11)$$

The total charge of bare and SAMs modified surfaces, Q(μC), is obtained by integrating the currents (μAs^{-1}). The inhibition of copper deposition during the underpotential deposition (UPD) from the $CuSO_4$ solution and the suppression of Faradaic processes, such as $Fe[(CN)_6]$ and $Fe[(H_2O)_6]$, may also be used to determine the blocking behaviour of the formed SAMs [177,180,181].

1.3.4.3 Electrode grafting

This method of modifying electrode surfaces was discovered two decades ago (1992) by Pinson and coworkers [223] and uses aryl diazonium compounds to be grafted onto an electrode surface of choice. It is based on the electrochemical reduction of aryl diazonium salt thus creating an aryl radical that is grafted onto the electrode

surfaces. Diazonium salts are commercially available and different functional groups such as carboxylic acid (-CO_2H) and nitro (-NO_2) may be incorporated. The functional groups of the immobilized diazonium salt have been used for the attachment of electroactive species such as ferrocene [224,225], cobalt tetracarboxyphthalocyanine (CoTCPc) [167] and biomolecules [226-231]. Apart from their commercial availability, diazonium salts can also be synthesized following reported methods [226,232,233] using aryl amines or functionalized aryl amines for specific applications. Grafting reactions involving diazonium salts have been explored for the functionalization of carbon nanotubes [234-238].

Figure 1.10 shows the method by which aryl diazonium salt is grafted or covalently attaches onto the electrode surface. The electrochemical reduction results in the loss of N_2 and the generation of aryl radical which then attaches onto the electrode surface [167,239] via the C-C bond (for carbon-based electrode surfaces) or M-C bond (for metal-based electrode surfaces). The bond formed during the attachment of aryl radicals is strong and stable enough to enable application in extreme conditions [240,241]. The majority of the work studied using diazonium electrode fabrication has been conducted on the carbon surfaces [167,224-230,239-246], different metal surfaces [225,226,241,246-253] with a few reports on gold surface modification [225,226,241,246,247,249,250]. The majority of the reported studies on diazonium gold electrode modification are on basic research, i.e. studying the immobilization of diazonium and the mechanism of how the electrode modifications occur. The applications of the diazonium modified electrode for detection and monitoring various analytes is of importance, especially in demonstrating the stability and applicability that this method offers compared to other methods.

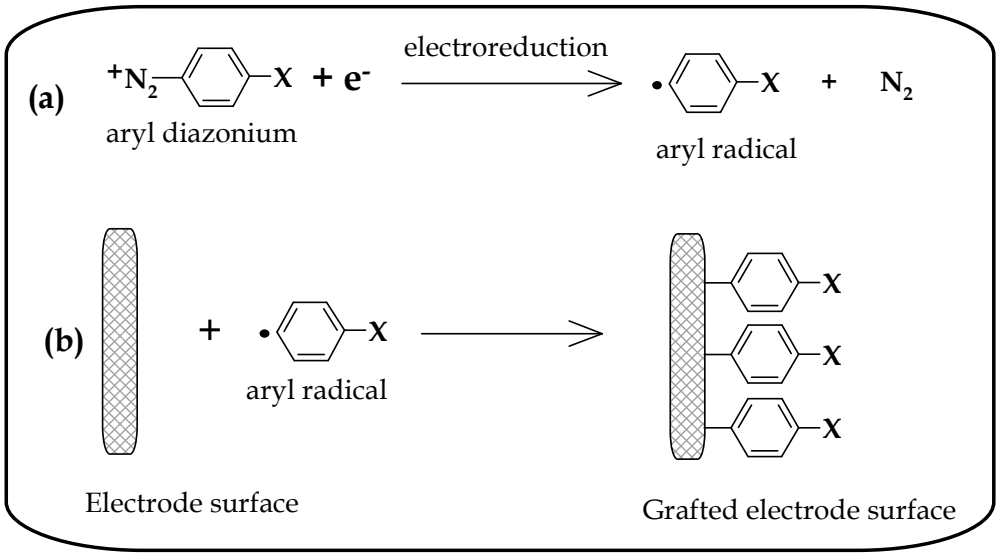

Figure 1.10: Electrode surface modification with aryl diazonium salt or functionalized aryl diazonium salt at position X (with any functional group of interest).

In this study, new method of covalently immobilizing electroactive metal tetra-amino phthalocyanine (MTAPc) complexes via Schiff-base reactions onto screen-printed gold electrodes pre-grafted with phenylamino monolayer is reported. The newly fabricated electrochemical systems with MTAPc monolayers will be studied for their electrocatalytic properties towards the detection and monitoring of hydrogen peroxide. This study will further explore the use of gold surfaces for the covalent immobilization of carbon nanotubes and electroactive MPc complexes as hybrids onto pre-grafted electrodes and investigation of their electrocatalytic applications.

1.3.5 H_2O_2 electrocatalysis using MPc complexes

Hydrogen peroxide (H_2O_2) as model analyte will be studied using MPc complexes immobilized onto gold and carbon electrode surfaces following different methods as already discussed. The choice of studying H_2O_2 was due to its importance in biomedical, environmental and industrial applications [254-260]. H_2O_2 is an

important oxidant for various industrial applications as a strong bleaching agent and it is produced as a by-product of many enzymatic reactions with flavin adenine dinucleotide (FAD) redox co-factor [261,262]. Several methods have and are being investigated for determination of H_2O_2 and these methods are electrochemistry [140,263-267], chemiluminescence [268], spectrometry [269], chromatography [270] and titrimetry [271]. Electrochemical methods are preferred for reasons already discussed. The materials studied for the detection of H_2O_2 are either biological molecules or electroactive synthetic compounds. The biological molecules studied are horse-radish peroxidase (HRP), catalase, cytochrome P-450 and myoglobin enzymes which are known to contain heme moiety as a redox active centre and responsible for electrocatalytic or enzymatic conversion of H_2O_2 to H_2O [34,272,273]. The electroactive synthetic compounds that have been employed for the H_2O_2 electrocatalysis are MPc and metal porphyrin complexes [140,265,274,275] and nanostructured materials and their conjugates [143]. Table 1.2 shows MPc complexes that have been reported for the electrocatalytic detection of H_2O_2; i.e. the electrode materials used, method of modification, H_2O_2 peak potential and limit of detection (LoD)[139,140,276-280]. From Table 1.2, one can clearly see that the use of MPc complexes for H_2O_2 electrocatalysis has not been exhausted. Therefore, there is a need to find new and innovative ways of electrode fabrication using MPc complexes for H_2O_2 electrocatalysis and these will be studied further in this thesis. New methods of detecting and monitoring H_2O_2 are still needed and this is due to the fact that the methods used currently are: (i) irreproducible (i.e. uses drop-dry method for the immobilization of the electrocatalysts), (ii) limited shelf-life (i.e. utilizes enzymes which denature easily), (iii) chemically and thermally unstable (i.e. SAMs and a layer-by-layer (LBL) self-assemby methods). The LBL method is based on complementary charge alternation adsorption of materials and this may also be affected by the pH variation and the solution ionic strength. The quest of further

investigation of systems that can detect H_2O_2 is also important in finding systems that can be employed as mediators for enzyme-based bioelectrocatalysis.

Table 1.2: Electrodes modified with MPc complexes for the electrocatalytic detection of H_2O_2 and the parameters obtained, i.e. E_p - peak potential, oxidation (ox.) or reduction (red.), LoD (limit of detection).

MPc Complex	Electrode	Method of modification	Medium	H_2O_2, E_p (V) ox. (red.)	LoD (μM)	Ref.
CoPc-$(CoTPP)_4$	GCE	Drop-Dry	pH 7.0 (pH 10[a])	0.45 (0.55[a])	80 (20)	[140]
CoPc	GCE	Drop-Dry	pH 7.0	0.40	---	[140]
CoPc	CPE	Paste	pH 7.4	0.50	---	[276]
CoPc	Sol-Gel	Paste	pH 7.4	0.30	---	[276]
CoPc	SPCE	Paste	pH 9.2	0.63 (-0.35)	---	[139]
FePc	SPCE	Paste	pH 9.2	0.16 (-0.16)	---	[139]
MnPc	SPCE	Paste	pH 9.2	0.35 (-0.61)	---	[139]
CoPc	SPCE	Paste	pH 7.3	0.4	---	[277]
FeTSPc	Au/PPy	Polymer	0.5 M H_2SO_4	0.7[b]	---	[278]
CoTSPc	Au/PPy	Polymer	0.5 M H_2SO_4	0.05[b]	---	[278]
CoPc	SPCE	Paste	pH 7.3	0.6	70	[279]
nanoCoPc	PGE	Drop-dry	pH 7	0.60	---	[280]
CoPc	PGE	Drop-dry	pH 7	0.58	---	[280]
nanoFePc	Au-DMAET-SWCNT	Layer-by-layer	pH 7.4	---	550	[143]

[a] Refers to the different pH used (pH 10). CoPc (cobalt phthalocyanine), CoTPP (cobalt tetra-phenyl porphyrin), FePc (iron phthalocyanine), MnPc (manganese phthalocyanine), FeTSPc (iron tetra-sulfonated phthalocyanine), CoTSPc (cobalt tetra-sulfonated phthalocyanine), PPy (polypyrrole).

The aim of this study:

- This study will investigate the use of MPc complexes and their carbon nanotube conjugates immobilized onto electrode surfaces as electrocatalysts for the determination of H_2O_2 in physiological conditions.

- Different methods of immobilizing MPc complexes onto the electrode surfaces will also be studied to perceive their advantages towards H_2O_2 electrocatalysis.

1.3.6 Aims of using MPcs in this work

a) New MPc complexes containing electroactive metal ions, such as manganese (Mn) and cobalt (Co), at the center of the ring system and also bearing eight hexylthio groups at the peripheral and non-peripheral positions are investigated their electrochemical properties.

b) The ability of these new MPc complexes to form SAMs will be studied and the effect of point of substitution towards electrocatalysis of H_2O_2 will also be evaluated for the first time using MPc-SAMs modified electrodes.

c) The immobilization of polyMTAPc complexes (with Co and Mn) onto gold electrode surfaces will be studied and their electrocatalysis towards H_2O_2 detection will be investigated.

d) Covalent immobilization of MTAPc complexes as monolayer onto pre-grafted electrode surface will be investigated using Schiff-base reactions for the first time

onto screen-printed gold electrodes. The surface characterization, electrocatalytic and electrocatalysis properties of the MTAPc monolayer will be studied.

e) Nanomaterials and MPc hybrids will be immobilized onto screen-printed gold electrode surfaces via Schiff-base reaction and these systems will be studied their electrocatalytic and electrocatalysis properties towards detecting H_2O_2.

1.4 Nanostructured material applications in electrochemistry

The revolutionary presentation in 1959 by Feynman titled "*There's plenty of room at the bottom*" [281,282] is believed to have invigorated the interest in the materials with small sizes, i.e microscale and nanoscale sizes. Merely a decade after this talk, in 1978 there was a discovery of carbon nanotubes by Wiles et. al. [283] and these nanostructured materials were made popular by Iijima's [284] rediscovery in 1991. The application of nanomaterials (i.e. carbon nanotubes) in this study is directed at investigating their electrochemical properties, i.e. their effect as electrode modifiers. In this section, the introduction of carbon nanotubes and their desired properties in electrochemical applications will be discussed.

The carbon nanotube materials are characterized as single-walled (SWCNT) and multi-walled carbon nanotubes (MWCNT). The SWCNT is a single graphite sheet rolled to form a tube and the MWCNT is multiple overlaying of graphite sheets rolled together as shown in Figure 1.11. Nowadays, it is possible to form double-walled carbon nanotubes (DWCNT) [285,286].

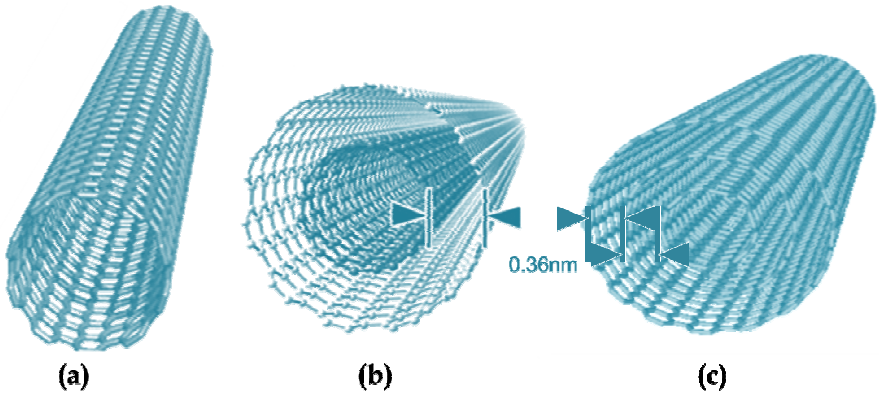

Figure 1.11: Illustration of (a) single-walled carbon nanotubes, (b) double-walled carbon nanotubes and (c) multi-walled carbon nanotubes.

The applications of SWCNT are very wide and an attempt to review all the work reported since their discovery would not do justice to this area of research. Majority of research applications where carbon nanotubes are used, exploit their unlimited properties, such as tremendous mechanical strength [287,288], thermal conductivity [289], high surface area [290], electronics [291], optical [292,293], photophysical [294] and electrochemical [295] properties, to name but a few. Electrochemical properties of carbon nanotubes will be explored in this study for the design and fabrication of sensors and biosensors. The applications of carbon nanotubes in electrochemical sensing require their immobilization onto electrode surfaces as electrocatalysts. Carbon nanotubes in electrochemistry have been found to enhance electron transfer when compared to other carbon based material. Carbon nanotubes as-prepared are insoluble in organic and aqueous solution, hence the need to functionalize them for increased solubility [235]. The most commonly used method for functionalization of carbon nanotubes is using acid treatment. This method introduces –COOH groups onto carbon nanotubes, hence making them soluble in organic solvents [296-300]. For immobilization of these materials onto electrode surfaces these functional groups are useful. The acid groups from the carbon nanotubes may further be used for the formation of amide or ester linkages with the surface functionalities or other compounds for the formation of hybrid systems. Other methods of functionalizing carbon nanotubes using grafting or derivatization have also been explored [301,302]. Several methods of immobilizing carbon nanotubes and their metallophthalocyanine conjugates on electrode surfaces have become a subject of research interest. The most recent studies involved, (i) the forming a CNT-MPc conjugate followed by the conjugate immobilization onto the electrode surfaces via drop-dry [303-305], (ii) covalent attachment of the CNT onto electrodes followed by MPc onto SAM's electrode surfaces [114,306] and (iii) using electrostatic charge alternation to adsorb the CNTs and MPcs onto an electrode surface via layer-by-layer method [143]. These methods have been employed in the electrocatalytic studies of several analytes and

the electrochemical signal was shown to improve when CNTs are used. However, these methods possess major disadvantages, hence limiting their applications. The drop-dry method is not reproducible thus leading to inconsistency in electrical signal; SAMs and layer-by-layer methods lack stability and require long immobilization times for their formation. Therefore, this thesis will investigate the covalent immobilization of CNTs onto an electrochemical grafted electrode surface for the first time. Electrochemical grafting technique provides great stability due to covalent attachment of electrocatalytic materials onto the electrode surface and the formed layers are stable under varied environmental and experimental conditions. The immobilized CNT will be studied for their potential as good electron conductors during the MPc-H_2O_2 electrocatalytic step. In comparison to the reported method [143], this thesis will present a new and stable electrode modification method and the resulting electrode will be employed for H_2O_2 determination.

Aims of using carbon nanotubes in this study:

- This study will investigate the covalent immobilization of CNTs onto an electrochemical grafted electrode surface. Electrochemical grafting technique provides great stability due to covalent attachment onto the electrode surface.
- The immobilized CNTs followed by MPc attachment, thus forming hybrids, will be studied and their potential as good electron conductors for the H_2O_2 electrocatalysis, evaluated.

This thesis investigates surface modifications for the design and fabrication of electrochemical sensors, biosensors and immunosensors; therefore the characterization of the bare and modified surfaces is an important and crucial step. Methods used for the characterication of the bare and modified surfaces are discussed in the next section.

1.5 Surface characterization techniques

Electrochemical characterization methods, expecially cyclic and square wave voltammetry, are used extensively in this thesis. In addition, electrochemical impedance spectroscopy (EIS), quartz-crystal microbalance (QCM), X-ray Photoelectron Spectroscopy (XPS), Raman Spectroscopy, Atomic Force Microscopy (AFM) and Scanninng Electron Microscopy (SEM) techniques are employed for surface characterization and also monitoring reactions taking place on the electrode surfaces. All these methods are useful in studying surface chemical properties and confirming the surface modifications.

1.5.1 Electrochemical impedance spectroscopy (EIS)

Impedance (Z or complex resistance) is obtained by applying sinusoidal potential, V(t), of a small amplitude to an electrical circuit and measure the resulting sinusoidal current, I(t), through the circuit. Therefore, the impedance is analoguous to resistance in that the impedance is described as the ratio between the applied sinusoidal potential and the measured sinusoidal current, $Z = V(t)/I(t)$. The sinusoidal potential and currents are represented as a function of time. EIS is a powerful and versatile electrochemical method used to study electrochemical properties of systems and their interfaces with conducting electrode surfaces [307-310]. The results obtained during the impedance measurements (done over suitable frequency range) can be related to the physical and chemical properties of electrode material and its modifiers. The impedance is a vector quantity with a magnitude and direction, the magnitude is Z(V/I) and the direction is represented as phase angle (θ), shown in Figure 1.12 and the notation of complex impedance is shown in equation 1.12:

$$Z = Z' + jZ'' = Z_{real} + jZ_{imaginary} \qquad (1.12)$$

where Z′ and Z″ are the real and imaginary parts of an impedance, respectively and j is a complex numer.

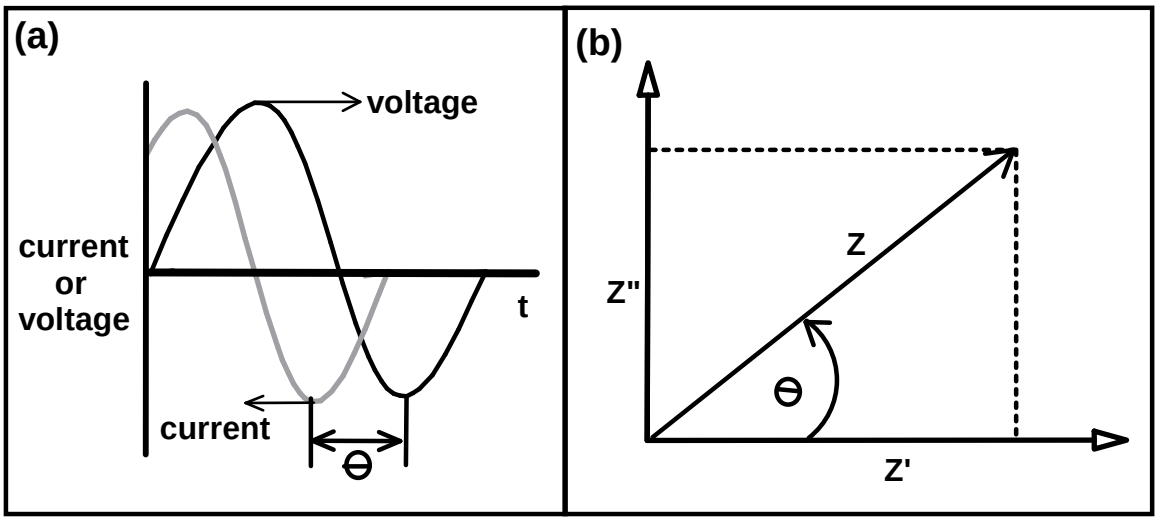

Figure 1.12: (a) Applied sinusoidal voltage and resulting current response and (b) vector representation of real (Z′) and imaginary (Z″) part of the impedance [308,309].

The impedance data can be represented and analysed as electrical equivalent circuits. The circuit consists of simple electrical elements such as resistors (resistance, R) and capacitors (capacitance, C) connected to model an electrochemical process investigated [308-310]. The resistance within the circuit represents the electrical conductivity of the electrolyte and that of the system investigated. The capacitance is either double-layer (C_{dl}) or constant phase element (CPE) and is caused by the excess charge at the electrode-electrolyte interface. The most widely used electrical circuit for the analysis of the impedance data is the Randles equivalent circuit shown in Figure 1.13 with (a) C_{dl} or (b) CPE capacitance connected. The Randles equivalent circuit shows the solution or electrolyte resistance (R_e) connected in series to the parallel combination of polarization or charge-transfer resistance (R_p) and the double

layer capacitance (C_{dl}), Figure 1.13 (a), or constant phase element (CPE), Figure 1.13(b). CPE is for the real, practical situations and occurs as a result of (i) the nature of the electrode, (ii) distribution of relaxation times due to heterogeneity occurring at the electrode-electrolyte interface, (ii) material porosity and (iv) dynamic disorder associated with diffusion [311]. In other systems, transport phenomenon might control the reaction rate and this effect needs to be taken into consideration. The measured impedance can be explained by an additional component in the electric circuit that will influence the conditions of transport or diffusion of the electroactive species and this component is called Warburg impedance (Z_w) connected as shown in Figure 1.13.

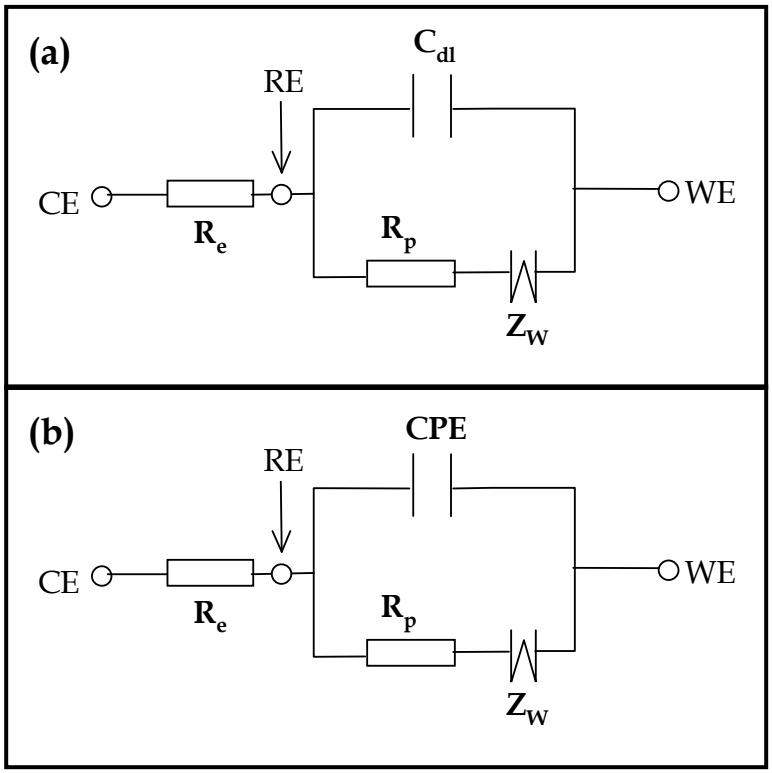

Figure 1.13: Randles equivalent circuit for an electrochemical system with diffusion-limited behavior, (a) Ideal behaviour and (b) real practical behaviour.

Amongst various graphical representations of impedance data, the Nyquist and Bode plots are the widely used. The Nyquist plot is a plot of the imaginary (Z″) versus the real (Z′) parts of the impedance, Figure 1.14(a). During the impedance measurements, the absolute impedance is measured at different frequency values as determined by the experiment. However, the Nyquist plot data representation shows no indication of the frequency where the impedance was measured. Therefore, there is a need to use another data representation for the display of the impedance measurements that gives additional frequency information at the measured impedance. The Bode plot gives the frequency information at the measured impedance [309,310]. Bode data representation is the plot of the -phase angle (ɵ) and the logarithm of impedance magnitude (log Z) versus the logarithm of the frequency (log f) as shown in Figure 1.14(b). Information about the resistance, i.e. charge transfer and solution resistance can be obtained from the Nyquist plot and the information about the nature of capacitance can be obtained from the Bode plot. The advantages that the EIS offers over other characterization techniques include (i) the use of low-amplitude sinusoidal voltage (about 5 mV) which makes the system remain at equilibrium, (ii) rapid acquisition and quantification of data such as ohmic resistance, double layer capacitance, conductivity of the film, as well as charge or electron transfer at the electrode-film interface and within the film in a single experiment, (iii) accurate, repeatable measurements can be acquired, (iv) high adaptability of this technique to different applications and (v) the characterizing interfacial properties in the absence of a redox reaction.

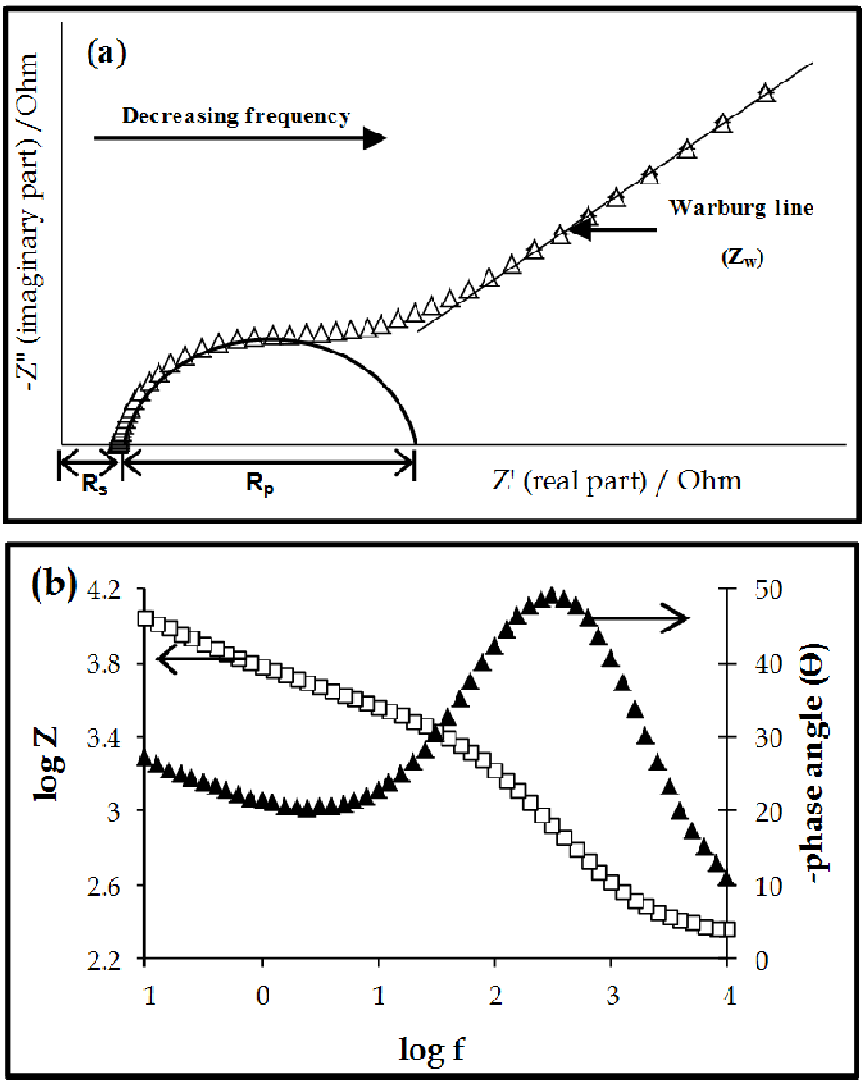

Figure 1.14: Impedance data representation (a) Nyquist plot and (b) corresponding Bode plot for Randles equivalent circuit.

1.5.2 Spectroscopic surface chacterization techniques

1.5.2.1 X-ray photoelectron spectroscopy (XPS)

XPS is an electron spectroscopic method used for the determination of chemical and elemental composition of materials or organic films on metal surfaces [180,312,313].

XPS is sometimes refered to as an electron spectroscopy for chemical analysis (ESCA) and is a well-established technique for the analysis of molecular information of organic thin films. XPS technique is based on a photoelectron effect [312,313] which occurs when the surface is irradiated with the photons (X-ray photons). The binding energy of the emitted electron is the characteristic of the atom from which it was ejected and also depends on the chemical environment of the atom. This phenomenon makes the XPS a very sensitive and material analysis technique. The use of XPS in conjunction with other surface techniques is desirable to further confirm surface modifications.

1.5.2.2 Raman spectroscopy

Raman spectroscopy is an analytical technique used to provide information about the chemical and structural information of the molecules based on their vibrational energy bands. Raman spectroscopy operates similarily to other spectroscopic techniques which involve the interaction of molecules with light (or energy). However, Raman is concerned with scattering of radiation by sample rather than the absorption process [314,315]. The Raman spectrum is shown in Figure 1.15.

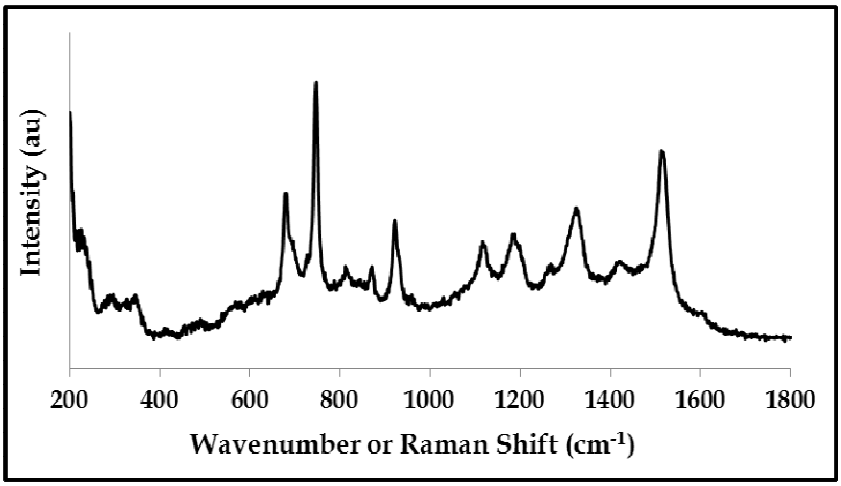

Figure 1.15: Raman spectrum of manganese phthalocyanine complex in their powder form (un-published work).

In this study, Raman spectroscopy has been used as the surface analytical technique for the confirmation of electrode surface modifications and in conjuction with different other surface techniques.

1.5.3 Microscopic surface characterization techniques

1.5.3.1 Scanning electron microscopy (SEM)

Scanning electron microscope (SEM) is a surface technique used to obtain the topographical image and the composition of the sample on the surface by employing high-energy beam of electrons in a raster scan manner. By scanning the surface, the interaction between the electrons (from the electron beam) and the surface occurs, resulting in the deflection of the electrons from the sample. The deflected electrons result in a signal that contains the information about the sample topography and composition [316,317]. The electrons are collected by secondary detector for imaging or backscatter detector for elemental composition. The elemental composition or chemistry of the sample may be obtained with an energy dispersive X-ray

spectrometer (EDS) [316,317]. EDS utilizes X-rays that are emitted from the specimen when bombarded by the electron beam to identify the elemental composition of the specimen. Figure 1.16 shows (a) the SEM image and (b) the corresponding EDS spectrum.

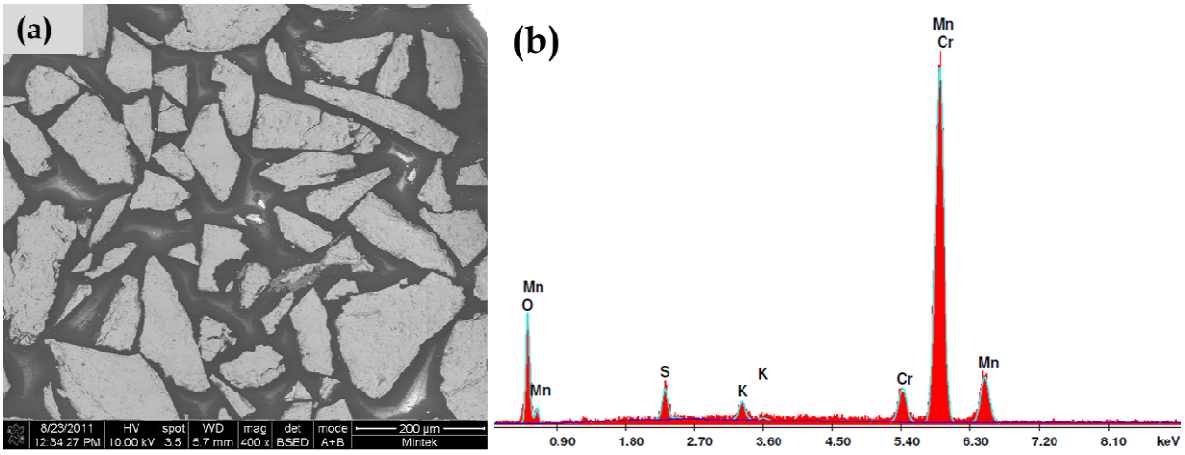

Figure 1.16: (a) Scanning electron microscope image of powder sample and (b) its corresponding energy dispersive X-ray spectrum (un-published work).

1.5.3.2 Atomic force microscopy

The atomic force microscope (AFM) is a surface characterization technique for measuring surface morphology and it uses the sharp probes to scan across the sample detecting interactions between the tip (made of silicon or silicon nitride) with the sample surface. During the AFM measurement, the tip scans across the surface and the cantilever deflects in response to the force between the tip and the surface. The deflection is monitored by bouncing a laser beam off the tip onto a photodetector. Figure 1.17 shows the operation of the AFM and the acquired images during measurement.

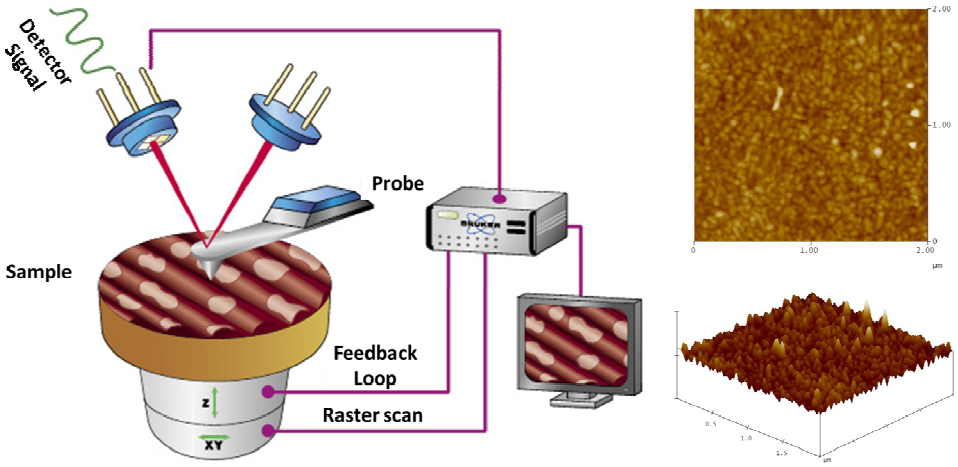

Figure 1.17: The operation of the AFM (image re-produced with permission from Bruker-Nano ™) and the acquired images during measurement (un-published results).

The AFM surface characterization was used in this work for characterization of bare and modified surfaces. Other parameters such as roughness factor, vertical height measurements and region analysis may be obtained.

1.5.4 Quartz crystal microbalance with dissipation (QCM-D)

The quartz crystal microbalance (QCM) has been described earlier as one of the two mass-sensitive techniques together with SPR. QCM-D is used in this thesis and hence it is briefly introduced. QCM is an ultra-sensitive weighing device that utilizes the mechanical resonance of the piezoelectric single crystalline quartz, and this techniques was first discovered by Pierre and Jacques Curie in 1880 [26]. The different materials are used as surface coatings depending on the experiment. The surface materials may be gold-coated, platinum-coated, etc. and these quartz crystals are used as weighing devices (AT-cut crystals). The AT-cut crystals ensure high temperature stability and pure shear motion when subjected to an electric field. The mechanical resonance (at applied electric field) is a phenomenon that induces a

mechanical strain in a crystal making it oscillate [318]. Figure 1.18 shows an illustration for the QCM principle where the thin crystal is sandwitched between a pair of circular metal electrodes [27-29].

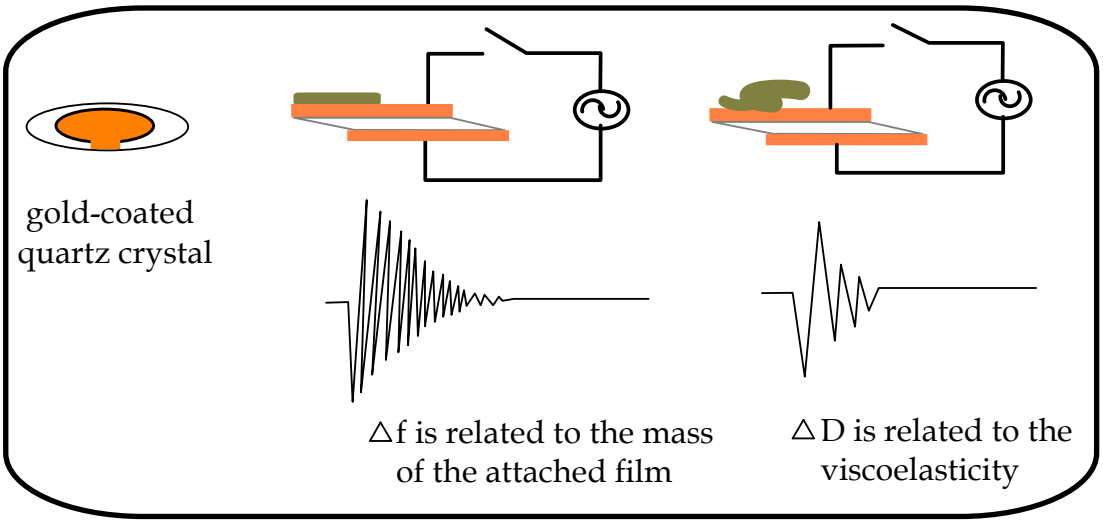

Figure 1.18: Schematic illustration of the QCM-D principle. The Δf (change in frequency) of the oscillating crystal is related to the total oscillating mass, while ΔD (energy dissipation) is related to the visco-elastic properties of the oscillating mass.

The resonating frequency of a crystal is obtained when the AC voltage is applied and it corresponds to the resonance frequency (f_o) of the crystal. This resonance frequency occurs when the thickness of the crystal is an odd integer number (or overtone number) of half-wavelength causing the oscillation to have its antinodes at each electrode interface. The resonance frequency of the crystal is directly proportional to the total mass on the crystal provided that a mass that is added (Δm) on the surface results in the change of frequency (Δf). The relationship between the frequency and the mass adsorbed was discovered by Sauerbrey and is shown in equation 1.13 [319].

$$\Delta m = -\frac{C_{MS}\Delta f}{n} \qquad (1.13)$$

where C_{MS} is the mass sensitivity constant (17.7 ng Hz $^{-1}$ cm^{-2} at an oscillation frequency of 5 MHz or overtone n = 1) and n is the overtone number (1, 3, 5, 7, 9…).

For the Sauerbrey equation 1.13 to be valid the following conditions should be met: (i) total mass of the adsorbed film should be small compared to the weight of the crystal, and (ii) the adsorbed film should be rigid and evenly distributed over the active area of the crystal. If these conditions are met, then the change in the total mass of the crystal (Δm) may be estimated using equation 1.13. The potential use of QCM in liquid or solution phase has resulted in an increase in number of applications for QCM in the field of biotechnology [320-326]. In order for the QCM to be useful in biotechnology applications, other parameters need to be taken into consideration. These parameters include (i) non-rigid character of the adsorbed film and (ii) water molecules trapped between the adsorped films and these makes the analysis difficult as the adsorbed film does not obey Sauerbrey relationship. Therefore, in trying to accommodate these film factors, the technique was upgraded so that it can provide further information such as change in energy dissipation, ΔD, of the oscillating crystal. In addition to the mass-adsorbed properties, the energy dissipation capability will measure the visco-elastic properties of the adsorbed layers and the equipment used is called QCM-D. Figure 1.19 shows the data representation as acquired with the QCM-D, showing both the changes in frequency (*f*) and the changes in dissipation (D).

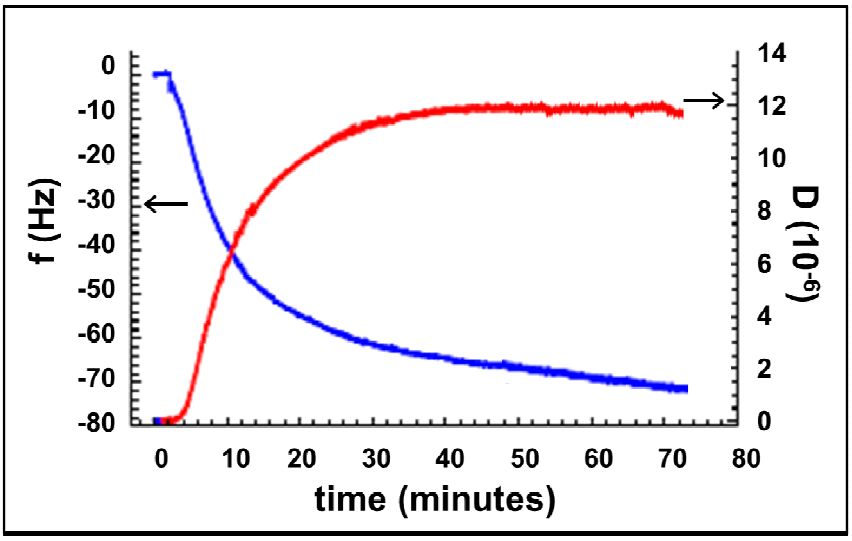

Figure 1.19: Frequency (f) and dissipation (D) shift following the immobilization of biomolecular layer on gold-coated surface.

In this thesis, the QCM-D was employed in monitoring (in real-time) the surface reactions, i.e. the mass and structural changes on the metal surface during the adsorption and binding of the antibody antigen reactions. The technique will be useful in estimating the amount (i.e. the mass of the adsorbed film), the thickness and the visco-elastic properties of the immobilized molecules.

1.6 Summary of thesis aims

The overall aims of this thesis are summarized as follows:

1) Synthesis of octa-substituted metallophthalocyanines bearing hexylthio substituents at peripheral and non-peripheral positions and study the effect of point of substitution on their electrocatalytic properties as self-assembled monolayers on gold electrode surfaces.

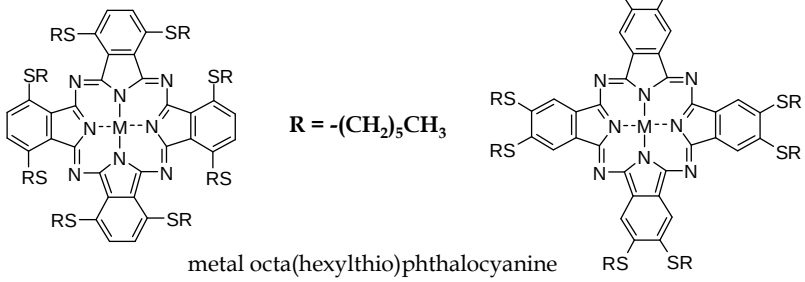

metal octa(hexylthio)phthalocyanine

α - substibuted
M = Co (CoOcHexTPc, **12**)
= Mn (AcMnOHTPc, **14**)

β - substituted
M = Co (CoOcHexTPc, **13**)
= Mn (AcMnOcHexTPc, **15**)

2) Investigation of the use of tetra-amino phthalocyanine (MTAPc) complexes containing cobalt (CoTAPc) and manganese (MnTAPc) as polymers and as grafted monolayers towards the electrocatalysis of hydrogen peroxide (H_2O_2).

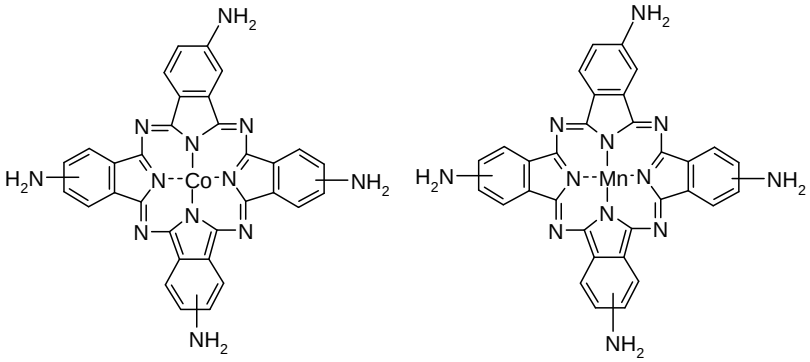

CoTAPc (16) **MnTAPc (17)**

metal tetraamino phthalocyanines

3) Investigation of the effect of single-wall carbon nanotubes covalent immobilization on the electrocatalysis of H_2O_2 by MTAPc complexes.

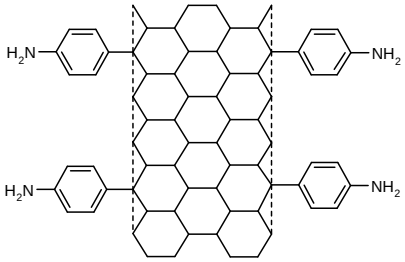

PA-SWCNT

phenylamino functionalized
single-walled carbon nanotube

4) Study the immobilization of biological molecules (measles antigens) onto electrode surfaces and investigate their measles antibody sensing abilities using labeled and label-free immunosensor designs.

Chapter 2:

Experimental

2 EXPERIMENTAL

2.1 Materials and reagents

2.1.1 General

Dimethylsulfoxide (DMSO), dimethylformamide (DMF), tetrabutyl ammonium tetrafluoro-borate ($TBABF_4$), single-walled carbon nanotubes (SWCNTs, 0.7 – 1.4 nm diameter, >90% carbon content and of it ≥ 77% carbon as SWCNT), 4-nitrobenzene diazonium tetrafluoro borate (4-NBD), benzene-1,4-dicarbaldehyde (BDCA), ammonium iron (III) sulphate, manganese (II) acetate, cobalt (II) chloride, 1-hexanethiol, 2,3-dicyanohydroquinone, 1,2-dichloro-4,5-dicyanobenzene, sodium dodecyl sulfate (SDS), p-toluenesulfonyl chloride (TsCl), 1,8-diazabicyclo{5.4.0}-undec-7-ene (DBU), glucose, ascorbic acid, uric acid, ethanol, 1-pentanol, 4-(2-aminoethyl) phenylamine, cysteamine (CA), glutaraldehyde (GA), sodium nitrite, tetrafluoroboric acid (HBF_4) and absolute ethanol were purchased from Sigma-Aldrich and used as received. Solvents were distilled and dried before use. H_2O_2 (32%) was purchased from SAARChem. Ultra-pure water was obtained from a Milli-Q water system (Millipore Corp. Bedford, MA, USA) and was used throughout the experiments. Acetonitrile (ACN), phosphate salts (NaH_2PO_4 and Na_2HPO_4), ferricyanide {$K_3[Fe(CN)_6]$} and ferrocyanide {$K_4[Fe(CN)_6]$} were purchase from ACE Chemicals. The phosphate salts were used to prepare phosphate buffer solutions, with sodium hydroxide (NaOH) and phosphoric acid (H_3PO_4) being added to adjust pH to appropriate values. Solutions in the electrochemical cell were de-aerated by bubbling argon or nitrogen prior to every experiment and the electrochemical cell was kept under argon atmosphere. Potassium carbonate, chloroform ($CHCl_3$), pyridine and dichloromethane (DCM) were procured from Merck (SA). Column chromatography was performed on Silica Gel 60 (0.04–0.063 mm). Thin layer chromatography was performed on Silica Gel 60P F254.

Cobalt and manganese tetra-amino phthalocyanines (CoTAPc and OH-Mn^{III}TAPc) were synthesized according to published methods [327,328]. Side-wall functionalization of SWCNTs with phenyl-amine group was achieved using the reported method [329,330].

2.1.2 Biologicals

Measles-antigen (Rubeola Edmonston strain, R9750), Mouse anti-Rubeola (R9570-11) is a monoclonal primary antibody (1°Mab) and Rabbit anti-Rubeola (R9750-10) is a polyclonal primary antibody (1°PAb) were purchased from USBiologicals. Horse-radish peroxidase (HRP) conjugated Rabbit anti-Mouse (610-4340) secondary antibody, i.e. (HRP)2^0MAb, and Donkey anti-Rabbit (611-701-127) secondary antibody, i.e. (HRP)2^0PAb, were purchased from Rockland. The required concentrations for all biological substances were prepared as per experimental requirement. All the antibodies studied here are of IgG isotype. Bovine serum albumin (BSA) purchased from Sigma-Aldrich (5% BSA) was prepared and used as the blocking buffer. TMB solution (3,3′,5,5′-tetramethyl-benzidine, T0440) for ELISA containing H_2O_2 was used as received as a colorimetric substrate. For electrochemical experiments, the TMB solution sometimes did not contain H_2O_2. Phosphate buffer saline (PBS) containing 8.0g sodium chloride, 1.3g dibasic sodium phosphate, 0.2g monobasic sodium phosphate in 1.0 liter ultra pure water, pH 7.4 was used. Phosphate buffered saline-Tween 20 solution (PBS-T) containing 0.05% Tween-20 was prepared from the tablet purchased from Sigma-Aldrich. ELISA 96-well microtiter plate purchased from Separations Laboratory Suppliers was used as received. H_2SO_4 (1 M) was prepared and used as stop buffer in ELISA studies.

The measles-antigen was used for the fabrication of the electrochemical immunosensors and for the detection of measles-specific antibodies. ELISA was used as a benchmark analysis method to confirm the formation of antibody-antigen

complex and to ascertain the binding affinity of the primary antibody towards measles-antigen.

2.2 Equipments and methods

2.2.1 General electrochemical methods

All electrochemical and impedance spectroscopy experiments were carried out using a computer-controlled Autolab Potentiostat/Galvanostat PGSTAT 302N (Eco Chemie, Utrecht, The Netherlands) driven by the General Purpose Electrochemical Systems data processing software (GPES software for electrochemistry) and FRA for impedance measurements and analysis. The electrochemical data was collected using a conventional three-electrode setup with either a bare or modified glassy carbon (GCE, radius (r) = 1.6 mm), gold (Au, r = 0.8 mm) both purchased from bioanalytical systems (BAS) or indium tin oxide (ITO) glass purchased from sigma-alrich south africa as working electrodes. Platinum wire was used as a counter electrode and silver|silver chloride (Ag|AgCl) wire as pseudo-reference electrode. The potential of Ag|AgCl pseudo-reference in aqueous conditions was less than the Ag|AgCl (3 M KCl) by 0.015 ± 0.003V. The screen-printed gold electrodes, SPAuE (C223AT purchased from Dropsens, Oviedo, Spain) were also used with three electronic contacts for gold (Au, r = 0.8 mm) as working electrodes, gold as counter electrode and silver|silver chloride (Ag|AgCl) as reference electrode. Electrochemical impedance spectroscopy (EIS) experiments were recorded in the frequency range between 10 kHz to 100 mHz at the half-wave potential ($E_{1/2}$) of $[Fe(CN)_6]^{3-/4-}$ redox couple for electrodes studied and with an amplitude of 5 mV rms sinusoidal modulation. All the experiments were conducted at 25°C in the jacketed cells and the temperature was controlled by Julabo model ED (Heating Immersion Circulator) purchased from Labotec.

Electrochemical characterization of metal octahexylthiol substituted phthalocyanines (MOcHexTPc): The electrochemical experiments for the characterization of thiol functionalized complexes were performed in dry pyridine containing $TBABF_4$ or TEAP (tetra-ethylammonium perchlorate) as supporting electrolytes. Prior to performing the experiments, the working electrode (glassy carbon electrode, GCE) was polished with alumina paste on a Beuhler felt pad, followed by washing thoroughly with deionized water and rinsing with pyridine. Square wave voltammetric parameters were: step potential 5 mV; amplitude 20 mV at frequency of 25 Hz. All the experiments were conducted in the solution first purged with argon and then the blanket of argon was kept over the solution to prevent the diffusion of oxygen into solution thus interfering with experiment.

Spectroelectrochemical data were obtained using a homemade optically transparent thin-layer electrochemical (OTTLE) cell which was connected to a Bioanalytic System (BAS) CV 27 voltammograph. UV-vis spectra were recorded on a Cary 50 UV-vis/NIR spectrophotometer.

2.2.2 Microscopy and Spectroscopy equipments and methods

Scanning electron microscopy (SEM) measurements: The SEM morphology images of the bare and modified electrodes were obtained on gold coated quartz crystal microbalance (QCM) crystals (AuCQC, 5MHz, O100RX1) purchased from Stanford Research Systems (SRS) or QSX-301 (AuCQC, 5 MHz AT-cut) purchased from QSense (Sweden) for SAMs studies. The SEM images were acquired using Nova NanoSEM 200 from FEI. Energy dispersive x-ray (EDX) analysis spectra were obtained using X-ray microanalysis system added as a module on the Nova NanoSEM 200.

Atomic force microscopy (AFM): The AFM images on ITO surfaces (polymer studies) were recorded in non-contact mode in air with a CPII scanning probe microscope from Veeco Instruments (Carl Zeiss, South Africa). For other studies, the AFM images were recorded using the Veeco Instrument - MultiMode scanning probe microscope (MM-SPM) controlled by the NanoScope IV Controller (Carl Zeiss, South Africa) in non-contact or tapping mode in air.

Transmission electron microscopy (TEM): The images were acquired using JEOL 2100F equipment and the copper grit coated (using drop-dry) with material to be investigated.

Raman spectroscopy: Raman spectra for powder samples finely ground with KBr were acquired using Thermo Nicolet Nexus 6700 FR-Raman spectrometer, with Nd:YAG laser 1064 nm. Surface-enhanced Raman spectra (SERS) were obtained using the Bruker Vertex 70-Ram II spectrometer equipped with a 1064 nm Nd:YAG laser and liquid cooled germanium detector. UV-vis spectra were recorded on a Perkin-Elmer Lambda 35 UV-vis spectrometer. IR spectra (KBr pellets) were recorded on a Perkin-Elmer Spectrum 2000 FTIR spectrometer.

X-ray photoelectron spectroscopy: Surface composition analysis, for screen-printed gold electrodes modified with grafted monolayers, using the X-ray photoelectron spectroscopy (XPS) was acquired using Quantum2000 with Al Kα (1468 eV) at NMISA (National Metrology Institute of South Africa).

2.2.3 Quartz crystal microbalance (QCM)

QCM electrochemical modification and frequency change monitoring: QCM200 purchased from SRS with AuCQC surface was connected as working electrode and this enabled

us to perform electrochemical modification for further microscopic measurements. Mass (frequency) changes on the QSX-301 crystals as reaction carriers, were conducted using quartz crystal microbalance with dissipation (QCM-D, QSense, Sweden).

2.2.4 Other equipments

Elemental analyses were performed at Rhodes University using a Vario Elementer Microcube ELIII. The proton nuclear magnetic resonance (^{1}H NMR, 400 MHz) spectra were acquired using Bruker AMX NMR spectrometer in either $CDCl_3$ or DMSO-d_6. Fast Atomic Bombardment Mass Spectrometer (FAB-MS) spectra were recorded on a VG70SE system at the Mass Spectrometry Service at the University of Witwatersrand, School of Chemistry.

2.2.5 Biological methods

ELISA Procedure: Briefly, the protocol used for ELISA was as follows with the results studied in triplicates for polyclonal (1°PAb) and monoclonal (1°MAb) primary antibodies. The measles-antigen (100 µl) solution and serial dilutions were incubated in ELISA plate 96 microtiter wells at 4°C overnight and sealed by parafilm. After the incubation the measles-antigen solution was decanted and the microtiter wells were washed thrice with PBS-T. The microtiter wells were blocked using 300 µl of 5% BSA solution and incubated at room temperature for 2 hours with gentle agitation. The blocking was done in order to reduce the overall background and to increase the sensitivity of the assay. After washing thrice with PBS-T, the wells were incubated with 100 µl of primary antibodies (1°PAb or 1°MAb) for 2 hours at room temperature and the plate was gently shaken. The wells were further washed thrice with PBS-T.

The wells were incubated with 100 µl of peroxidase (HRP) conjugated secondary antibodies, i.e. (HRP)2°PAb or (HRP)2°MAb at room temperature with gentle agitation. After 2 hours, the wells were washed three times with PBS-T to remove loosely bound secondary antibodies.

Colorimetric ELISA measurements were accomplished by adding 100 µl of chromagen (TMB solution containing H_2O_2) into each well and the plate was incubated at room temperature for 15 min in the dark. The colour in each microtiter well turned blue immediately after adding TMB. After 15 minutes of TMB addition the absorbance at 660 nm was determined with the Labsystems Multiscan RC ELISA reader. The data was collected and analyzed. The mean and the standard deviation of the triplicates were calculated for each point. The stop solution (1M H_2SO_4) was added, the solution turned yellow and after 15 minutes the absorbance read at 450 nm using the Labsystems Multiscan RC ELISA reader. The data was collected and analyzed. The mean and the standard deviation of the triplicates were calculated for each point.

2.3 Synthesis β- and α- hexylthio substituted phthalocyanines

2.3.1 Synthesis of non-peripherally (α) MOcHexTPc complexes (12) and (14), Scheme 3.1

The non-peripherally (α) substituted cobalt (**12**) and manganese phthalocyanine (**14**) complexes were synthesized following the procedure reported in the literature for pentylthio derivatives [65,77] with slight modifications as follows:

*2.3.1.1 3,6-Bis(4'-methylphenylsulfonyloxy) -4,5-dicyanobenzene (**8**)*

Ts (p-toluenesulfonyl) chloride (5.2 g, 27 mmol) was added to a mixture of 2,3-dicyanohydroquinone (**7**) (2 g, 13 mmol) and potassium carbonate (6.9 g, 50 mmol) in acetone (15 ml). The mixture was heated to reflux for 2 h. Thin layer chromatography (TLC) was performed to determine the consumption of compound (**7**). The mixture was cooled to room temperature and poured into water (40 ml), and stirred for 1 h. The light brown product (**8**) was filtered and oven dried. Yield: 4.5 g (79%). IR (υ_{max}/cm^{-1}]: 3102, 3098, 3053, 2241 (CN), 1932, 1713, 1655, 1594, 1467, 1376, 1239, 1204, 1174, 1123, 1009, 946, 853, 814, 800, 790, 749, 694, 638, 614. ^{1}H NMR($CDCl_3$), ppm: 7.84 (6H, t, Ar-H), 7.42-7.40 (4H, d, Ar-H), 2.50 (6H, t, $-CH_3$).

*2.3.1.2 3,6-Bis(hexylthio)-4,5-dicyanobenzene (**9**)*

1-Hexanethiol (2.4 g, 23 mmol) was dissolved in DMSO under nitrogen atmosphere and **8** (4.3 g, 9.2 mmol) was added. The mixture was stirred for 15 min and finely ground anhydrous potassium carbonate (5.1 g, 37 mmol) was added portion-wise for

two hours while stirring. The mixture was stirred under nitrogen atmosphere for 12 h. Water was added and the aqueous phase extracted using chloroform (3 x 50 ml). The extracts were further treated with 5% sodium carbonate solution (2 x 250 ml). The solution was further treated with water (2 x 250 ml), and the solvent evaporated off. The product (**9**) was recrystallized from ethanol. Yield: 2.2 g (71.7%). IR (υ_{max}/cm^{-1}): 3080, 2928, 2853, 2225 (CN), 1467, 1455, 1422, 1300, 1284, 1275, 1207, 1169, 1144, 846, 833, 728 (C-S-C), 448. ^1H NMR($CDCl_3$), ppm: 7.51 (2H, s, Ar-H), 3.05–3.02 (4H, t, $-CH_2-$), 1.73–1.66 (4H, m, $-CH_2-$), 1.50– 1.43 (4H, m, $-CH_2-$), 1.36–1.30 (8H, m, $-CH_2-$), 0.91–0.88 (6H, t, $-CH_3$).

*2.3.1.3 1,4,8,11,15,18,22,25-Octahexylthiophthalocyanato cobalt (II) (**12**)*

3,6-Bis(hexylthio)-4,5-dicyanobenzene (**9**) (0.4 g, 1.2 mmol) in 1-pentanol (3.5 ml) was refluxed under a nitrogen atmosphere and cobalt (II) chloride (0.069 g, 0.40 mmol) was added. After the addition of DBU (0.13 ml, 0.86 mmol), the reaction was continued for 6 h. The mixture was cooled and column chromatography over silica was done using $CHCl_3$ as eluent. Yield: 0.23 g (42%). MS (m/z): Calc. 1499. Found: 1496 [M-3H]. UV/vis ($CHCl_3$): λ_{max} (nm) (log ε): 337(5.3), 492 (4.2), 774(5.4). IR [(KBr) (υ_{max}/cm^{-1})]: 2960, 2924, 2869, 2582, 1589, 1459, 1414, 1377, 1326, 1261, 1092, 1023, 958, 866, 742 (C-S-C), 706, 662, 512. Anal. Calc. for $C_{80}H_{112}N_8S_8Co$: C, 62.53; H, 7.36; N, 7.29. Found: C, 62.48; H, 7.15; N, 7.10%.

*2.3.1.4 1,4,8,11,15,18,22,25-Octahexylthiophthalocyanato manganese (III) (acetate) (**14**)*

The synthesis and purification of (**14**) was the same as for (**12**) except the manganese (II) acetate was used as a metal source. Yield: 0.32 g (42%). FAB-MS (m/z): Calc. 1495. Found: 1492 [M-3H]. UV/Vis ($CHCl_3$): λ_{max} (nm) (log ε): 357(5.0), 555 (4.7), 779

(4.9), 888 (5.5). IR [(KBr) υ_{max}/cm^{-1}]: 2955, 2868, 2548, 2364 (S-C), 1510, 1488, 1463, 1364, 1312, 1284, 1261, 1221, 1191, 1150, 1129, 1114, 1072, 932, 800 (Mn-O), 750 (C-S-C), 650. Anal. Calc. for (Ac)$C_{80}H_{112}MnN_8S_8$: C, 63.24; H, 7.51; N, 7.20; S, 16.48%. Found: C, 62.76; H, 6.86; N, 7.06; S, 17.38%.

2.3.2 Synthesis of peripherally (β) MOcHexTPc complexes (13) and (14), Scheme 3.1

The synthesis of the complexes (β-CoOcHexTPc, **13**) was reported in literature by Gurek et. al. [331]. The same procedure was used for the synthesis of manganese octa-hexylthio phthalocyanine (β-MnOcHexTPc, **15**) as shown below.

*2.3.2.1 1,2-Bis(hexylthio)-4,5-dicyanobenzene (**11**)*

1-Hexanethiol (7.165 g, 60.6 mmol) was dissolved in DMSO (35 ml) under argon atmosphere and 1,2-dichloro-4,5-dicyanobenzene (**10**) (5.91 g, 30 mmol) was added. The mixture was stirred for 15 min; finely ground anhydrous potassium carbonate (15 g, 109 mmol) was added portion-wise in 2 h with efficient stirring. The reaction mixture was stirred under argon at room temperature for 12 h. Then water (100 ml) was added and the aqueous phase extracted with chloroform (3 x 50 ml). The extracts were treated first with 5 % sodium carbonate solution then with water and dried over anhydrous sodium sulfate. The solvent was evaporated and the oily product was crystallized from ethanol and oven dried to yield product **11**. Yield: 7.3 g (67.2%). IR (υ_{max}/cm^{-1}): 3080, 2953, 2928, 2859, 2229 (CN), 1561, 1459, 1433, 1347, 1279, 1258, 1225, 1210, , 1117, 932, 899, 737 (C-S-C), 529, 447. ^{1}H NMR($CDCl_3$), ppm: 7.40 (2H, s, Ar-H), 3.03–2.99 (4H, t, –CH_2-), 1.78–1.70 (4H, m, –CH_2-), 1.53– 1.45 (4H, m, –CH_2-), 1.34–1.32, (8H, m, –CH_2-), 0.92–0.89 (6H, t, –CH_3).

*2.3.2.2 2,3,9,10,16,17,23,24-Octahexylthiophthalocyanato manganese (III) (**15**)*

1,2-Bis(hexylthio)-4,5-dicyanobenzene (**11**) (0.4 g, 1.2 mmol) in 1-pentanol (3.5 ml) was refluxed under a nitrogen atmosphere and manganese (II) acetate (0.069 g, 0.40 mmol) was added. After the addition of DBU (0.13 ml, 0.86 mmol), the reaction was continued for 6 h. The mixture was cooled and column chromatography over silica was done with $CHCl_3$ as eluent. Yield: 0.31 g (39%). MS (m/z): Calc. 1495. Found: 1493 [M -3H]. UV/Vis ($CHCl_3$): λ_{max} (nm) (log ε): 392 (5.1), 462 (5.2), 522 (5.1), 688 (4.8), 768 (5.5). IR [(KBr) υ_{max}/cm^{-1}]: 2952, 2929, 2854, 2583, 2361 (S-C), 1590, 1560, 1531, 1512, 1465, 1414, 1327, 1308, 1233, 1113, 1077, 1070, 959, 898, 860 (Mn-O), 782, 740 (C-S-C). Anal. Calc. for Anal. Calc. for $C_{80}H_{112}N_8S_8Mn$ (Ac): C, 63.24; H, 7.51; N, 7.20; S, 16.48%. Found: C, 62.58; H, 7.20; N, 7.09; S, 17.12%.

2.4 Measles immunosensor design experimental

The measles antigen immobilization was achieved by first forming phenylethylamino monolayers from 4-(2-aminoethyl) benzene diazonium salt (AEBD) followed by covalent attachment of measles-antigen.

2.4.1 Synthesis of 4-(2-aminoethyl) benzene diazonium (AEBD) salt

The synthesis of AEBD salt was accomplished following the reported method [226, 233]. Briefly, 15 mmol of 4-(2-aminoethyl) aniline was added to 3 ml tetrafluoroboric acid and the solution was cooled for 15 minutes while stirring vigorously. To this solution an ice cold 30 mmol of sodium nitrite ($NaNO_2$, dissolved in water) was added drop-wise and the solution stirred vigorously. The mixture was allowed to react for 40 minutes after which the precipitate formed. The precipitate was filtered

and washed with petroleum ether, dried in vacuum and stored at -20°C. Yield = 62%. H^1 NMR (400 MHz, D_2O): δ (ppm) 3.32 – 3.36 (t, 2H), 3.42 – 3.46 (t, 2H), 7.92 – 7.94 (d, 2H), 8.57 – 8.59 (d, 2H). IR (KBr): λ (cm^{-1}) 3280 (N-H), 3110 (C-H), 2287 (N_2), 1619, 1591, 1502, 1473, 1429, 1401, 1319, 1293, 1267, 1197, 1160 (C-N), 1104, 938, 850, 823,542, 525.

2.4.2 Covalent immobilization of measles-antigen, Scheme 6.1

The attachment of the measles-antigen onto gold electrode surface was achieved following the method shown in Figure 1.3, where the linker is the grafted phenylethylamino (PEA) monolayer. Briefly, the gold electrode was modified using electrochemical grafting, as shown in Figure 1.10 and X = ethylamino group, from 1 mM AEBD salt in acetonitrile solution containing 0.1 M $TBABF_4$ (five cycles). The formed PEA monolayer was activated using 5% glutaraldehyde in ethanolic solution for 1 hour, represented as Au-PEA-GA in Scheme 6.1. The Schiff-base product forms between the glutaraldehyde group and the PEA group on gold surface. This functionalization exposes the other aldehyde group for further reactions with the antigen amino groups. The immobilization of measles antigen was accomplished by immersing the glutaraldehyde activated electrode onto the measles-antigen solution (20 $\mu g.ml^{-1}$) and incubated at 4^oC overnight. The non-specific binding sites on the electrodes and the deactivation of the unreacted aldehyde groups were blocked by incubating the measles-antigen modified electrode with 2% BSA at 37^oC for 1 hour; represented as Au-PEA-GA-antigen/BSA in Scheme 6.1. The measles-antigen modified electrode was used for the detection of measles-specific primary antibodies electrochemically using label and label-free detection methods.

2.4.3 Quartz-crystal microbalance with dissipation (QCM-D) measurements

2.4.3.1 Quartz crystal pre-treatment and SAM functionalization (Scheme 6.2)

Prior to QCM-D measurement, brand new crystals were pre-treated by first rinsing with absolute ethanol and dried in nitrogen. The old and used crystals were cleaned using the reported method [221,320,332]. The crystals were cleaned thoroughly by first sonicating in 1% SDS solution for 2 minutes. This is then followed by immersing the quartz crystals in the solution of H_2O:H_2O_2:NH_3 in the ratio 5:1:1 and heated to 75 °C for 5 minutes. The crystals were thoroughly rinsed with water and dried under nitrogen gas and then exposed to ultraviolet light (UV-O) for 5 minutes. The new or freshly prepared crystals were immersed in the cysteamine solution for 24 hours to form a thioethylamino functionalized self-assembled monolayer. The amino functionalized gold surface was then immersed in the 5% GA solution exposing the other aldehyde group so it can react with other amino groups from the biomolecules (i.e. measles-antigen). The GA functionalized gold coated quartz crystal coated surfaces were used for QCM-D studies, i.e. AuCQC-CA-GA in Scheme 6.2

2.4.3.2 Measles-antigen immobilization monitoring with QCM-D

The QCM-D analysis took place under the following parameters: 30 °C temperature and a flow rate of 100 $\mu l.min^{-1}$. Following the pre-treatment and activation of the crystal with thioethylamino-glutaraldehyde SAM (electrode represented as AuCQC-CA-GA, in Scheme 6.2), the QCM-D experiment was then commenced. The measles-antigen (1 $\mu g.ml^{-1}$) layer was immobilized onto the GA functionalized gold surface and simultaneous measurement of the change in frequency (Δf) and energy dissipation (ΔD) was obtained. The blocking of GA activated and sites that might give non-specific binding was achieved by using 2% BSA which was monitored as

the second layer; this layer was represented as AuCQC-CA-GA-antigen/BSA in Scheme 6.2. The interaction of the immobilized measles-antigen with the measles-specific primary antibody (1 $\mu g.ml^{-1}$) was achieved by running the antibody solution onto an antigen/BSA modified gold surface; represented as AuCQC-CA-GA-antigen/BSA, thus forming an antibody modified surface (AuCQC-CA-GA-antigen/BSA-antibody) as shown in Scheme 6.2.

2.4.3.3 QCM-D data acquisition, analysis and fitting

The changes in frequency (*f*) and dissipation (D) are obtained by periodically switching off the driving power of the oscillation of the sensor crystal and by recording the decay of the damped oscillation. The time constant of the decay is inversely proportional to D, and the period of the decaying signal gives *f*. The noise level of *f* and D factor with liquid loads are ~0.3 Hz and ~2 x 10^{-7}, respectively. The Sauerbrey sensitivity of these crystals is 1 Hz = 17.7 $ng.cm^{-2}$. The frequency and dissipation responses were recorded using overtones (n=3, 5, 7, 9, 11). For analysis, the frequency and dissipation data for 7th, 9th and 11th overtones or harmonics were used. Data at other overtones are included for the modeling of the effective mass loading, effective thickness and shear viscosity using Kevin-Voigt model [221,320,332]. During the measurements, the crystals were mounted in a liquid chamber, designed to provide a rapid, non-perturbing exchange of the liquid (non-flowing liquid) over one side of the sensor. The biomolecules studied were prepared in 0.01 M phosphate buffer saline (PBS, pH 7.4) solution. Parameters for the Kevin-Voigt model were set to have the viscosity (kg/ms) between 0.01 and 100, the shear force (Pa) between 1000 and 1 × 10^{9}, and the film thickness (m) forced between 1 × 10^{-11} and 1 × 10^{-6}. The film density on the gold surface was assumed to be 1100 $kg.m^{-3}$. From QCM-D frequency and dissipation data, the deposited layer thickness, d, was calculated using Voigt viscoelastic modeling for a film in liquid and was fitted using

Q-Sense software (Q-Tools) with built-in equations. The fitting results can be generated automatically for the user.

2.5 Electrodes pretreatment and their modification

2.5.1 Electrode pretreatments

Prior to electrode modification, the electrode surfaces were cleaned using reported methods for gold [333,334] and glassy carbon [105].

Briefly, the gold electrode was first polished using an aqueous slurries of alumina (<10 μm) on a SiC-emery paper (type 2400 grit), and then to a mirror finish on a Buehler felt pad with alumina slurries (1, 0.5, 0.03 μm). The electrode was then rinsed with copious amount of deionized water and then placed in ethanol where it subjected to ultrasonic vibration to remove residual alumina particles that might be trapped on the surface. After this mechanical treatment, the gold electrode was chemically treated by etching for about two minutes in a "Piranha" solution {3:1 (v/v) 30% H_2O_2 and concentrated H_2SO_4} and then rinsed with copious amounts of ultra-pure Milli-Q water followed by ethanol. The chemical treatment with "Piranha" solution serves to remove the organic contaminants on the gold electrode surface. The cleanliness of the bare gold electrode surface was finally established by placing the electrode in 0.5 M H_2SO_4 and scanning the potential between -0.5 to 1.0 V (versus Ag|AgCl pseudo-reference) at a scan rate of 50 mV/s, until reproducible scans were obtained.

The glassy carbon electrode was polished with alumina (1, 0.5 and 0.03 μm) on a Buehler-felt pad followed by washing thoroughly with de-ionized water and ultra-pure water collected from Milli-Q water purification system. The electrode was then

subjected to ultrasonic vibration in ethanol. Finally the electrode is washed with respective solvent before transferring to the electrochemical cell solution containing same solvent.

The new indium tin oxide (ITO) coated glass slides were pre-conditioned and subjected to ultrasonic vibration in water for 10 minutes and further rinsed with water and allowed to dry. The ITO glass slides were mainly used to study the morphology of the polymer thin films using atomic force microscopy.

2.5.2 Electrode modification: Electropolymerization

The electrosynthesis of polymers of MTAPc (M = Co or Mn) on different substrates were carried out by repetitive cyclic voltammetry of 1 mM monomer (MTAPc) in DMF solution containing 0.1 M $TBABF_4$ as a supporting electrolyte at a scan rate = 0.1 V/s. Different potential windows were investigated to find the optimum window for a highly conducting polymer. The electrodes were rinsed in DMF and water.

2.5.3 Electrode modification: Grafting method

2.5.3.1 Formation of PA-MTAPc monolayer, Scheme 4.1

The SPAuE surfaces were modified by electrochemical grafting of 1.0 mM 4-nitrobenzene diazonium salt (4-NBD) in DMSO or ACN solution containing 0.1 M $TBABF_4$ thus forming phenylnitro monolayer (both solvents gave similar results). The potential range used was from -0.4 to +0.4 V and five scans were used. The formed phenylnitro group was electrochemically reduced to form phenylamino (PA) monolayer by cycling in aprotic solution (1:9) ethanol/water solution containing 0.1 M KCl. The PA functionalized SPAuEs were activated by immersing in the ethanolic

solution of benzene-1,4-dicarbaldehyde (BDCA) thus forming the Schiff-base product and exposing the aldehyde group; the electrode is represented as SPAuE-PA/BDCA Activated, in Scheme 4.1. The exposed aldehyde group was further reacted with amino groups from the CoTAPc and MnTAPc complexes dissolved in DMF (1 mM), thus forming the CoTAPc and MnTAPc monolayer via the formation of the Schiff-base products; represented as SPAuE-PA-MTAPc (M = Co^{II} or OH-Mn^{III}) in Scheme 4.1. The gold coated QCM crystals were modified similarly for use in obtaining SEM and AFM images and are represented as AuCQC, AuCQC-PA, AuCQC-PA-MTAPc (M= Co^{II} or (OH)Mn^{III}). After deposition or covalent attachment, the electrodes were rinsed using DMF and water.

2.5.3.2 Formation of PA-SWCNT-MTAPc monolayers, Scheme 4.2

The fabrication of SPAuE with the PA monolayer and their activation with BDCA was described above. Further functionalization was accomplished using PA-SWCNT to form SPAuE-PA-SWCNT, in Scheme 4.2(iii), monolayer from the exposed aldehyde (after activating with BDCA) and Schiff-base reactions were used here. The SPAuE-PA-SWCNT modified electrode surfaces were activated using BDCA and the immobilization of MTAPc complexes was achieved, the electrodes are represented as SPAuE-PA-SWCNT-MTAPc (M = Co^{II} or OH-Mn^{III}) in Scheme 4.2(v). Microscopic characterization using AFM and SEM required the use of smooth gold surfaces and AuCQC surfaces were employed following the similar procedure for SPAuE surfaces. The modified electrode are represented as AuCQC, AuCQC-PA, AuCQC-PA-SWCNT, AuCQC-PA-SWCNT-MTAPc (M = Co^{II} or OH-Mn^{III}). After deposition or covalent attachment, the electrodes were rinsed using DMF and water.

2.5.3.3 Formation of phenylethylamino (PEA) monolayer for antigen attachment

The procedure for the functionalization of gold electrode surfaces with PEA monolayer followed the similar protocol as the 4-NBD above with slight modification, i.e. AEBD salt was used instead of 4-NBD. After the formation of PEA monolayer, further electrode modifications were carried out as described in section 2.4.2 for the immobilization of measles-antigen.

2.5.4 Electrode modification: Self-assembled monolayers

Before SAM formation the clean electrodes were rinsed with copious amounts of ultra-pure water produced from the Millipore water system and then rinsed in distilled dichloromethane. Following the treatment, the electrodes were immersed in the argon-purged solutions of MPc complexes (**12-15**). The SAMs are represented as **12**-SAM, **13**-SAM, **14**-SAM and **15**-SAM for complexes **12-15**, respectively. The SAMs were allowed to form for 48 hours and the modified electrodes were first rinsed with dichloromethane to remove physically adsorbed complexes and then rinsed with ultra-pure water before use.

Results and Discussion

The results and discussion chapter has been split into several chapters:

Chapter 3: Synthesis, spectral and electrochemical properties of synthesized metallophthalocyanine complexes

Chapter 4: Surface fabrication and characherization using various surface techniques.

Chapter 5: Electrocatalytic and electroanalytical studies of metallophthalocyanine complexes and carbon nanotubes modified surfaces towards detection of H_2O_2

Chapter 6: Immuno-biosensor design and development for the detection of measles virus-specific antibodies using label and label-free methods

Majority of the work presented from this chapter onwards has been published:

1. Philani Mashazi, Chamunorwa Togo, Janice Limson, Tebello Nyokong. **Applications of polymerized metal tetra-amino phthalocyanines towards H_2O_2 detection**. *Journal of Porphyrins and Phthalocyanines*, 2010 (**14**) 252 – 263,

2. Philani Mashazi, Tebello Nyokong. **Electrocatalytic studies of the covalently immobilized metal tetra-amino phthalocyanines onto derivatized screen-printed gold electrodes**. *Microchimica Acta*, 2010 (**171**) 321 - 332,

3. Philani Mashazi, Edith Antunes, Tebello Nyokong. **Probing electrochemical and electrocatalytic properties of cobalt (II) and manganese (III) octakis(hexylthio) phthalocyanine as self-assembled monolayers.** *Journal of Porphyrins and Phthalocyanines*, 2010 (**14**) 932 – 947,

4. Philani Mashazi, Tawanda Mugadza, Ndabenhle Sosibo, Phumlani Mdluli, Sibulelo Vilakazi, Tebello Nyokong. **Effect of carbon nanotubes on the electrocatalysis of hydrogen peroxide by metallo-phthalocyanines**. *Talanta*, 2011 (**85**) 2202 - 2211.

5. Philani Mashazi, Sibulelo Vilakazi, Tebello Nyokong. **Electrochemical impedimetric immunosensor for the detection of measles-specific Immunoglobulin G antibodies**. *Patent Application*, 2011.

6. Philani Mashazi**,** Sibulelo Vilakazi, Tebello Nyokong. **The detection of measles virus specific antibodies using peroxidase labeled secondary antibodies**. *Patent Application*, 2011.

Other papers published but not related or discussed in this thesis

1. Phumlani S. Mdluli, Ndabenhle M. Sosibo, Philani N. Mashazi, Tebello Nyokong, Robert T. Tshikhudo, Amanda Skepu, Elma van der Lingen, **Selective adsorption of PVP on the surface of silver nanoparticles: A molecular dynamic study,** *Journal of Molecular Structure* 2011 (**1004**) 131 - 137**.**

2. Ndabenhle M. Sosibo, Phumlani S. Mdluli, Philani N. Mashazi, Busiswa Dyan, Neerish Nevaprasadu, Tebello Nyokong, Robert T. Tshikhudo, Amanda Skepu, Elma van der Lingen, **Synthesis, density functional theory, molecular dynamic and electrochemical studies of 3-thiopheneacetic acid-capped gold nanoparticles,** *Journal of Molecular Structure* 2011 (**1006**) 494 - 501**.**

3. Ndabenhle Sosibo, Phumlani Mdluli, Philani Mashazi, Robert Tshikhudo, Amanda Skepu, Sibulelo Vilakazi, Tebello Nyokong, **Facile deposition of gold nanoparticle thin films on semi-permeable cellulose membrane,** *Material Letters* 2011, *in preparation***.**

Chapter 3:

Synthesis, spectral and electrochemical properties of synthesized MPc complexes

3 SYNTHESIS AND CHARACTERIZATION OF PHTHALOCYANINE COMPLEXES

The syntheses and characterization of CoTAPc and MnTAPc complexes have been reported in literature and their spectral characterization is well known. The synthesis and characterization of metal octa(hexylthio)phthalocyanines (**12**-**15**) (MOcHexTPc) complexes containing cobalt (CoOcHexTPc) and manganese (MnOcHexTPc) are studied in detail in this work using spectroscopy and electrochemistry. Table 3.1 shows the list of MPc complexes synthesized and used in this thesis.

Table 3.1: List of the MPc complexes synthesized and used in this thesis.

Name of the complex	Abbreviation	Number
α-Cobalt octa(hexylthio)phthalocyanine	**α-CoOcHexTPc**	**12**
β-Cobalt octa(hexylthio)phthalocyanine	**β-CoOcHexTPc**	**13**
α-Manganese octa(hexylthio)phthalocyanine	**α-(Ac)MnOcHexTPc**	**14**
β-Manganese octa(hexylthio)phthalocyanine	**β-(Ac)MnOcHexTPc**	**15**
Cobalt tetraaminophthalocyanines	**CoTAPc**	**16**
Manganese tetraaminophthalocyanines	**(OH)MnTAPc**	**17**

α- or β- denotes the position of the substituents

From Table 3.1, the manganese complexes have either OH or Ac as an axial ligand. During the synthesis of MnTAPc complex (**17**) the $MnCl_2$ was used as metal salt and during the purification strong basic solutions (NaOH) are used resulting in ligand exchange and formation of OH axial ligand. For the synthesis of MnOcHexTPc (**14** and **15**), the $Mn(Ac)_2$ salt was used resulting in the Ac axial ligand.

3.1 Synthesis and characterization of metal tetraaminophthalocyanine complexes

The synthesized metal tetra-amino phthalocyanine (CoTAPc and MnTAPc) complexes gave satisfactory spectroscopic and electronic spectral data for their characterization, which were according to literature methods [327,328]. Figure 3.1 shows the electronic absorption spectra of (i) CoTAPc and (ii) MnTAPc complexes in DMF. The electronic spectra in Figure 3.1 show Q bands at 710 nm and 800 nm for CoTAPc and MnTAPc, respectively. The red-shifted Q band for the MnTAPc compared to CoTAPc is typical [328,335] of manganese phthalocyanine complexes with Mn(III) oxidation state. For both complexes the presence of electron donating amino groups results in red shifting of the Q band when compared to their unsubstituted derivatives with Q bands at 659 nm and 705 nm for CoPc and MnPc [219], respectively. The manganese complex (MnTAPc) exhibited an extra absorption band at about 500 nm and this is a charge transfer band and is typical of the manganese phthalocyanine complexes [335,336]. The charge transfer band at 500 nm is known to be due to the electron transfer from the electron rich amino groups to the electron deficient central metal ion [107,337].

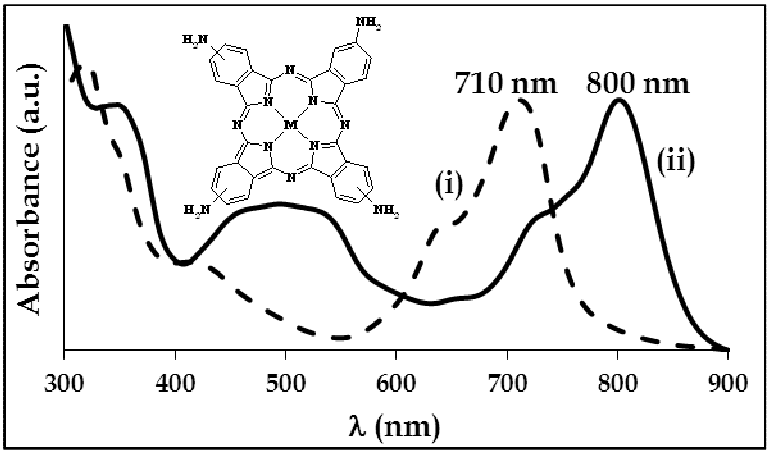

Figure 3.1: UV-vis spectra of 1 x 10^{-5} M (i) CoTAPc and (ii) MnTAPc in DMF. Inset: molecular structure of MTAPc.

The electrochemical characterization of these complexes has been done before, especially at carbon electrodes and their electrochemical and spectroelectrochemical properties have also been investigated [102,105,107,338]. In this thesis, the metal tetra-amino phthalocyanine complexes will be studied as polymers on both glassy carbon (GCE) and gold (Au) electrodes. Therefore, the solution electrochemistry of metal tetra-amino phthalocyanines on gold electrode was investigated. Figure 3.2 shows cyclic voltammograms of 1 mM (a) CoTAPc and (b) MnTAPc in DMF solution containing 0.1 M $TBABF_4$ at gold electrode surfaces.

The CoTAPc complex showed two redox couples due to cobalt reduction (Co^{II}/Co^{I}) at negative potentials (**I**) and cobalt oxidation (Co^{III}/Co^{II}) (**II**) at positive potentials and a peak for amino group oxidation (NH_2^+) (**III**). The MnTAPc complex also showed two redox couples due to manganese reduction (Mn^{III}/Mn^{II}) at negative potentials (**I**), manganese oxidation (Mn^{IV}/Mn^{III}) at positive potentials (**II**) and a peak due to amino group oxidation (NH_2^+) (**III**). The redox peaks and their assignments on both gold and glassy carbon electrodes are summarized in Table 3.2 and are comparable to the reported results also in Table 3.2 [102,105,107,338]. The assignments are done in comparison with literature. No further characterization was done on the metal tetra-amino phthalocyanines complexes and these complexes were used for further studies as will be discussed in the following chapters.

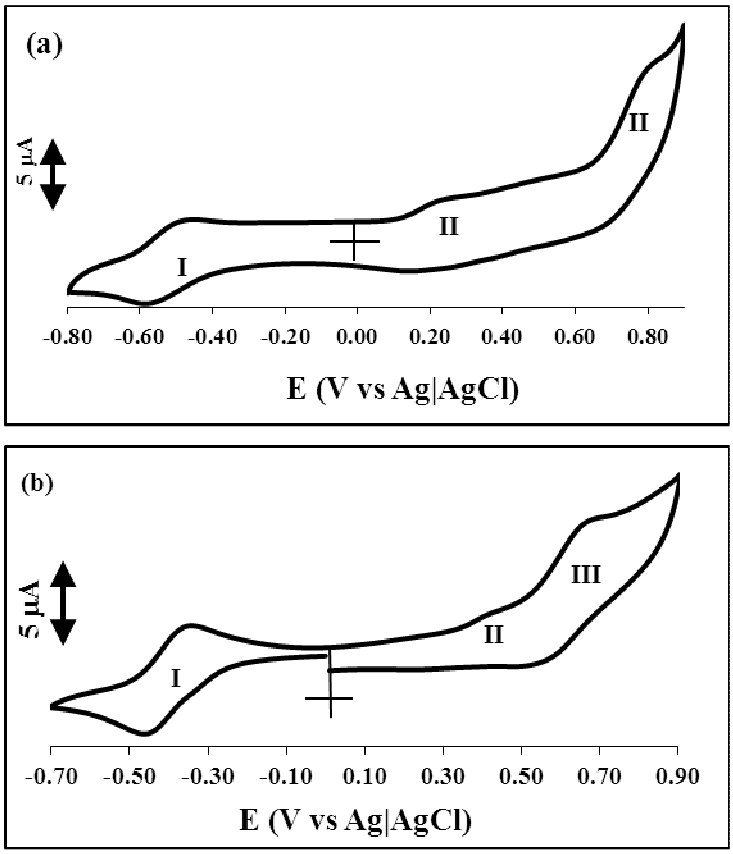

Figure 3.2: Cyclic voltammograms of 1 mM (a) CoTAPc and (b) MnTAPc in 0.1 M $TBABF_4$ DMF solution at gold electrode. Scan rate = 25 $mV.s^{-1}$.

Table 3.2: Electrochemical properties: redox couples and peak potentials and their assignments obtained for 10^{-3} M MTAPc complexes in DMF containing 0.1 M $TBABF_4$ on glassy carbon (GCE) and gold (Au) electrodes. Scan rate = 25 $mV.s^{-1}$.

		$E_{1/2}$ (V vs Ag|AgCl)		E_p (V vs Ag|AgCl)	
Complexes	**Electrodes**	**I**	**II**	**III**	**Ref.**
		(Co^{II}/Co^{I})	(Co^{III}/Co^{II})	(NH_2 oxidation)	
β–CoTAPc	GCE	-0.50 V	+0.20 V	+0.76 V	tw
β–CoTAPc	Au	-0.47 V	+0.20 V	+0.78 V	tw
β–CoTAPc	GCE	-0.52 V	+0.17 V	+0.70 V[a]	[338]
β–CoTAPc	GCE	-0.55 V	+0.33 V	+0.63 V	[102]
		(Mn^{III}/Mn^{II})	(Mn^{IV}/Mn^{III})	(NH_2 oxidation)	
β–MnTAPc	GCE	-0.38 V	+0.43 V	+0.84 V	tw
β–MnTAPc	Au	-0.41 V	+0.43 V	+0.67 V	tw
β–MnTAPc	GCE	-0.31 V	+0.58 V	+0.75 V[b]	[105]
α–MnTAPc	GCE	-0.31 V	+0.56 V	+1.05 V	[107]

tw (this work), [a] ring decomposition or NH_2 oxidation process, [b] ring decomposition. β and α refers to the substituent position, i.e. peripheral (β) and non-peripheral (α).

3.2 Synthesis and characterization of thiol substituted metal phthalocyanines

3.2.1 Synthesis of β- and α-MOcHexTPc

The synthesis of complexes (**12-15**) was accomplished following the method shown in Scheme 3.1 (same as Scheme 1.3).

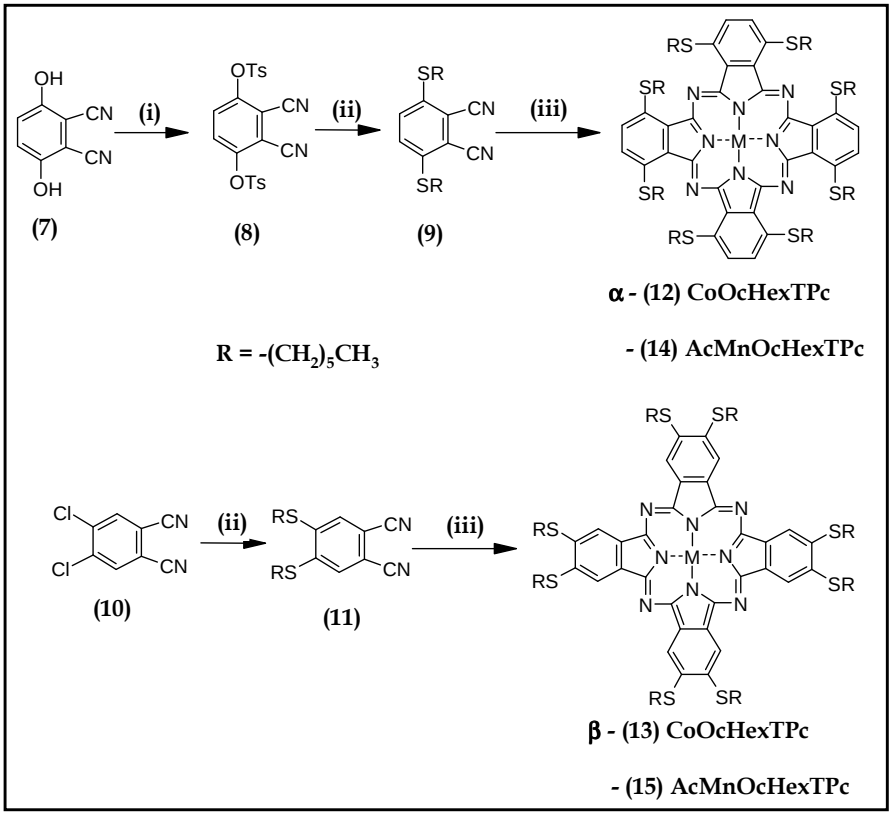

Scheme 3.1: Synthesis of manganese and cobalt octa(hexylthio)phthalocyanine substituted at non-peripherally (α-MOcHexTPc, **12** and **14**) and peripherally (β-MOcHexTPc, **13** and **15**) positions. Reagents: (i) TsCl, Acetone, K_2CO_3. (ii) 1-hexanethiol, K_2CO_3, DMSO. (iii) $CoCl_2$ or $Mn(Ac)_2$, 1-pentanol, DBU. Ac = acetate and TsCl = p-toluenesulfonyl chloride.

Prior to the synthesis of the metallophthalocyanine complexes, the precursor compounds (**9**) and (**11**) were synthesized. 2,3-Dicyanohydroquinone (**7**) was converted to the tosylated compound in basic conditions (K_2CO_3) to form 3,6-tosylated-4,5-dicyanobenzene (**8**). The nucleophilic substitution reaction of the 3,6-tosylated-4,5-dicyanobenzene (**8**) and 1,2-dichloro-4,5-dicyanobenzene (**10**) to their respective 3,6-bis(hexylthio)-4,5-dicyanobenzenes (**9**) and 1,2-bis(hexylthio)-4,5-dicyanobenzene (**11**), was obtained in the presence of the potassium carbonate as the base. The synthesis of metallated phthalocyanine complexes (**12-15**) was achieved by direct conversion of (**9**) and (**11)** *via* cyclotetramerization reaction [65,66,77] in the presence of the $MnAc_2$ (Ac = acetate) or $CoCl_2$ metal salts.

3.2.2 Spectroscopic characterization of synthesized compounds and complexes

The formation of the substituted metal phthalocyanine complexes was monitored by the disappearance of the CN vibration of phthalonitriles at 2225 (**9**) and 2229 (**11**) cm^{-1}. During the formation of the metallophthalocyanine complexes, the solution colour changed from yellowish solution to blue or green (for CoPc derivatives), purple or brownish colour (for MnPc derivatives). The manganese phthalocyanine complexes gave vibration peaks corresponding to the C-S-C stretches at 750 cm^{-1} for (**14**) and 740 cm^{-1} for (**15**) and this confirmed that the substituents were still bound to the phthalocyanine ring after cyclotetramerization reaction. A distinct peak due to the Mn-O stretch attributed to the acetate axial ligand on the central metal at 800 cm^{-1} for (**14**) and 860 cm^{-1} for (**15**) was also observed. These values are within range for the Mn-O reported values [65,105,107]. For the cobalt phthalocyanine complexes, similar vibrations due to C-S-C stretches at 742 cm^{-1} for (**12**) and 750 cm^{-1} for (**13**) were also observed. The mass spectra analysis gave the reasonable molecular ions at *m/z* = 1492 and 1496 for the (Ac)MnOcHexTPc (**14** and **15**) and CoOcHexTPc (**12** and **13**)

complexes, respectively. The obtained *m/z* values were due to $[M-3H]^+$. The *m/z* values were about 3 *m/z* values less than the expected 1495 and 1499 for $[M]^+$ of (Ac)MnOcHexTPc and CoOcHexTPc, respectively). MPc complexes have been observed to degrade with molecular ion peaks $[M]^+$, $[M+nH]^+$ or $[M-nH]^+$ (n = 1–3) [339], hence the observed mass spectral data are not surprising.

Figure 3.3 shows the UV-vis spectra of the synthesized complexes, CoOcHexTPc in Figure 3.3(a) and (Ac)MnOcHexTPc in Figure 3.3(b). The UV-vis for complexes (**12**) and (**14**) show a red shifted Q band absorption at 774 nm for (**12**) and 888 nm for (**14**) compared to their respective complexes (**13**) and (**15**) with Q bands at 704 nm and 768 nm, respectively. The positions of the substituents are known to affect the Q band maxima [340,341]. Thus the Q band maxima for complex (**12**) was at 774 nm and is more red-shifted than that of complex (**13**) at 704 nm. The enhanced red-shift to 774 nm for complex (**12**) is due to, in addition to the electron donating group of sulfur substituent [74], substitution at non-peripheral (α) position [65,66,74,340]. The same applies to MnOcHexTPc complexes (**14**) and (**15**). In general, electron donating substituents in MPc complexes destabilize the highest occupied molecular orbital (HOMO) rather than the lowest unoccupied molecular orbital (LUMO), resulting in red-shifting of the spectra [342,343]. As a result of the linear combinations of the atomic orbital (LCAO) coefficients at the non-peripheral positions of the HOMO being greater than those at the peripheral positions, the HOMO level is destabilized to a greater extent on substitution at the non-peripheral position than it is at the peripheral position, resulting in a red shift.

The manganese complexes (**14**) and (**15**) showed an even more red-shifted Q band maxima at 768 nm and 888 nm, respectively, compared to their cobalt counterparts and this is typical of the manganese (III) complexes as has been reported before [222] and stated above. Furthermore, the manganese complexes showed several bands in

the region between 450-550 nm and these bands are associated with the charge transfer bands in MnPc complexes. An increase in concentration of the complexes also showed no new bands and therefore no aggregation for these complexes, Figure 3.4 for CoOcHexTPc (**13**). All the complexes (**12-15**) synthesized in this work obey Beer-Lambert law for concentration less than 10^{-5} mol.dm^{-3}.

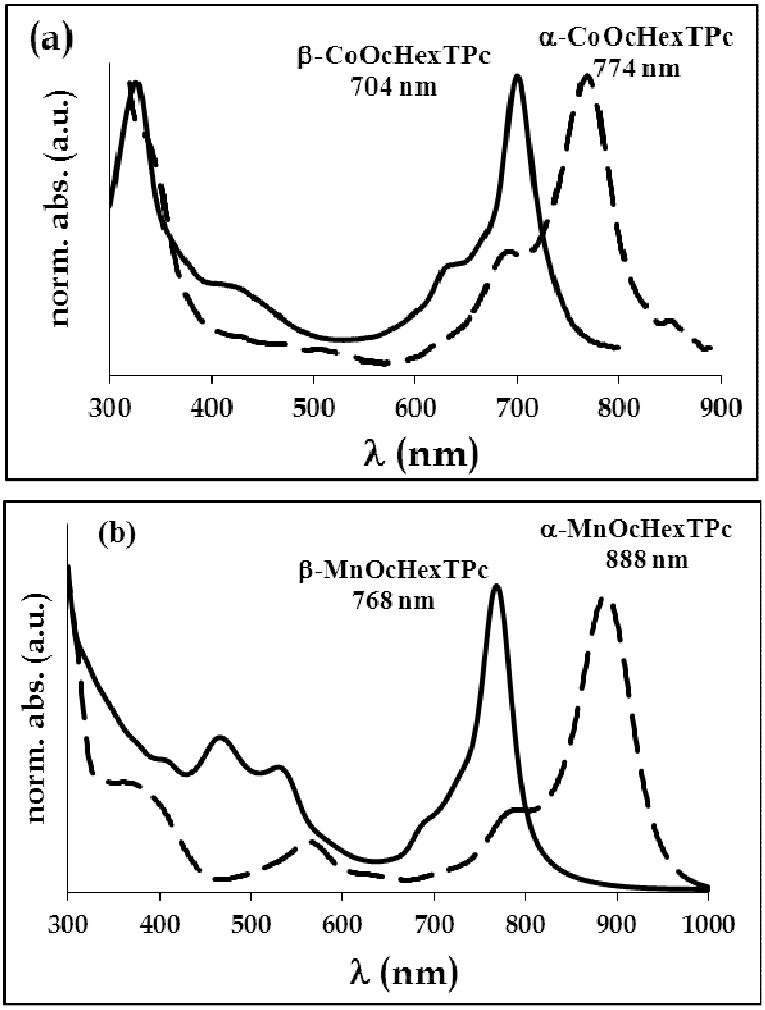

Figure 3.3: Electronic absorption spectra of 1 x 10^{-5} M complexes (a) CoOcHexTPc (**12** and **13**) and (b) AcMnOcHexTPc (**14** and **15**) in $CHCl_3$.

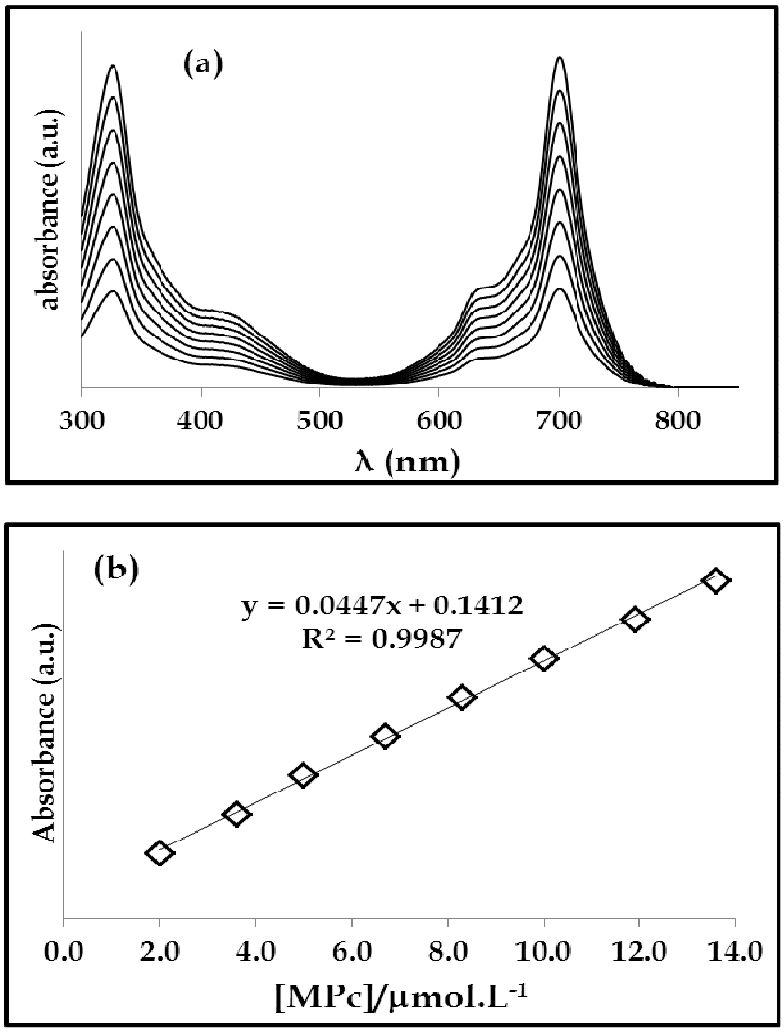

Figure 3.4: (a) Absorption spectra changes observed on increasing the concentration and (b) Beer–Lambert's plot of β-CoOcHexTPc complexes (13) in $CHCl_3$. Concentration range: 2.0 $\mu mol.L^{-1}$ to 13.6 $\mu mol.L^{-1}$.

3.2.3 Electrochemical characterization of the synthesized MOcHexTPc complexes

*3.2.3.1 CoOcHexTPc complexes (**12**) and (**13**)*

The synthesis of β-CoOHTPc (**13**) and its characterization using various techniques has been reported before [331], however the electrochemistry and spectroelectrochemistry studies of this complex was not studied, hence are investigated together with those of MOcHexTPc complexes **12**, **14** and **15**.

Figure 3.5 shows the cyclic and square-wave voltammograms of CoOcHexTPc complexes (a) **12** and (b) **13** performed in de-aerated pyridine solution containing 0.1 M $TBABF_4$ as an electrolyte. The synthesized complexes were soluble in pyridine, chloroform and dichloromethane; and in pyridine the cyclic voltammograms gave well-resolved peaks as shown in Figure 3.5. Both CoOcHexTPc complexes (**12**) and (**13**) exhibited four redox processes labeled (**I-IV**). For complex **12**, in Figure 3.5(a), the processes were observed at half-wave potentials ($E_{1/2}$) = +212 mV (**I**), +864 mV (**II**, E_P), -460 mV (**III**) and -1304 mV (**IV**) vs Ag|AgCl within the -1600 mV to +1000 mV potential window. The redox couples for complex **13**, in Figure 3.5(b), were at $E_{1/2}$ = +380 mV (**I**), +1140 mV (**II**), -450 mV (**III**) and -1170 mV (**IV**) vs Ag|AgCl within the -1400 mV to +1400 mV potential window. The half-wave peak potentials are summarized in Table 3.3. The redox processes labeled (**I**, **III** and **IV**) for complex **12** and **I-IV** for **13** in Figure 3.5 are quasi-reversible according to their peak-to-peak separation (ΔE) and the ratio of the anodic to cathodic peak currents. Process **II** for complex (**12**) is essentially irreversible, a typical behavior for alkylthio- and arylthio substituted MPc complexes [344]. The smaller potential scan range for reduction or oxidation sides was applied in trying to improve the reversibility with no success.

The oxidation peak **II**, Figures 3.5(a), for complex **12**, is not well resolved, but was more resolved for complex **13** with much higher anodic currents compared to the rest of the redox processes. The differences between complexes **12** and **13** show the effects of the point of substitution on the electrochemistry of these complexes. A shift in potentials was observed when comparing the $E_{1/2}$ for complex **12** and **13** in that the oxidation potentials were observed at less positive values for complex **12** compared to complex **13**, while the latter showed the reduction potentials at less negative values. This observation could be attributed to the substituent position; in that peripheral substitution for **13** made this complex easier to reduce (and more difficult to oxidize) while non-peripheral substitution made complex **12** easier to oxidize (and more difficult to reduce). This observation has been noted in the literature [120]. The presence of the substituents clearly lowers the reduction potentials compared to un-substituted cobalt phthalocyanine [345] which show higher reduction potentials for both metal and ring processes, Table 3.3.

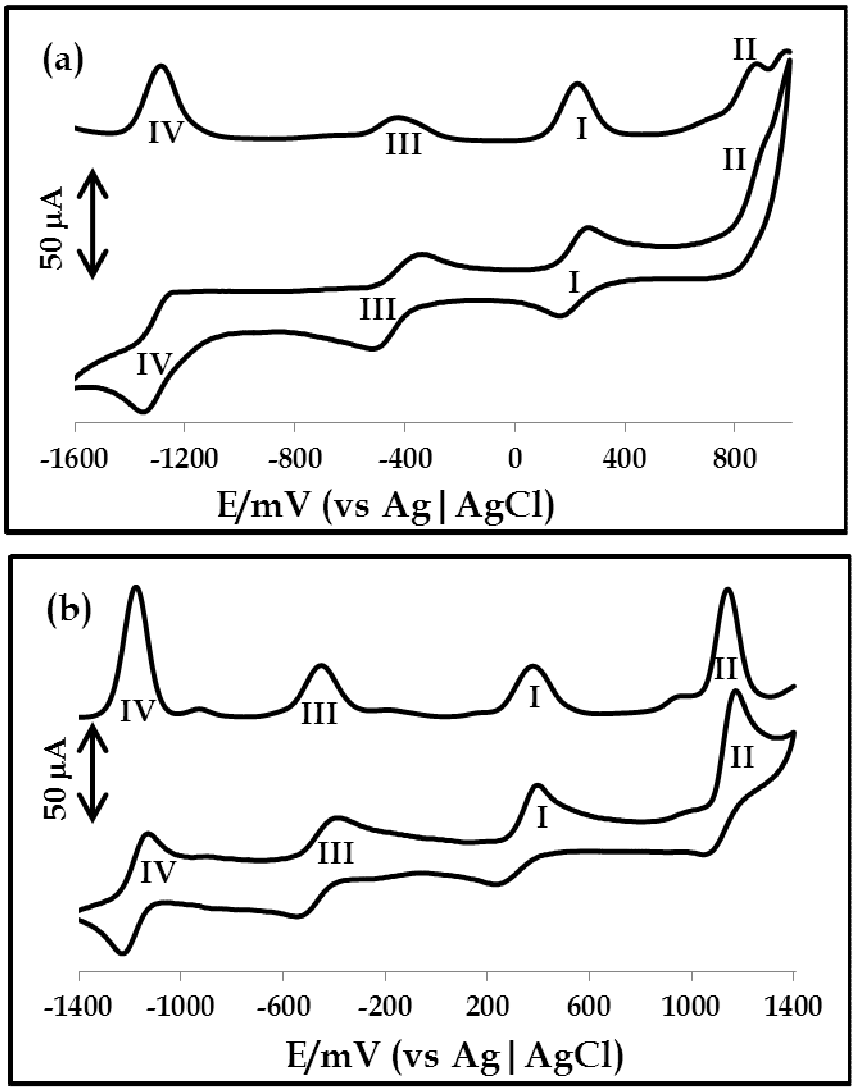

Figure 3.5: Cyclic and square wave voltammograms of 1 mM CoOcHexTPc complexes (a) **12** and (b) **13**, in pyridine containing 0.1 M $TBABF_4$. Scan rate = 25 $mV.s^{-1}$.

Table 3.3: Summary of redox potentials for complexes **12** and **13** in pyridine solution containing $TBABF_4$ unless otherwise stated. Scan rate = 25 $mV.s^{-1}$.

	$E_{1/2}$ (mV vs. Ag|AgCl)				
CoPc complexes	**IV** $Co^{I}Pc^{-2}/Co^{I}Pc^{-3}$	**III** $Co^{II}Pc^{-2}/Co^{I}Pc^{-2}$	**I** $Co^{III}Pc^{-2}/Co^{II}Pc^{-2}$	**II** $Co^{III}Pc^{-1}/Co^{III}Pc^{-2}$	Ref.
12	-1304	-460	212	864	tw
13	-1170	-450	380	1140	tw
CoPc[a,b]	-1375	-555	235	___	[345]

tw = this work. [a]A correction factor of 0.045 V has been applied to convert potentials to Ag|AgCl [123]. [b]Electrolyte tetrabutylammonium perchlorate.

Spectroelectrochemical studies using the optically transparent thin-layer electrochemical (OTTLE) cell were used to further examine the nature of the redox processes observed in Figure 3.5 for the CoOcHexTPc complexes **12** and **13** (using **12** as an example). Figure 3.6 shows the UV-vis spectral changes observed during controlled potential at the oxidation (**I** and **II**) and the reduction (**III** and **IV**) potentials for complex **12**.

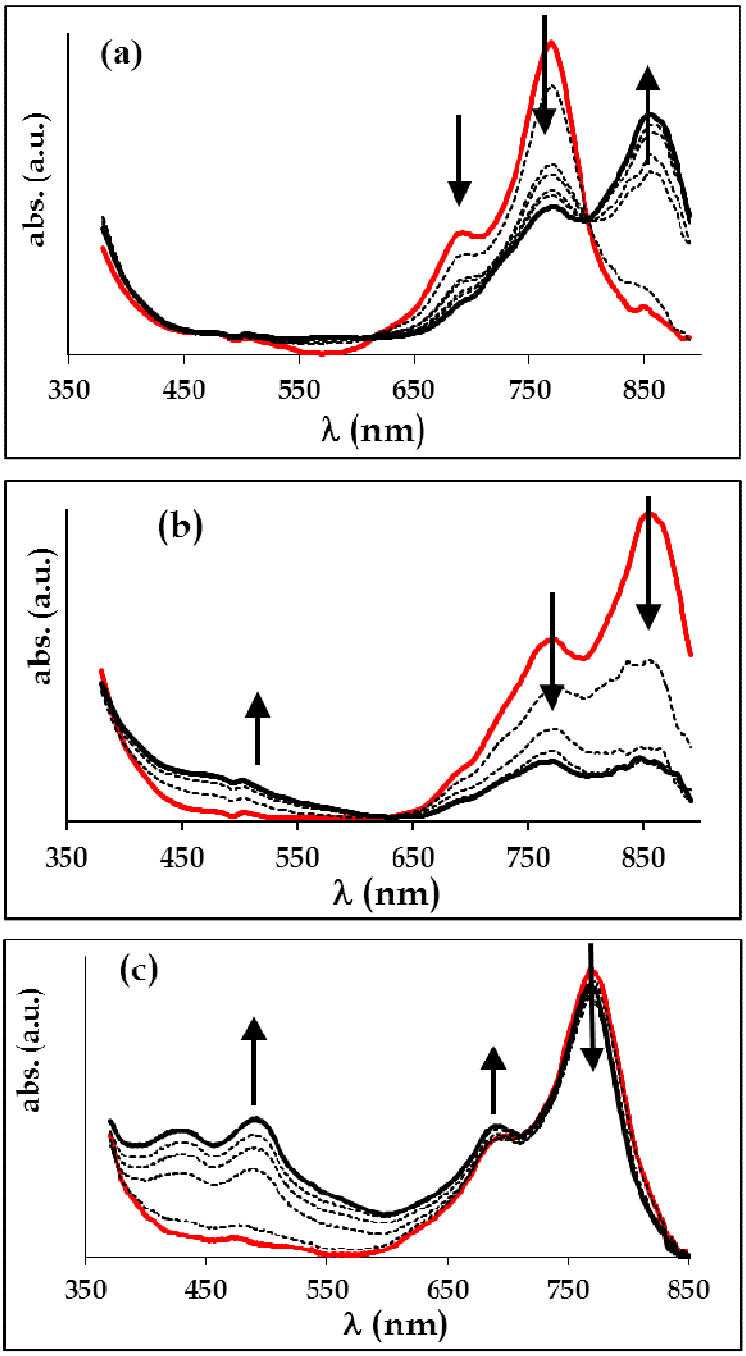
(a)
abs. (a.u.)
350
450
550
650
750
850
λ (nm)
(b)
abs. (a.u.)
350
450
550
650
750
850
λ (nm)
(c)
abs. (a.u.)
350
450
550
650
750
850
λ (nm)

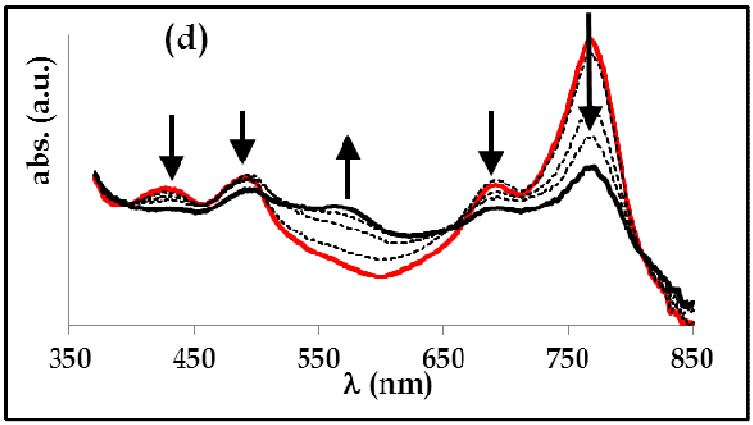

Figure 3.6: UV-vis spectral changes of the 1 mM complex (**12** in pyridine containing 0. 1 M $TBABF_4$ observed during application of controlled potential of the following processes: (a) **I** (380 mV), (b) **II** (1140 mV), (c) **III** (-450 mV) and (d) **IV** (-1170mV).

The application of the first oxidation potential corresponding to the redox process (**I**) exhibited the spectral changes shown in Figure 3.6(a). The spectral changes showed a decrease in Q band at 774 nm and the vibrational band at 696 nm and the emergence of the peak at 861 nm was observed. These spectral changes are typical [335] of a metal based oxidation process in MPcs suggesting the formation of the $Co^{III}OcHexTPc^{-2}$ species from the $Co^{II}OcHexTPc^{-2}$ species. Clear isosbestic points were observed at 806 nm, 615 nm and 515 nm, suggesting that only two species were present during the electrochemical oxidation of the $Co^{II}OcHexTPc^{-2}$ to $Co^{III}OcHexTPc^{-2}$. Further oxidation at potentials of process **II** resulted in the decrease in the Q band at 861 nm. This was also accompanied by the increase in intensity in the region 400 to 560 nm as shown in Figure 3.6(b). These spectral changes are typical of the ring-based process in MPcs and therefore suggest oxidation of $Co^{III}OcHexTPc^{-2}$ to $Co^{III}OcHexTPc^{-1}$.

The applications of the reduction potentials of process **III** resulted in the spectral changes observed in Figure 3.6(c). The decrease in Q band at 774 nm was accompanied by a concomitant increase the peaks at 696 nm, 496 nm and 430 nm.

The observed changes are typical of the metal based reduction processes of CoPc complexes and the formation of the $Co^{I}OcHexTPc^{-2}$ species from $Co^{II}OcHexTPc^{-2}$ species. The envelope bands at about 400-500 nm are typical of $Co^{I}Pc^{-2}$ species as have been reported before [120,163, 335,346]. The Q band at 774 nm did not shift even though the presence of an envelope of bands between 400 and 500 confirmed the presence of the $Co^{I}OcHexTPc^{-2}$ species. The reluctance of the expected Q band shift could be due to a solvent effect, attributed to the binding of pyridine as an axial ligand to the $Co^{II}OcHexTPc$ resulting in the presence of both $Co^{I}OcHexTPc^{-2}$ and persistent $Co^{II}OcHexTPc^{-2}$ species. This is not surprising as cobalt phthalocyanine complexes are known [219,347] to form axial ligands with pyridine-like or N-donor molecules from solution. Further reduction at process **IV** potentials resulted in the decrease in the bands at 774 nm, 696 nm, 496 nm and 430 nm accompanied by the increase in intensity in the 500 to 650 nm region, Figure 3.6(d). These spectral changes are typical of the ring based process, thus confirming the reduction of $Co^{I}OcHexTPc^{-2}$ to $Co^{I}OcHexTPc^{-3}$. The observed spectral changes and assignments are similar to the reported CoPc complexes [120,163,335,346]. Similar spectral changes with similar assignments were observed for complex **13** at the applied potentials obtained in Figure 3.5(b) for processes (**I-IV**). There was a 90% regeneration of the original species when O V potential was applied thus confirming the reversibility of reduction processes as shown in cyclic voltammetry. The proposed mechanism of reduction and oxidation of the cobalt complexes **12** and **13** was based on electrochemistry and is shown in equations (3.1) – (3.4):

$$Co^{II}OcHexTPc^{-2} \longrightarrow [Co^{III}OcHexTPc^{-2}]^{+} + e^{-} \quad \text{(process I)} \qquad (3.1)$$

$$[Co^{III}OcHexTPc^{-2}]^{+} \longrightarrow [Co^{III}OcHexTPc^{-1}]^{2+} + e^{-} \quad \text{(process II)} \qquad (3.2)$$

$$Co^{II}OcHexTPc^{-2} + e^{-} \longrightarrow [Co^{I}OcHexTPc^{-2}]^{-} \quad \text{(process III)} \qquad (3.3)$$

$$[Co^{I}OcHexTPc^{-2}]^{-} + e^{-} \longrightarrow [Co^{I}OcHexTPc^{-3}]^{2-} \quad \text{(process IV)} \qquad (3.4)$$

*3.2.3.2 MnOcHexTPc complexes (**14**) and (**15**)*

Figure 3.7 shows a cyclic and square wave voltammograms of the MnOcHexTPc complexes **14** and **15** performed in de-aerated pyridine solution containing $TBABF_4$ as an electrolyte. The MnOcHexTPc complexes (**14**) and (**15**) both exhibited three redox processes and their half-wave potentials ($E_{1/2}$) are summarized in Table 3.4. The three redox processes labeled (**I-III**) for complex **14**, in Figure 3.7(a), were observed at $E_{1/2}$ = +5 mV (**I**), -640 mV (**II**) and -1380 mV (**III**) vs Ag|AgCl within the -1600 mV to +1000 mV potential window. The redox couples for complex **15** in Figure 3.7(b) were at $E_{1/2}$ = -27 mV (**I**), -530 mV (**II**) and -1270 mV (**III**) vs Ag|AgCl within the -1500 mV to +1000 mV potential window. The redox processes for both complexes **14** and **15** in Figure 3.7 are not completely reversible according to their peak-to-peak separation (ΔE) and the ratio of the anodic to cathodic peak currents. The small potential scan range was applied in trying to improve the reversibility with no success. For complex **15**, in Figure 3.7(b) a shoulder or broader peak was observed for the first redox process (labeled **I**) probably due to aggregation which will be more pronounced in peripherally substituted MPc complexes (**15**) compared to non-peripherally substituted (**14**) counterparts [121].

Similar properties to those of cobalt phthalocyanine complexes discussed above were also observed in the manganese complexes **14** and **15**, in that complex **15** was easier to reduce than complex **14**. The potentials for the complexes studied in this work are almost similar to the reported values for similar compounds with shorter chains [75]. However these values are less negative than the values reported [348] for the unsubstituted MnPc complex in pyridine, Table 3.4. Clearly the presence of the substituents has an effect on the potential values for redox processes labeled (**II**) and (**III**) of the MnPc complexes in that the values appear at less negative potentials compared to unsubstituted MnPc complex. It would have been expected that the

presence of electron donating sulfur atoms would make reduction more difficult in complexes **14** and **15** compared to unsubstituted MnPc, but this is not the case as shown by the values in Table 3.4. The same was observed in CoPc derivatives where the alkylthio substituted **12** and **13** were easier to reduce than unsubstituted CoPc.

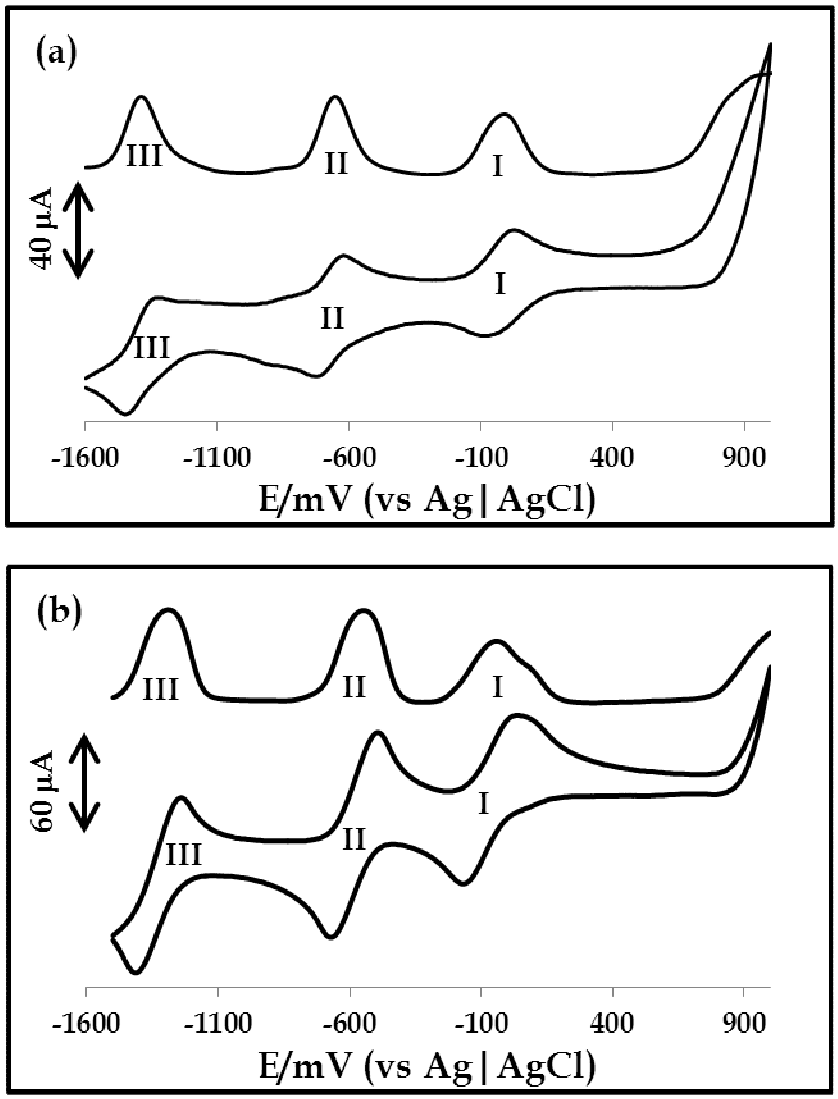

Figure 3.7: Cyclic and square wave voltammograms of (a) complex (**14**) and (b) complex (**15**), MnOcHexTPc (1 mM) in pyridine containing 0.1 M $TBABF_4$. Scan rate = 25 mV s^{-1}.

Table 3.4: Summary of redox potentials for complexes **14** and **15** in pyridine solution containing $TBABF_4$ unless otherwise stated. Scan rate = 25 mV s^{-1}.

MnPc complexes	$E_{1/2}$ (V vs Ag|AgCl)			
	III $Mn^{I}Pc^{-2}/Mn^{I}Pc^{-3}$	**II** $Mn^{II}Pc^{-2}/Mn^{I}Pc^{-2}$	**I** $Mn^{III}Pc^{-2}/Mn^{II}Pc^{-2}$	Ref.
14	-1380	-640	5	tw
15	-1270	-530	-27	tw
MnPc[a,b]	-1475	-740	50	[348]

tw = this work. [a]Electrolyte = tetrabutylammonium perchlorate. [b]Electrolyte = tetraethyl-ammonium perchlorate.

Spectroelectrochemical studies were also carried out for the manganese complexes **14** and **15** in order to assign the cyclic voltammetry processes. Figure 3.8 shows the spectral changes during the application of the reduction (**I** and **II**) potentials for complex **15**. The reduction at potentials of process **I** resulted in the observed spectral changes in Figure 3.8(a). The Q band at 768 nm was observed shifted to 669 nm. This transformation resulted in the colour change from purple to green and was accompanied by the decrease in intensity for a charge transfer band at around 500 nm region. Clear isosbestic points were observed at 716 nm and 587 nm further suggesting that only two species are present during the reduction of this phthalocyanine complex. The spectral changes observed are typical of the metal based reduction process in MnPc and are similar to those reported in literature [75,335] and thus are consistent with the metal reduction from $Mn^{III}OcHexTPc^{-2}$ to $Mn^{II}OcHexTPc^{-2}$.

Further reduction of process **II** resulted in the spectral changes observed in Figure 3.8(b) which consisted of a decrease in the Q-band intensity at 669 nm with a

simultaneous increase in intensity in the 500 to 600 nm region. These spectral changes are typical of the ring based reduction process, confirming the reduction of $Mn^{II}OcHexTPc^{-2}$ to $Mn^{II}OcHexTPc^{-3}$. Further reductions are expected to be of a ring based nature and therefore reduction at processes **III** is a further ring reduction from $Mn^{II}OcHexTPc^{-3}$ to $Mn^{II}OcHexTPc^{-4}$. Similar spectral changes for the manganese complex **14** were observed when potentials at processes (**I** and **II**) in Figure 3.7(a) were applied. The species formed during the applied potential could be regenerated to about 90% and this signified the reversibility of the processes as observed in the cyclic voltammetry. Based on the observed spectral changes and electrochemistry data obtained, the following mechanism for the reduction of the manganese complexes (**8**) and (**9**) is proposed, equation (3.5 – 3.7):

$$[Mn^{III}OcHexTPc^{-2}]^{+} + e^- \longrightarrow Mn^{II}OcHexTPc^{-2} \quad \text{(process } \mathbf{I}\text{)} \qquad (3.5)$$

$$Mn^{II}OcHexTPc^{-2} + e^- \longrightarrow [Mn^{II}OcHexTPc^{-3}]^{-} \quad \text{(process } \mathbf{II}\text{)} \qquad (3.6)$$

$$[Mn^{II}OcHexTPc^{-3}]^{-} + e^- \longrightarrow [Mn^{II}OcHexTPc^{-4}]^{2-} \quad \text{(process } \mathbf{III}\text{)} \qquad (3.7)$$

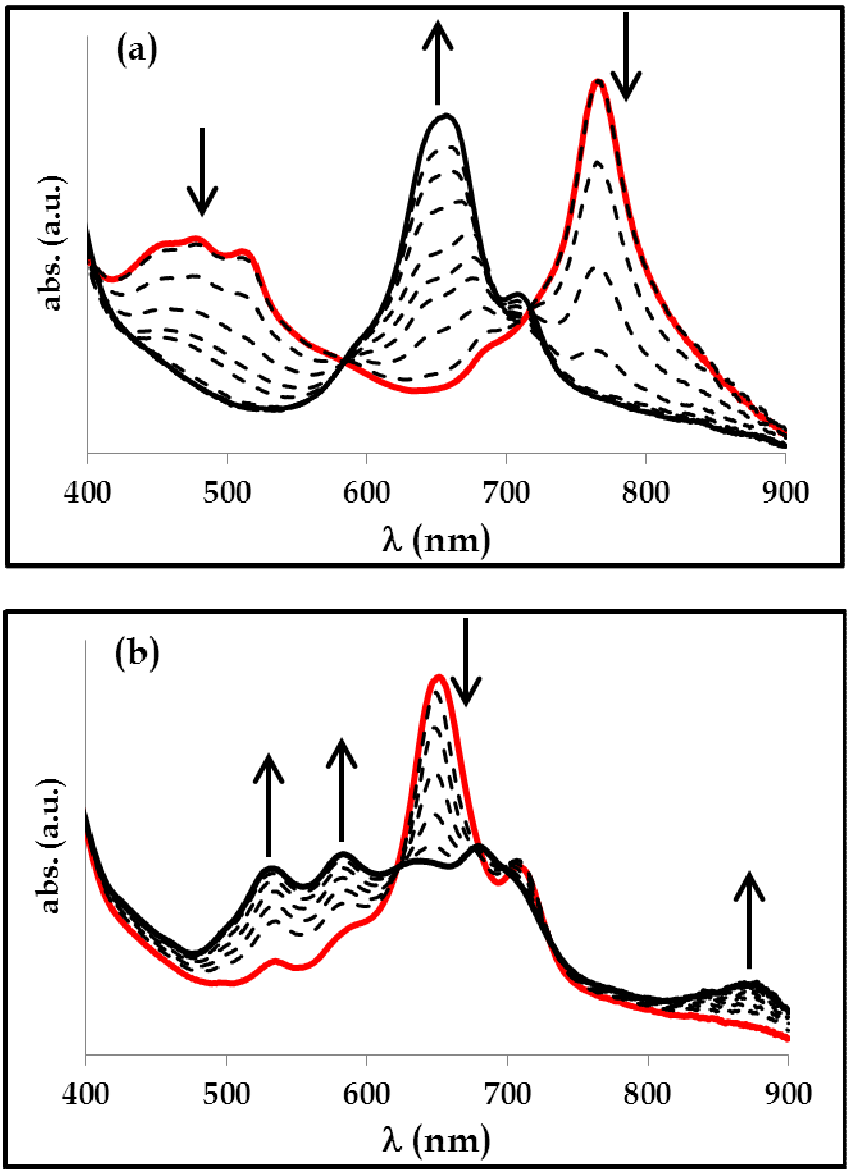

Figure 3.8: UV-vis spectral changes of the complex (**15**) in pyridine solution containing 0.1 M $TBABF_4$ observed during application of controlled potential of the following processes: (a) **I** (-100 mV) and (b) **II** (-600 mV).

Chapter 4:

Electrode fabrication and characterization using electrochemistry and other surface techniques

This chapter describes the different immobilization strategies of MPc complexes onto electrode surfaces and their characterization using electrochemical based techniques and other surface analysis techniques

4 ELECTRODE FABRICATION AND CHARACTERIZATION

The synthesized MPc complexes (**12** - **17**) discussed in chapter 3 were studied for their thin film forming capabilities. The thiol-functionalized MPc complexes (**12** - **15**) were immobilized onto gold electrode surfaces as self-assembled monolayers. The tetraamino functionalized MPc complexes (**16** and **17**) were immobilized as polymers onto indium tin oxide (ITO), glassy carbon electrode (GCE) and gold (Au) electrode surfaces. Further immobilization of MTAPc complexes (**16** and **17**) was achieved using covalent attachment onto screen-printed gold electrode surfaces. Single-walled carbon nanotubes were also immobilized (covalently) onto screen-printed electrode surfaces together with MTAPc complexes as hybrid systems.

4.1 Immobilization and characterization of MOcHexTPc complexes (12 – 15) onto gold electrode surfaces as SAMs

The characterization of the surface modifications was accomplished by using electrochemical and microscopic methods. Cyclic voltammetry [68,77,79,349-351] was used to elucidate the MPc SAMs properties and atomic force microscopy [77,349] was used to study surface topography before and after electrode modification. These methods complement each other in demonstrating the presence of the MPc SAMs on gold surface. The formation of arylthio and alkylthio substituted MPc SAMs has been shown to take place without the cleavage of the S-R bond [68].

4.1.1 Cyclic voltammetric characterization of SAMs on gold surface

A number of electrochemical experiments were investigated in order to confirm the immobilization of the MPc complexes (**12** - **15**) onto gold electrode surfaces. These include the blocking of gold oxidation and reduction which occurs in the presence of the oxygen in solution, blocking of $[Fe(H_2O)_6]^{3+}/[Fe(H_2O)_6]^{4+}$ couple and copper ad-atom deposition. The bare electrode behaviour was studied in basic media (0.01 M KOH), 1 mM $Fe(NH_4)(SO_4)_2$ in 1 mM $HClO_4$, 2 mM $CuSO_4$ in 0.5 M H_2SO_4 and in 1 mM $K_3Fe(CN)_6$ in 0.1 M KCl.

4.1.1.1 Copper deposition

Figure 4.1(a) shows the cyclic voltammograms (CV) of bare and MPc SAMs modified gold electrodes in 2 mM $CuSO_4$ in 0.5 M H_2SO_4 solution. At the bare gold electrode in Figure 4.1(a)(i), a redox process (labeled **I**) due to metal reduction from Cu^{II} to Cu^{I} was observed. The second reduction peak labeled (**II**) at E_p = -0.2 V was due to further reduction (Cu^{I} to Cu^{0}) and the deposition of metallic Cu^{0} to gold electrode, thus forming a Cu ad-atom on the gold surface. The return scan showed a large oxidation peak at E_p = 0.10 V and this peak corresponds to the stripping of the copper metallic layer from the gold surface. This is a well known process for the characterization of a bare gold electrode [180]. This reaction was not observed after the gold electrodes were modified with MPc SAMs in Figure 4.1(a)(ii-v). This confirmed the formation of SAMs onto gold electrode surfaces.

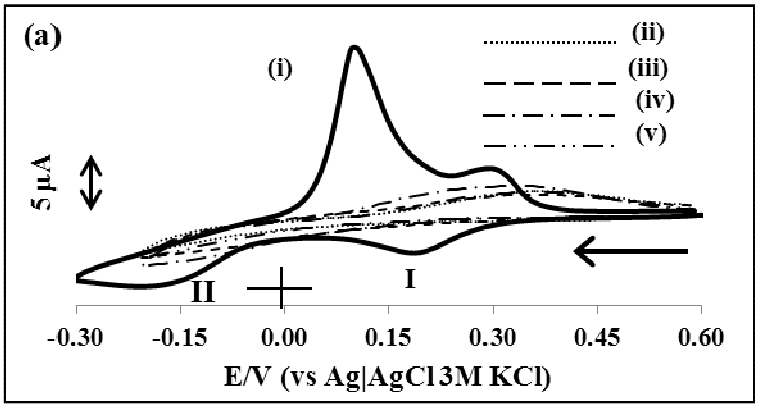
(a)
(i)
(ii)
(iii)
(iv)
(v)
5 µA
II
I
-0.30 -0.15 0.00 0.15 0.30 0.45 0.60
E/V (vs Ag|AgCl3M KCl)

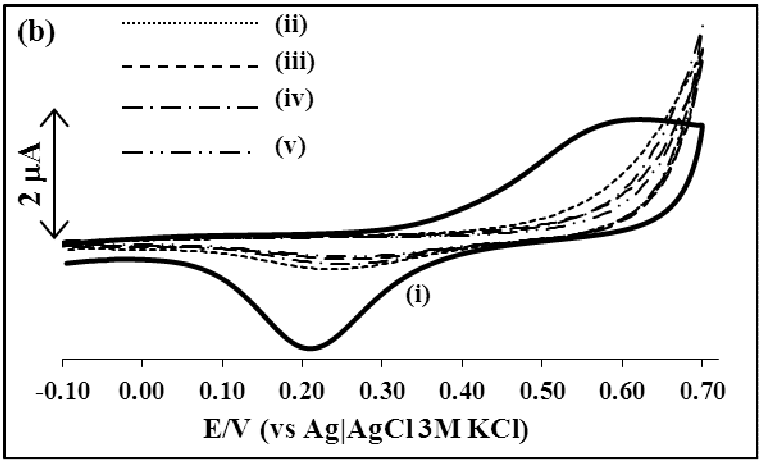
(b)
(ii)
(iii)
(iv)
(v)
2 µA
(i)
-0.10 0.00 0.10 0.20 0.30 0.40 0.50 0.60 0.70
E/V (vs Ag|AgCl3M KCl)

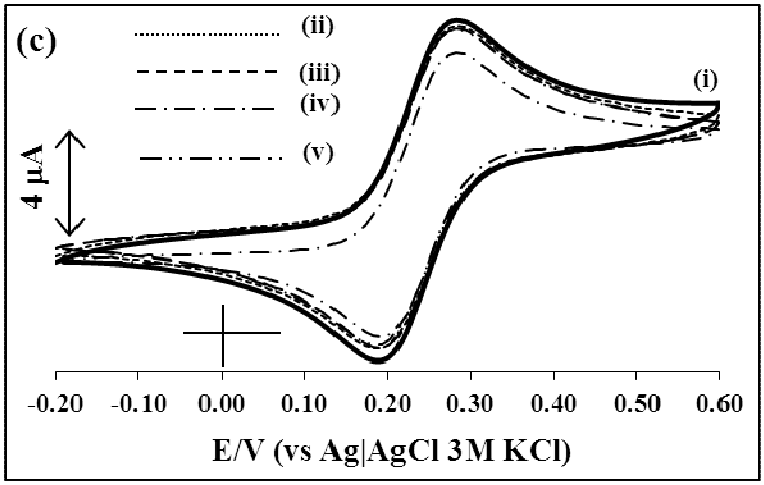
(c)
(ii)
(iii)
(iv)
(v)
(i)
4 µA
-0.20 -0.10 0.00 0.10 0.20 0.30 0.40 0.50 0.60
E/V (vs Ag|AgCl 3M KCl)

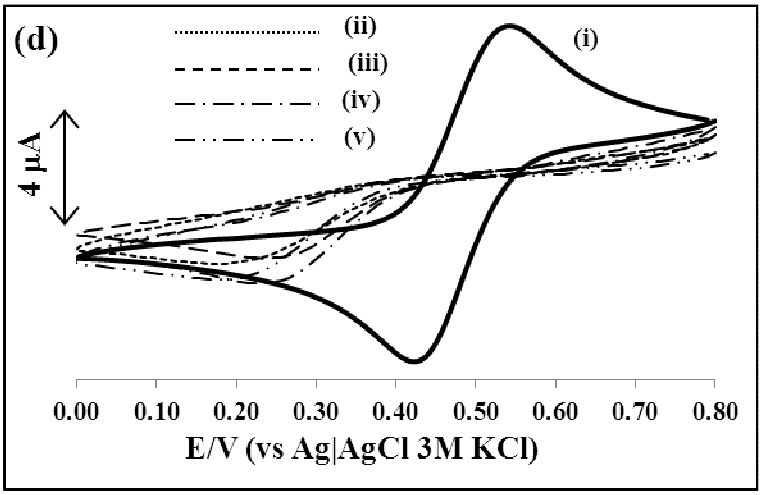

Figure 4.1: Cyclic voltammograms of (i, solid) bare gold electrodes, (ii, dotted) **12**-SAM, (iii, dashed) **13**-SAM, (iv, dash-dot) **14**-SAM and (v, dash-dot-dot) **15**-SAM in (a) 2.0 mM $CuSO_4$ in 0.5 M H_2SO_4, (b) 0.01 M KOH, (c) (1:1) $K_3/K_4Fe(CN)_6$ in 0.1 M KCl and (d) 1.0 mM $Fe(NH_4)(SO_4)_2$ in 1.0 mM $HClO_4$. Scan rate = 50 $mV.s^{-1}$.

4.1.1.2 Gold oxidation

The blocking of oxidation and reduction of oxygen on gold was studied to further confirm the formation of SAMs. Figure 4.1(b) shows the cyclic voltammograms of the (i) bare gold electrode and (ii-v) MPc SAM modified electrodes obtained in 0.01 M KOH solution. The gold oxidation and reduction peaks were observed at bare gold electrodes in Figure 4.1(b)(i) and these reactions, especially the oxidation peak, were blocked after the gold electrodes were modified with MPc SAMs in Figure 4.1(b)(ii-v). The presence of the small reduction peak may be attributed to the pinholes in the MPc SAMs modified electrodes. The SAMs were further characterized by determining the ion barrier factor (Γ_{ibf}) according to equation 1.11 [180]. The Γ_{ibf} values for all the MPc SAMs modified electrodes were found to be between 0.70 and 0.87. The Γ_{ibf} value equal to unity indicates that the electrode is completely covered by the SAMs and the ions cannot pass through the formed monolayer. In this study, the Γ_{ibf} values were less than

unity and this is again attributed to the presence of pinholes, allowing the solution ions to reach the electrode surface.

4.1.1.3 Ferri/Ferrocyanine studies

The redox probing species which consisted of $K_3Fe(CN)_6/K_4Fe(CN)_6$ and 0.1 M KCl as an electrolyte were investigated. Figure 4.1(c)(i-v) shows the bare and MPc SAMs modified gold electrodes and their behaviour in $K_3/K_4Fe(CN)_6$ containing solution. The electrodes displayed a different trend (than the previous two experiments) in that the bare and modified electrodes gave almost the same cyclic voltammograms and the $[Fe(CN)_6]^{-3/-4}$ redox process was not blocked by the SAMs. The presence of the redox couple, even after the electrodes were modified with MPc SAMs, was attributed to the fact that the $[Fe(CN)_6]^{-3/-4}$ is a fast electron transfer species, mass transport determines the rate determining step even at small overpotentials. The inability of the MPc SAMs to block $[Fe(CN)_6]^{-3/-4}$ has been reported in literature [113,196] to be due to the SAMs acting as electronic conductors, thus catalyzing this redox couple.

4.1.1.4 Ferrous ammonium sulphate studies

Figure 4.1(d) shows the cyclic voltammograms of the (i) bare gold electrode and (ii-v) MPc SAM modified gold electrodes in 1 mM $Fe(NH_4)(SO_4)_2$ in 1.0 mM $HClO_4$ solution. The unmodified gold electrode exhibited a clear reversible redox process due to $[Fe(H_2O)_6]^{3+/2+}$. After the bare electrodes were modified with the MPc SAMs, Figure 4.1(d)(ii-v), the redox process, in particular the oxidation peak, disappeared. The reduction peak was still observed at potentials less positive than those of the unmodified electrode. The MPc SAMs electronic conducting and catalyzing properties obtained in $Fe(CN)_6^{-3/-4}$ solution were not observed in the $Fe(NH_4)(SO_4)_2$ solution. This

could be attributed to the fact that $[Fe(CN)_6]^{-3/-4}$ and $[Fe(H_2O)_6]^{3+/2+}$ are two different species with different chemistries and redox behaviour.

4.1.1.5 Buffer (pH 7.4) studies

The MPc SAM modified electrodes were cycled in the blank pH 7.4 buffer solution in order to determine SAMs formation on gold electrodes. Figure 4.2 shows the cyclic voltammograms for (a) CoOcHexTPc complexes (i) bare gold, (ii) **12**-SAM and (iii) **13**-SAM and (b) MnOcHexTPc complexes (i) bare gold, (ii) **14**-SAM and (iii) **15**-SAM in pH 7.4 buffer solution. The cyclic voltammograms of bare gold electrode in Figure 4.2(i) surfaces showed no peak at the studied potential scan range. The redox peaks due to the central metal ion oxidation, i.e. $Co^{III}Pc^{-2}/Co^{II}Pc^{-2}$ and $Mn^{IV}Pc^{-2}/Mn^{III}Pc^{-2}$ were observed in Figure 4.2(a) and (b), respectively. In Figure 4.2(a), metal redox processes was observed for complexes (**12** and **13**) due to $Co^{II}Pc^{-2}/Co^{III}Pc^{-2}$ oxidation for both complexes at $E_{1/2} \approx 0.2$ V and these peaks are close to those observed in solution, Figure 3.5, especially for complex **12**. The oxidation peak observed for the SAM of complex **13** in Figure 4.2(a) were lower (0.2V) than those observed during the solution electrochemistry (0.38 V) in Figure 3.5. Figure 4.2(b) shows the metal redox processes at $E_{1/2} \approx 0.15$ V and these redox peaks were attributed to the manganese metal oxidation ($Mn^{IV}Pc^{-2}/Mn^{III}Pc^{-2}$) in comparison to earlier reports [79]. The $Mn^{IV}Pc^{-2}/Mn^{III}Pc^{-2}$ couple was not observed in solutions above, Figure 3.7. These studies clearly confirm the presence of the MOcHexTPc complexes (**12 - 15**) as SAMs on gold electrodes.

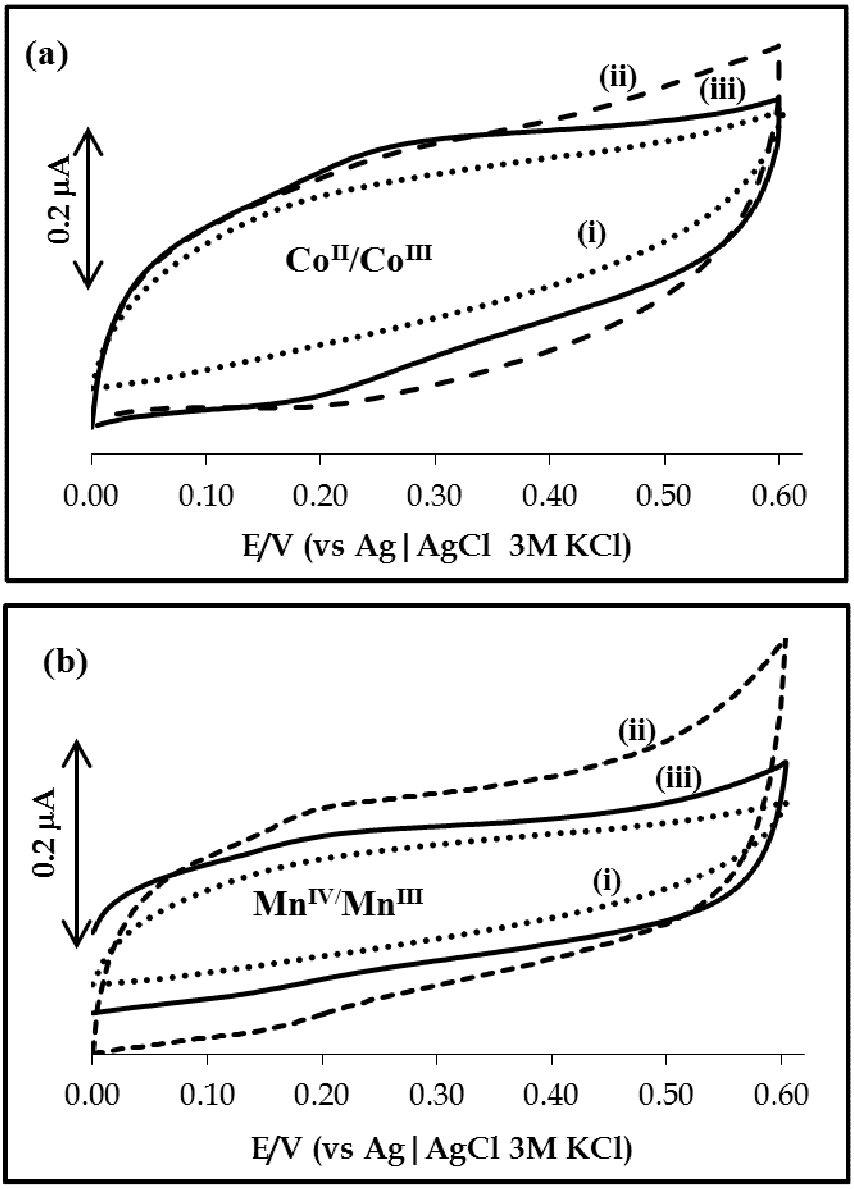

Figure 4.2: Cyclic voltammograms of complexes (a)(i) bare gold, (ii) **12**-SAM and (iii) **13**-SAM and (b)(i) bare gold, (ii) **14**-SAM and (iii) **15**-SAM in pH 7.4 buffer solution. Scan rate = 50 $mV.s^{-1}$.

The MOcHexTPc SAMs modified electrodes were further characterized using the reductive desorption methods in an alkaline medium. Alkylthiols and thiol derivative compounds are known to undergo desorption, i.e. oxidative [352] or reductive [180, 181], in strong alkaline solutions and this occurrence was investigated to confirm the

presence of MPc SAMs on gold electrodes. The reductive desorption experiments were performed for the SAMs modified electrodes in 0.2 M KOH in the potential window of –0.2 to –1.0V vs Ag|AgCl. The SAMs desorb quantitatively from gold surface at this potential scan range. Figure 4.3 shows the first reduction scan of the cyclic voltammograms recorded during the reductive desorption of (a) (i) **12**-SAM and (ii) **13**-SAM and (b) (i) **14**-SAM and (ii) **15**-SAM in 0.2 M KOH solution. There was no peak observed at bare gold electrodes in 0.2 M KOH solution within the studied potential range (-0.2 to -1.0 V). The reduction scan of the SAMs gold electrodes modified with complexes **12** in Figure 4.3(a)(i) and **14** in Figure 4.3 (b)(i) showed broad reductive desorption peaks. The SAMs of complexes **13** and **15** exhibited sharp reduction peaks in Figure 4.3(a)(ii) and Figure 4.3(b)(ii), respectively. The reduction peaks correspond to the desorption of the SAMs from the gold electrode surface according to equation 4.1 (same as equation 1.10).

$$\text{Au-SR} + e^- \longrightarrow \text{Au} + \text{RS}^- \qquad (4.1)$$

The reductive desorption method is often employed in calculating the surface coverage values (Γ_{SAM}/ mol.cm^{-2}) according to equation 4.2 (same as equation 1.8).

$$\Gamma_{SAM} = \frac{Q}{nFA} \qquad (4.2)$$

where Q is the charge under the reductive desorption peak (Coulombs), F is Faradays constant (96,485 Coulombs.mol^{-1}), n is number of electron transferred (=1), and A is the geometric area of gold electrode (= 0.0201 cm^2). The surface coverage (Γ) values for the gold electrodes modified with the SAMs of complexes **12 - 15** were found to be 1.12 x 10^{-10} mol.cm^{-2} for **12**-SAM, 4.90 x 10^{-10} mol.cm^{-2} for **13**-SAM, 0.77 x 10^{-10} mol.cm^{-2} for **14**-SAM and 1.74 x 10^{-10} mol.cm^{-2} for **15**-SAM, Table 4.1. The values for complexes **12** and **14** (α substituted) are within the approximate value (1.0 x 10^{-10} mol.cm^{-2}) for the MPc complexes lying flat [80] on the electrode surface thus forming an octopus orientation

[80,353]. The surface coverages for the peripherally substituted complexes (**13** and **15**) were higher than those of non-peripherally substituted complexes (**12** and **14**). This may be attributed to position of the substituents, which results in different orientation (rather than octopus) for the peripherally substituted derivatives. The cobalt phthalocyanine complexes (**12** and **13**) also gave higher surface coverages compared to their respective manganese phthalocyanine complexes (**14** and **15**) substituted at the same position. This may be attributed to the effect of acetate axial ligand on the manganese phthalocyanine complexes affecting the immobilization of these complexes.

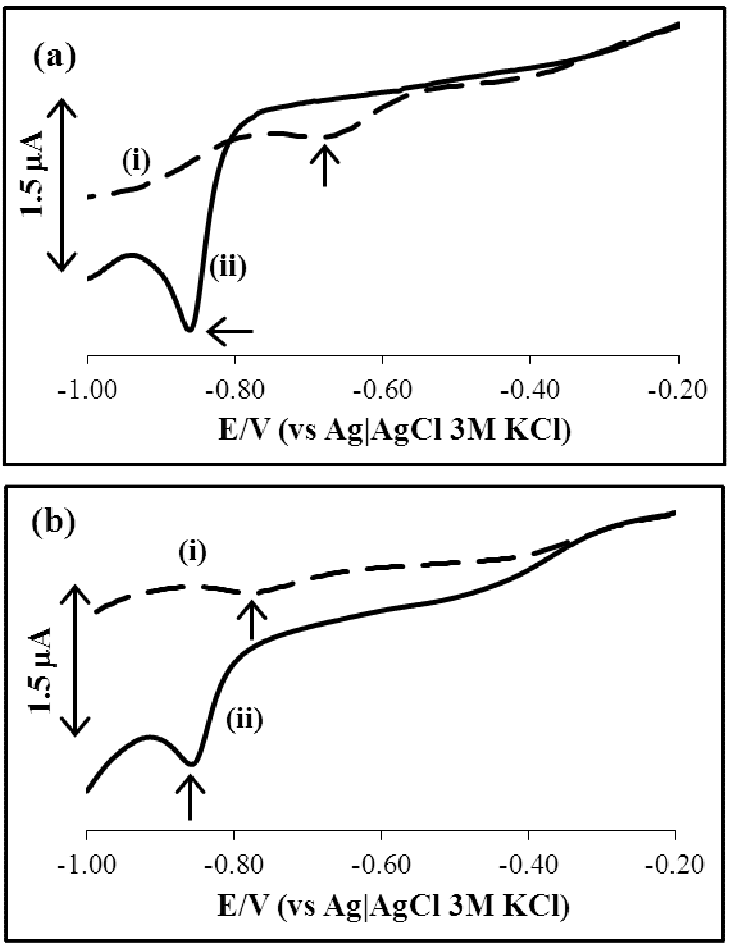

Figure 4.3: Reduction scan of the cyclic voltammograms of (a) (i) **12**-SAM and (ii) **13**-SAM and (b) (i) **14**-SAM and (ii) **15**-SAM in 0.2 M KOH solution. Scan rate = 100 $mV.s^{-1}$.

4.1.2 AFM characterization of SAMs on gold surface

For the morphology studies, the AFM measurements were carried out to further confirm the formation of SAMs of MOcHexTPc complexes (**12** - **15**) on the gold-coated quartz crystal. Figure 4.4 shows the 3D AFM images of (a) **12**-SAM (inset: bare gold surface), (b) **13**-SAM, (c) **14**-SAM and (d) **15**-SAM. The analysis of the AFM images showed the changes in morphologies with an increase in surface roughness factor values at the MOcHexTPc SAM modified surfaces. The bare gold surfaces (inset in Figure 4.4(a)) gave a mean roughness factor value (Ra) of 2.17 nm, and after modifying the gold surfaces with MOcHexTPc SAMs, the mean roughness factor values increased to 2.95 nm for **12**-SAM in Figure 4.4(a), 3.55 for **13**-SAM in Figure 4.4(b), 3.09 nm for **14**-SAM in Figure 4.4(c) and 3.28 nm for **15**-SAM in Figure 4.4(d). The increase in the mean surface roughness factor values from bare to MOcHexTPc SAM modified electrodes is a clear indication that the MOcHexTPc complexes have been immobilized on the gold surfaces. The comparison of the AFM images were almost similar to the naked eye and this is attributed to the immobilized molecules taking the morphology of the underlying gold surface. The increase in surface roughness factor values also indicates that the pinholes are present within the SAMs. For a completely covered gold surface, the MOcHexTPc SAMs will take on the underlying surface features, as a result the mean surface roughness factor values will be the same as that of the bare gold surfaces. Therefore, the presence of the pinholes leads to rougher surfaces and this has been shown to affect the mean roughness factor values [77]. The presence of the pinholes were also observed in the electrochemistry experiments above. The high roughness factor values for β (**13** and **15**) compared to α (**12** and **14**) could be due to differences in MPc molecular orientation.

Table 4.1: Surface parameters (i.e. surface coverages, oxidation potentials for SAMs and AFM roughness factor values). Scan rate = 50 mV.s^{-1}.

Electrodes	Γ_{SAM} (x 10^{-10}), mol.cm^{-2}	M_{ox} ($E_{1/2}$), V	Roughness factor (RF), nm
Au bare	---	---	2.17
12-SAM	1.12	~0.20	2.95
13-SAM	4.90	~0.20	3.55
14-SAM	0.77	~0.15	3.09
15-SAM	1.74	~0.15	3.28

Γ_{SAM} = surface coverage of SAMs, M_{ox} = metal oxidation, $E_{1/2}$ = half wave potential.

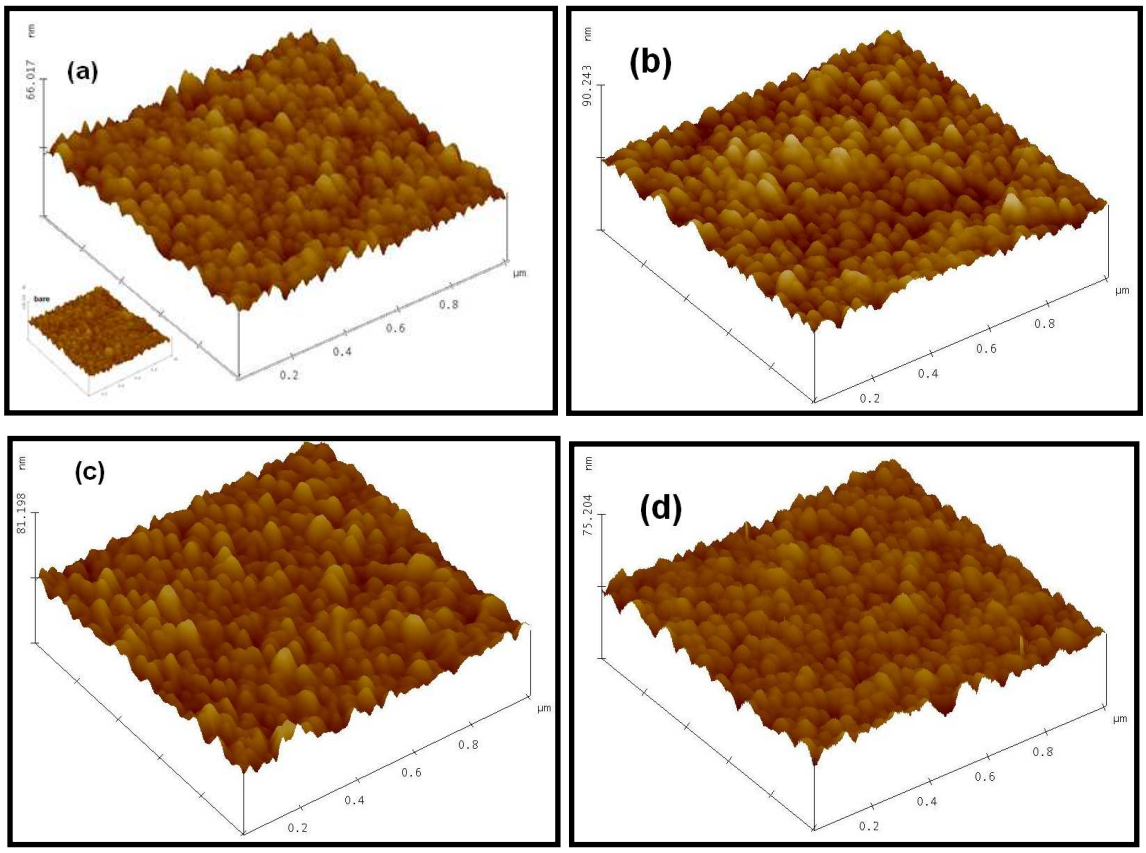

Figure 4.4: The 3D AFM images of MOcHexTPc SAMs modified gold surfaces with (a) **12**-SAM (inset: bare gold surface), (b) **13**-SAM, (c) **14**-SAM and (d) **15**-SAM in air non-contact or tapping mode.

4.2 Electropolymerization studies of MTAPc complexes

4.2.1 Electrosynthesis of metal tetraaminophthalocyanine polymers

MTAPc complexes (i.e. CoTAPc, CuTAPc and FeTAPc) have been studied as SAMs on Au and Ag [113]. In this study, the Au and GCE electrodes modified with polymers of CoTAPc and MnTAPc were compared. Since the electrosynthesis of CoTAPc and MnTAPc polymers onto carbon electrodes has been widely studied and this work therefore investigates their electrosynthesis on gold electrode surfaces. Figure 4.5 shows the electropolymerization of 1 mM (a) CoTAPc and (b) MnTAPc in DMF containing 0.1 M $TBABF_4$ on gold electrode and (c) polyCoTAPc formation on ITO (small scan range). ITO was used for AFM studies.

The electropolymerization of MTAPc leading to the deposition of the polymeric thin film on gold, GCE or ITO surface was obtained by repetitive potential cycling in 1 mM MTAPc monomer in DMF solution containing 0.1 M $TBABF_4$. The Au oxide and stripping peaks were not observed under the conditions (organic media) of the electropolymerization process. The first scan in Figure 4.5 for both complexes is different from the second and subsequent scans, suggesting the formation of the polymer film on the electrode, represented as polyMTAPc. The increase in currents on repetitive scanning is also attributable to the growth of conducting polymeric species deposited onto the electrode surface. On gold electrodes, SAMs are not expected to form since it takes >24 hrs to form SAMs. Figure 4.5(c) shows 30 repetitive scans during the electrosynthesis of polyCoTAPc and the increase in current was due to the polymer formation on ITO surface.

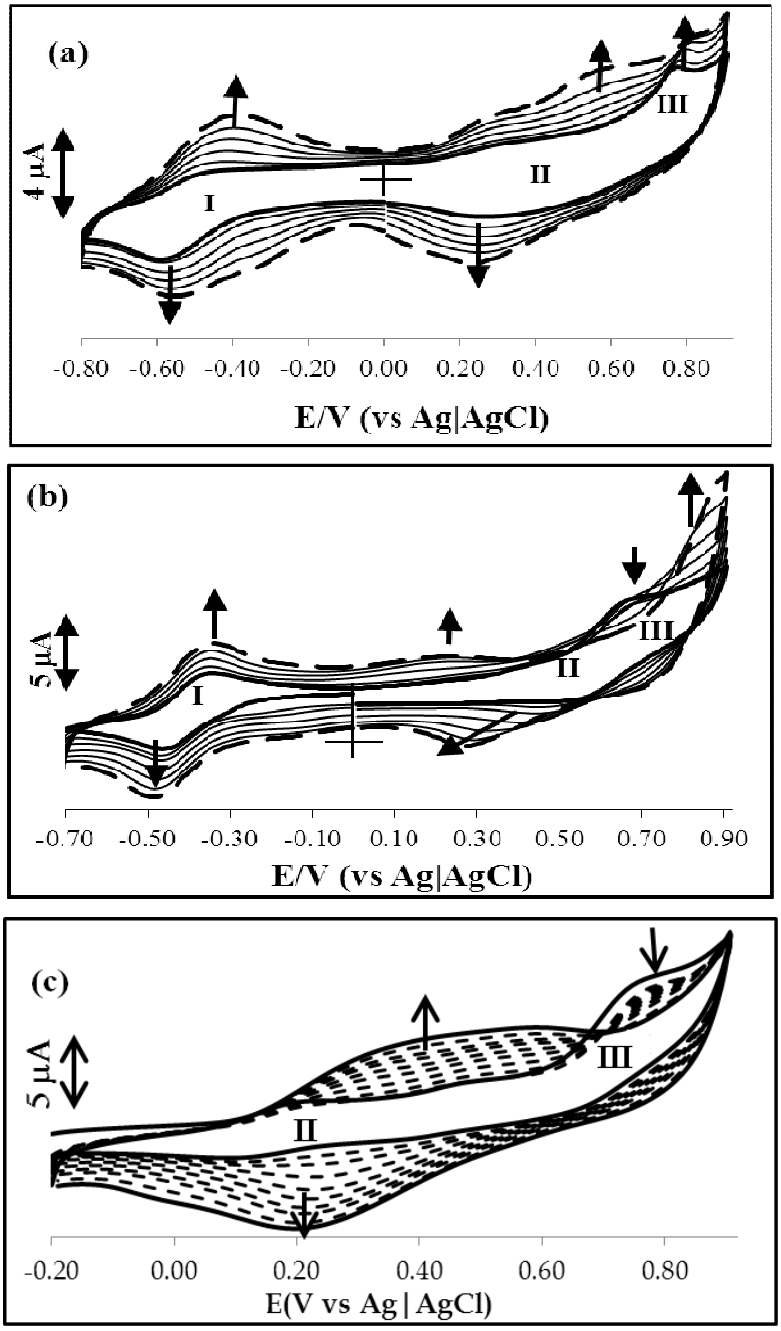

Figure 4.5: Evolution of the cyclic voltammograms of 1 mM (a) CoTAPc and (b) MnTAPc in DMF containing 0.1 M $TBABF_4$ during the formation of polymers on gold electrode and (c) evolution and formation of polyCoTAPc in DMF containing 0.1 M $TBABF_4$ on ITO. Scan rate = 100 $mV.s^{-1}$.

4.2.2 Cyclic voltammetry characterization of polymer modified surfaces

4.2.2.1 Electrolyte solution studies

During the conditioning step, the polyMTAPc modified electrodes were cycled in an electrolyte solution of DMF containing $TBABF_4$ until reproducible background, i.e. 20 scans. The reversible redox reactions of the electroactive species adsorbed on the electrodes were observed. Figure 4.6 shows cyclic voltammograms of (a) GCE-polyCoTAPc, (b) Au-polyCoTAPc, (c) GCE-polyMnTAPc and (d)Au-polyMnTAPc films in freshly prepared electrolyte solution (DMF + 0.1 M $TBABF_4$), (i) is the first cycle and (ii) is the 20th cycle.

For polyCoTAPc electrodes in Figure 4.6(a) and (b), two redox processes labeled **I** and **II** were observed at regions known for metal redox processes. The redox process labeled **I** corresponds to $Co^{II}Pc/Co^{I}Pc$ and the redox process labeled **II** occur at regions for $Co^{III}Pc/Co^{II}Pc$. The redox processes **I** and **II** in Figure 4.6(a) occur at $E_{1/2}$ = -0.38V and +0.32 V, respectively, Table 4.2 on GCE. In Figure 4.6(b), the redox processes **I** and **II** occur at $E_{1/2}$ = -0.45 V and +0.45 V, respectively, Table 4.2 on Au electrode for polyCoTAPc. For the polyMnTAPc modified electrodes in Figure 4.6(c) and (d) only one redox process, labeled **I,** was observed at $E_{1/2}$ = -0.22 V for both electrodes, Table 4.2, at the region for $Mn^{III}Pc/Mn^{II}Pc$ reduction process. In Figure 4.6(a) and (b), there is a peak observed close to 0 V which is attributed to the polymeric species of the MTAPc complexes. The observed redox processes confirm the presence and the formation of the polymer. The metal redox processes were broad and this is typical of the phthalocyanine polymers [100] adsorbed on the electrode surfaces. The polymer modified electrodes were also studied in pH 7.4 solution (Figure not shown). The reduction scans exhibited reduction peaks with potentials shown in Table 4.2 (in brackets).

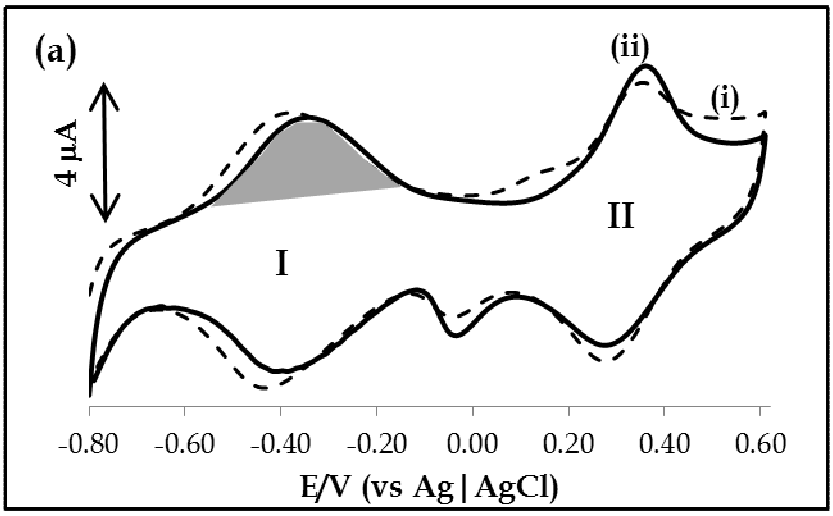
(a)
(ii)
(i)
4 µA
II
I
-0.80 -0.60 -0.40 -0.20 0.00 0.20 0.40 0.60
E/V (vs Ag | AgCl)

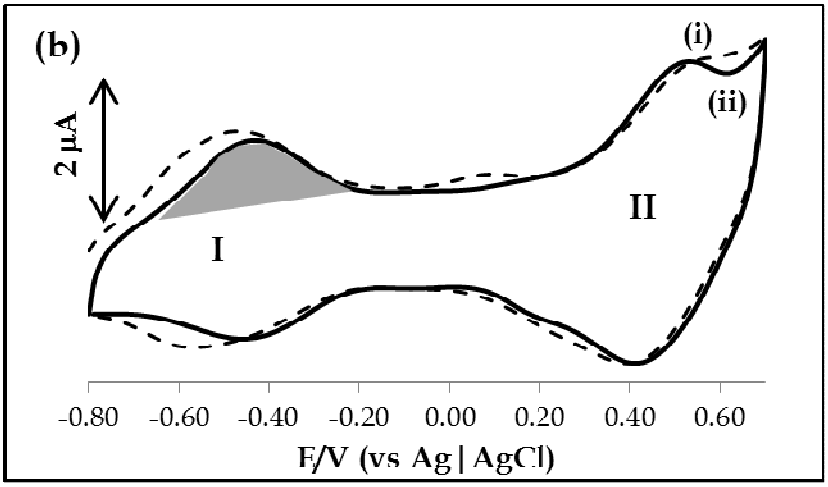
(b)
(i)
(ii)
2 µA
II
I
-0.80 -0.60 -0.40 -0.20 0.00 0.20 0.40 0.60
E/V (vs Ag | AgCl)

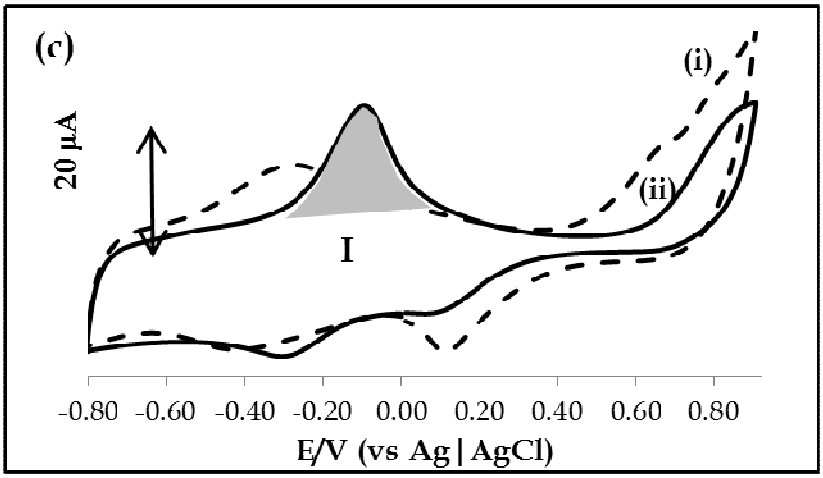
(c)
(i)
20 µA
(ii)
I
-0.80 -0.60 -0.40 -0.20 0.00 0.20 0.40 0.60 0.80
E/V (vs Ag | AgCl)

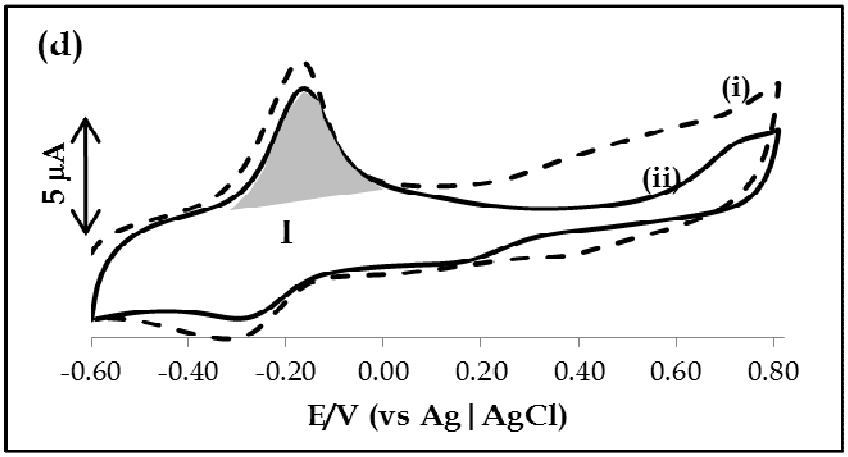

Figure 4.6: Cyclic voltammograms of (a) GCE-polyCoTAPc, (b) Au-polyCoTAPc, (c) GCE-polyMnTAPc and (d) Au-polyMnTAPc films, after being transfer to fresh DMF + 0.1 M $TBABF_4$ solution and then continuously scanned. Scan rate: 25 $mV.s^{-1}$. (i) is the 1st scan and (ii) is the 20th scan.

Table 4.2: Electrochemical properties: $E_{1/2}$ and E_p potentials of complexes in DMF containing 0.1 M $TBABF_4$ on glassy carbon and gold electrodes. Scan rate: 25 $mV.s^{-1}$.

Modified electrodes	**M_{red} ($E_{1/2}$ or E_p) (V)**	**M_{ox} (E_p) (V)**	**$\Gamma_{polyMTAPc}$ ($mol.cm^{-2}$)**
GCE-polyCoTAPc	-0.38 (-0.29)	+0.32	8.6×10^{-10}
Au-polyCoTAPc	-0.45 (-0.42)	+0.45	1.3×10^{-9}
GCE-polyMnTAPc	-0.22 (-0.43)	---	8.2×10^{-10}
Au-polyMnTAPc	-0.22 (-0.35)	---	3.4×10^{-9}

- $\Gamma_{polyMTAPc}$ = surface coverage for polymer modified electrodes. M_{red} = metal reduction, M_{ox} = metal oxidation, $E_{1/2}$ = half-wave potential and E_p = peak potential values in brackets were obtained in pH 7.4.

The surface coverage values ($\Gamma_{polyMTAPc}$) of polymer modified electrodes were estimated by integrating the charge under the redox peak (shaded areas in Figure 4.6) using equation 4.2. Due to mechanical treatment (i.e. polishing) of the electrodes the real

surface area will vary, therefore the geometric areas, i.e. for Au = 0.0201 cm^2 and for GCE = 0.0707 cm^2, were used to estimate surface coverages and for comparison purposes. The integrated charge under the peaks and the corresponding surface coverage values for the polyMTAPc electrodes were 5.53 µC ($\Gamma_{GCE\text{-}polyMnTAPc}$ = 8.2 x 10^{-10} mol.cm^{-2}) and 5.78 µC ($\Gamma_{GCE\text{-}polyCoTAPc}$ = 8.6 x 10^{-10} mol.cm^{-2}) on GCE, and 2.59 µC ($\Gamma_{Au\text{-}polyCoTAPc}$ = 1.3 x 10^{-9} mol.cm^{-2}) and 6.54 µC ($\Gamma_{Au\text{-}polyMnTAPc}$ = 3.4 x 10^{-9} mol.cm^{-2}) on Au (Table 4.2). The surface coverage values for the Au-polyMTAPc electrodes were higher than those of GCE-polyMTAPc considering they share same MTAPc complex. The observed differences in surface coverages for Au-polyMTAPc and GCE-polyMTAPc electrodes may be attributed to the differences in polymer formation (nucleation and growth) on different substrates with different surface functionalities. For example, the GCE surface contains a conjugated carbon-based material whereas Au is an inert metal and these functionalities influence the formation of polymer differently, hence different surface coverages. The surface coverage (Γ) values are slightly higher than ~ 1 x 10^{10} mol cm^{-2} approximated for a Pc molecule lying flat on the electrode surface [80].

4.2.2.2 $K_3/K_4Fe(CN)_6$ solution

Figure 4.7 shows the cyclic voltammograms of the (i) bare or unmodified electrodes and (ii) polyCoTAPc and (iii) polyMnTAPc modified (a) Au and (b) GCE electrodes in the presence of $[Fe(CN)_6]^{3-/4-}$ redox probe in solution. The cyclic voltammograms at bare Au in Figure 4.7(a)(i) and GCE in Figure 4.7(b)(i) electrodes exhibited a reversible $[Fe(CN)_6]^{3-/4-}$ redox couple with the peak-to-peak separation (ΔE) of 80 and 87 mV for Au and GCE electrodes, respectively.

A quasi-reversible $[Fe(CN)_6]^{3-/4-}$ redox couple was observed on the polyCoTAPc modified Au and GCE electrodes, in Figure 4.7(a)(ii) and (b)(ii), with ΔE = 100 mV for

both electrodes. For polyMnTAPc modified electrodes the ΔE values were 191 mV and 100 mV on Au and GCE electrodes in Figure 4.7(a)(iii) and (b)(iii), respectively. The increase in ΔE at polyMnTAPc and polyCoTAPc modified electrodes compared to bare electrode is attributed to the presence of the polymer thin film. The slight increase in current was observed, especially on polyCoTAPc modified electrodes in Figure 4.7(a)(ii) and (b)(ii), and this may be attributed to the electrocatalytic or conducting properties for the polyCoTAPc polymers.

The polyMnTAPc modified electrodes in Figure 4.7(a)(iii) and (b)(iii) behaved differently from those of polyCoTAPc. In Figure 4.7(a)(iii), the Au-polyMnTAPc showed a pronounced decrease in current and broadening of the oxidation peak due to $[Fe(CN)_6]^{3-/4-}$ compared with a well-defined reduction peak. The possible reasons for the broad $[Fe(CN)_6]^{3-/4-}$ oxidation peak and an increase in ΔE could be due to slow electrode kinetics on Au-polyMnTAPc compared to Au-polyCoTAPc in Figure 4.7(a) (ii), which showed a good redox couple, with both oxidation and reduction components intact. High film thickness in Au-polyMnTAPc compared to Au-polyCoTAPc, in Table 4.2, may result in electron transfer inhibition for the $Fe(CN)_6]^{3-/4-}$ couple even at highly conducting polymers as in this work. The surface coverage value in Table 4.2 for the polyMnTAPc is higher than those of polyCoTAPc and this may be the reason of the slow electrode kinetics on the Au-polyMnTAPc. The effect of film thickness was only observed on Au-polyMnTAPc electrode and not on GCE-polyMnTAPc and clearly confirming the differences in surface properties of these polymers on Au and GCE surfaces. The lack of inhibition of $[Fe(CN)_6]^{-3/-4}$ redox peak by modified electrodes has been observed before and discussed in section 4.1. At GCE-polyMnTAPc modified electrode, in Figure 4.7(b)(iii), the $[Fe(CN)_6]^{-3/-4}$ redox couple was observed together with the additional redox peak at $E_{1/2}$ = +0.45 V. This additional peak at +0.45 V is attributed to Mn^{III}/Mn^{IV} oxidation also observed in literature [105]. The Co^{III}/Co^{II} couple is not clear in Figure 4.7.

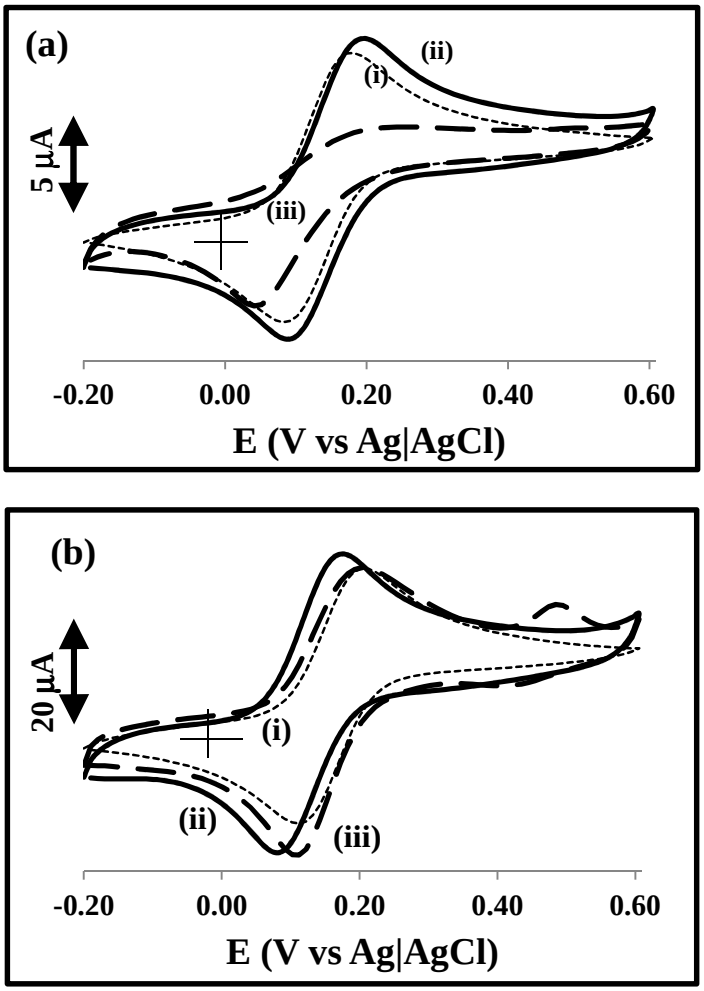

Figure 4.7: Cyclic voltammograms of (i) bare or unmodified electrodes and (ii) polyCoTAPc and (iii) polyMnTAPc modified (a) gold and (b) glassy carbon electrodes in 1 mM $[Fe(CN)_6]^{3-/4-}$ in 0.1 M KCl. Scan rate: 25 $mV.s^{-1}$.

4.2.3 Atomic force microscopy (AFM) studies

The potential window used during the electrosynthesis of polymeric materials is known [105,354] to affect the formation of the polymers and their conducting properties. The formation of conducting polymers of MTAPc complexes was followed using electrochemistry and atomic force microscopy. Indium tin oxide (ITO) substrates were

used for the formation of the polymers at wide and narrow potential windows. The smooth ITO glass slides were choosen for their ease of mounting on the atomic force microscope and these substrates will also make surface modifications easier to understand. Electropolymerization at wide potential windows may result in either over-oxidative or over-reductive reactions that will result in the polymer losing its conjugation and consequently its conductivity and electroactivity. This fact has been reported for the formation of polypyrrole [354] and phthalocyanine polymers [105].

Figure 4.8 shows the 2D and the 3D AFM images of (a) bare and (b) polyCoTAPc modified ITO substrates after 30 scans on a wide potential window (-1.20 V to +1.00 V). The cyclic voltammogram showed similar peaks as for narrow potential range, Figure 4.5 on ITO except for additional couple on the reduction side. The differences on ITO surfaces before and after modification can be clearly observed on these two images confirming the modification of the ITO. The polyCoTAPc film was also visible from the transparent ITO substrate as a green thin film. The AFM images show a distinct difference on these two surfaces with the bare showing a very smooth ITO surface with the mean roughness value of 0.40 nm. Upon modifying the ITO surface with polyCoTAPc for 30 scans, the mean roughness factor value increased to 4.40 nm. The differences in surface morphologies confirm the modification of the ITO surface with the polyCoTAPc film and the cluster-like morphology was observed on the 2D AFM image of the modified ITO electrode, in Figure 4.8(b).

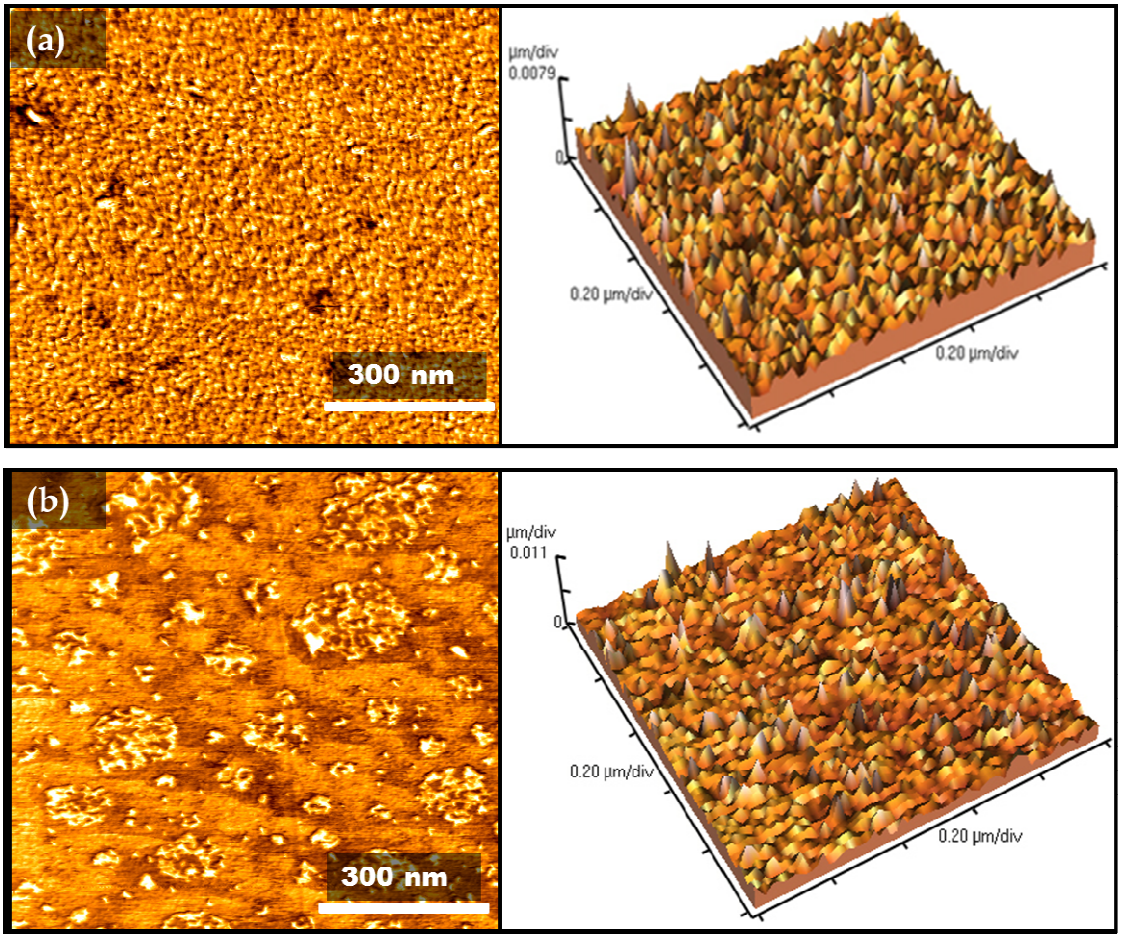

Figure 4.8: 2D and 3D AFM (1 x 1 µm) micrographs of (a) bare ITO and (b) $[polyCoTAPc]_{30}$ modified ITO at wide potential window (-1.20 to +1.00 V vs Ag|AgCl). Subscript 30 is the number of cycles during polymer formation.

Figure 4.9 shows the 2D and the 3D AFM micrographs of the polyCoTAPc-modified ITO electrodes on the narrow potential window, -0.2 to 0.9 V (CV shown as Figure 4.5(c)). After 30 scans the AFM image shown in Figure 4.9(a) exhibited a well-defined globular-like morphology of polyCoTAPc with a mean roughness factor value of 5.54 nm. The differences observed in AFM images and the increase in mean roughness factor values from 4.40 nm (Figure 4.8(b), wide potential range) to 5.54 nm (Figure 4.9(a), narrow potential range) shows the effect of the potential window applied for the deposition of polyCoTAPc after 30 scans. In addition to roughness factor, cluster-like

morphologies of the AFM images were observed for a wide potential scan, in Figure 4.8(b), compared to globular-like morphology for a narrow potential scan, in Figure 4.9(a). The changes clearly demonstrate the effect of the applied potential scan range during electropolymerization. It has been reported [105] that at wide potentials window, the phthalocyanine polymer losses its conjugation.

The effect of scan numbers (n) for $[polyCoTAPc]_n$ where n = 30 and 50 were investigated on the narrow potential scan range in Figure 4.9. The AFM images in Figure 4.9 show differences in morphologies and this was further confirmed by different mean roughness values obtained after image analysis. The image obtained at 30 scans in Figure 4.9(a), show well-defined globular-like structural morphology, whereas the image obtained after 50 scans in Figure 4.9(b) does not show a well-defined morphology. The analysis of these micrographs gave mean roughness factor values for the images which increased with an increasing scan numbers up to 30 scans (5.54 nm) and slightly decreased after 50 scans to 5.30 nm. The polymer thin film for 30 scans gave a well-defined globular-like morphology; therefore, 30 scans at the narrow potential window were treated as the optimum conditions for the electrodeposition of polymer thin films on ITO surfaces.

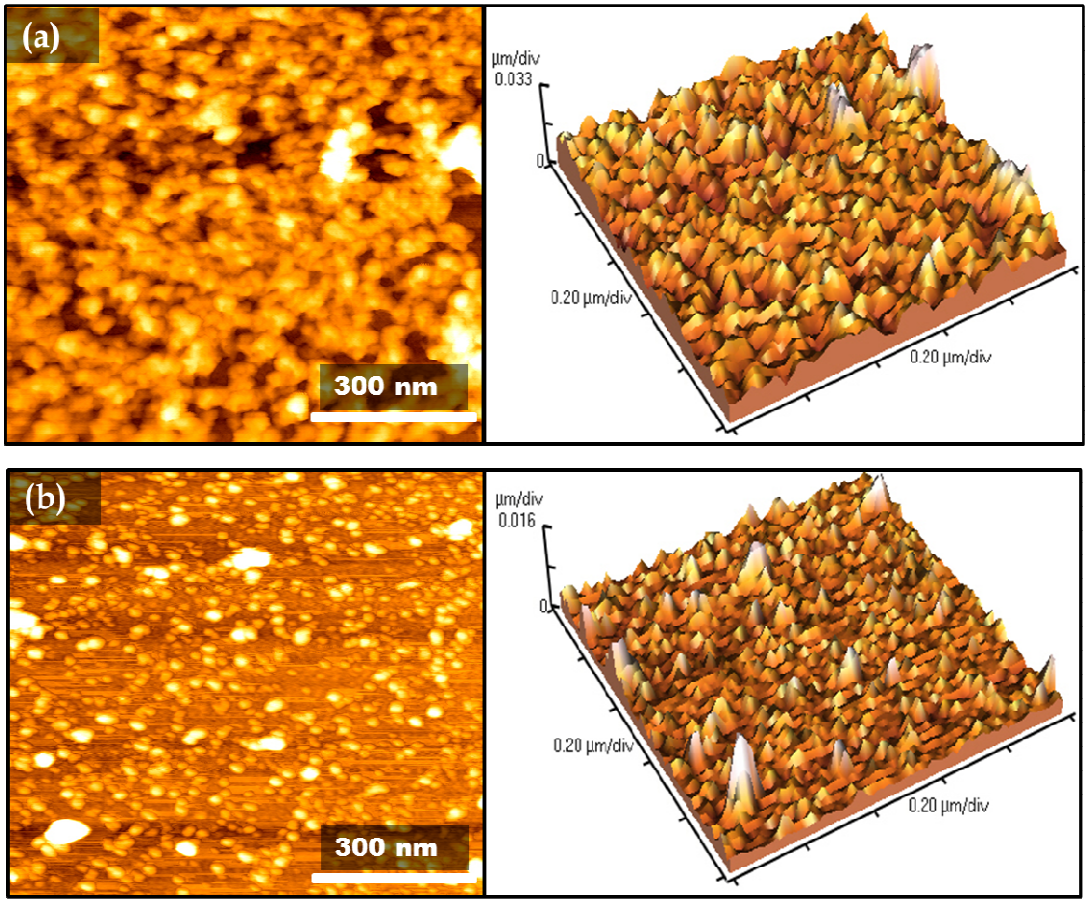

Figure 4.9: AFM 2D and 3D (1 x 1 µm) micrographs for $[polyCoTAPc]_n$ formed at different scan numbers n = (a) 30 and (b) 50. Scan range -200 to 900 mV on ITO surfaces.

4.2.4 Electrochemical impedance spectroscopy (EIS) characterization

The bare and polymer modified electrodes were further investigated for their electron transfer properties using electrochemical impedance spectroscopy (EIS) in the presence of $[Fe(CN)_6]^{3-/4-}$ as a redox probe. The two data representation (Nyquist and Bode plots) were used for the analysis of the impedance data. The Nyquist plot (-Z″ vs Z′) was fitted and analyzed using the Randles equivalent circuit which takes into consideration the diffusion and kinetic control parameters [310,355, 356]. The Bode plot (-phase angle vs log f) was used to obtain more useful information of the electrical properties of the

electrode coated with polymer films. The Randles equivalent circuit used for fitting impedance data was as shown in Figure 1.13(b) and consisted of the solution or electrolyte resistance (R_S) connected in series to the parallel combination of the capacitance and charge-transfer resistance (R_{CT}) in series with Warburg impedance (Z_W), i.e. $R_S(CPE(R_{CT}\ Z_W))$.

Figure 4.10 shows the Nyquist plots (-Z″ vs Z′) and their corresponding bode plots (-phase angle vs log f) for (i) the bare (ii) polyCoTAPc and (iii) polyMnTAPc modified Au (a,b) and GCE (c,d) electrodes. The Nyquist plots in Figure 4.10(a)(i, bare) and 4.10(a)(ii, polyCoTAPc) are dominated by diffusion controlled features with small charge-transfer resistance (R_{CT}) at high frequency regions for Au (5.47 kΩ.cm^{-2}) and Au-polyCoTAPc (16.62 kΩ.cm^{-2}), Table 4.3. The R_{CT} for Au-polyMnTAPc in Figure 4.10(a)(iii) was higher (36.77 kΩ.cm^{-2}) meaning the electron transfer inhibition is more pronounced at this electrode. The increase in R_{CT} followed this trend Au (5.47 kΩ.cm^{-2}) < Au-polyCoTAPc (16.62 kΩ.cm^{-2}) < Au-polyMnTAPc (36.77 Ω.cm^{-2}), Table 4.3. The increase in R_{CT} and ΔE values from bare Au and after modifying the Au electrode with the phthalocyanine polymers could be attributed to the presence of the surface confined polymer films that impede electron transport. This behaviour may be interpreted as the result of increased electrical resistance to mass transport through the film thickness. At GCE electrodes, similar results to those of Au electrodes were observed and the trend of increasing R_{CT} values was as follows: GCE (0.33 kΩ.cm^{-2}) < GCE-polyCoTAPc (0.41 kΩ.cm^{-2}) < GCE-polyMnTAPc (0.86 kΩ.cm^{-2}), Table 4.3 Figure 4.10(c). The R_{CT} values for bare and polymer modified GCE electrodes were much less than those of bare and polymer modified Au electrodes. The GCE electrodes exhibit higher conductivity compared to the Au electrodes and this is due to the differences in nature of surface materials, Table 4.3.

Table 4.3: The summary of the parameters obtained from cyclic voltammetry and electrochemical impedance spectroscopy experiments. Scan rate: 25 mV.s^{-1}.

Electrodes	k_{app} x10^{-4} (cm.s^{-1})	$Fe(CN)_6$	EIS			
		CV ΔE (mV)	R_S (kΩ.cm^{-2})	R_{CT} (kΩ.cm^{-2})	CPE (µF.cm^{-2})	n
Au	1.10	87	12	5.47	213	0.78
Au-polyCoTAPc	0.36	100	12	16.62	512	0.74
Au-polyMnTAPc	0.16	191	13	36.77	318	0.78
GCE	1.50	80	3	0.33	21	0.90
GCE-polyCoTAPc	1.19	100	4	0.41	32	0.83
GCE-polyMnTAPc	0.57	100	2	0.86	32	0.70

The R_S and CPE values were also obtained from fitting the data and are shown in Table 4.3. The Rs values in Table 4.3 do not vary significantly from a bare and after modifying the electrode with the polyMTAPc film. This was expected as the polymer films adsorbed on the electrode surfaces are conducting films. Using the charge-transfer resistance values, one can also calculate the apparent electron-transfer rate constant (k_{app}) by employing the conventional equation 4.3 [357,358]. This method investigates the outer sphere kinetic properties of the immobilized thin films and their interaction with the redox probe in solution.

$$k_{app} \approx k^0 = \frac{RT}{n^2F^2AR_{CT}c} \qquad (4.3)$$

where c is a concentration of $[Fe(CN)_6]^{3-/4-}$ (2 mM), R_{CT} (charge transfer from fitted data in Table 4.3), A is the geometric area of the gold electrode (0.0201 cm^2) and GCE (0.0707 cm^{-2}), n = 1 (electron transferred in the $[Fe(CN)_6]^{3-/4-}$ redox process), R, T and F have their usual meanings.

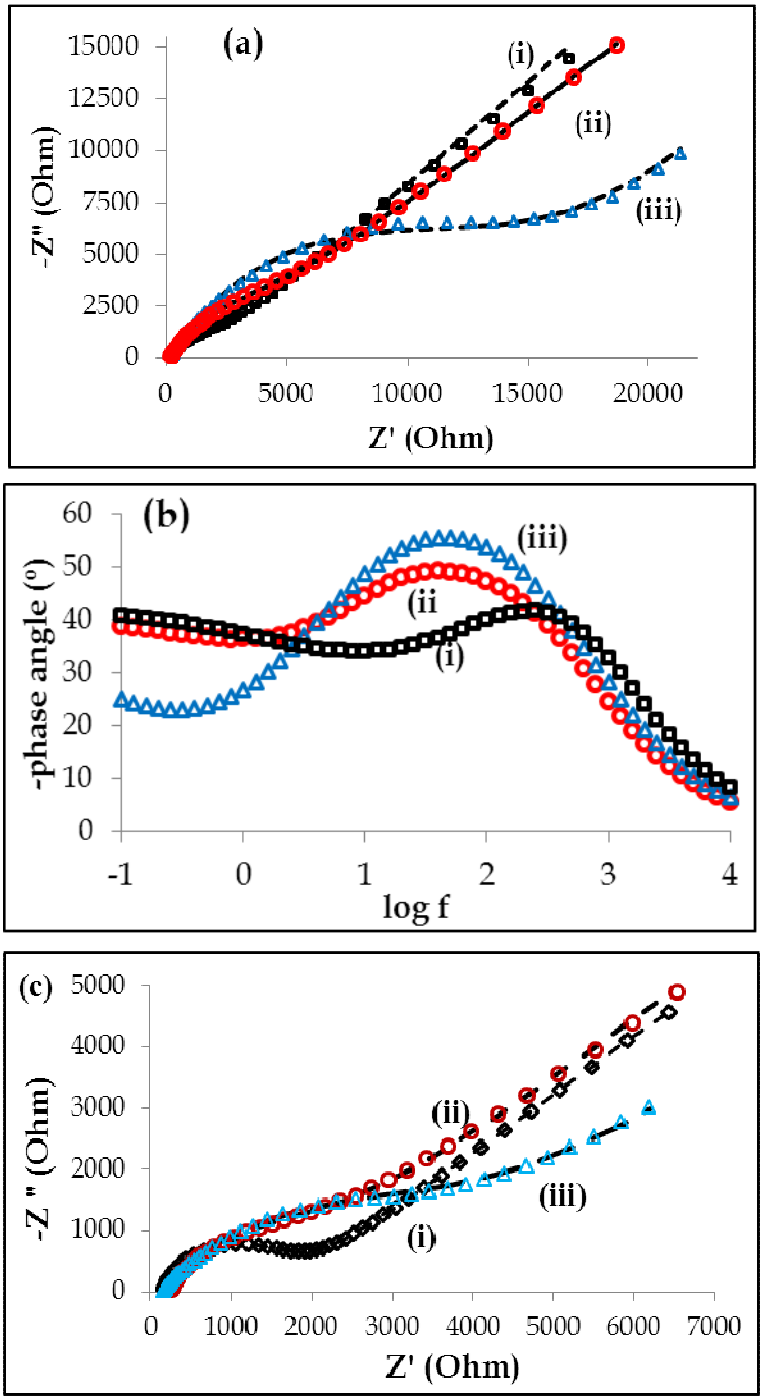
(a)
(i)
(ii)
(iii)
-Z'' (Ohm)
Z' (Ohm)
15000
12500
10000
7500
5000
2500
0
0
5000
10000
15000
20000
(b)
(iii)
(ii)
(i)
-phase angle (°)
log f
60
50
40
30
20
10
0
-1
0
1
2
3
4
(c)
(ii)
(iii)
(i)
-Z '' (Ohm)
Z' (Ohm)
5000
4000
3000
2000
1000
0
0
1000
2000
3000
4000
5000
6000
7000

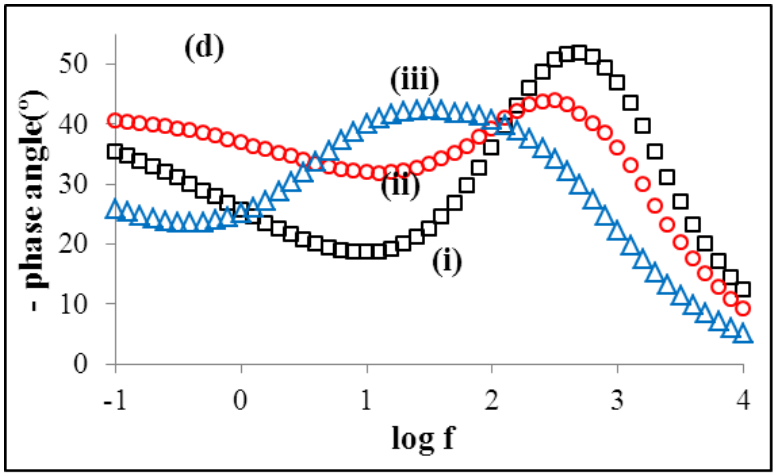

Figure 4.10: Nyquist plots of (i) bare electrodes, (ii) polyCoTAPc and (iii) polyMnTAPc at (a) GCE and (c) Au electrodes. The corresponding Bode plots of (i) bare electrodes, (ii) polyCoTAPc and (iii) polyMnTAPc at (b) GCE and (c) Au electrodes. The electrodes were measured in (1:1) 1 mM $K_4/K_3[Fe(CN)_6]$ solution containing 0.1 M KCl. Applied potential corresponds to $E_{1/2}$ of ferricyanide redox couple.

The bare gold and glassy carbon electrode surfaces gave the k_{app} value of 1.10 and 1.50 x 10^{-4} cm.s^{-1}, respectively, Table 4.3. Upon modifying the electrodes with the polyMTAPc complexes, the k_{app} values decreased. The polymer modified electrodes gave values ranging from 0.16 – 1.19 x 10^{-4} cm.s^{-1} and GCE-polyCoTAPc gave the highest (1.19 x 10^{-4} cm.s^{-1}) k_{app} value amongst the modified electrodes and the lowest value was obtained for Au-polyMnTAPc (0.16 x 10^{-4} cm.s^{-1}).

The Bode plots are shown in Figure 4.10(b) and (d) for bare and modified gold and glassy carbon electrodes, respectively. The shift of the symmetrical peak to lower frequency (log f) values confirms the different surface properties introduced on the electrode by modifying with the polymer thin films. The phase angle values for all the electrodes studied are less than the ideal -90° for a true capacitor leading to the conclusion that these electrodes have capacitive-like behaviour [359]. From Table 4.3, it is important to mention the n values (where n is an exponent-related to the depression

angle [357]) observed for the fitted data and ranged from 0.7 – 0.9. The n values for a pure resistor (n = 0), for Warburg diffusion (n = 0.5) and for pure capacitor (n = 1). The observed range for the n values lie between the Warburg diffusion (n = 0.5) and the true capacitor (n = 1). These values are close to unity and thus leading to the conclusion that the electrodes have a capacitive-like behaviour. This conclusion confirms the results obtained with the phase angle values which were less than -90° due to the capacitive-like nature of the studied electrodes.

4.3 Covalent immobilization of MTAPc onto screen-printed gold electrode (SPAuE)

4.3.1 Electrode fabrication using electrochemical grafting method

In this section, immobilizing of MTAPc on screen-printed gold electrode surface is presented, Scheme 4.1. Screen-printed gold electrodes were chosen to demonstrate the possibility of miniaturizing these systems as stated above.

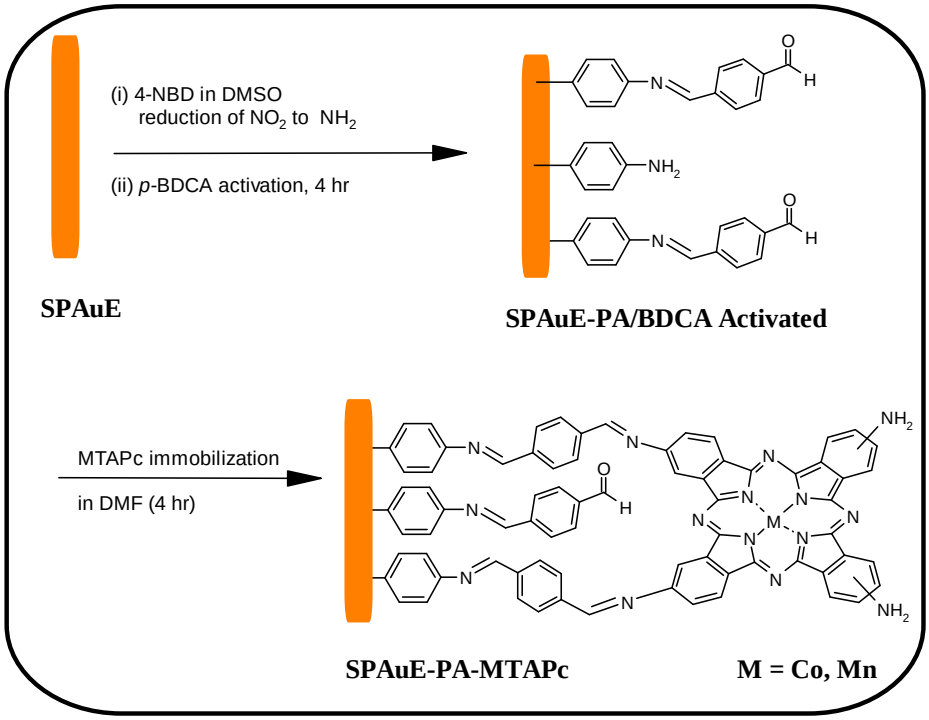

Scheme 4.1: Schematic representation of covalent immobilization of MTAPc onto phenyl-amino (PA) pre-grafted SPAuE.

The first step in electrode modification is the functionalization of the electrode surface with a phenylamino group. This was achieved in two steps; the first step in Scheme 4.1

is electrochemical grafting of the 4-nitrobenzene diazonium (4-NBD) salt which is then followed by the reduction of the phenylnitro to form a phenylamino group. The phenylamino group is then activated by the benzene-1,4-dicarbaldehyde (BDCA) thus forming a Schiff-base product and exposing the other aldehyde group for further reaction with the amino groups from the phthalocyanine ring. This reaction of an amino group and an aldehyde is well-known for the immobilization of biomolecules [360] and glutaraldehyde is used as a cross-linker. The formation of Schiff-base products using benzene-1,4-dicarbaldehyde as a cross linker has been reported before for the formation of the heterobinuclear porphyrin dimers [361]. The choice of using benzene-1,4-dicarbaldehyde as a cross-linker in this study is to allow for the extension of the electronic delocalization of the phthalocyanine ring. This extension of electronic delocalization is expected to lower the reduction potential and increase the electro-catalytic activity of the metallophthalocyanine complexes immobilized onto the electrode surfaces. This reduction of potential, influenced by delocalization, has been reported before for the conjugated porphyrin complexes [362].

Figure 4.11 shows the cyclic voltammograms recorded during the (a) electrochemical reduction of the 4-NBD and the formation of the phenylnitro monolayer and (b) the electrochemical reduction of phenylnitro group to phenylamino (PA) group. The first scan, in Figure 4.11(a), shows the reduction peak at ~0.027 V corresponding to the electrochemical reduction of the diazonium salts and formation of aryl radicals. The reduction peak disappeared during the second and subsequent scans, thus confirming the formation of phenylnitro monolayer.

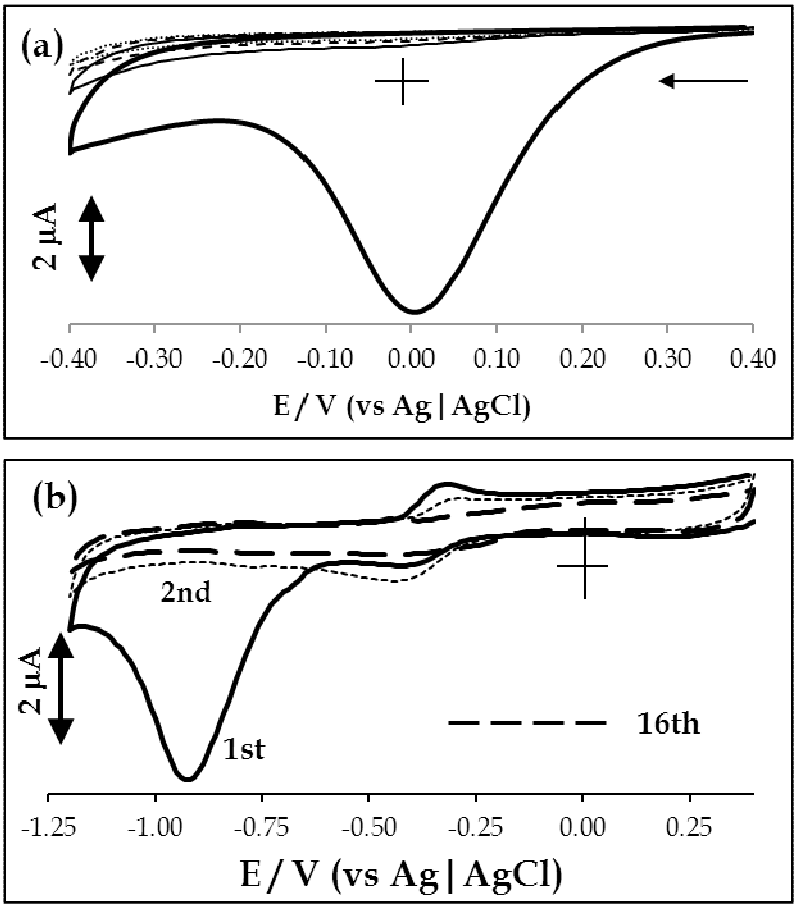

Figure 4.11: Cyclic voltammograms of (a) SPAuE recorded for the fabrication of phenylnitro monolayer from 1 mM 4-NBD in DMSO containing 0.1 M $TBABF_4$ in 4 cycles and (b) reduction of NO_2 to NH_2 in (1:9, ethanol: water) solution containing 0.10 M KCl. Scan rate 50 mV/s.

This method of modifying electrodes resulting in the formation of phenylnitro monolayer is well-known [167,223,363], where 4-nitrobenzene diazonium salt is electrochemically reduced in a one electron process leading to the formation of an aryl radical and loss of N_2. The aryl radical then attacks the surface and form a monolayer of phenylnitro on the electrode surface. The controlled formation of the monolayer has also been reported [239,246,364], where a small number of cycles (<5) gives the monolayer coverage. Therefore, 4 cycles were used in an attempt to form a phenylnitro monolayer functionalized surface. This monolayer was then electrochemically reduced to phenylamino group in an aprotic (1:9, ethanol:water) solution containing 0.1 M KCl,

hence forming phenylamino (PA) monolayer functionalized electrode surface. The reduction of the phenylnitro group to form phenylamino group has been reported before in aqueous solutions (i.e. aprotic solution) [167,243]. Figure 4.11(b) shows the cyclic voltammograms for the electrochemical reduction of the phenylnitro group to form phenylamino group (1-16 scans). In the first cycle, the well-defined reduction peak at -0.92 V corresponds to the reduction of the phenylnitro group to phenylhydroxyl-amine group. The phenylhydroxylamine group undergoes oxidation at -0.33 V to form phenylnitroso group, which is then finally reduced at -0.42 V to form the phenylamino group. This overall process of reducing phenylnitro groups to form phenylamino groups is known [167,243] to involve six electrons and six protons as shown in equation 4.4.

$$SPAuE\text{-}ArNO_2 + 6e^- + 6H^+ \longrightarrow SPAuE\text{-}ArNH_2 + 2H_2O \qquad (4.4)$$

The reduction of phenylnitro group to phenylhydroxylamine group is a complete one-step reaction. The reversible couple at $E_{1/2}$ = -0.38 V decreased in current as the modified electrode was continuously cycled. These cyclic voltammetric changes confirmed the formation of the phenylamino groups on the electrode surfaces. The surface coverage of the phenylnitro monolayer was calculated by integrating the charge under the well-defined reduction peak at -0.92 V, in Figure 4.11(b) and was found to be 2.79×10^{-9} mol.cm^{-2}. This surface coverage was found to be consistent with the reported values for a closely packed monolayer of the grafted phenylnitro groups onto the electrode surfaces [223].

The phenylamino group (SPAuE-PA) was then further activated with the BDCA for the immobilization of MTAPc molecules, following the procedure in Scheme 4.1. The activation of the phenylamino modified electrode results in the formation of the Schiff-base product between the amino group of the functionalized electrode and the

aldehyde group of BDCA to yield an aldehyde activated monolayer. The unreacted aldehyde of BDCA was used to further immobilize MTAPc complexes (CoTAPc and MnTAPc) onto the electrode thus resulting in the formation of MTAPc monolayers (SPAuE-PA-MTAPc).

4.3.2 Cyclic voltammetry characterization of modified electrodes

Figure 4.12 shows the cyclic voltammograms of (a) (i) bare SPAuE, (ii) SPAuE-PA and (iii) SPAuE-PA-CoTAPc and (b) (i) SPAuE, (ii) SPAuE-PA, (iii) SPAuE-PA-MnTAPc in 0.10 M KOH solution and (c) (i) SPAuE-PA-CoTAPc and (ii) SPAuE-PA-MnTAPc in 0.01 M pH 7.4 PBS solution.

The characterization of the electrodes clearly shows the presence of the MTAPc monolayer in Figure 4.12(a)(iii) and (b)(iii) for SPAuE-PA-CoTAPc and SPAuE-PA-MnTAPc, respectively, in basic media (0.10 M KOH). At unmodified (i) and phenyl-amino (ii) modified electrodes, there were no peaks observed for both in Figure 4.12(a,b). After modifying the activated electrodes with CoTAPc or MnTAPc molecules, the peaks due to either metal reduction or oxidation were observed. In Figure 4.12(a)(iii), an oxidation peak at approximately ~0.35 V for SPAuE-PA-CoTAPc was observed (Table 4.4), this peak occurred at potentials close to $Co^{III}Pc/Co^{II}Pc$ oxidation and has a return at 0.15 V. The $Co^{III}Pc/Co^{II}Pc$ process is known to be irreversible [91] and notoriously difficult to observe for adsorbed or immobilized CoPc complexes, hence its irreversibility is not surprising. The cathodic peak at -0.38 V in Figure 4.12(b)(iii), Table 4.4 is due to the $Mn^{III}Pc/Mn^{II}Pc$ in comparison with literature for polymerized MnTAPc complexes [105] at alkaline conditions (pH 11) and has a split anodic component at -0.20. The split nature of the peak at -0.20 V could be related to both the $Mn^{III}Pc/Mn^{II}Pc$ and $Mn^{IV}Pc/Mn^{III}Pc$ at more positive potentials.

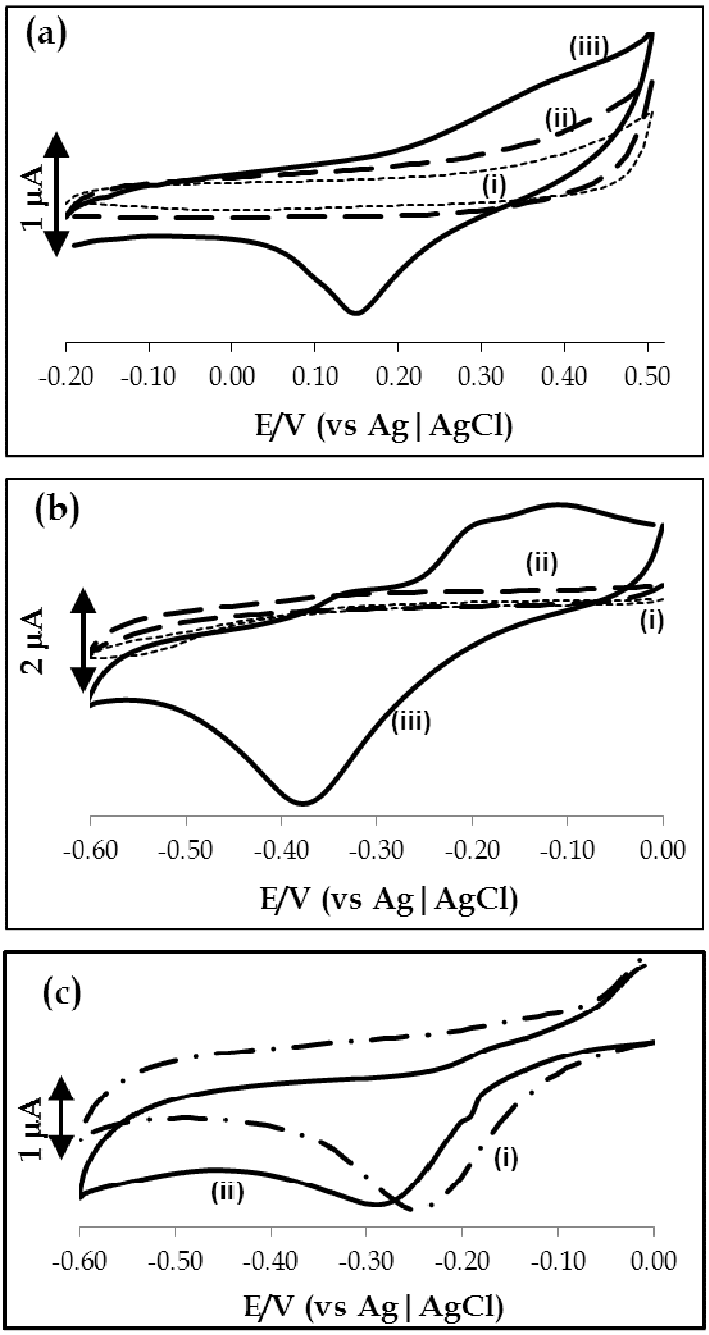

Figure 4.12: Cyclic voltammograms of (a) (i) SPAuE, (ii) SPAuE-PA and (iii) SPAuE-PA-CoTAPc, (b) (i) SPAuE, (ii) SPAuE-PA and (iii) SPAuE-PA-MnTAPc in 0.10 M KOH, (c) (i) SPAuE-PA-CoTAPc and (ii) SPAuE-PA-MnTAPc in pH 7.4 PBS solution. Scan rate = 25 $mV.s^{-1}$.

When pH 7.4 was employed, Figure 4.12(c), reduction peaks which were assigned to (i) $Co^{II}Pc/Co^{I}Pc$ at -0.24 V and (iii) $Mn^{III}Pc/Mn^{II}Pc$ at -0.30 V, were observed Table 4.4. The latter pH was employed since the detection of the analyte of interest (H_2O_2) will be determined at this pH. The peaks due to central metal ions appear at less negative potentials than those obtained on the polymer modified gold electrodes (Table 4.4) which were observed at -0.42 V and -0.35 V for Au-polyCoTAPc and Au-polyMnTAPc electrodes (Table 4.4), respectively, at the same pH, but not grafted onto the electrode.

Table 4.4: Electrochemical properties, i.e. peak potentials and surface coverages, for SPAuE-PA-MTAPc modified electrode surfaces in pH 7.4 buffer solution. Scan rate: 25 $mV.s^{-1}$.

Modified surfaces	**$M_{red} = E_p$ (V)**	**$\Gamma_{PA\text{-}MTAPc}$ ($mol.cm^{-2}$)**
SPAuE-PA-MnTAPc	-0.30 (-0.38[b])	1.31×10^{-9} (1.03×10^{-9}[b])
SPAuE-PA-CoTAPc	-0.24 (-0.35[b])	1.66×10^{-9} (1.55×10^{-9}[b])
GCE-polyCoTAPc[a]	-0.29	8.6×10^{-10}
Au-polyCoTAPc[a]	-0.42	1.3×10^{-9}
GCE-polyMnTAPc[a]	-0.43	8.2×10^{-10}
Au-polyMnTAPc[a]	-0.35	3.4×10^{-9}

$\Gamma_{PA\text{-}MTAPc}$ = surface coverage for PA-MTAPc modified electrodes. [a] Surface coverage values were obtained in DMF containing 0.1 M $TBABF_4$ on glassy carbon and gold electrodes, M_{red} = metal reduction peak and $E_{1/2}$ = half-wave potential. [b] Values in brackets are in 0.10 M KOH.

The observed changes in the cyclic voltammograms (Figure 4.12) in the presence of MTAPc complexes clearly confirmed the successful modification of the electrodes using the proposed method in Scheme 4.1. Furthermore, the use of strong alkaline (0.10 M KOH) solution for the characterization of these electrodes and the persistence of the

metal redox peaks during multiple scans indicates the stability of the modified electrodes. The surface coverages ($\Gamma_{PA\text{-}MTAPc}$) of the MTAPc modified electrodes were estimated by integrating the charge under the metal reduction or oxidation peaks in 0.10 M KOH solutions. Equation 4.2 was used for the estimation of surface coverage. The real surface area of SPAuE was calculated using the conventional method [180] applying equation 4.5 (Randles-Sevcik equation).

$$I_{pa} = (2.69 \times 10^5) n^{3/2} D^{1/2} \nu^{1/2} AC \qquad (4.5)$$

where n = 1 is the number of electrons transferred, D diffusion coefficient of the redox active species $[Fe(CN)_6]^{3-/4-}$ (7.6×10^{-6} $cm^2.s^{-1}$), ν is the scan rate (0.05 $V.s^{-1}$), C (2 mM) is the bulk concentration of $[Fe(CN)_6]^{3-/4-}$. The geometric area (0.0201 cm^{-2}) of the electrode was calculated from the diameter of 1.6 mm (r = 0.8 mm). The surface roughness factor of the electrode (1.75) was obtained from the ratio of real electrode surface area to electrode geometric area. The real surface area of the electrode was found to be higher than the geometric area and this is due to the fact that the active surface area is rough and uneven, this contributes to the roughness of the electrode. The surface coverage values were then calculated using equation (4.2) and the real area of the electrode (0.0352 cm^2). The surface coverage values were found to be 1.55×10^{-9} and 1.03×10^{-9} $mol.cm^{-2}$ for SPAuE-PA-CoTAPc and SPAuE-PA-MnTAPc, respectively, shown in Table 4.4.

Also in pH 7.4 PBS solution, these electrodes exhibited reduction peaks due to the metal ion and by integrating the charges under these peaks we were able to get surface coverage values of 1.66×10^{-9} $mol.cm^{-2}$ and 1.31×10^{-9} $mol.cm^{-2}$ for PA-CoTAPc and PA-MnTAPc modified electrodes, respectively, shown in Table 4.4. These surface coverage values were within the experimental errors similar for both MTAPc complexes in 0.10 M KOH and 0.01 M pH 7.4 PBS solutions. Since the real surface area of the electrodes

was used to calculate the surface coverages of the immobilized complexes, these values represent the actual concentration of the complexes onto electrode surfaces. These surface coverage values of the CoTAPc modified electrode were comparable to the reported values where cobalt tetracarboxyphthalocyanine (CoTCPc) complex was immobilized onto an aryl radical modified glassy carbon electrode [167]. In this study, the surface coverages for the immobilized MTAPc molecules are much higher than 1.0 x 10^{-10} mol.cm^{-2} for MPcs lying flat on the surface [80]. The higher surface coverages obtained in this work confirms that the MTAPc molecules assume a perpendicular orientation onto the gold surface as proposed in the immobilization method in Scheme 4.1. The surface coverage values for CoTAPc modified electrode are slightly higher than that of the (OH)MnTAPc modified surface and this could be attributed to the presence of the OH axial ligand on the MnTAPc [327,328]. The surface coverage values were of the same order of magnitude as for Au-polyMTAPc electrodes, Table 4.4.

The electrochemical properties of bare and modified electrodes were investigated using cyclic voltammetry in solutions containing redox probing species. These experiments were studied to further explore the electrocatalytic properties of the monolayers modified electrode surfaces. Figure 4.13 shows the cyclic voltammograms of (i) bare and modified electrodes with (ii) phenylamino (PA), (iii) PA-CoTAPc and (iv) PA-MnTAPc monolayers in (a) 1.0 mM $NH_4Fe(SO_4)_2$ in 1.0 mM $HClO_4$ and (b) (1:1) 2.0 mM $K_4/K_3Fe(CN)_6$ in 0.10 M KCl.

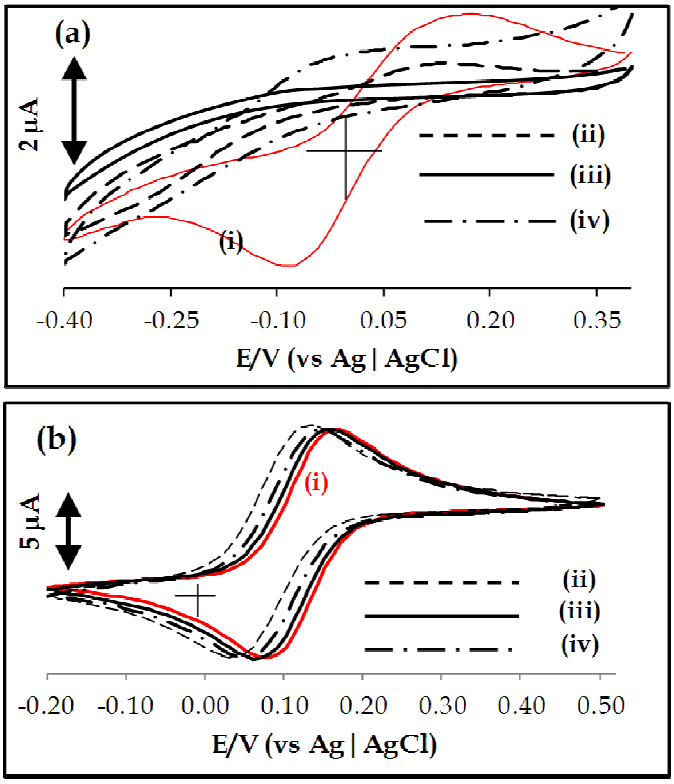

Figure 4.13: Cyclic voltammograms of (i) SPAuE, (ii) SPAuE-PA, (iii) SPAuE-PA-CoTAPc and (iv) SPAuE-PA-MnTAPc. (a) 1.0 mM $NH_4Fe(SO_4)_2$ in 1.0 mM $HClO_4$ and (b) (1:1) 2.0 mM $K_4/K_3Fe(CN)_6$ in 0.10 M KCl. Scan rate: 25 $mV.s^{-1}$.

The cyclic voltammograms of the bare screen-printed electrode in Figure 4.13(a)(i) exhibited a broad anodic peak at ~0.15 with a cathodic component at ~-0.09 V. This redox process is due to $[Fe(H_2O)_6]^{2+/3+}$ which shows slow electrode kinetics. Upon modifying the electrode with the PA and PA-MTAPc monolayers the reduction peak disappeared completely while the oxidation peak was still observed at PA monolayer with the decrease in current. The peak observed at ~0 V for PA-MnTAPc is due to metal based redox processes of MTAPc. The blocking capabilities of the monolayers towards the $[Fe(H_2O)_6]^{2+/3+}$ redox couple is a clear confirmation of the successful electrode modification. The blocking ability of the electrode was studied using the $[Fe(CN)_6]^{3-/4-}$ couple which is a fast electron transfer redox couple. In Figure 4.13(b), the cyclic voltammograms of the (i) bare electrodes shows the reversible redox couple due to

$[Fe(CN)_6]^{3-/4-}$ with the peak-to-peak separation (ΔE) of 81 mV. Upon modifying the electrodes with the PA group, in Figure 4.13(b)(ii) ΔE increased to 90 mV and this is attributed to the insulating layer of phenylamino that has formed on the electrode surfaces. However, the redox peak due to $[Fe(CN)_6]^{3-/4-}$ was not hindered. Furthermore, the modification of the electrodes with the MTAPc in Figure 4.13(b)(iii-iv) showed that the reversibility was restored and ΔE was the same as that of the bare (81 mV), but less than that for PA monolayer (90 mV) modified electrodes. It is of interest to note the work by Somashekarappa et. al. [113] where the MTAPc complexes were immobilized as SAMs on gold electrode and the electron transfer of the modified electrodes towards $[Fe(CN)_6]^{3-/4-}$ was not hindered by MTAPc SAMs. In this study, the PA monolayer gave higher ΔE values compared to PA-MnTAPc and PA-CoTAPc electrodes. The immobilization of MTAPc complexes onto the phenylamino modified electrodes without BDCA activation gave a ΔE value of 90 mV. Since this value is the same as for PA alone, it clearly indicates that in the absence BDCA as a cross-linker, the immobilization of MTAPc complexes did not take place. This experiment confirmed that the activation of the PA modified electrode with the aldehyde group from the BDCA group is necessary for the covalent immobilization of the MTAPc complexes.

4.3.3 Microscopic characterization of modified surfaces

Microscopic measurements were conducted on the gold-coated quartz crystals (AuCQC) rather than the screen-printed gold ecetrodes (SPAuE). The use of AuCQC surface is due to the fact that they are smoother when compared to the rough SPAuE and this will enhance and make visible the surface modification changes with monolayer thin films. Figure 4.14 shows the SEM images of the bare gold-coated quartz crystals (AuCQC) and screen-printed electrode surface (SPAuE). As can be seen in Figure 4.15, the SPAuE surface is rough when compared to the AuCQC surface.

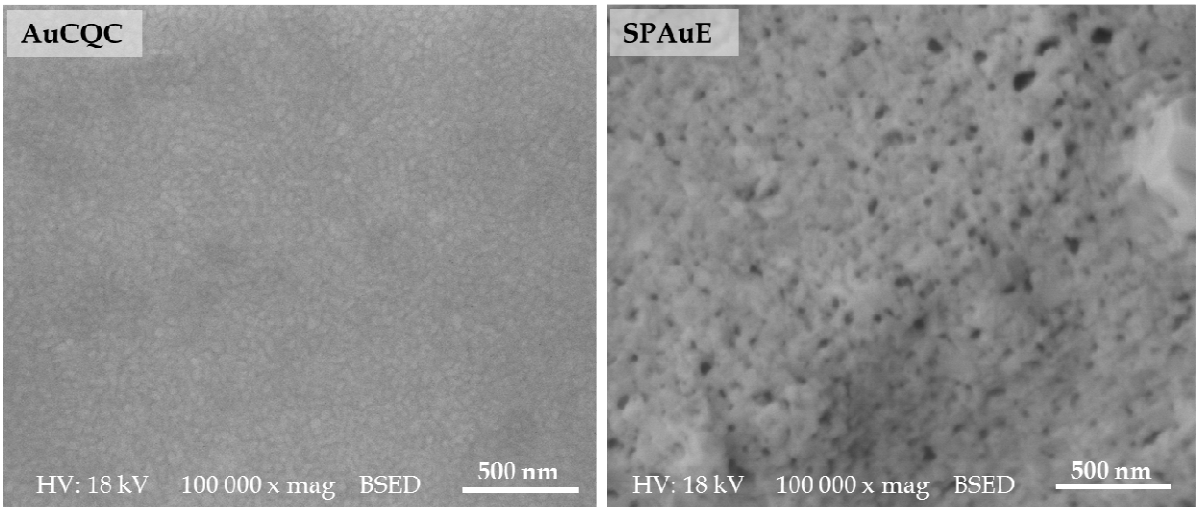

Figure 4.14: HRSEM images of bare gold coated quartz crystals (AuCQC) and screen-printed gold electrode (SPAuE).

4.3.3.1 HRSEM characterization of the bare, PA and PA-MTAPc modified gold electrodes

The HRSEM characterization of the bare and electrodes modified with phenylamino group and MTAPc complexes were carried out. Figure 4.15 shows the morphology of the (a) bare AuCQC surface, (b) AuCQC-PA, (c) AuCQC-PA-MnTAPc and (d) AuCQC-PA-CoTAPc electrodes and their corresponding energy dispersive X-ray spectroscopy (EDS) spectra.

It is discernible that electrode modification indeed took place as the morphology of these images was different, especially for the MTAPc modified surfaces as compared to bare AuCQC and AuCQC-PA surfaces. The morphologies of the bare AuCQC in Figure 4.15(a) and the AuCQC-PA in Figure 4.15(b) surfaces were similar. The phenylamino layer is very thin and the observed similarities in the surface SEM images are attributed to a very thin phenylamino layer.

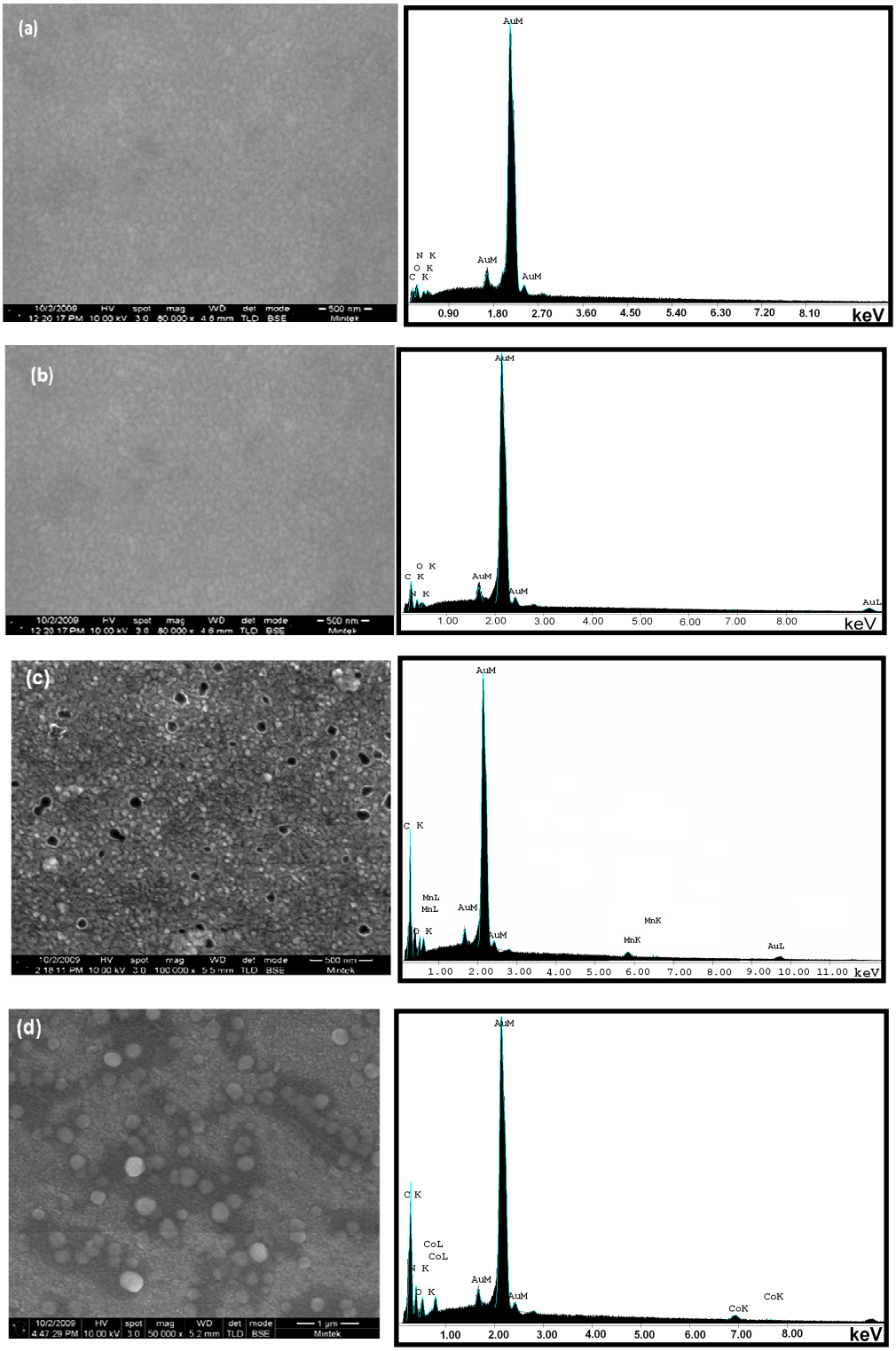

Figure 4.15: HRSEM images and their corresponding EDS spectra for (a) bare AuCQC, (b) AuCQC-PA, (c) AuCQC-PA-MnTAPc and (d) AuCQC-PA-CoTAPc modified surfaces.

The morphological comparison becomes clearer when the bare and phenylamino modified electrode surfaces are compared to the MTAPc modified surfaces, i.e. AuCQC-PA-MnTAPc in Figure 4.15(c) and AuCQC-PA-CoTAPc in Figure 4.15(d). The differences in morphologies between the AuCQC-PA-CoTAPc and AuCQC-PA-MnTAPc modified surfaces could be attributed to the difference in the individual bare AuCQC surfaces or to the aggregation of these molecules. The latter could be a logical reason to explain the observed morphological differences because there were no differences (compared to AuCQC surfaces used for Figure 4.15(a)) in surface morphologies of individual bare AuCQC surfaces before the immobilization of MTAPc complexes. Even though the modified surfaces were recorded with different scales, the CoTAPc molecules formed aggregated spherical species on AuCQC-PA-CoTAPc surfaces than the MnTAPc molecules on AuCQC-PA-MnTAPc surfaces. The latter contains an –OH axial ligand which may reduce aggregation [327,328]. The energy dispersive X-ray (EDX) analysis was also performed since it provides information on the materials present on the modified surfaces. The energy dispersive X-ray spectrum of bare AuCQC surface showed the dominating gold (Au M) peaks and this was expected as the AuCQC surfaces used were Au coated. The residues due to carbon (C K), oxygen (O K) and nitrogen (N K) were observed and these are due to the impurities and are always present in the spectrum in small quantities. The AuCQC-PA modified surface energy dispersive spectrum showed the presence of the dominating gold (Au M) and residual carbon (C K), nitrogen (N K) and oxygen (O K) materials. The residual peaks due to carbon and nitrogen at the AuCQC-PA monolayer modified electrodes could not be attributed to the presence of the PA monolayer because the electron beam is too strong and will penetrate this very thin monolayer, but a slight increase in the carbon peak was observed. The EDX measurements for the AuCQC-PA-MnTAPc were obtained from the dark sports observed after modifying the electrodes. Similarly with the AuCQC-PA-CoTAPc, the EDX measurements were obtained from the globular-like or spherical morphologies observed after modifying the electrodes with CoTAPc. The

EDX spectra, for the AuCQC-PA-CoTAPc and AuCQC-PA-MnTAPc modified electrode exhibited an increase in the carbon (C K) peak intensities with the presence of the peaks due to Co and Mn (L and K) from the AuCQC-PA-CoTAPc and AuCQC-PA-MnTAPc, respectively. The increase in the carbon (C K) materials in the AuCQC-PA-MTAPc (M = Co, Mn) modified electrodes is attributed to the presence of a more bulky PA-MTAPc compared to the bare or PA modified surfaces. The presence of the Co and Mn (L and K) peaks from the CoTAPc and MnTAPc modified gold electrodes clearly shows the presence and the successful immobilization of these complexes. The EDX results also offer quantification analysis, where the percentage weight (wt%) of the observed elements are shown in Table 4.5. From the data in Table 4.5, the increase in the carbon peak was observed and this was more prominent on the AuCQC-PA-MTAPc modified electrodes. Also the weight percent showed the presence of the metal peaks due to cobalt for AuCQC-PA-CoTAPc and manganese for AuCQC-PA-MnTAPc. No conclusion could be drawn from the nitrogen (N K) and the oxygen (O K) peaks as these varied randomly from surface to surface. The SEM characterization in its nature may not be used for quantification purposes and therefore, the obtained quantification results do not represent the exact quantities of elements found on the surface and also the presence of residual carbon, nitrogen and oxygen may vary from surface to surface hence giving inaccurate result. The data shown in the Table 4.5 confirms the presence of the modifiers and more accurate quantification techniques (such as XPS) will be used for the exact amount of elements on the electrode surfaces.

Table 4.5: Elemental quantification, weight percent (wt%) for the elements obtained using the EDX spectra of bare and modified gold surfaces.

Electrodes (elements)	AuCQC (wt%)	AuCQC-PA (wt%)	AuCQC-PA-CoTAPc (wt%)	AuCQC-PA-MnTAPc (wt%)
Carbon (C K)	4.96	8.54	43.33	40.52
Nitrogen (N K)	3.78	2.53	3.51	5.14
Oxygen (O K)	1.12	1.78	3.02	2.51
Cobalt (Co K)	-	-	3.54	-
Manganese (Mn K)	-	-	-	2.34
Gold (AuL)	90.13	87.24	44.92	47.82

4.3.3.2 AFM characterization of the bare and modified gold electrodes

AFM was used to investigate the surface morphology of the bare and modified surfaces with PA and PA-MTAPc. Figure 4.16 shows the 2D and their corresponding 3D AFM micrographs for the (a) bare AuCQC, (b) AuCQC-PA, (c) AuCQC-PA-MnTAPc and (d) AuCQC-PA-CoTAPc. At first glance, the surface morphologies are different, except for the bare in Figure 4.16(a) and the PA modified gold surface in Figure 4.16(b) which showed similar images. The images of the bare and PA-MTAPc modified electrodes clearly showed a huge difference which is attributed to the PA-MTAPc modification, Figure 4.16(c) and (d). The differences in surface morphologies are attributed to the immobilization of the MTAPc complexes onto aldehyde functionalized surfaces. The analysis of the surfaces gave roughness factors of 1.693 nm for bare AuCQC, 2.584 nm for AuCQC-PA, 3.497 nm for AuCQC-PA-MnTAPc and 4.951 nm for AuCQC-PA-CoTAPc. The increase in surface roughness factor values is a clear indication of the modification of AuCQC surfaces as proposed in Scheme 4.1. The section analysis was also conducted and vertical distances measured from the line analysis taking the highest peak. The section analysis also showed an increase with each surface

modification. The vertical distance values were 4.411 nm for AuCQC, 7.916 nm for AuCQC-PA, 21.659 nm for AuCQC-PA-MnTAPc and 21.061 nm for AuCQC-PA-CoTAPc, clearly confirming the surface modifications as proposed in Scheme 4.1.

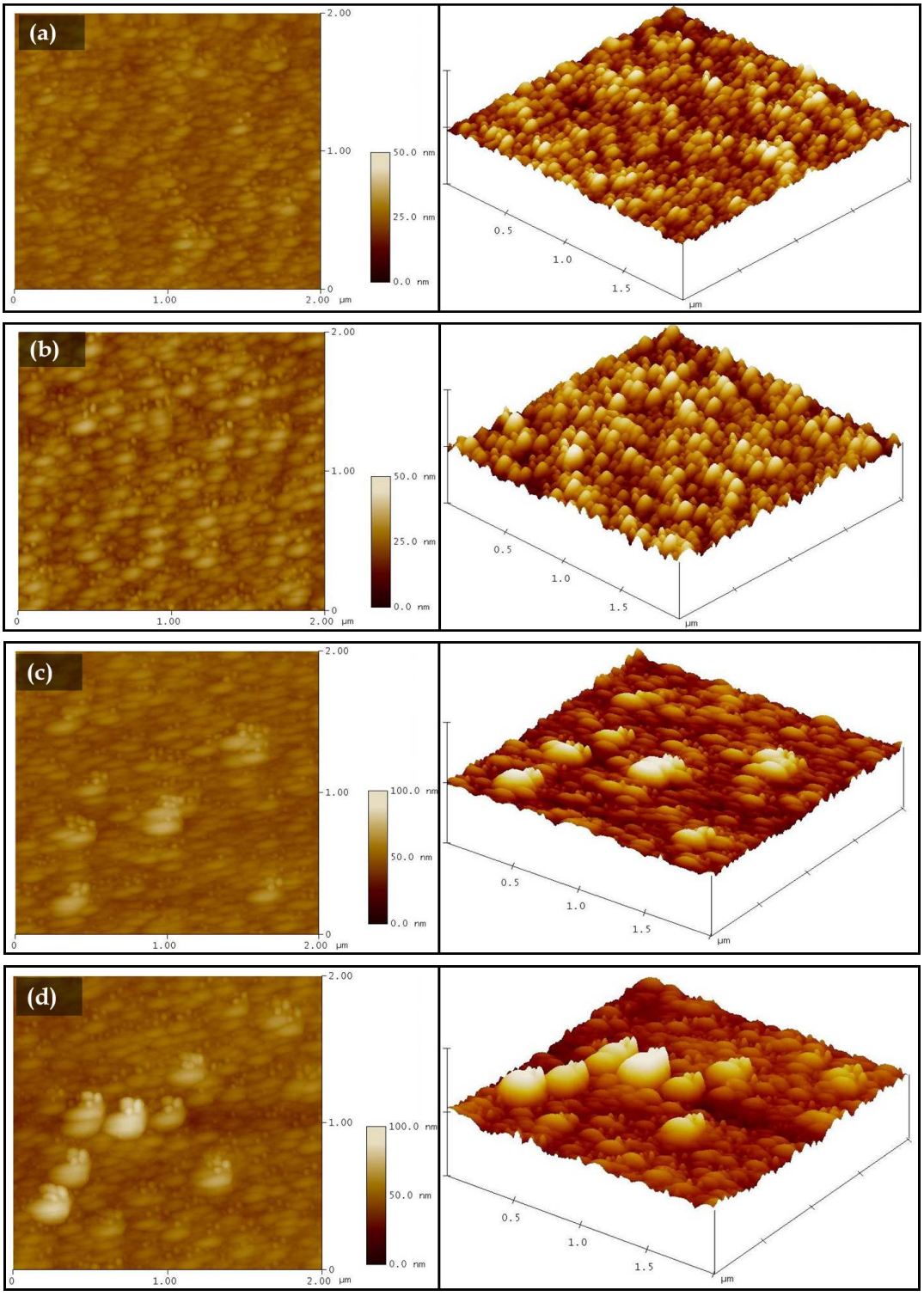

Figure 4.16: 2D and 3D AFM images images for (a) bare AuCQC, (b) AuCQC-PA, (c) AuCQC-PA-MnTAPc and (d) AuCQC-PA-CoTAPc.

4.3.4 Spectroscopic characterization

4.3.4.1 Surface Raman characterization of modified gold electrodes

Further confirmation of the surface modification was accomplished using Raman spectroscopy measurements. Figure 4.17 shows the Raman spectra of (a) powder samples of unbound (i) MnTAPc and (ii) CoTAPc and (b) SPAuE surface bound (i) PA (SPAuE-PA), (ii) MnTAPc (SPAuE-PA-MnTAPc) and (iii) CoTAPc (SPAuE-PA-CoTAPc) electrodes. The Raman peaks for MTAPc complexes are similar to those observed for MPc complexes reported [365-370] and their assignments are summarized in the Table 4.6. The MnTAPc complex exhibited an additional peak at 940 cm^{-1} in Figure 4.17(a) which is an out-of-plane ring deformation and due to the OH axial ligand. The spectra of the modified SPAuE surfaces showed intense peaks. It is discernible from the spectra that the surface modification indeed took place as the Raman peaks due to the materials (PA and MTAPc complexes) were observed. The peaks were however shifted slightly and this could be attributed to the materials immobilized onto an electrode surface, Figure 4.17 compared to when they are in their powder form. It was also interesting to observe peaks at the metallic region (100 – 550 cm^{-1}) and due to Au-C bending and stretching bands for the SPAuE modified surfaces and Mn-O (at 341 cm^{-1}) for the SPAuE-PA-MnTAPc surface further confirming the presence of the OH axial ligand. These experiments confirmed the immobilization of the materials as proposed in the protocol in Scheme 4.1.

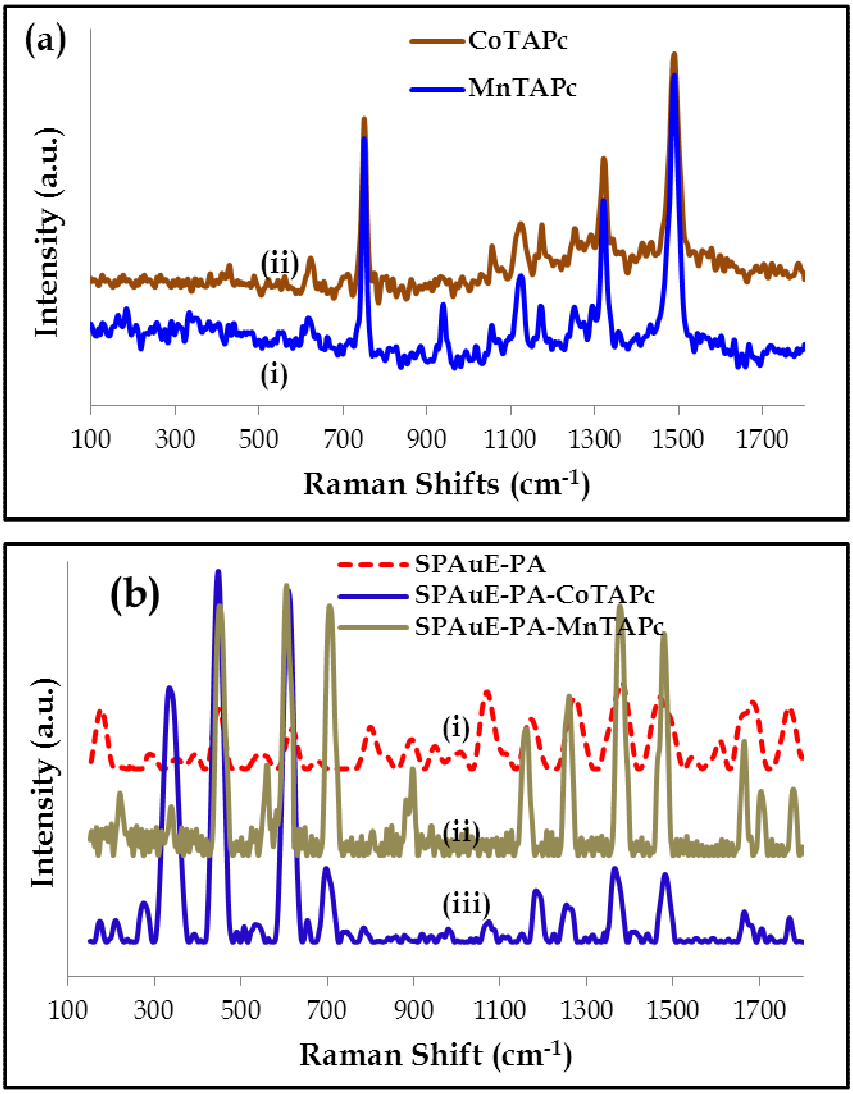

Figure 4.17: (a) Raman spectra for (i) MnTAPc and (ii) CoTAPc complexes in their powder form and (b) SPAuE surfaces modified with (i) PA, (ii) PA-MnTAPc and (iii) PA-CoTAPc.

Table 4.6: Positions of molecular Raman bands for SPAuE-PA-CoTAPc and SPAuE-PA-MnTAPc and their interpretation.

SPAuE Modified		
SPAuE-PA-MnTAPc (cm^{-1})	**SPAuE-PA-CoTAPc (cm^{-1})**	**Interpretation**
222	218, 284	**Au-C bending**
341	__	**Mn-O**
454	454, 550	**Au-C stretch**
612, 710	607, 658, 704	**Ring deformation**
899, 902	__	**Out-of-plane bending**
__	1086	**C-H bending**
1163, 1262	1194, 1269	**C-H bending**
1381	1371	**C-N breathing**
1480	1487	**C=C pyrrole stretch**
1666, 1707, 1782	1670, 1728, 1775	**C=C stretch**

4.3.4.2 XPS characterization of modified gold surfaces

XPS measurements are very useful in studying the surface film composition and therefore confirming the modification and formation of monolayers as predicted. Figure 4.18 shows the (a) survey spectra, (b) C1s high resolution region and (c) N1s high resolution region for (i) SPAuE-PA, (ii) SPAuE-PA-CoTAPc, (iii) SPAuE-PA-MnTAPc. The presence of N and C were expected as the materials used for the electrode modifications contained these elements. The peaks due to metal ions (i.e. Co and Mn) were also not observed after modifying gold surfaces with MTAPc complexes. The MTAPc complexes contain carbon conjugated networks and these are observed. But due to the small quantities of the metal ions when compared to carbon, these are not observed even after the high resolution and extended acquisition run.

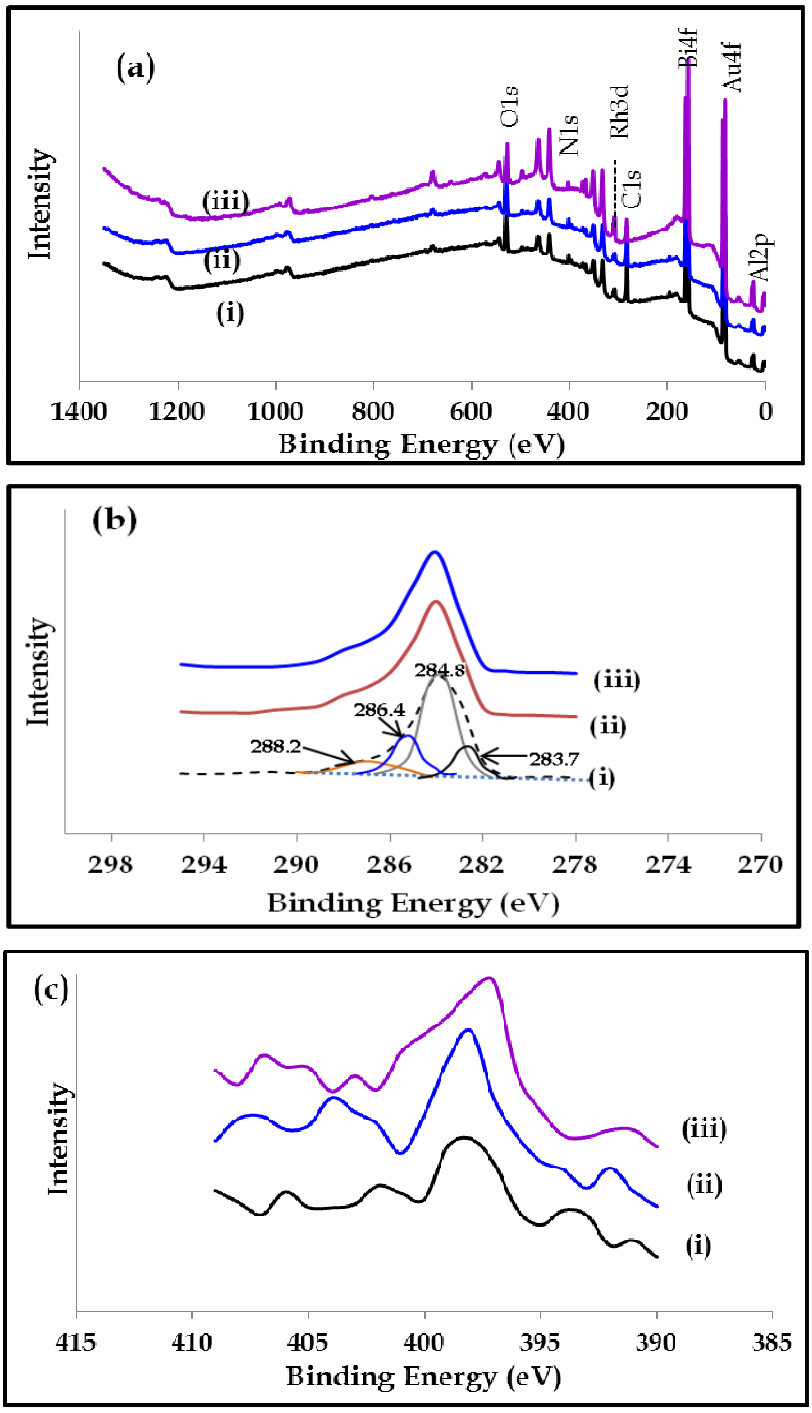

Figure 4.18: XPS analysis (a) survey spectra, (b) C1s high resolution region and (c) N1s high resolution region for the SPAuE surfaces modified with (i) PA, (ii) PA-SWCNT-MnTAPc and (iii) PA-SWCNT-CoTAPc.

The presence of other elements such as (Au, Bi, Rh, Ag, Al and O) on the measured surfaces was attributed to the gold coated ceramic substrate (screen-printed gold electrodes). According to the supplier information these elements can be picked up, especially using a sensitive surface technique such as XPS.

The high resolution spectra of C1s are shown in Figure 4.18(b). The SPAuE-PA surfaces (i) gave four peaks centred at 283.7 eV, 284.8 eV, 286.4 eV and 288.2 eV. The peak at 284.8 eV was more intense than the other three peaks and it corresponds to the C-C or C=C bonds which form bulk of the materials used. The other peak of importance is obtained at 283.7 eV which correspond to formation of the gold carbide (Au-C) bond. The peak at 283.7 eV was important in demonstrating the chemisorption of the diazonium onto gold electrode surface via the formation of Au-C bond during electrochemical grafting. The Au-C bond was observed at positions typical [225] of the carbide bonds formed on metal surfaces. Several reports using XPS have demonstrated that this bond forms on electrografted metal surfaces such as gold, copper and iron surfaces with diazonium salts [225,247,252,253]. The observation of this peak clearly confirms the formation of the PA monolayer as proposed in Scheme 4.1. The other peaks observed at 286.4 eV and 288.2 eV are attributed to the C-H and C-N or C=N species, respectively. The binding energy values for the Au-C, C-H, C-C, C-N and C=N bonds on other surfaces in Figure 4.18(b)(ii) and (iii) were also observed at similar positions to those shown in Figure 4.18(b)(i).

The analysis of high resolution spectra of N1s region is shown in Figure 4.18(c). The nitrogen peaks were observed at 399.9 eV in very low intensities, therefore the fitting was not done. The presence of the nitrogen peak (though in small quantities) confirmed the immobilized materials, i.e PA, PA-CoTAPc and PA-MnTAPc which bears the nitrogen group.

The experimental percentage composition of the elements observed in the survey spectra was conducted and the results are summarized in Table 4.7. In Table 4.7, the increase in carbon percentage composition, from 34.0% for SPAuE-PA to 57.3% for SPAuE-PA-MnTAPc and 61.8% for SPAuE-PA-CoTAPc surfaces, was observed when the gold surfaces were functionalized with PA-MTAPc complexes confirming the presence of the bulky MTAPc complexes onto gold surfaces.

Table 4.7: Experimental percentage composition of elements found on electrografted gold surfaces with PA, PA-MnTAPc and PA-CoTAPc.

Elements / Electrodes	C1s	N1s	O1s	Au4f	Bi4f	Rh4f	Ag3d
PA	34.0 %	11.5 %	33.7%	16.6%	11.5%	2.80%	1.30%
PA-MnTAPc	57.3%	2.20%	25.1%	7.80%	4.40%	1.10%	0.50%
PA-CoTAPc	61.8%	6.80%	23.6%	2.60%	2.70%	0.70%	0.20%

4.3.5 Electrochemical impedance spectroscopy characterization

The electrochemical impedance spectroscopy (EIS) measurements in $[Fe(CN)_6]^{3-/4-}$ solution were also performed in order to assess the electron transfer properties of the modified electrodes. Figure 4.19 shows (a) the Nyquist plots, (b) their corresponding Bode plots for the (i) SPAuE, (ii) SPAuE-PA, (iii) SPAuE-PA-CoTAPc and (iv) SPAuE-PA-MnTAPc electrodes.

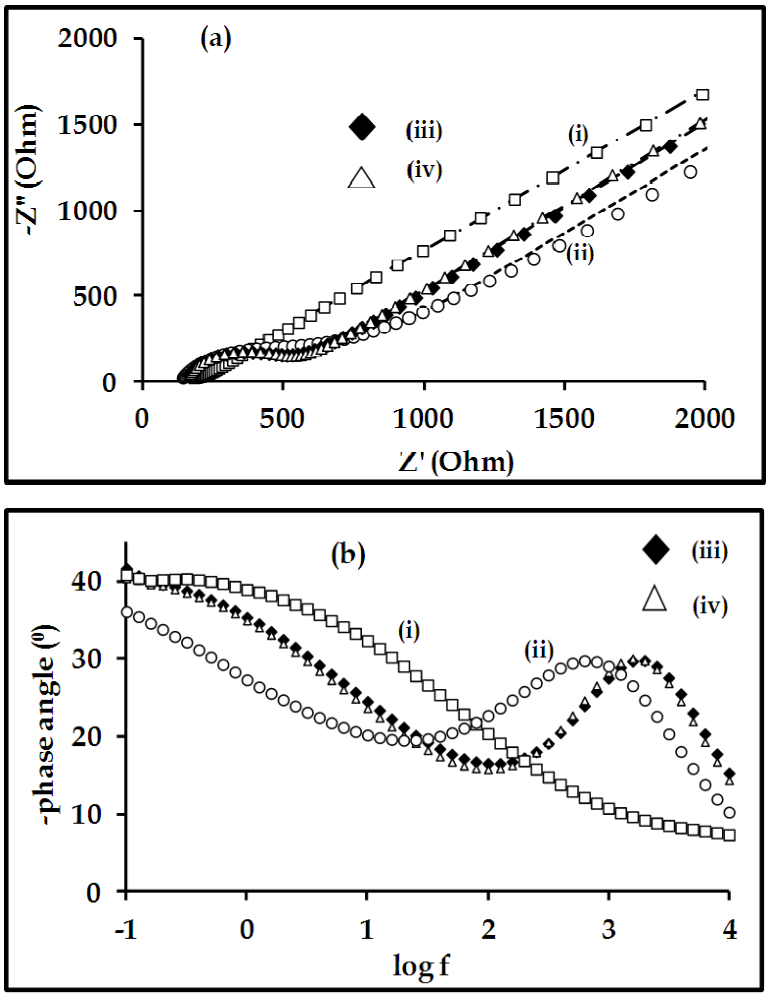

Figure 4.19: (a) Nyquist and (b) Bode plots of (i) bare SPAuE, (ii) SPAuE-PA, (iii) SPAuE-PA-CoTAPc and (iv) SPAuE-PA-MnTAPc in (1:1) 2 mM $Fe(CN)_6^{-3/-4}$ solution with 0.1 M KCl.

The Nyquist plots in Figure 4.19(a)(i), for bare SPAuE, shows a small semi-circle at kinetically controlled regions and this semi-circle increases after modifying the electrodes with the PA and PA-MTAPc monolayers. The fitted data is shown in Table 4.8, where R_{CT} exhibited an increase from bare to modified surfaces. For the bare electrode surface, R_{CT} = 1.79 kΩ.cm^{-2} and this value increased to 43.67 kΩ.cm^{-2} for PA, 9.66 kΩ.cm^{-2} for PA-CoTAPc and 9.69 kΩ.cm^{-2} for PA-MnTAPc electrodes. The increase in R_{CT} from a bare to PA modified electrodes is due to the formed insulating layer

which slows electron transfer. The decrease in R_{CT} after modifying the electrode with MTAPc is attributed to the known catalytic properties of the metallophthalocyanines and hence the electron transfer is enhanced. MPcs, especially those containing cobalt and manganese metal centers are known [219] to be good electrocatalysts and enhance the electron transfer hence the decrease in R_{CT}. The Rs value did not show any significant changes before and after modifying the electrodes with PA and PA-MTAPc. This was expected as the surface modification was not expected to change the solution resistance as already discussed. The capacitance values (CPE) are affected by the electrode modification as the increase in capacitance (CPE values) after modifying electrode surfaces with PA monolayer was observed. Upon modifying the electrodes with MTAPc the CPE decreased and this is attributed to the already observed phenomenon on R_{CT} values.

The Bode plots after modifying the electrode in Figure 4.19(b) showed the presence of a symmetrical peak which was clearly not observed at the bare electrode. The phase angle (Θ) maxima of the symmetric peaks were observed to be -29.87^{o} at log f = 2.8 Hz (for PA modified electrode), -29.72^{o} at log f = 3.2 Hz (for PA-CoTAPc) and (-30.08^{o} at log f = 3.2 Hz (for PA-MnTAPc), Table 4.8. The presence and the shift of the symmetrical peak to lower log f values (compared to bare gold electrode) confirms the different surface properties introduced on the electrode after modifying with MTAPc. The phase angle values for all the electrodes studied are much less than the ideal -90° for a true capacitor leading to the conclusion that these electrodes have capacitive-like behaviour [359]. From Table 4.8, n values are all ~0.9, hence are close to unity and thus leading to the conclusion that the electrodes have a capacitive-like behaviour discussed above for the polymer modified electrodes. This conclusion confirms the results obtained from the phase angle values which were less than -90° due to the capacitive-like nature of the thin films studied and further confirms surface modification as intended.

Table 4.8: The summary of the parameters obtained from electrochemical impedance spectroscopy experiments in $Fe(CN)_6$ solution.

Electrodes	R_S ($k\Omega.cm^{-2}$)	R_{CT} ($k\Omega.cm^{-2}$)	n	CPE ($\mu F.cm^{-2}$)	θ (°)	k_{app} x 10^{-4} ($cm.s^{-1}$)
SPAuE	4.72	1.79	0.87	56	-	1.20
SPAuE-PA	4.12	43.67	0.88	94	-29.87	0.049
SPAuE-PA-CoTAPc	4.43	9.66	0.92	22	-29.72	0.22
SPAuE-PA-MnTAPc	4.32	9.69	0.94	22	-30.08	0.22

Θ is phase angle values which were obtained from the Bode plot.

The apparent electron-transfer rate constants (k_{app}) were also studied here, as discussed above using the equation 4.3. The redox probe $[Fe(CN)_6]^{3-/4-}$ was also used and the R_{CT} values obtained in Table 4.8, were used to calculated the k_{app}. Similar to the measurements above for the polymer studies, this method also investigates the outer sphere kinetic properties of the immobilized monolayer thin films and their interaction with the redox probe in solution. The bare electrode surface gave the k_{app} value of 1.20 x 10^{-4} $cm.s^{-1}$. Upon modifying the electrodes with PA and PA-MTAPc monolayers the k_{app} decreased to 0.049 x 10^{-4} $cm.s^{-1}$ and 0.22 x 10^{-4} $cm.s^{-1}$ for PA and PA-MTAPc modified electrodes, respectively, Table 4.8. The PA-MTAPc modified electrodes exhibited the conducting properties as the k_{app} values were higher than those of the PA monolayer modified electrodes. This confirms the previously obtained results of R_{CT} showing that the PA-MTAPc modified electrodes exhibited conducting properties. The electrode modification clearly affects the k_{app} values and this was also reported [77] where an increase in R_{CT} (hence decrease in k_{app}) was observed with increasing deposition time for the SAMs. The electrode modification with PA and the covalent attachment of the MTAPc complexes onto the phenylamino-aldehyde activated surfaces is expected to yield a closely packed monolayer. This closely packed monolayer has resulted in the

decrease in k_{app} compared to the unmodified electrodes, hence the conclusion that electrode modification leads to the decrease in the electron-transfer rate constants. The PA modified electrode gave a very low k_{app} and this is attributed to the insulating properties of the PA monolayer.

4.4 Immobilization and characterization of carbon nanotubes and MTAPc hybrids onto SPAuE surfaces

Figure 4.20 shows the TEM images of (a) CoTAPc, (b) MnTAPc and (c) PA-SWCNT after the materials were initially dispersed in DMF solution through ultra-sonication followed by evaporation of the solvent on a carbon-coated copper grit. The CoTAPc TEM image in Figure 4.20(a) showed high intermolecular aggregation and this aggregation was less visible on the MnTAPc TEM image in Figure 4.20(b). The difference in the TEM images is due to the fact that MnTAPc has an –OH axial ligand, Mn(OH)TAPc, which reduces intermolecular aggregation. The TEM image of PA-SWCNT in Figure 4.20(c) showed a well dispersed PA-SWCNTs with diameter ranging from 0.7-10 nm. The original diameter for the SWCNT not functionalized as per the supplier information is 0.7–1.4 nm, therefore the increase in diameter of up to 10 nm shows that the functionalization of the SWCNT with phenylamino group has occurred. This increase in SWCNT diameter could be attributed to (i) the nanotubes intertwined together or (ii) dual functionalization of the benzene-1,4-diamine forming a benzene-1,4-*bis*-diazonium (N_2^+) on both amine groups leading to two or more SWCNT coming together forming a polymeric SWCNT conjugate.

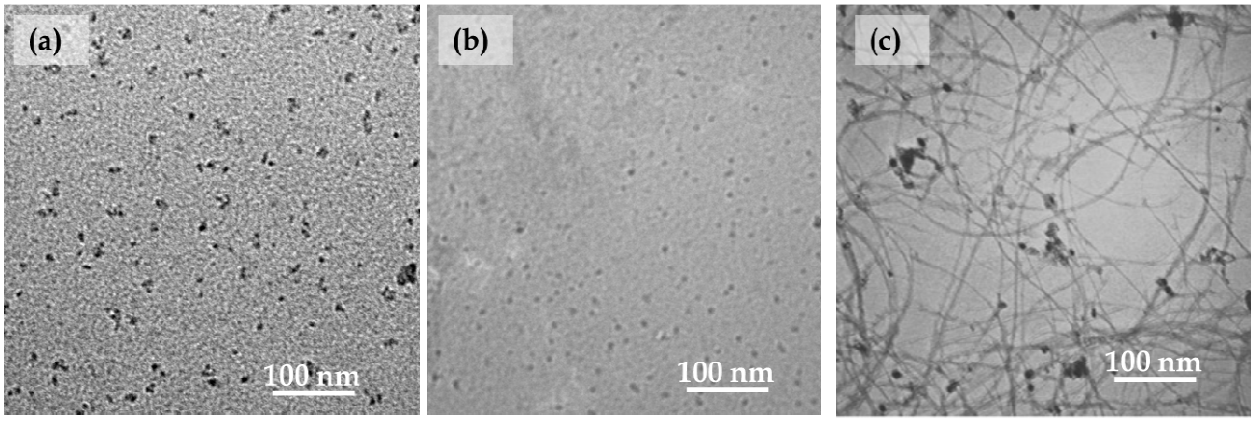

Figure 4.20: TEM images of (a) CoTAPc, (b) MnTAPc and (c) phenyl-amine side walled functionalized SWCNT dispersed in DMF and modified onto mesh copper grit with solvent evaporated.

The previous section 4.3 showed without doubt the immobilization of MTAPc and in this section the PA-SWCNT and MTAPc immobilization are investigated following the method outlined in Scheme 4.2.

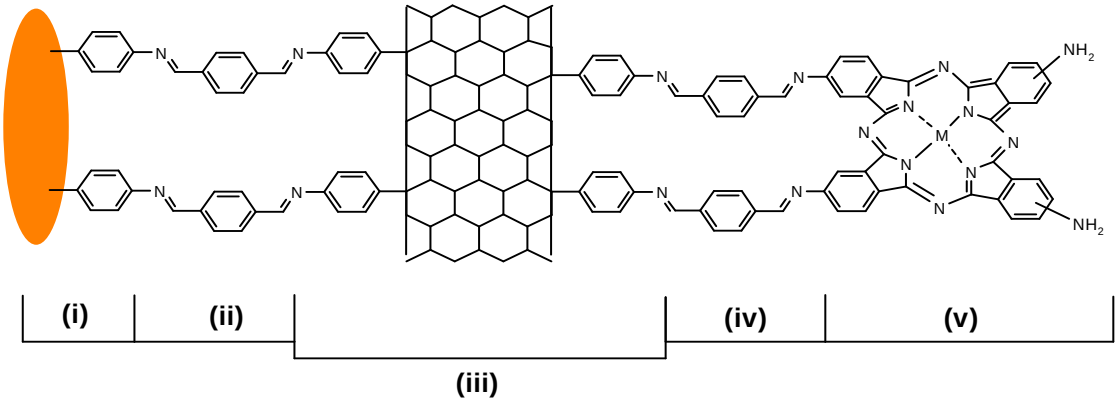

Scheme 4.2: The immobilization PA-SWCNT and MTAPc (M = Co or Mn) onto phenyl-amine grafted SPAuE. Step (i): electrografting of 4-NBD in ACN solution containing $TBABF_4$ and reduction of NO_2 group to form NH_2 (aprotic solution). Step (ii): activation of the amino group using BDCA ethanol solution. Step (iii): immobilization of PA-SWCNT (5% w/w) in DMF. Step (iv) activation in BDCA mixed solution DMF/ethanol (1:1, v/v) and (v) immobilization of MTAPc in DMF.

The order in which the metallophthalocyanine complexes and carbon nanotubes are immobilized onto gold electrode surface has an impact on the electron-transfer and electrocatalysis properties [143]. In the reported work [143], the authors found better electrocatalytic properties when nanostructured iron phthalocyanines were immobilized on top of the carbon nanotubes. Therefore, the immobilization of MTAPc complexes will be the layer exposed to the solution, i.e. at the electrode-solution interface. This immobilization of MTAPc complexes on top of the PA-SWCNT is important because the metal ion centres from MTAPc complexes contribute to the overall mechanism for H_2O_2 electrocatalysis which will be discussed in detail in chapter 5. The SWCNT-MTAPc hybrid systems are expected to have enhanced electrocatalytic properties due to the synergistic effect expected when the two materials act together.

4.4.1 Microscopic characterization for the immobilization of MTAPc-SWCNT

4.4.1.1 HRSEM characterization of PA-SWCNT and PA-SWCNT-MTAPc modified surfaces

The HRSEM characterization of the AuCQC electrode modified with phenyl-amino group, PA-SWCNT and MTAPc complexes was carried out. AuCQC was used since it is smoother when compared to the SPAuE surfaces making surface modification with monolayer thin films relatively easier to observe than on the SPAuE. Figure 4.21 shows the SEM micrographs of (a) bare AuCQC, (b) AuCQC-PA-SWCNT, (c) AuCQC-PA-SWCNT-MnTAPc and (d) AuCQC-PA-SWCNT-CoTAPc modified surfaces following the procedure in Scheme 4.2. From the HRSEM images, it is clear that electrode modification indeed took place as the morphology of these images was different, especially between the bare (AuCQC) in Figure 4.21(a) and AuCQC-PA-SWCNT in Figure 4.21(b) which showed a dense film of PA-SWCNT deposited. The film was even thicker and denser when MnTAPc in Figure 4.21(c) and CoTAPc in Figure 4.21(d) were

immobilized; confirming the attachment of MTAPc complexes onto PA-SWCNT functionalized gold surfaces.

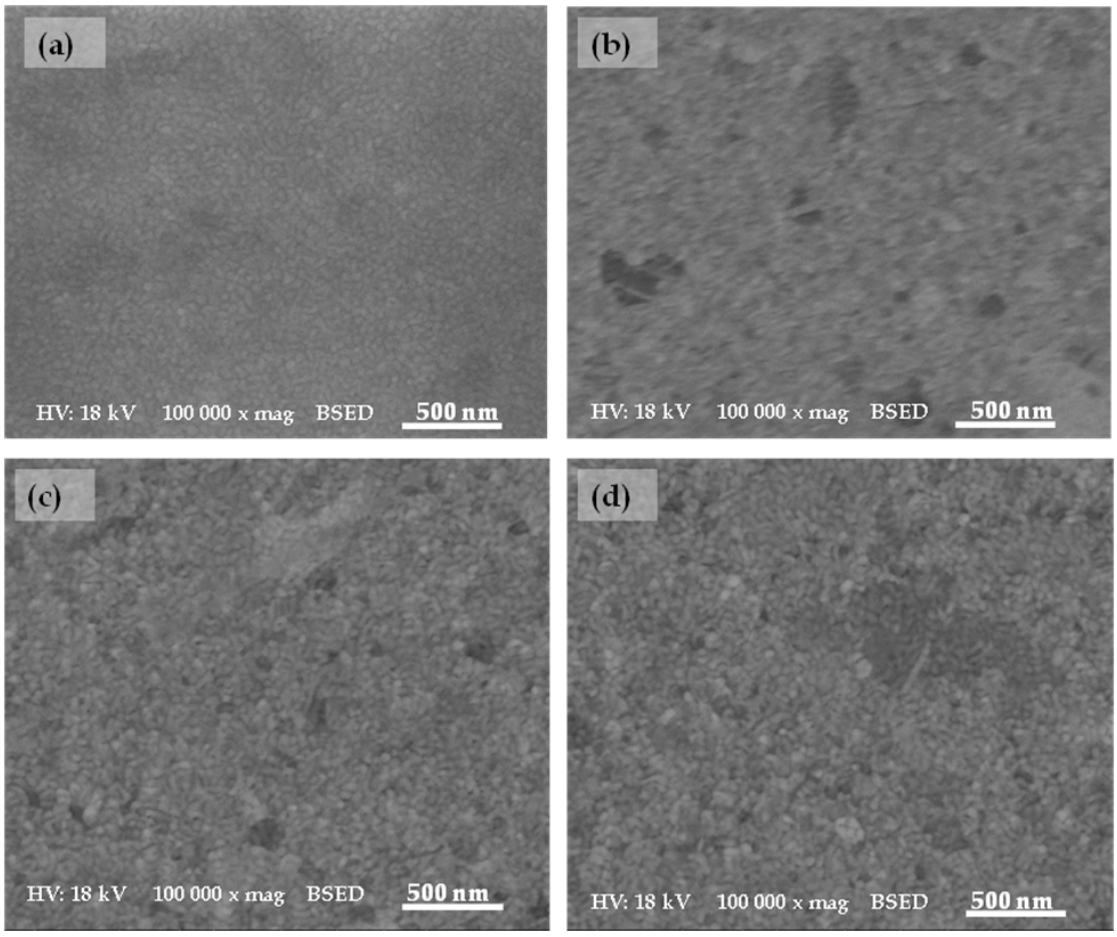

Figure 4.21: HRSEM micrographs for (a) bare AuCQC, (b) AuCQC-PA-SWCNT, (c) AuCQC-PA-SWCNT-MnTAPc and (d) AuCQC-PA-SWCNT-CoTAPc modified electrodes.

The EDX analysis of the bare and modified surfaces further confirmed the surface modifications with PA-SWCNT and the MTAPc (MnTAPc and CoTAPc) for the formation of PA-SWCNT-MTAPc hybrid sensing layer. At bare AuCQC in Figure 4.22(a) a dominating gold peaks (Au M) was observed and this was expected as the AuCQC was used as the substrate and is similar to the studies shown in Figure 4.15(a).

There was a significant increase in the carbon (C K) peak after modifying the surface with PA-SWCNT, Figure 4.22(b). The increase in the C K is attributed to the presence of the highly carbon-based material (PA-SWCNT) immobilized onto the AuCQC surface forming an AuCQC-PA-SWCNT. As the CK peak increased, the Au M peak intensity decreased, signifying the coverage of gold surface with carbonaceous material (PA-SWCNT). CoTAPc complex was immobilized onto PA-SWCNT surface to yield an AuCQC-PA-SWCNT-CoTAPc and the increase in C K peak was also observed, due to the attachment of CoTAPc, Figure 4.22(c). The results obtained from the immobilization of MnTAPc were similar to those of CoTAPc. The other elements, oxygen (O K) and nitrogen (N K) did not show any reasonable increase or decrease before and after modification. Therefore, no conclusion could be drawn from the N K and O K peaks. It was interesting to note that at MTAPc modified surfaces, the metal ion peaks were not present as observed at AuCQC-PA-MTAPc (above section 4.3). This could be due to the high carbon content on the SWCNT presence on the electrode surface, hence the metal ion peaks are very small and buried under other highly intense carbon and gold peaks. The results from EDX spectra and the elemental analysis clearly show the presence and the successful immobilization of PA, PA-SWCNT and PA-SWCNT-MTAPc complexes (CoTAPc and MnTAPc) onto gold electrode surfaces.

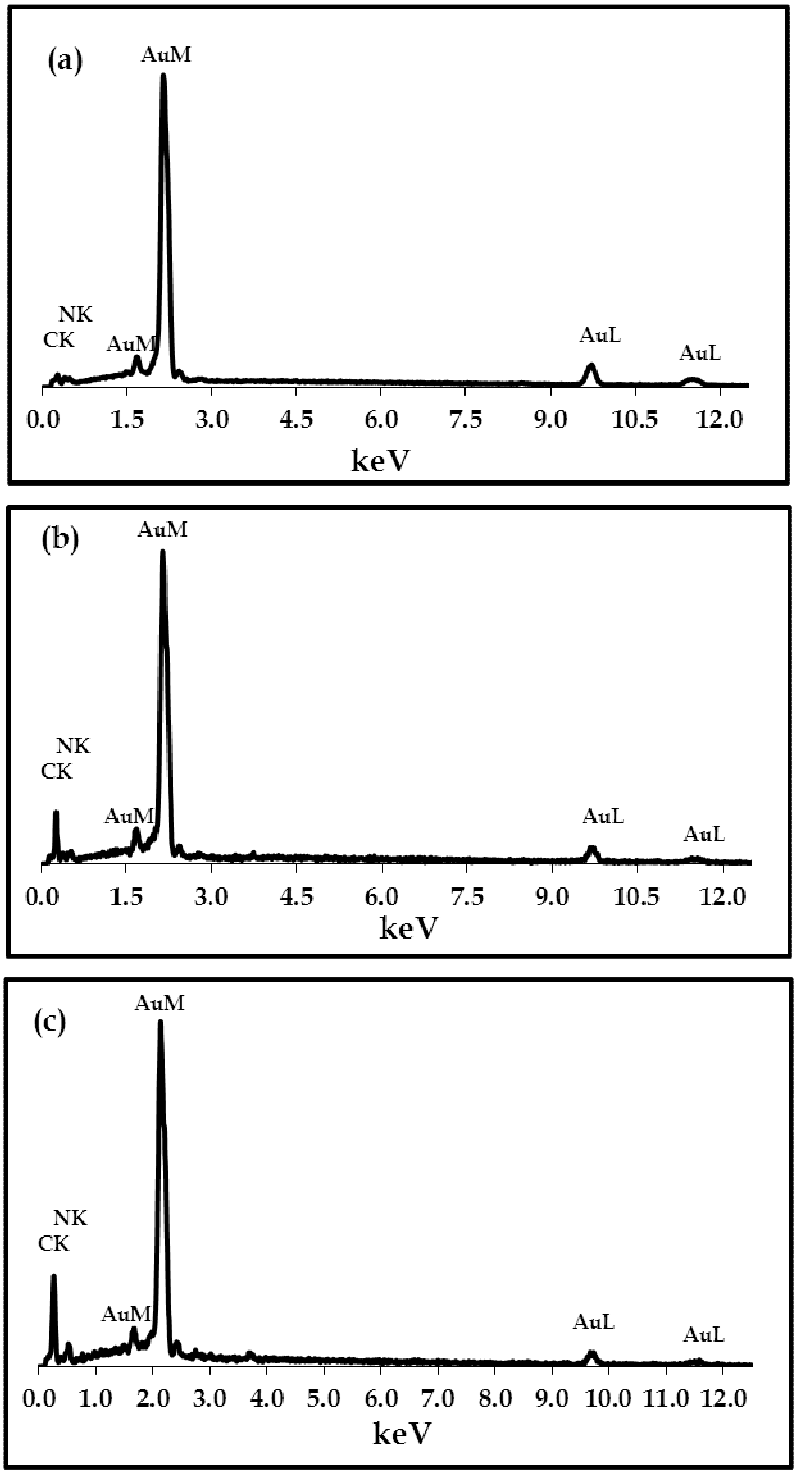

Figure 4.22: Energy dispersive x-ray spectroscopy (EDS) spectra for (a) bare AuCQC, (b) AuCQC-PA-SWCNT and (c) AuCQC-PA-SWCNT-CoTAPc.

Table 4.9: Elemental quantification, weight percentage (wt%) for the elements obtained using EDX spectra of the modified gold surfaces.

Electrodes / Elements	AuCQC-PA-CoTAPc (wt%)	AuCQC-PA-MnTAPc (wt%)	AuCQC-PA-SWCNT (wt%)	AuCQC-PA-SWCNT-CoTAPc (wt%)	AuCQC-PA-SWCNT-MnTAPc (wt%)
Carbon (C K)	43.33	40.52	21.45	31.46	31.56
Nitrogen (N K)	3.51	5.14	2.36	3.56	4.11
Oxygen (O K)	3.02	2.51	1.88	3.00	4.50
Cobalt (Co K)	3.54	—	—	—	—
Manganese (Mn K)	—	2.34	—	—	—
Gold (Au L)	44.92	47.82	74.30	61.97	59.84

Table 4.9 shows the weight percent (wt%) of elements found on the gold surfaces. The increase in carbon (C K) wt% was observed as the electrode was modified with PA-MTAPc, PA-SWCNT and PA-SWCNT-MTAPc layers. At PA-MTAPc modified surfaces (without SWCNT), the wt% due to carbon was higher than in the presence of SWCNT surfaces in Table 4.9 and this is attributed to the fact that the PA-MTAPc surfaces showed agglomerated species, Figure 4.15(c) and (d). The increase in carbon wt% was also observed for PA-SWCNT-MTAPc modified electrodes when compared to PA-SWCNT alone, clearly showing the immobilization of MTAPc. As the carbon wt% increased, the gold (Au L) wt% decreased and this is attributed to the immobilization of carbonaceous materials (i.e. PA-SWCNT, PA-MTAPc and PA-SWCNT-MTAPc) onto gold electrode surfaces.

4.4.1.2 AFM characterization of the bare and modified gold electrodes

The AFM was also used to investigate the surface morphology of the bare and modified surfaces with PA-SWCNT and PA-SWCNT-MTAPc. Figure 4.23 shows the 2D and 3D

AFM micrographs for the (a) AuCQC-PA-SWCNT, (b) AuCQC-PA-SWCNT-CoTAPc and (c) AuCQC-PA-SWCNT-MnTAPc. The AFM micrographs for the bare AuCQC and the Au-CQC-PA are the same as observed in Figure 4.16(a) and (b), hence not shown in this section. The surfaces were modified with PA-SWCNT forming AuCQC-PA-SWCNT and the AFM micrograph is shown in Figure 4.23(a). As can be noticed this image is different from AuCQC-PA obtained in Figure 4.16(b) above. The analysis of the surface gave the roughness factor (RF) of 3.096 nm and this value is higher than that of AuCQC (1.693 nm) and AuCQC-PA (2.584 nm), Table 4.10. This increase in roughness together with the changes in the observed morphologies, confirm the immobilization of PA-SWCNT. The AuCQC-PA-SWCNT surfaces were modified with MTAPc complexes, i.e. CoTAPc in Figure 4.23(b) and MnTAPc in Figure 4.23(c). The AuCQC-PA-SWCNT-MTAPc modified surface micrographs were different from that of AuCQC-PA-SWCNT in Figure 4.23(a). The analysis of the surfaces with MTAPc, i.e. AuCQC-PA-SWCNT-CoTAPc and AuCQC-PA-SWCNT-MnTAPc, gave the roughness factor of 3.628 nm and 4.388 nm, respectively. These roughness factor values were higher than those of AuCQC-PA-SWCNT modified surfaces (3.069 nm). The increase in surface roughness factor confirms the immobilization of MTAPc complexes. The AFM micrographs clearly showed the thick film formation after modification with PA-SWCNT-MTAPc and these surface changes are consistent with the observed SEM images in Figure 4.21(c) and (d). The vertical distance (VD) values were 17.818 for AuCQC-PA-SWCNT, 23.502 nm for AuCQC-PA-SWCNT-CoTAPc and 30.138 nm for AuCQC-PA-SWCNT-MnTAPc (Table 4.10), clearly confirming the surface modifications as proposed in Scheme 4.2. The RF and VD values exhibited an increase from AuCQC to AuCQC-PA and a further increase was observed for PA-MTAPc modified surfaces. The AuCQC-PA-CoTAPc showed high RF values when compared to AuCQC-PA-MnTAPc for surfaces without SWCNT, Table 4.10. At the SWCNT modified surfaces the RF values were higher for SPAuE-PA-SWCNT-MnTAPc compared to the SPAuE-PA-SWCNT-CoTAPc, Table 4.10. The VD values for AuCQC-PA-CoTAPc were less than that of AuCQC-PA-MnTAPc. At PA-

SWCNT modified surfaces, small RF and VD values for AuCQC-PA-SWCNT-CoTAPc were observed and cold be due to less CoTAPc molecules immobilized compared to AuCQC-PA-SWCNT-MnTAPc surfaces with high RF and VD values.

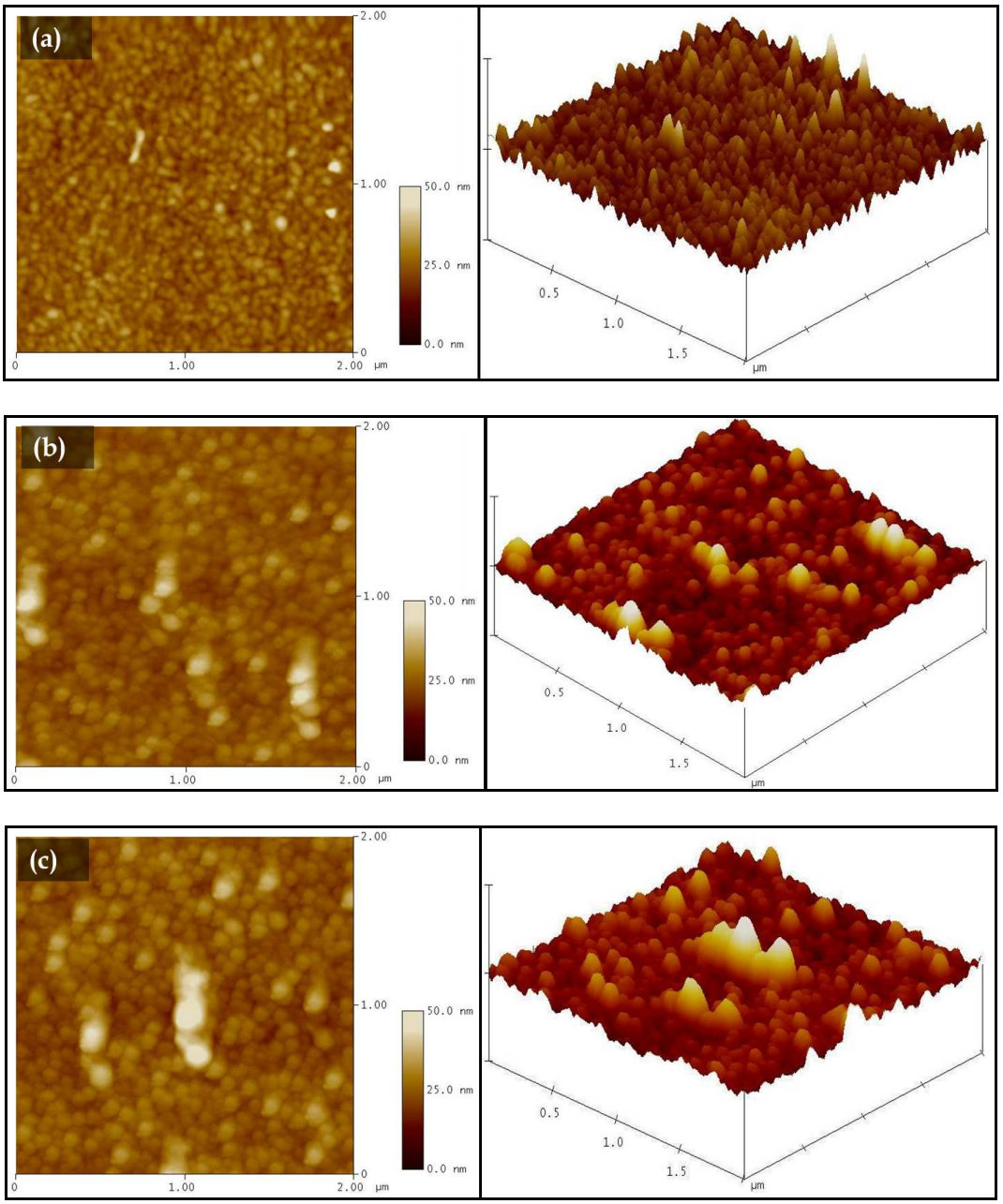

Figure 4.23: 2D and 3D AFM images for (a) AuCQC-PA-SWCNT, (b) AuCQC-PA-SWCNT-CoTAPc and (c) AuCQC-PA-SWCNT-MnTAPc surfaces.

Table 4.10: AFM analysis parameters, roughness factor (RF) and vertical distance (VD).

Electrodes	Roughness factor (RF), nm	Vertical distance (VD), nm
AuCQC	1.693	4.411
AuCQC-PA	2.584	7.916
AuCQC-PA-MnTAPc	3.497	21.659
AuCQC-PA-CoTAPc	4.951	21.061
AuCQC-PA-SWCNT	3.096	17.818
AuCQC-PA-SWCNT-MnTAPc	4.388	30.138
AuCQC-PA-SWCNT-CoTAPc	3.268	23.502

4.4.2 Spectroscopic characterization of bare and modified electrodes

4.4.2.1 Surface Raman characterization modified gold electrodes

The surface modification and covalent immobilization of PA, PA-SWCNT and MTAPc (CoTAPc and MnTAPc) complexes was further confirmed using Raman spectroscopy. Figure 4.24 shows the Raman spectra of SPAuE modified surfaces. It is discernible, from the spectra in Figure 4.24, that the surface modification indeed took place as the Raman peaks due to the immobilized materials (PA-SWCNT and MTAPc) were observed. PA-SWCNT modified surface gave Raman bands which are characteristic of SWCNT G- and D-bands, shown in Table 4.11. Further modification of the PA-SWCNT functionalized surfaces with CoTAPc and MnTAPc complexes resulted in the emergence of new multiple bands different from that of PA-SWCNT bands, Table 4.11. The new bands are typical of phthalocyanine Raman bands [236] and confirm the immobilization of the MTAPc complexes onto PA-SWCNT modified surface. The

Raman surface measurements clearly confirmed the surface modifications following the proposed method in Scheme 4.2.

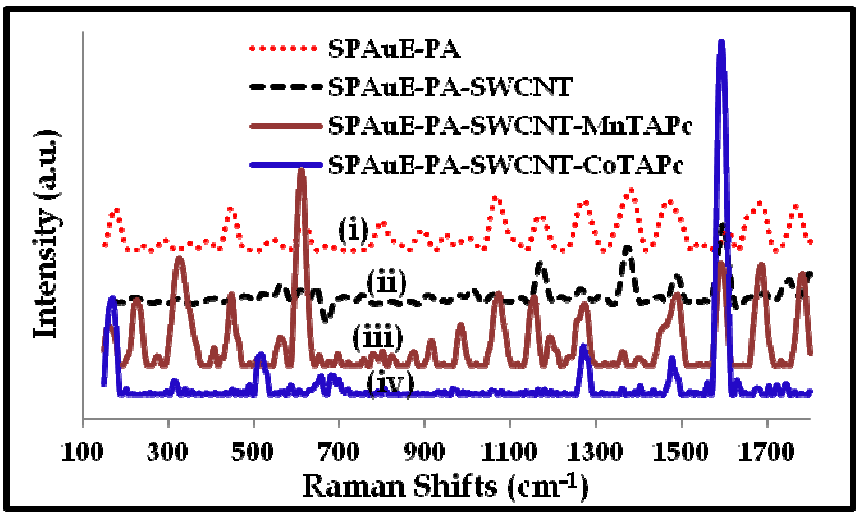

Figure 4.24: Raman spectra of gold surfaces modified (i) PA (SPAuE-PA), (ii) PA-SWCNT (SPAuE-PA-SWCNT), (iii) MnTAPc (SPAuE-PA-SWCNT-MnTAPc) and (iv) CoTAPc (SPAuE-PA-SWCNT-CoTAPc).

It was interesting to notice the presence of the Raman bands at the metallic region of the spectrum, i.e. between 100 and 500 cm^{-1}. The bands due to Au-C bending were observed at 233 cm^{-1}, 231 cm^{-1} and 318 cm^{-1} for SPAuE-PA-SWCNT, SPAuE-PA-SWCNT-MnTAPc and SPAuE-PA-SWCNT-CoTAPc, respectively. The Au-C stretching bands were observed between 450 and 620 cm^{-1} for SPAuE-PA-SWCNT-MTAPc modified surfaces. These bands at the metallic region of the spectrum for PA-SWCNT and PA-SWCNT-MTAPc shifted to slightly higher positions when compared to PA-MTAPc modified surfaces without SWCNT. At MnTAPc modified electrode surfaces, the Mn-O band was observed at 332 cm^{-1} for SPAuE-PA-MnTAPc and 341 cm^{-1} for SPAuE-PA-SWCNT-MnTAPc. The presence of Mn-O band is attributed to the presence of OH axial ligand on the (OH)MnTAPc complexes. Also a slight shift of Mn-O band was observed betweed these two surfaces. The SPAuE-PA-SWCNT-MnTAPc and SPAuE-PA-

SWCNT-CoTAPc surfaces also exhibited bands at 168 cm^{-1} and 171 cm^{-1}, respectively. These bands are attributed to the radial breathing mode (RBM) of the SWCNT [293,302,303,371,372].

Table 4.11: Raman band positions of PA-SWCNT, CoTAPc and MnTAPc immobilized onto functionalized gold surface and their interpretation.

Surface (SPAuE) Modified					Interpretation
PA-MnTAPc	PA-CoTAPc	PA-SWCNT	PA-SWCNT-MTAPc		
			MnTAPc	CoTAPc	
__	__	__	168	171	**RMB SWCNT**
222	218, 284	233	231	318	**Au-C bending**
341	__	__	332	__	**Mn-O**
454	454, 550	571, 617	451, 590	519, 588	**Au-C stretch**
612, 710	607, 658, 704	659	613	681, 688	**Ring deformation**
899, 902	__	__	920, 987	__	**Out-of-plane bending**
__	1086	1016, 1174	1074, 1150	__	**C-H bending**
1163, 1262	1194, 1269	__	1197, 1277	1273	**C-H bending**
__	__	1269	__	__	**D-band**
1381	1371	__	__	__	**C-N breathing**
__	__	1377	__	__	**C-N stretch**
1480	1487	__	__	__	**C=C pyrrole stretch**
__	__	1495	__	1479	**C=C stretch**
__	__	1600	1595	1595	**G-band**
1666, 1707,1782	1670, 1782, 1775	1755	1689	__	**C=C stretch**

4.4.2.2 XPS characterization of modified surfaces with PA-SWCNT and PA-SWCNT-MTAPc

The XPS analysis of the modified samples was also carried out to further investigate the immobilization of the PA-SWCNT and MTAPc complexes, i.e. CoTAPc and MnTAPc. The XPS measurements of modified SPAuE surfaces were performed and the spectra were similar to Figure 4.18. The survey spectra showed the presence of the peaks due to various elements such as Au, Bi, Rh, C, Ag, N and O as discussed above. The

percentage elemental composition results are summarized in Table 4.12. The increase carbon (C1s) percentage composition was observed when the electrodes are modified SPAuE-PA-SWCNT and SPAuE-PA-SWCNT-MTAPc surfaces compared to PA alone. The values for carbon (C1s) were higher than those observed for SPAuE-PA-MTAPc modified surfaces without SWCNT, Table 4.12. This increase in the carbon percentage was attributed to the presence and the modification of SPAuE surfaces with PA-SWCNT and PA-SWCNT-MTAPc (M = Co or Mn). The nitrogen (N1s) and gold (Au4f) percentages decreased from SPAuE-PA when compared to surfaces modified with PA-SWCNT and PA-SWCNT-MTAPc and this is attributed to an increase in carbon content on other materials. The results confirm the modification of electrodes.

Table 4.12: XPS experimental composition of elements found on SPAuE modified surfaces with; PA, PA-SWCNT, PA-SWCNT-MnTAPc and PA-SWCNT-CoTAPc.

Elements / Electrodes	C1s	N1s	O1s	Au4f	Bi4f	Rh4f	Ag4f
PA	34.0 %	11.5 %	33.7%	16.6%	11.5%	2.80%	1.30%
PA-SWCNT	65.1 %	3.60%	22.5 %	4.70%	2.10%	0.90%	1.10%
PA-SWCNT-MnTAPc	66.3 %	5.10%	22.0 %	3.50%	1.30%	0.60%	1.10%
PA-SWCNT-CoTAPc	63.8 %	6.20%	21.5 %	3.80%	1.80%	0.70%	2.20%
PA-MnTAPc	57.3%	2.20%	25.1%	7.80%	4.40%	1.10%	0.50%
PA-CoTAPc	61.8%	6.80%	23.6%	2.60%	2.70%	0.70%	0.20%

4.4.3 Electrochemical characterization

Figure 4.25 shows the cyclic voltammograms of (i) SPAuE-PA-SWCNT-MnTAPc and (ii) SPAuE-PA-SWCNT-CoTAPc in pH 7.4 buffer solution. The PA-SWCNT-MTAPc modified

electrodes showed the reduction peaks at -0.39 V and -0.31 V for SPAuE-PA-SWCNT-MnTAPc and SPAuE-PA-SWCNT-CoTAPc, respectively, Table 4.13.

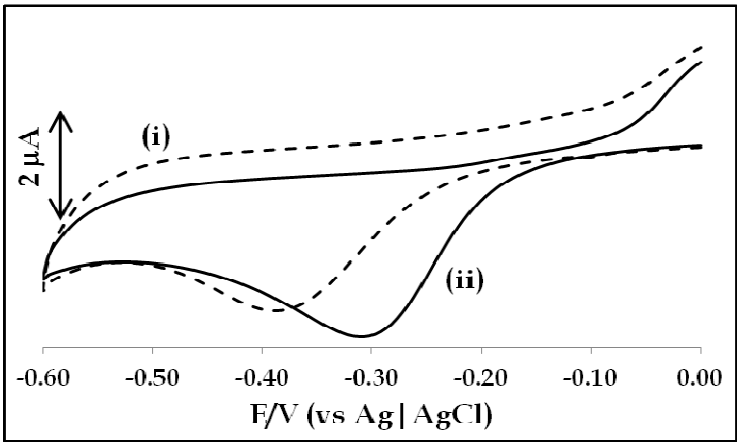

Figure 4.25: Cyclic voltammograms of (i) SPAuE-PA-SWCNT-MnTAPc and (ii) SPAuE-PA-SWCNT-CoTAPc in pH 7.4 buffer solution. Scan rate: 25 $mV.s^{-1}$.

The observed reduction peaks are due to Mn^{III}/Mn^{II} and Co^{II}/Co^{I} for SPAuE-PA-SWCNT-MnTAPc and SPAuE-PA-SWCNT-CoTAPc, respectively and are in the range observed for polyMTAPc, Table 4.13. The surface coverages or concentrations ($\Gamma_{PA\text{-}SWCNT\text{-}MTAPc}$) for modified surfaces were calculated by integrating the charge under the reduction peaks due to the metal ions using equation 4.2, using the real area of (0.0352 cm^{-2}) of the screen-printed gold electrode surface. The surface coverage values were 1.60 x 10^{-9} $mol.cm^{-2}$ for SPAuE-PA-SWCNT-MnTAPc and 2.68 x 10^{-9} $mol.cm^{-2}$ for SPAuE-PA-SWCNT-CoTAPc and were of the same order of magnitude as for Au-polyMTAPc, Table 4.13. The surface coverage values were slightly higher than the values previously reported for phthalocyanine molecules attached directly onto the PA monolayer, Table 4.13. Since the electrode surfaces used were similar, the increase in surface coverage values indicates an increase in surface area due to the immobilized PA-SWCNT allowing for more MTAPc complexes to be covalently attached onto the electrode surface.

Table 4.13: Electrochemical properties, i.e. peak potentials and surface coverages, for SPAuE-PA-SWCNT-MTAPc surfaces in pH 7.4 buffer solution or unless otherwise stated. Scan rate: 25 $mV.s^{-1}$.

Electrodes	$M_{red} = E_p$ (V)	$\Gamma_{PA\text{-}SWCNT\text{-}MTAPc}$ ($mol.cm^{-2}$)
SPAuE-PA-SWCNT-MnTAPc	-0.39	1.60×10^{-9}
SPAuE-PA-SWCNT-CoTAPc	-0.31	2.68×10^{-9}
SPAuE-PA-MnTAPc	-0.38	1.31×10^{-9}
SPAuE-PA-CoTAPc	-0.24	1.66×10^{-9}
GCE-polyCoTAPc[a]	-0.29	8.6×10^{-10}
Au-polyCoTAPc[a]	-0.42	1.3×10^{-9}
GCE-polyMnTAPc[a]	-0.43	8.2×10^{-10}
Au-polyMnTAPc[a]	-0.35	3.4×10^{-9}

- $\Gamma_{PA\text{-}SWCNT\text{-}MTAPc}$ = surface coverage for PA-MTAPc modified electrodes. [a] Surface coverage values were obtained in DMF containing 0.1 M $TBABF_4$ on glassy carbon and gold electrodes, M_{red} = metal reduction peak and E_p= peak potential.

The electrochemical properties of modified electrodes were investigated in the presence of ferricyanide $[Fe(CN)_6]^{3-/4-}$ as a redox probe in solution using cyclic voltammetry and impedance spectroscopy as discussed in the previous section. The results obtained are summarized in Table 4.14 for EIS.

Table 4.14: The summary of parameters obtained from cyclic voltammetry and electrochemical impedance spectroscopy experiments in $Fe(CN)_6^{3-/4-}$ solution. Scan rate: 25 mV.s^{-1}.

Electrodes	EIS Parameters				CV	k_{app} x 10^{-4} (cm.s^{-1})
	R_S (kΩ.cm^{-2})	R_{CT} (kΩ.cm^{-2})	n	Q (μF.cm^{-2})	ΔE (mV)	
SPAuE	4.72	1.79	0.87	56	81	1.20
SPAuE-PA	4.12	43.67	0.88	94	90	0.049
SPAuE-PA-SWCNT	5.38	3.07	0.90	31	80	0.70
SPAuE-PA-SWCNT-CoTAPc	4.52	1.76	0.87	143	80	1.22
SPAuE-PA-SWCNT-MnTAPc	4.62	0.88	0.85	85	80	2.44
SPAuE-PA-CoTAPc	4.43	9.66	0.92	22	80	0.22
SPAuE-PA-MnTAPc	4.32	9.69	0.94	22	80	0.22

The cyclic voltammetry experiments showed peak-to-peak separations (ΔE) at the bare SPAuE and SPAuE-PA surfaces that were similar to those in Figure 4.13 and as discussed in section 4.3.2 and will not be discussed further.

The R_{CT} values showed an increase at SPAuE-PA and SPAuE-PA-SWCNT compared to the bare SPAuE and a decrease at SPAuE-PA-SWCNT-MnTAPc and SPAuE-PA-SWCNT-CoTAPc surfaces. The R_{CT} value was the smallest at SPAuE-PA-SWCNT-MnTAPc compared to all other electrodes. The decreased in R_{CT} value at PA-SWCNT-MTAPc is attributed to (i) SWCNTs being a good conductor of electrons [143,357] and (ii) the combination of the two electrocatalytic materials (SWCNT and MTAPcs) having synergistic effect in terms of enhancing electron transfer to and from the electrode surface. The values of SPAuE-PA-SWCNT-MTAPc modified gold surfaces were much less than those of SPAuE-PA-MTAPc modified gold surfaces without SWCNT, Table 4.14, showing the conducting effects of SWCNT.

PA-SWCNT gave the k_{app} values of 0.70 x 10^{-4} cm.s^{-1}, Table 4.14. The increase in k_{app} value at PA-SWCNT compared to PA alone could be attributed to the SWCNT being a good conductor of electrons. SWCNT are metallic and semiconductor in their nature [293], hence the electrode sees a continuation of its metallic and semiconducting properties. The k_{app} value for PA-SWCNT being 0.70 x 10^{-4} cm.s^{-1} is still less than that of bare SPAuE (1.20 x 10^{-4} cm.s^{-1}) and this is due to the fact that SWCNTs are carbon-based materials compared to pure metal gold. There was a significant increase in the k_{app} values at SPAuE-PA-SWCNT-CoTAPc (1.22 x 10^{-4} cm.s^{-1}) and SPAuE-PA-SWCNT-MnTAPc (2.44 x 10^{-4} cm.s^{-1}) even better than that of bare SPAuE (1.20 x 10^{-4} cm.s^{-1}), Table 4.14. The observed increase in k_{app} values could be attributed to the synergistic effect of the conducting and electrocatalytic SWCNT and MTAPc hybrids. The SWCNTs clearly have additional advantages when immobilized on the electrode surface and when combined with the electrocatalytic MTAPc complexes. The combination of the two materials clearly shows an increase in the apparent electron transfer rate constants. This is also evidenced by lower k_{app} values for PA-CoTAPc and PA-MnTAPc in the absence of SWCNT, Table 4.14. The R_S (solution resistance) did not change with electrode modification. This is expected as already explained. The Q (double-layer capacitance) varied with the surface modification but there was no well-defined trend. The n values ranges from 0.85 to 0.94 and are all close to unity (= 1) indicating that the electrode behaves like a capacitor.

In conclusion, this chapter convincingly demonstrated the successful immobilization and modification of electrode surfaces following the proposed protocols. Different surface techniques were successfully employed for the electrode characterization and the methods used are cyclic voltammetry, electrochemical impedance spectroscopy, X-ray photoelectron spectroscopy, Raman spectroscopy, scanning electron microscopy and atomic force microscopy. The electrode modification were successful and the

characterization techniques were in agreement in demonstrating and showing the convincing evidence of the presence of materials as proposed.

Chapter 5:

MPc Electrocatalysts for H_2O_2 Detection

This chapter investigates the potential applications of MPc electrocatalysts immobilized onto electrode surfaces using different methods towards the detection and monitoring of H_2O_2

5 MPc ELECTROCATALYTIC STUDIES TOWARDS H_2O_2

The analytical application of the modified electrodes in electrochemical sensing of hydrogen peroxide is investigated.

5.1 MOcHexTPc SAMs

The electrocatalytic properties of MOcHexTPc (**12** - **15**) SAMs towards the detection of H_2O_2 was investigated, Figure 5.1. The cyclic voltammograms for the bulk bare gold electrode did not show any peaks within the studied potential scan range, i.e. -0.60 V and +0.60 V. The potential scan range, -0.60 V to +0.60 V used in Figure 5.1, was carefully selected to avoid the electroreductive desorption of SAMs as shown in Figure 4.3. In Figure 5.1(ii), H_2O_2 exhibited an increase in reduction currents and the peak due to H_2O_2 was observed. For CoOcHexTPc SAMs, an electrocatalytic reduction peak was observed at -0.37 V and -0.36 V for α-CoOcHexTPc (**12**-SAM) in Figure 5.1(a)(ii) and β-CoOcHexTPc (**13**-SAM) in Figure 5.1(b)(ii) complexes, respectively (Table 5.1). The metal redox processes were observed at -0.41 V in Figure 5.1 (a)(i) for α-CoOcHexTPc (**12-**SAM) and -0.43 V in Figure 5.1(b)(i) for β-CoOcHexTPc (**13-**SAM) complexes, Table 5.1. These metal redox process for CoOcHexTPc are at position for Co^{II}OcHexTPc/Co^{I}OcHexTPc metal reduction peaks. The electrocatalytic peak currents due to H_2O_2 was observed close to where these metal redox processes occur. This clearly shows that the participation of these metal redox processes from the MOcHexTPc SAMs towards H_2O_2 electrocatalytic reduction. Similar results were also obtained for the MnOcHexTPc SAMs with the H_2O_2 electrocatalytic reduction peaks observed at -0.52 V and -0.44 V for α-

MnOcHexTPc (**14**-SAM) in Figure 5.1(c)(ii) and β-MnOcHexTPc (**15**-SAM) in Figure 5.1(d)(ii) complexes, respectively, Table 5.1.

Table 5.1: Electrocatalytic and electroanalytic parameters for the determination of H_2O_2 at SAMs modified gold electrodes with complexes **12 - 15** in pH 7.4. Scan rate: 25 $mV.s^{-1}$.

SAMs of (12-15)	E_p H_2O_2 (V)	$E_{1/2}$ M_{red} (V)	Γ_{SAM} x 10^{-10} ($mol.cm^{-2}$)	LoD (10^{-7} M)	LCR (μM)	Sensitivity ($mA.mM^{-1}.cm^{-2}$)
12-SAM	-0.37	-0.41	1.12	7.5	9.90 -74.07	0.118
13-SAM	-0.36	-0.43	4.90	4.3	9.90 -74.07	0.068
14-SAM	-0.52	-0.31	0.77	1.0	9.90 -74.07	0.262
15-SAM	-0.44	-0.42	1.74	2.4	9.90 -74.07	0.078

E_p = peak potential, $E_{½}$ = half-wave potential, LoD = Limit of detection, $M_{red.}$ = metal reduction couple, Γ_{SAM} = surface coverage and LCR = Linear concentration range. Darker highlighted columns for data obtained from the CV.

The metal redox processes for these complexes were observed at -0.31 V for α-MnOcHexTPc (**14**-SAM) in Figure 5.1(c)(i) and -0.42 V for β-MnOcHexTPc (**15**-SAM) in Figure 5.1(d)(i) (Table 5.1). These metal redox process for the MnOcHexTPc complexes are at the position for Mn^{III}OcHexTPc /Mn^{II}OcHexTPc reduction peaks. This redox process is therefore involved in the electrocatalytic reduction of H_2O_2. It is of interest to note that the electroreduction peak of H_2O_2 at MOcHexTPc modified electrodes occur at potentials similar to those of oxygen electroreduction by MPc compounds [373]. However, the elimination of oxygen interference was accomplished by purging the solution thoroughly with argon and the electrochemical cell was kept under argon atmosphere. The electrocatalytic reduction peak for H_2O_2 occurred at potentials that are similar to those observed on other MPcs modified surfaces [140]. For **12**-SAM, the electrocatalytic oxidation peak was observed at +0.54 V due to H_2O_2 oxidation and similar to the reported results [276,

279,280]. However, only **12**-SAM displayed an increase in the H_2O_2 electrocatalytic oxidation and this could be attributed to lowering of the metal oxidation process to less positive values due to the position of the substituents, i.e. non-peripheral position.

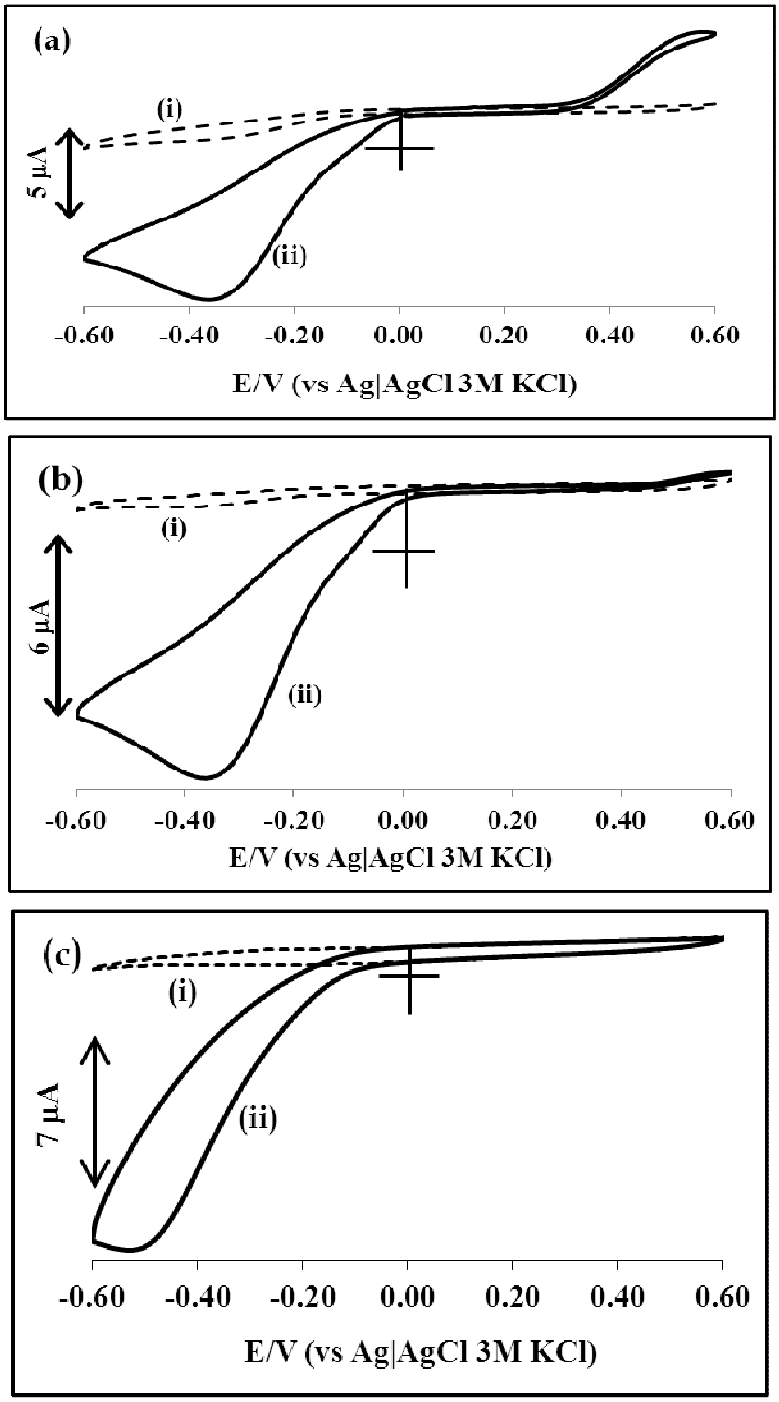
(a)
(i)
5 µA
(ii)
-0.60 -0.40 -0.20 0.00 0.20 0.40 0.60
E/V (vs Ag|AgCl 3M KCl)
(b)
(i)
6 µA
(ii)
-0.60 -0.40 -0.20 0.00 0.20 0.40 0.60
E/V (vs Ag|AgCl 3M KCl)
(c)
(i)
7 µA
(ii)
-0.60 -0.40 -0.20 0.00 0.20 0.40 0.60
E/V (vs Ag|AgCl 3M KCl)

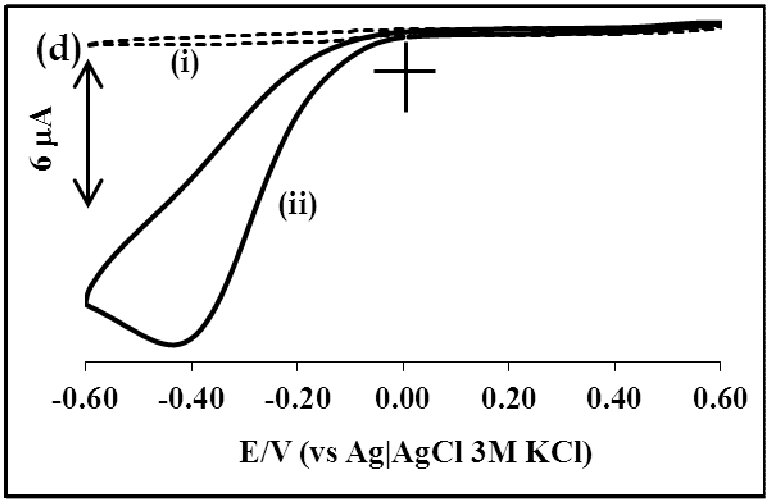

Figure 5.1: Cyclic voltammograms of the MOcHexTPc SAMs in the (i) absence and (ii) presence of 1.0 mM H_2O_2 at (a) **12**-SAM, (b) **13**-SAM, (c) **14**-SAM and (d) **15**-SAM in pH 7.4 buffer solution. Scan rate: 25 $mV.s^{-1}$.

The MOcHexTPc SAMs modified electrodes were reproducible and the catalytic currents due to H_2O_2 were stable when these electrodes were cycled for about 10 cycles in pH 7.4 buffer solution containing 1.0 mM H_2O_2 (using **12**-SAM and **15**-SAM, as an example), Figure 5.2. The **15**-SAM modified electrode did not loose the electrocatalytic current at all and the **12**-SAM only loosing 5% of the catalytic current after 7 scans. The current loss was only up to 10% for the **14**-SAM and 5% for **13**-SAM modified electrodes. The regeneration of these electrodes for electrocatalysis was achieved by firstly cycling in the freshly prepared pH 7.4 buffer solutions before analysis.

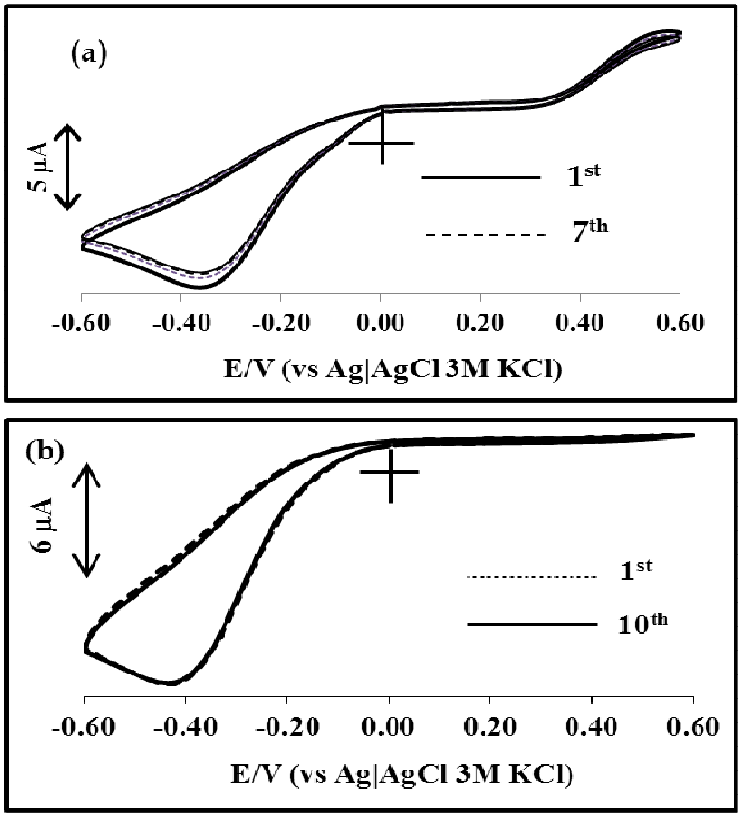

Figure 5.2: Cyclic voltammograms showing the electrocatalytic current stability at (a) **12**-SAM after 7 scans and (b) **15**-SAM modified gold electrode after 10 scans. [H_2O_2]= 1.0 mM. Scan rate: 25 mV.s^{-1}.

The analysis of H_2O_2 was accomplished using chronoamperommetry and the applied potentials was at -0.37V for **12**-SAM, -0.36V for **13**-SAM, -0.52V for **14**-SAM and -0.44V for **15**-SAM. Figure 5.3 shows (a) chronoamperommogram of **15**-SAM (as an example) during the addition of H_2O_2 (indicated by arrows) and (b) the corresponding calibration curves for **15**-SAM. The chronoamperomograms of other MOcHexTPc SAM modified electrodes displayed similar trends, i.e. the current increased with the increasing H_2O_2 concentrations. The current response of H_2O_2 increased linearly with the increasing concentration of H_2O_2 within the range investigated, i.e. 9.9 – 74.0 µM. The limit of detection (LoD) obtained using signal-to-noise ratio of 3 for the SAMs modified electrodes were ranged between 1.0 – 7.5 x 10^{-7}

M and comparable or even smaller when compared to other MPc modified electrodes [140,143,279] which were of the order of 10^{-7} M but these LoD values were less than values reported for HRP enzyme-based sensors [264,265]. The SAMs modified electrodes gave a good sensitivity ranging from 0.068 – 0.262 $mA.mM^{-1}.cm^{-2}$, Table 5.1. The sensitivities for the SAMs of complexes (**12** and **14**), were higher than those of SAMs formed by complexes (**13** and **15**). The reason for the observed better sensitivity on SAMs of complexes **12** and **14** could be attributed to the position of the substituents, i.e. the non-peripherally substitution for complex **12** and **14** compared to peripherally substituted complexes **13** and **15**. The LCR (linear concentration range) of 9.9 - 74.0 µM was obtained for the MOcHexTPc SAMs modified electrode surfaces. The proposed mechanism of H_2O_2 electrocatalytic reduction by MOcHexPc SAM modified gold electrode surfaces is summarized in equations 5.1 and 5.2 for MnOcHexTPc and equations 5.3 and 5.4 for CoOcHexTPc.

$$Mn^{III}OcHexTPc + e^- \longrightarrow [Mn^{II}OcHexTPc]^- \quad (5.1)$$

$$[Mn^{II}OcHexTPc]^- + \tfrac{1}{2}H_2O_2 + H^+ \rightarrow Mn^{III}OcHexTPc + H_2O \quad (5.2)$$

$$Co^{II}OcHexTPc + e^- \longrightarrow [Co^{I}OcHexTPc]^- \quad (5.3)$$

$$[Co^{I}OcHexTPc]^- + \tfrac{1}{2}H_2O_2 + H^+ \rightarrow Co^{II}OcHexTPc + H_2O \quad (5.4)$$

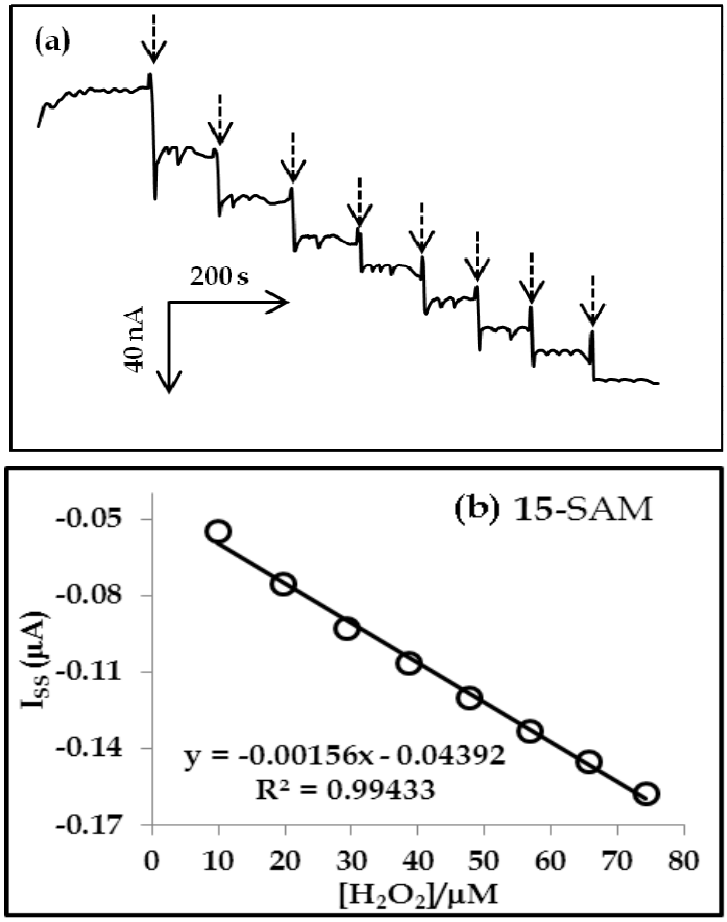

Figure 5.3: (a) Steady-state amperometric response and (b) the calibration curve of β-MnOcHexTPc (**15**) SAM during the additions of H_2O_2. [H_2O_2] ranged from 9.9 to 74.0 µM.

The selectivity studies of MOcHexTPc SAMs modified electrodes were conducted. These experiments are important in studying the ability of the design system to discriminate between the interfering species commonly present in similar physiological environment with the target analyte. The effect of the common electroactive interferents such as glucose, uric acid, ethanol and ascorbic acid to the response of H_2O_2 were investigated using the mixed solution method [374]. Chrono-amperommetry in 0.1 mM H_2O_2 alone and in the mixed solution of 0.1 mM H_2O_2 and 1 mM interfering substances were measured (data not shown), but similar to Figure 5.3(a).

The degree to which these species interfere with the electrocatalytic signal due to H_2O_2 was further evaluated using the amperometric selectivity coefficients (K_{amp}) values which were determined using equation 5.5 [374].

$$K_{amp} = \left(\frac{\Delta I_{mixture}}{\Delta I_{hydrogen\ .peroxide}} - 1 \right) \frac{[hydrogen\ \ peroxide\ ]}{[int\ erferent\ ]} \qquad (5.5)$$

where $\Delta I_{mixture}$ and $\Delta I_{hydrogen\ peroxide}$ are the background corrected current responses of hydrogen peroxide in the presence and absence of an interferent, respectively. K_{amp} values of the orders of magnitude higher than 10^{-3} denotes strong interferent, while values close to 10^{-3} indicates weak interferent and values less than 10^{-3} suggests no interference. Values of K_{amp}, obtained for the interferents at different SAMs modified electrodes showed that the majority of the studied species interfere with the electrocatalytic signal due to H_2O_2 and the K_{amp} values were either of the orders of 10^{-3} and higher, Table 5.2. The **12**-SAM modified electrodes gave K_{amp} values of 10^{-2} for ascorbic acid as a strong interferent and 10^{-3} for glucose, uric acid and ethanol acid indicating that these are weak interferents. The SAM of complex **13** only showed weak interferent by ascorbic acid and all other species (glucose, uric acid and ethanol) strongly interfered, Table 5.2. For **14**-SAM only uric acid showed weak interferent and other species strongly intefered with the electrocatalytic signal of H_2O_2. The SAM of complex **15** for all studied species exhibited strong interferent with K_{amp} values of 10^{-2} except for ethanol which showed weak interferent (10^{-3}). There was no observable trend of the interfering species as these were different at each electrode. The studied interfering species are all high molecular weight compounds than H_2O_2 and the use of membranes, either ion or size exclusion membranes, will improve the selectivity of the electrodes towards the H_2O_2 detection.

Table 5.2: Amperometric coefficients of SAMs of complexes **12** to **15** in solutions containing 0.1 mM hydrogen peroxide and interferents concentrations were 1 mM.

SAMs of complexes (12 -15)	K_{amp}			
	glucose	**Uric acid**	**Ethanol**	**Ascorbic acid**
12-SAM	1.95×10^{-3}	4.88×10^{-3}	2.44×10^{-3}	2.38×10^{-2}
13-SAM	5.90×10^{-2}	1.90×10^{-2}	6.90×10^{-2}	1.00×10^{-3}
14-SAM	1.67×10^{-2}	5.56×10^{-3}	1.67×10^{-2}	1.67×10^{-2}
15-SAM	1.85×10^{-2}	1.85×10^{-2}	7.31×10^{-3}	6.30×10^{-2}

5.2 Electrocatalytic and electroanalysis of H_2O_2 at polymer electrodes

Figure 5.4 shows the response of polymer modified electrodes (a) Au-polyCoTAPc, (b) GCE-polyCoTAPc, (c) Au-polyMnTAPc and (d) GCE-polyMnTAPc in the (i) absence and (ii) presence of 0.1 mM H_2O_2 in phosphate buffer solution (pH 7.4). The blank pH 7.4 solutions, Figure 5.4(curves, i) showed the irreversible metal reduction (M_{red} $E_{1/2}$, V), processes with values listed in Table 5.3 also in Table 4.2. The electrocatalytic peaks for the reduction of H_2O_2 were observed, in Figure 5.4(ii) at potentials close to where the metal reduction redox processes occur for all the polymer modified electrodes in pH 7.4. Therefore, these redox couples mediate the electrocatalytic reduction of H_2O_2. Similar peak shapes for the electrocatalytic reduction of H_2O_2 on polyMTAPc modified Au and GCE in Figure 5.4, were observed but they appeared at slightly different potentials, Table 5.3. For both complexes, the GCE polymer modified electrodes gave higher catalytic current densities compared to their Au counterparts for the same H_2O_2 concentrations. Even though the GCE-polyMTAPc electrodes gave a lower surface coverages Table 5.3,

they exhibited an enhanced catalytic currents towards hydrogen peroxide compared to Au-polyMTAPc. The order of enhancement of hydrogen peroxide catalytic currents by MTAPc complexes is as follows: GCE-polyCoTAPc = GCE-polyMnTAPc > Au-polyCoTAPc > Au-polyMnTAPc. In terms of surface coverage values, in Table 5.3, the opposite was obtained, i.e. Au-polyMnTAPc > Au-polyCoTAPc > GCE-polyCoTAPc ≥ GCE-polyMnTAPc and this is attributed to the fact that only the outer layer is involved in the electrocatalysis.

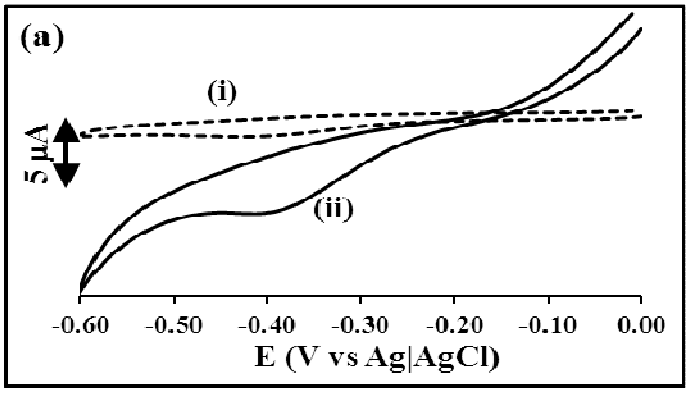
(a)
(i)
5 µA
(ii)
-0.60 -0.50 -0.40 -0.30 -0.20 -0.10 0.00
E (V vs Ag|AgCl)

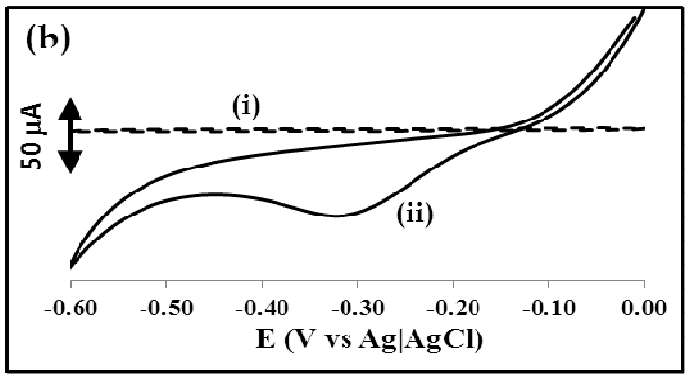
(b)
50 µA
(i)
(ii)
-0.60 -0.50 -0.40 -0.30 -0.20 -0.10 0.00
E (V vs Ag|AgCl)

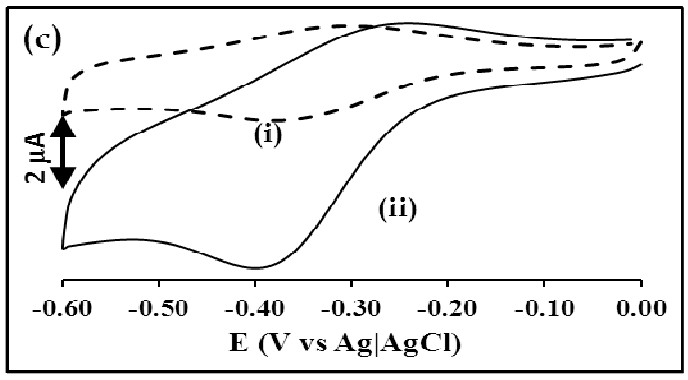
(c)
2 µA
(i)
(ii)
-0.60 -0.50 -0.40 -0.30 -0.20 -0.10 0.00
E (V vs Ag|AgCl)

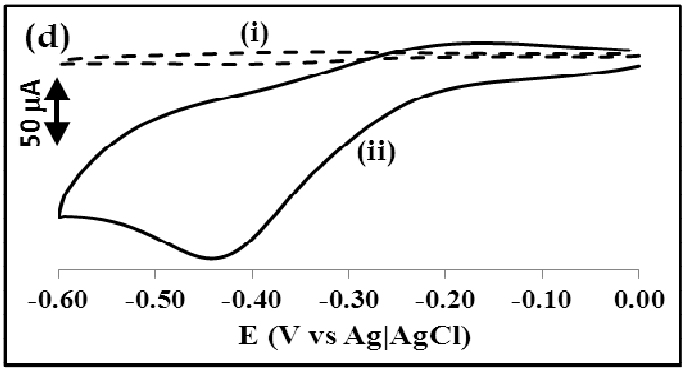

Figure 5.4: CVs of (a) Au-polyCoTAPc, (b) GCE-polyCoTAPc, (c) Au-polyMnTAPc and (d) GCE-polyMnTAPc modified electrode (i) without H_2O_2 and (ii) with 0.1 mM H_2O_2 in pH 7.4. Scan rate: 25 $mV.s^{-1}$.

Chronoamperomograms of polymer modified electrodes exhibited an increase in reduction currents with the increasing H_2O_2 concentrations similar to Figure 5.3 and linearity was observed using the applied potentials on each sensor for electroreduction of H_2O_2 from Table 5.3.

The linear variation of the electrocatalytic current plateaus (steady-state currents) with H_2O_2 concentrations was observed in the range of 0.99 – 8.26 µM for Au and 0.50 - 4.46 µM for GCE polymer modified electrodes, Table 5.3. The calculated sensitivities of the sensors (obtained from the slopes of the linear plots) ranged from 6.00 – 15.40 $mA.mM^{-1}.cm^{-2}$, Table 5.3. GCE-polyMTAPc modified electrodes gave better sensitivities compared to Au-polyMTAPc modified electrodes. The limits of detection (LoD) based on a signal-to-noise ratio of 3 were of the order of 10^{-7} M, Table 5.3. The LoD values became lower (more favorable) with the following trend for polyMTAPc modified electrodes: Au-polyCoTAPc (0.364 µM) > Au-polyMnTAPc (0.277 µM) > GCE-polyCoTAPc (0.145 µM) > GCE-polyMnTAPc (0.106 µM). Thus the LoDs are lower for GCE-polyMTAPc electrodes than for Au-polyMTAPc electrodes. The obtained parameters for the detection of H_2O_2 at polyMTAPc modified electrode surface in terms of LoD were within the same order of magnitudes as the values

obtained when the MOcHexTPc SAMs are employed, Tables 5.1 and 5.3. However, the polyMTAPc modified electrodes gave high sensitivity than the MOcHexTPc SAMs modified electrodes. Other parameters were similar, especially the potentials at which the electrocatalytic peak reduction and metal reduction were at similar potential values.

Table 5.3: Electrocatalytic and electroanalytic parameters for the determination of H_2O_2 at polyMTAPc thin film modified gold and glassy carbon electrodes, pH 7.4. Scan rate: 25 $mV.s^{-1}$.

Electrodes	E_p H_2O_2 (V)	M_{red} E_p (V)	I ($\mu A.cm^{-2}$)	LoD (10^{-7} M)	LCR (μM)	Sensitivity ($mA.mM^{-1}.cm^{-2}$)	Γ x 10^{-10} ($mol.cm^{-2}$)
Au-polyCoTAPc	-0.41	-0.42	249	3.64	0.99 – 8.26	6.00	13.0
GCE-polyCoTAPc	-0.32	-0.29	707	1.45	0.50 – 4.46	15.40	8.60
Au-polyMnTAPc	-0.40	-0.35	99	2.77	0.99 – 8.26	6.90	34.0
GCE-polyMnTAPc	-0.42	-0.43	707	1.06	0.50 – 3.85	7.40	8.2
12-SAM	-0.37	-0.41	__	7.50	9.90 – 74.07	0.12	1.12
13-SAM	-0.36	-0.43	__	4.30	9.90 – 74.07	0.068	4.90
14-SAM	-0.52	-0.31	__	1.00	9.90 – 74.07	0.26	0.77
15-SAM	-0.44	-0.42	__	2.40	9.90 – 74.07	0.078	1.74

E_p = peak potential, $E_{½}$ = half-wave potential, LoD = Limit of detection, $M_{red.}$ = metal reduction couple, Γ = surface coverage, I = current densities and LCR = Linear concentration range. Darker highlighted columns for data obtained from the CV.

The reproducibility and stability studies for the polyMTAPc modified electrodes surfaces were also conducted. The stability studies of the polyMTAPc modified electrode surfaces confirmed the presence of the conducting polymer even after long time (5 weeks) of storage in the dark. The catalytic activity was observed to decrease

by less than 10% after a day of storage and this value remained the same for five weeks of storage in pH 7.4 buffer solution in the dark. The modified electrodes could be regenerated by rinsing and subjecting them to repetitive cycling (20 scans) in freshly prepared pH 7.4 buffer solution within the potential range between 0 to -0.6V). The results obtained for these electrode systems show that these sensors can potentially be used for the determination and monitoring of H_2O_2. The mechanism for the reduction of H_2O_2 on polyMTAPc modified Au and GCE surfaces is the same as equations 5.1 to 5.4 for MnTAPc and CoTAPc complexes.

5.3 Electrocatalysis and electroanalysis of H_2O_2 at SPAuE-PA-MTAPc electrodes

The electrocatalytic properties of the PA-MTAPc modified screen-printed gold electrode surfaces were investigated for the detection of H_2O_2 in physiological conditions, Figure 5.5. Clearly there was no peak at the bare SPAuE surface in Figure 5.5(a)(i) and after modifying with PA monolayer in Figure 5.5(a)(ii) in the presence of 1.0 mM H_2O_2 in pH 7.4 phosphate buffer solution. The electrocatalytic behaviour was observed for MTAPc modified electrode surfaces. Figure 5.5 shows the cyclic voltammograms for (b) SPAuE-PA-MnTAPc and (c) SPAuE-PA-CoTAPc in the (i) absence and (ii) presence of 1.0 mM H_2O_2 in pH 7.4 phosphate buffer soltution. In the absence of H_2O_2, the metal reduction peaks were observed at -0.24 V (Co^{II}/Co^{I}) for SPAuE-PA-CoTAPc and at -0.30 V (Mn^{III}/Mn^{II}) for SPAuE-PA-MnTAPc electrodes, Table 5.4.

The electrocatalytic peaks due the reduction of H_2O_2 occurred at potentials close to where the metal reduction peaks were observed for all the modified electrodes in pH 7.4. The MTAPc modified electrodes exhibited much higher currents in pH 7.4 phosphate buffer solution containing 1.0 mM H_2O_2 and peaked at about -0.31 V and -0.28 V for SPAuE-PA-CoTAPc and SPAuE-PA-MnTAPc electrodes, respectively. These electroreduction peaks due to H_2O_2 occurred at potentials which were less negative compared to the electrode modified with polymers of these complexes, in Figure 5.4, Table 5.3 which were observed at -0.41 V and -0.40 V for Au-polyCoTAPc and Au-polyMnTAPc, respectively. The appearance of the H_2O_2 electrocatalytic reduction peaks close to the observed metal reduction peaks clearly indicates the involvement of the metal ion in the electrocatalytic process. This observation is also similar to the results obtained for SAM in Figure 5.1. Therefore, the metal ions mediate the electrocatalytic reduction of H_2O_2. The use of screen printed electrodes in this work clearly shows the potential of miniaturizing these systems for field-test applications.

Table 5.4: Electroanalytical properties of electrodes modified with PA-MTAPc in varied concentrations of H_2O_2 and at different electrocatalytic peak potentials. Scan rate: 25 $mV.s^{-1}$.

Electrodes	E_p, H_2O_2 (V)	M_{red}, $E_{½}$ (V)	I ($\mu A.cm^{-2}$)	LoD (10^{-7} M)	LCR (μM)	Sensitivity ($mA.mM^{-1}.cm^{-2}$)	$\Gamma \times 10^{-10}$ ($mol.cm^{-2}$)
SPAuE-PA-CoTAPc	-0.31	-0.24	707	5.82	1.0 – 30.0	0.19	16.6
SPAuE-PA-MnTAPc	-0.28	-0.30	726	1.17	1.0 – 30.0	0.15	13.1
Au-polyCoTAPc	-0.41	-0.42	249	3.64	0.99 – 8.26	6.00	13.0
GCE-polyCoTAPc	-0.32	-0.29	707	1.45	0.50 – 4.46	15.40	8.60
Au-polyMnTAPc	-0.40	-0.35	99	2.77	0.99 – 8.26	6.90	34.0
GCE-polyMnTAPc	-0.42	-0.43	707	1.06	0.50 – 3.85	7.40	8.2
12-SAM	-0.37	-0.41	__	7.50	9.90 – 74.07	0.12	1.12
13-SAM	-0.36	-0.43	__	4.30	9.90 – 74.07	0.068	4.90
14-SAM	-0.52	-0.31	__	1.00	9.90 – 74.07	0.26	0.77
15-SAM	-0.44	-0.42	__	2.40	9.90 – 74.07	0.078	1.74

E_p = peak potential, $E_{½}$ = half-wave potential, LoD = Limit of detection, $M_{red.}$ = metal reduction couple, Γ = surface coverage, I = current densities and LCR = Linear concentration range. Darker highlighted columns for data obtained from the CV.

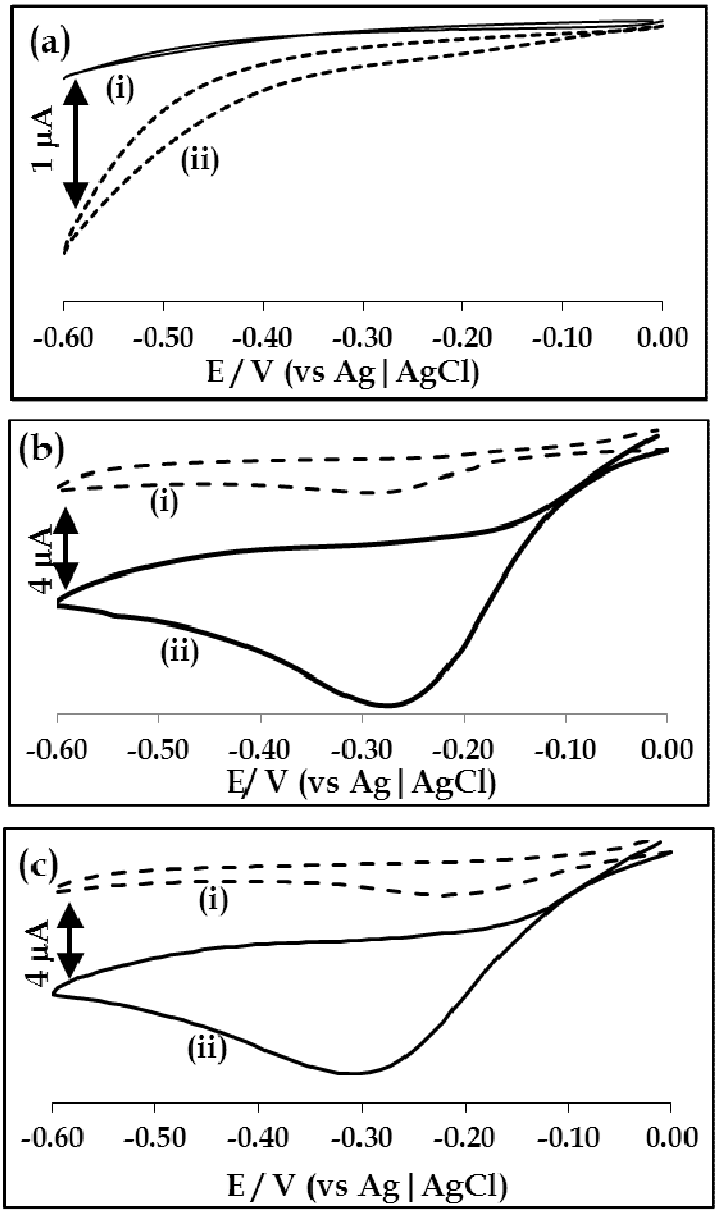

Figure 5.5: Cyclic voltammograms of (a) (i) bare and (ii) SPAuE-PA monolayer modified in 1.0 mM H_2O_2 PBS (pH 7.4) solution; (b) SPAuE-PA-MnTAPc and (c) SPAuE-PA-CoTAPc electrodes in pH 7.4 PBS solution (i) without and (ii) with 1.0 mM H_2O_2. Scan rate: 25 $mV.s^{-1}$.

The mechanism involved in the electrocatalytic reduction of H_2O_2 is simply illustrated as shown in Figure 5.6. For SPAuE-PA-CoTAPc and SPAuE-PA-MnTAPc monolayer modified electrodes, the metal reduction processes Co^{II}/Co^{I} and Mn^{III}/Mn^{II}, respectively, are involved in the electrocatalytic reduction processes.

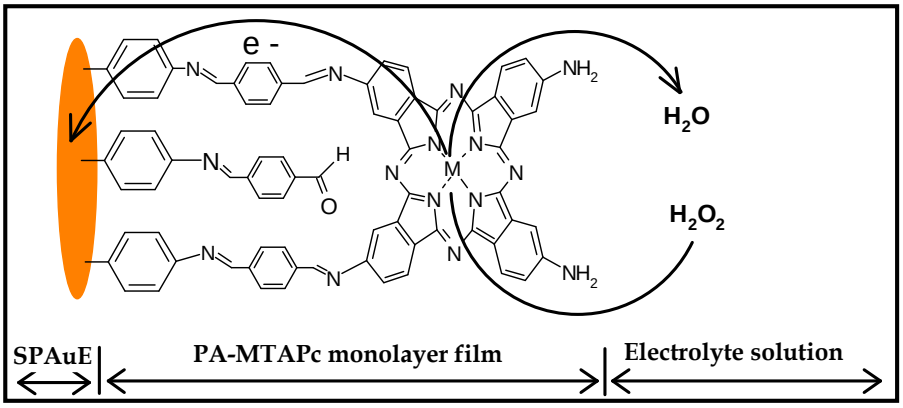

Figure 5.6: Illustration of the proposed electrocatalytic reduction of H_2O_2 at SPAuE-PA-**M**TAPc, **M** = **Co** (CoTAPc) or **Mn** (MnTAPc) monolayer modified surfaces.

The electroanalytical properties of SPAuE-PA-MTAPc modified electrode surfaces were studied using chronoamperometry method, Figure 5.7. The amperometric response at SPAuE-PA-MnTAPc modified electrode was similar to that of SPAuE-PA-CoTAPc electrode in Figure 5.7(a), hence only the SPAuE-PA-CoTAPc shown. The applied potential of -0.31 V for the amperometric measurement, in Figure 5.7(a) were obtained from Table 5.4. The increasing concentration of H_2O_2 resulted in a negative increase in the steady-state currents as observed in Figure 5.7(a) for SPAuE-PA-CoTAPc electrode. Figure 5.7(b) shows a linear relationship between the steady-state currents (I_{SS}) vs concentration of H_2O_2 ($[H_2O_2]$). The limits of detection (LoD) for the studied SPAuE-PA-MTAPc modified surfaces were of the orders of 10^{-7} M using the 3δ notion, Table 5.4. The studied SPAuE-PA-MTAPc electrodes gave a good linear relationship for the studied concentration ranging from 1.0 – 30.0 µM. The sensitivity of the electrodes studied were 0.15 and 0.19 $mA.mM^{-1}.cm^{-2}$ for SPAuE-PA-MnTAPc and SPAuE-PA-CoTAPc modified electrodes, respectively. The sensitivity values were similar to those of electrodes modified with MOcHexTPc SAM in Table 5.4 and much less than the electrodes modified with polyMTAPc in Table 5.4.

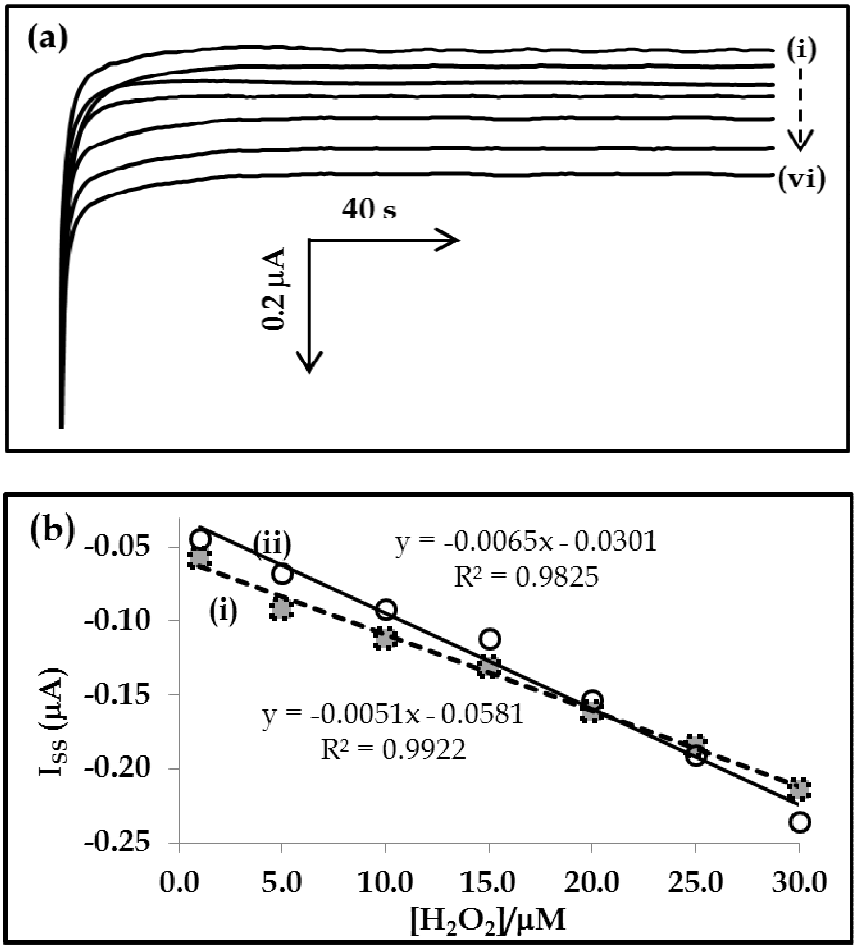

Figure 5.7: (a) amperometric response at SPAuE-PA-CoTAPc and (b) calibration curves for steady-state currents at varied concentrations ranging from 1.0 – 30 µM at (i) SPAuE-PA-CoTAPc and (ii) SPAuE-PA-MnTAPc modified electrode surfaces.

The electrodes were further studied for their reproducibility and three screen-printed gold electrodes for each complex were modified following the method shown in Scheme 4.1, Figure 5.8 (each done in triplicates). The electrocatalytic peaks in Figure 5.8 were observed at potentials close to where the original peak potentials in Figure 5.5 occurred. At SPAuE-PA-MnTAPc modified electrodes, in Figure 5.8(a), the H_2O_2 peak potential shifted slightly from -0.27 V to -0.32 V with similar current densities. At SPAuE-PA-CoTAPc modified electrodes, in Figure 5.8(b), the H_2O_2 peak potentials and current densities varied slightly with the potentials changing from -

0.27 V to -0.29 V. These results clearly shows that the different electrodes modified using the reported method are reproducible and gave very similar results. The surface coverages estimated from the different electrodes measured in phosphate buffer solution (pH 7.4) were also similar with slight deviation and were found to be $1.31 \pm 0.86 \times 10^{-9}$ mol.cm^{-2} and $1.66 \pm 0.52 \times 10^{-9}$ mol.cm^{-2} for SPAuE-PA-MnTAPc and SPAuE-PA-CoTAPc, respectively. The long term use of these electrodes was also investigated and the surfaces can be regenerated by cycling in phosphate buffer solution (pH 7.4). The regenerated MTAPc modified electrodes gave good catalytic currents of about 87% for SPAuE-PA-CoTAPc and 85% for SPAuE-PA-MnTAPc after three weeks of storage.

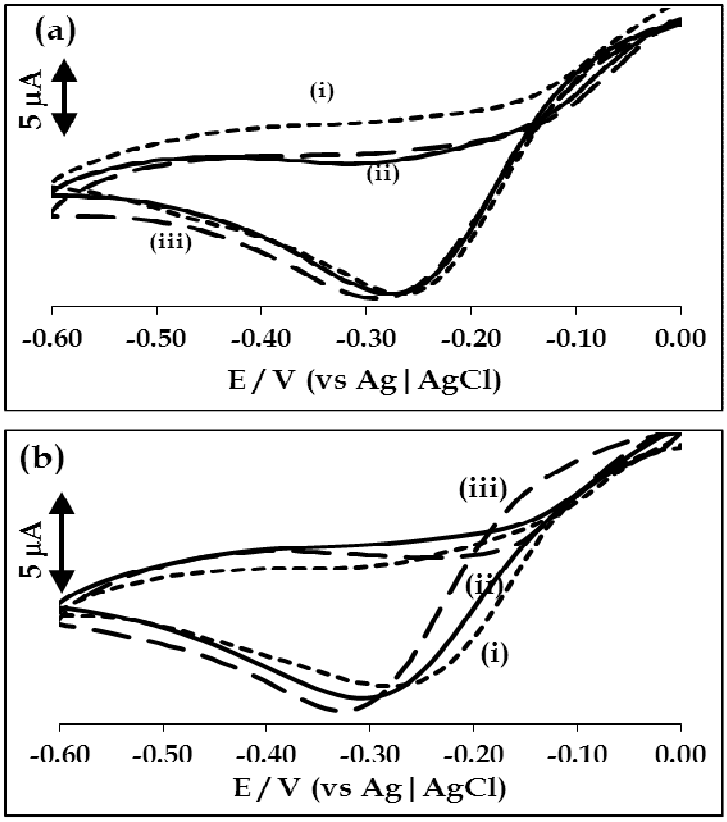

Figure 5.8: Cyclic voltammograms of 1.0 mM H_2O_2 in phosphate buffer solution (pH 7.4) recorded on three different modified electrodes with (a) SPAuE-PA-MnTAPc and (b) SPAuE-PA-CoTAPc. Scan rate: 25 mV.s^{-1}.

5.4 Electrocatalysis and electroanalysis of H_2O_2 at SPAuE-PA-SWCNT-MTAPc

The electrocatalytic properties of the PA-SWCNT and MTAPc hybrid modified screen-printed gold electrodes were investigated for the detection of H_2O_2 in physiological conditions (pH 7.4), Figure 5.9.

At SPAuE and SPAuE-PA modified electrode surfaces in Figure 5.9(a), there was no well-defined electrocatalytic peak observed due to H_2O_2 electrocatalysis only the increase in currents was observed as stated above. The SPAuE-PA-SWCNT electrode surface showed further increase in currents confirming conducting properties of SWCNT. In Figure 5.9(b)(i) and (c)(i) pH 7.4 buffer alone, the PA-SWCNT-MTAPc modified electrodes showed the reduction peaks at -0.39 V and -0.31 V for SPAuE-PA-SWCNT-MnTAPc and SPAuE-PA-SWCNT-CoTAPc, respectively. The observed reduction peaks are due to Mn^{III}/Mn^{II} and Co^{II}/Co^{I} for SPAuE-PA-SWCNT-MnTAPc and SPAuE-PA-SWCNT-CoTAPc, respectively. When compared to the surface without PA-SWCNT, the metal reduction peak potentials moved to more negative potential values, Table 5.4.

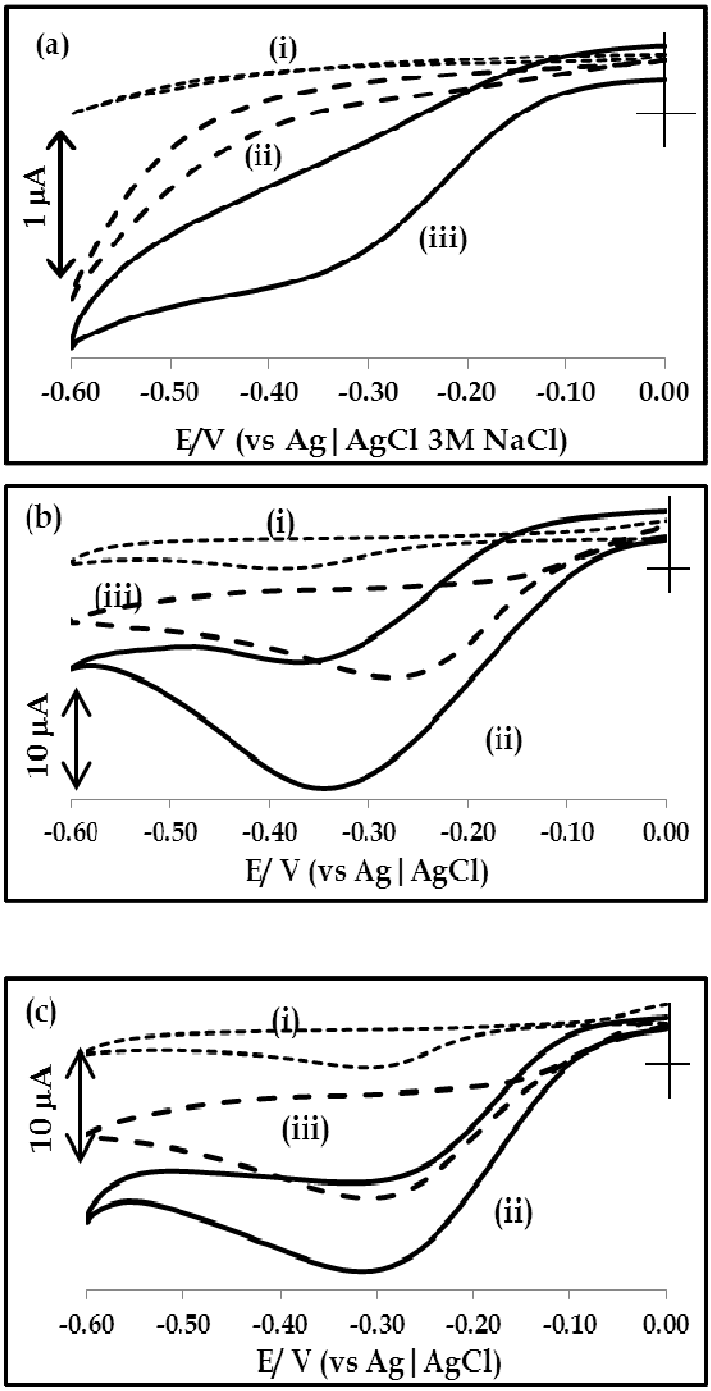

Figure 5.9: Cyclic voltammograms of (a) 1.0 mM H_2O_2 in pH 7.4 for (i) SPAuE, (ii) SPAuE-PA and (iii) SPAuE-PA-SWCNT; (b) SPAuE-PA-SWCNT-MnTAPc in (i) pH 7.4 and in (ii) 1.0 mM H_2O_2 and (iii) SPAuE-PA-MnTAPc in 1.0 mM H_2O_2; and (c) SPAuE-PA-SWCNT-CoTAPc in (i) pH 7.4 and (ii) 1.0 mM H_2O_2 and (iii) SPAuE-PA-CoTAPc in 1.0 mM H_2O_2. Scan rate: 25 $mV.s^{-1}$.

Table 5.5: Electroanalytical properties of electrodes modified with PA-MTAPc in varied concentrations of H_2O_2 and at different electrocatalytic peak potentials. Scan rate: 25 mV.s^{-1}.

Electrodes	E_p, H_2O_2 (V)	M_{red}, $E_{½}$ (V)	I (mA.cm^{-2})	LoD (10^{-7} M)	LCR (μM)	Sensitivity (mA.mM^{-1}.cm^{-2})	Γ x 10^{-10} (mol.cm^{-2})
SPAuE-PA-SWCNT-CoTAPc	-0.30	-0.31	1.290	6.34	1.0 – 30.0	5.16	16.0
SPAuE-PA-SWCNT-MnTAPc	-0.38	-0.39	1.070	4.42	1.0 – 30.0	2.79	26.8
SPAuE-PA-CoTAPc	-0.31	-0.24	0.707	5.82	1.0 – 30.0	0.19	16.6
SPAuE-PA-MnTAPc	-0.28	-0.30	0.726	1.17	1.0 – 30.0	0.15	13.1
Au-polyCoTAPc	-0.41	-0.42	0.249	3.64	0.99 – 8.26	6.00	13.0
GCE-polyCoTAPc	-0.32	-0.29	0.707	1.45	0.50 – 4.46	15.40	8.60
Au-polyMnTAPc	-0.40	-0.35	0.099	2.77	0.99 – 8.26	6.90	34.0
GCE-polyMnTAPc	-0.42	-0.43	0.707	1.06	0.50 – 3.85	7.40	8.2
12-SAM	-0.37	-0.41	__	7.50	9.90 – 74.07	0.12	1.12
13-SAM	-0.36	-0.43	__	4.30	9.90 – 74.07	0.068	4.90
14-SAM	-0.52	-0.31	__	1.00	9.90 – 74.07	0.26	0.77
15-SAM	-0.44	-0.42	__	2.40	9.90 – 74.07	0.078	1.74

E_p = peak potential, $E_{½}$ = half-wave potential, LoD = Limit of detection, $M_{red.}$ = metal reduction couple, Γ = surface coverage, I = current densities and LCR = Linear concentration range. Darker highlighted columns for data obtained from the CV.

The enhancement in the electrocatalytic peak current due to 1.0 mM H_2O_2 was observed at SPAuE-PA-SWCNT-MTAPc modified electrodes in Figure 5.9 (b and c)(curves, ii) compared to SPAuE-PA-MTAPc modified electrode surfaces without SWCNT in Figure 5.9(b and c)(curves, iii). This peak current enhancement was attributed to the immobilized PA-SWCNTs being good in shuttling and amplifying electrons between the MTAPc electrocatalytic sites and the electrode surface. The

electrocatalytic peaks due to electroreduction of 1.0 mM H_2O_2 were observed at -0.38 V for SPAuE-PA-SWCNT-MnTAPc and -0.30 V for SPAuE-PA-SWCNT-CoTAPc. The electroreduction peaks of H_2O_2 appeared close to where the metal reduction peaks occurred clearly showing the involvement of the phthalocyanine central metal ions in the electrocatalytic process even in the presence of PA-SWCNT. The MTAPc complexes participate in the electrocatalytic reduction mechanism of H_2O_2 while SWCNTs assist in the communication (i.e. relay and amplification of transferred electrons) between the electrode and the MTAPc electrocatalytic site. Figure 5.10 shows the proposed mechanism by which the electrocatalytic process takes place on the PA-SWCNT-MTAPc modified surface, which is similar to Figure 5.6 without SWCNTs. The reduction of H_2O_2 to water takes place at the MTAPc electrocatalytic site and mediated by the central metal ion.

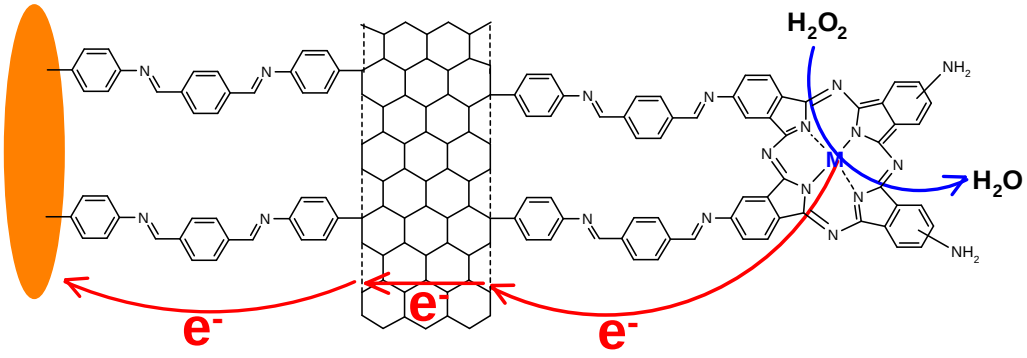

Figure 5.10: Proposed mechanism by which the electrocatalytic process takes place on the SPAuE-PA-SWCNT-MTAPc.

The electroanalytical properties of SPAuE electrodes modified with PA-SWCNT-MTAPcs towards H_2O_2 were studied using chronoamperometry method and the results similar to Figure 5.7 were obtained. The results of electrocatalysis and electroanalysis of H_2O_2 are summarized in Table 5.5. The limit of detection (LoD) for the PA-SWCNT-MTAPc modified electrodes were of the orders of 10^{-7} M using the

3δ notation and the modified electrodes gave good linear calibration curves for H_2O_2 concentrations ranging from 1.0 – 30.0 μM similar to without SWCNT, Table 5.5. The sensitivity values of these electrodes were 2.79 and 5.16 $mA.mM.cm^{-2}$, for SPAuE-PA-SWCNT-MnTAPc and SPAuE-PA-SWCNT-CoTAPc, respectively. When compared to the SPAuE-PA-MTAPc electrodes surfaces, the SPAuE-PA-SWCNT-MTAPc electrode surfaces exhibited better sensitivity, Table 5.5. The limit of detection (LoD) values obtained in this study were much less than those obtained for the gold electrode modified with SWCNTs-nanoFePc using a layer-by-layer self-assembly monolayer method [143]. The results obtained show that the electrodes can potentially be used for the analysis of H_2O_2 and the calibration curves will allow for unknown sample analysis.

In conclusion, this chapter has demonstrated the potential applications of the modified electrodes using MPc complexes and their immobilization onto electrode surfaces using different methods; such as self-assembly, electropolymerization and electrochemical grafting. The modified electrode surfaces exhibited good electrocatalytic and electroanalytical applications towards the detection of H_2O_2. The electroanalytical parameters obtained during the studies conducted show that the limits of detection were all of the order of 10^{-7} M. The sensitivities were high for polyMTAPc and PA-SWCNT-MTAPc modified electrodes, with SAMs and PA-MTAPc modified electrodes giving small sensitivities. The electrocatalytic potential values for H_2O_2 reduction were all close to where the metal reduction peaks were observed, hence the involvement of the metal ions in the electrocatalytic mechanisms as proposed.

Chapter 6:

Electrochemical immunosensors for the detection of measles-specific antibodies using HRP-labeled and label-free methods

6 ELECTROCHEMICAL DETECTION OF MEASLES ANTIBODIES

Preamble: Measles antibody detection using electrochemical methods

The previous chapter demonstrated the detection of an electroactive compound (hydrogen peroxide) using electrochemical methods by employing modified electrode surfaces with electroactive MPc complexes. The studies of non-electroactive biomolecules such as antibody and antigen affinity are based on mechanism of interaction that does not have recognizable electrochemical signal. Therefore, the use of indirect electrochemical detection methods will be investigated in the current chapter. The use of impedance for label-free detection and cyclic voltammetry for an enzyme-labeled detection will be investigated as electrochemical detection methods. These electrochemical methods will be employed for monitoring the antigen and antibody recognition on an electrode surface.

Currently measles-virus or measles-specific antibody detection is achieved using the well-established ELISA method which is in its nature a laboratory based method. The selectivity and specificity of this method is based on the high affinity recognition between the antigen-antibody and antibody-antibody reactions using absorbance rather than electrochemistry used in this work.

This section of work therefore, reports for the first time (according to candidates knowledge), the detection of measles-specific antibodies using electrochemical-based methods (enzyme-label and label-free). The choice of antibodies, i.e. rabbit anti-rubeola polyclonal primary antibody (1°PAb) or mouse anti-rubeola monoclonal primary antibody (1°MAb), which are suitable for studies will be assessed by the ELISA experiment. The detection of measles-specific antibodies is of importance

because the analyte samples can be easily obtained from saliva or other bodily fluids such as nasopharynx fluids via a non-invasive method. The viability of the design for immunosensors requires an intimate connection of the sensing element onto an electrode surface. Therefore, the covalent attachment of the measles-antigen (sensing element) on the electrode pre-grafted with the phenylethylamino (PEA) monolayer is investigated. The detection methods are based on enzyme-label (using horse-radish peroxidase) and label-free methods as shown in Figure 1.3.

6.1 Antigen-antibody binding affinity using ELISA

The ELISA method was used to test the affinity of the measles-antigen (Ag) and primary antibody (1°PAb or 1°MAb), and to ascertain which primary antibody, 1°PAb or 1°MAb, exhibits better sensitivity. The results were conducted in triplicates (rows A1-A8, B1-B8 and C1-C8) for 1°PAb (rabbit anti-rubeola) and rows F1-F8, G1-G8 and H1-H8 for 1°MAb (mouse anti-rubeola) primary antibodies. In the microtitre wells in Table 6.1, the concentration of measles-antigen was in 10-fold dilution series with column 1 being more concentrated (X1 = 200 $\mu g.ml^{-1}$) and column 8 being the least concentrated (X8 = 20 $pg.ml^{-1}$). The concentration of both primary antibodies was the same (100 $\mu g.ml^{-1}$) for polyclonal (1°PAb) and monoclonal (1°MAb). The detection was achieved using the horse-radish peroxidase (HRP) conjugated secondary antibody, represented as (HRP)-2°PAb or (HRP)-2°MAb and the concentration used was 50 $\mu g.ml^{-1}$. The antibodies were of IgG isotype and secondary antibodies were specific to the primary antibodies. For an example, the HRP conjugated rabbit anti-*mouse* (HRP-2°MAb) secondary antibody was specific to monoclonal *mouse* anti-rubeola (1°MAb) antibody and HRP conjugated donkey anti-*rabbit* (HRP-2°PAb) secondary antibody was specific to polyclonal *rabbit* anti-rubeola (1°PAb) antibody. Table 6.1 shows the ELISA experimental setup.

Table 6.1: ELISA experimental setup for testing antigen-antibody binding and ascertain which antibody exhibits greater binding affinity. The concentration in column 1 (X1 = 200 $\mu g.ml^{-1}$) 10-fold diluted to column 8 (X8 = 20 $pg.ml^{-1}$).

	1	2	3	4	5	6	7	8	9	10	11	12
A	X1	X2	X3	X4	X5	X6	X7	X8	/	NC	NC	NC
B	X1	X2	X3	X4	X5	X6	X7	X8	/	NC	NC	NC
C	X1	X2	X3	X4	X5	X6	X7	X8	/	NC	NC	NC
D	/	/	/	/	/	/	/	/	/	/	/	/
E	/	/	/	/	/	/	/	/	/	/	/	/
F	X1	X2	X3	X4	X5	X6	X7	X8	/	NC	NC	NC
G	X1	X2	X3	X4	X5	X6	X7	X8	/	NC	NC	NC
H	X1	X2	X3	X4	X5	X6	X7	X8	/	NC	NC	NC

Grey coloured wells were for polyclonal primary antibody (1°PAb), while green wells were for the monoclonal primary antibody (1°MAb). NC: negative control wells with no measles-antigen. The antigen concentration ranged from 200$\mu g.ml^{-1}$ (X1) - 20 $pg.ml^{-1}$ (X8). The primary antibodies had a concentration of 100 $\mu g.ml^{-1}$ and for detection the HRP conjugated secondary antibody, i.e. (HRP)2°PAb and (HRP)2°MAb, concentration was 50 $\mu g.ml^{-1}$.

The procedure for confirming the affinity of the measles-antigen and primary antibody is demonstrated in Figure 6.1. The colour changes will take place only if the all binding steps (labeled 1-3) have occured for the positive identification of the primary antibody binding to the measles-antigen. It is important to note that (HRP)2°PAb or (HRP)2°MAb binds to measles-antigen via primary antibody, i.e. 1°PAb for polyclonal or 1°MAb for monoclonal. The positive test well will contain: measles-antigen – primary antibody (1°PAb or 1°MAb) – HRP conjugated secondary antibody (2°PAb or 2°MAb) and this will lead to colour change to blue of the TMB + H_2O_2 solution. The negative test wells are without measles-antigen, the solution will remain colourless as no secondary antibody binding will occur. The negative control

(NC) wells were blocked for non-specific binding using BSA, i.e. A10 - C12 and F10 – H12.

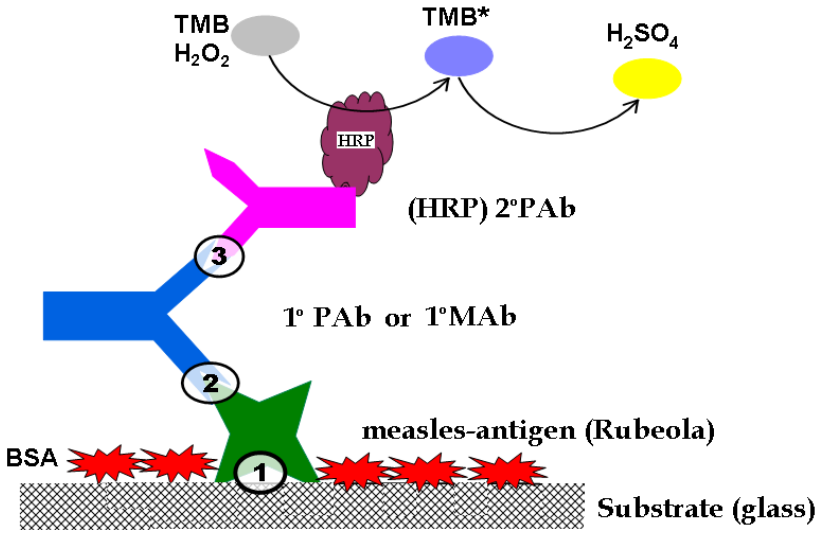

Figure 6.1: Schematic representation of the immobilization protocol for the positive ELISA studies and the use of TMB (H_2O_2) as the substrate and the 1.0 M H_2SO_4 as the stopper. (1) measles-antigen, (2) 1°PAb or 1°MAb, (3) (HRP)2°PAb or (HRP)2°MAb.

After the procedure for modifying the ELISA microtitre wells was carried out, the addition of TMB (H_2O_2) chromagen solution was used to confirm the antigen-antibody interaction. Figure 6.2 shows the colour changes at each well after the addition of (a) TMB (H_2O_2) substrate and (b) 1.0 M H_2SO_4 stop solution. The blue colour observed when the TMB (H_2O_2) substrate was added confirmed that the antigen-antibodies immune complex formed for both primary antibodies, i.e. 1°PAb and 1°MAb, Figure 6.2(a). The observed colour changes only occur more intensely on the positive microtitre wells, i.e. columns 1-8 containing measles-antigen. In the negative control wells (A10 - C12, see Table 6.1 for numbering) where there was no antigen, the light blue colour was observed for the 1°PAb antibodies and is due the fact that TMB is light sensitive, even though the reactions were conducted in the dark the images were taken in the presence of light. In the 1°MAb antibodies, no colour change was observed in the control wells (F10 – H12) except for one well that had a

blue colour and this could be due to cross contamination which may have occurred during experiment preparation. Upon adding 1M H_2SO_4, the colour in the well changed to yellow, Figure 6.2(b).

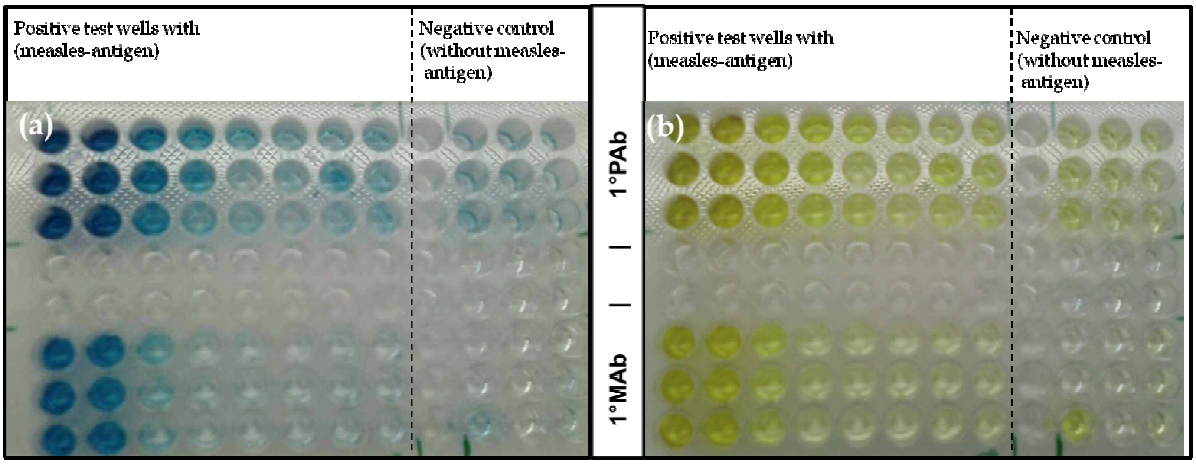

Figure 6.2: ELISA results for testing antigen-antibody binding (a) after the addition of TMB (H_2O_2) substrate and (b) after adding 1M H_2SO_4 stop solution. See Table 6.1 for numbering.

The optical density (OD) values were recorded using the spectrophotometer at 660 nm in the presence of TMB(H_2O_2) substrate and 450 nm after the addition of 1.0 M H_2SO_4 stop solution from the ELISA plate, in Figure 6.1(a) and (b), respectively. The mean values of the data obtained were plotted against the concentration of the measles-antigen. Figure 6.3 shows the dose response curves of OD measured at (a) 660 nm and (b) 450 nm for (i) 1°PAb and (ii) 1°MAb. It is discernible from these curves that the polyclonal (1°PAb) primary antibody is more sensitive than the monoclonal (1°MAb) primary antibody, since higher OD values at low measles-antigen concentrations were observed for the polyclonal (1°PAb) antibody. However, after the addition of 1M H_2SO_4 in Figure 6.1(b), the solution turned yellowish and the OD values at 450 nm, Figure 6.3(b), were obtained and were also plotted against concentration of measles-antigen. The trend in which the values were displayed was different from those of TMB (H_2O_2) solution. There were still differences between the

1°PAb and 1°MAb, with the 1°PAb showing better sensitivity at low measles-antigen concentrations compared to higher measles-antigen concentrations.

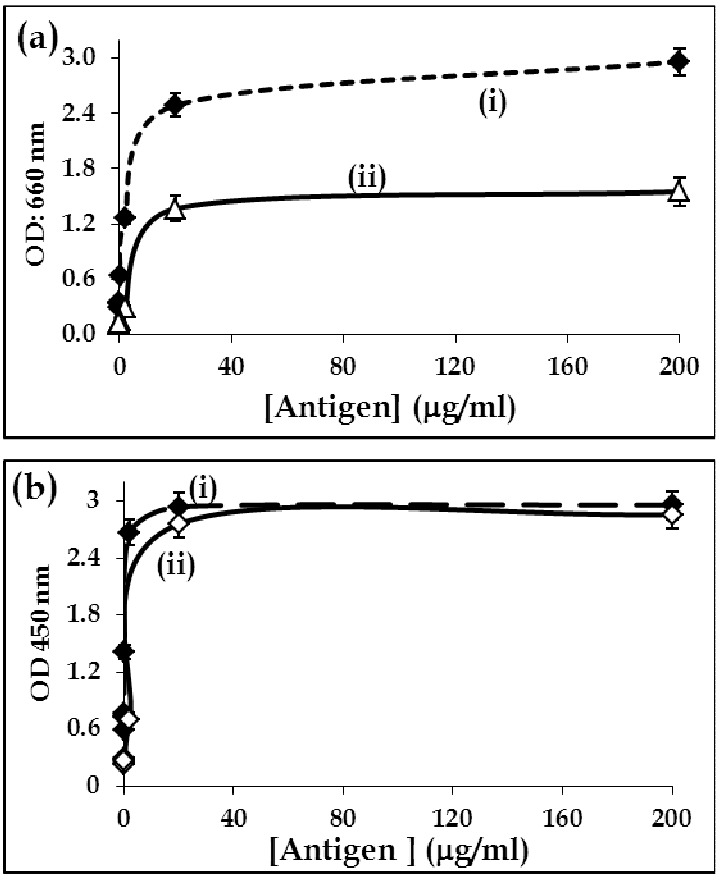

Figure 6.3: Dose response curve with OD readings at (a) 660 nm after the addition of TMB (H_2O_2) chromagen solution and (b) 450 nm after the addition of 1M H_2SO_4 all plotted against the concentration of the measles-antigen for (i) 1°PAb and (ii) 1°MAb.

The observed better sensitivity of the polyclonal 1°PAb as compared to monoclonal 1°MAb is that the latter recognizes one specific binding site (epitope) on the measles-antigen. If the measles-antigen binding to the surface (ELISA plate) blocks this antibody binding site; then the 1°MAb antibody will not recognize the antigen, even though it is present on the surface. The polyclonal antibody (1°PAb) recognizes several epitopes on the measles-antigen and therefore even if the measles-antigen

binding blocks one epitope, the antibody binds using the other available binding sites. The ELISA studies confirmed the affinity of the antibody-antigen reaction and clearly the polyclonal antibody (1°PAb) showed better sensitivity than monoclonal antibody (1°MAb). The increase in the absorbance values in Figure 6.3 reached saturation at the measles-antigen concentration of 20 $\mu g.ml^{-1}$ and this indicates a complete coverage of the measles-antigen bound onto the electrode surface with the measles-antibodies. The washing steps (thrice with PBS-Tween 0.05%) performed in-between the modification steps eliminate the possible physical adsorbed species that may give false positive. The resultant colour changes is an indication of the enzymatically catalyzed conversion of TMB into a blue coloured product (TMB*) [34,272]. This reaction is known to occur only in the presence of H_2O_2 and follows the mechanism shown in equation (6.1) to (6.3):

$$\text{(HRP)2°PAb} + H_2O_2 \longrightarrow \text{(Compound A)2°PAb} + H_2O \quad (6.1)$$

$$\text{(Compound A)2°PAb} + \text{TMB} \longrightarrow \text{(Compound B)2°PAb} + \text{TMB*} \quad (6.2)$$

$$\text{(Compound B)2°PAb} + \text{TMB} \longrightarrow \text{(HRP)2°PAb} + \text{TMB*} \quad (6.3)$$

Equation 6.1 is a two-electron enzymatic oxidation reaction of HRP(Fe^{3+}) in the presence of H_2O_2 which results in Compound A consisting of oxyferryl iron (Fe^{4+}=O) and a porphyrin л cation radical. Equation 6.2, in the presence of an electron donor compound (TMB), Compound A accepts one electron from TMB resulting in the oxidation of TMB* (blue coloured product) and Compound B (oxidation state = 4+) is formed. As the HRP returns to its native oxidation state (+3) from Compound B, it accepts another electron from electron donor TMB resulting to even more TMB molecules getting oxidized to TMB*, equation 6.3.

The successful validation of the antibody-antigen affinity towards one another clearly shows that the measles-antigen can bind to the primary antibodies (1°PAb

and 1°MAb) with the polyclonal (1°PAb) showing better sensitivity. Since high sensitivity was observed when 1°PAb was employed, this work will therefore investigate the detection of polyclonal antibodies (1°PAb) using electrochemical methods.

The ELISA experiment uses the physical adsorption method for the immobilization of the sensing element into microtitre wells. The electrochemical studies for measles-specific antibody (1°PAb) detection require the use of electrodes modified with sensing elements (measles-antigen) and monitor their binding with antibodies available in the analyte test solution. Electrode modification with the sensing element is a crucial and relevant step in the design of electrochemical immunosensor or sensors. In this study, the covalent immobilization of measles-antigen onto a gold electrode surfaces was investigated using electrochemical grafted with phenylethylamine (PEA) monolayer.

6.2 Covalent attachment of measles-antigen as sensing element

The modification of gold electrode was first through electrochemical grafting of diazonium salt and 2-aminoethylbenzene diazonium (AEBD) salt was used in this study. The synthesis of AEBD was accomplished following the reported method [226, 233] also described in experimental section. The NMR showed the purity of the product (AEBD) and the expected protons after integrating the peaks confirmed the synthesis of the AEBD. The IR characterization confirmed the successful synthesis and an N_2 intense stretch at 2287 cm^{-1} clearly indicating the successful conversion of the arylamino ($-NH_2$) group to diazonium (N_2^+) group. Other functional groups of

the original compound were not interrupted and the IR spectrum showed peaks or stretches due to NH_2 (3280 cm^{-1}), C-H (3110 cm^{-1}) and C-N (1160 cm^{-1}).

Scheme 6.1 shows the step-by-step modification of gold electrodes via the electrochemical grafting method and immobilization of measles-antigen.

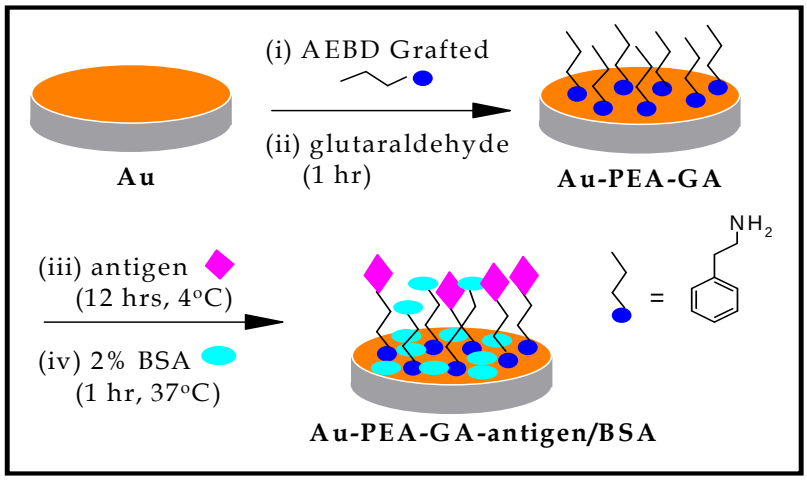

Scheme 6.1: Schematic representation of the electrode modification, whereby first the electrode was modified via (i) electrochemical grafting with the 4-(2-aminoethyl)benzene diazonium salt (AEBD), (ii) activation of the electrode with 5% glutaraldehyde (GA), (iii) immobilization of measles-antigen and (iv) non-specific site blocking using 2% BSA to achieve an antigen sensor.

The first step in electrode modification involved the electrochemical grafting of the gold electrode with AEBD, thus forming phenylethylamino group (PEA) according to Figure 1.10. This step has been reported before [226] for the immobilization of PEA monolayer onto gold electrode surface. Figure 6.4 shows the cyclic voltammograms of the electrochemical grafting of the AEBD salt onto the gold electrodes. Two scans were enough to achieve a monolayer covered surface as the electrode surface was

passivated with PEA monolayer after the first cycle. The first scan showed a reduction peak at E_p = 0.027 V vs Ag | AgCl and this peak is due to the generation of PEA radical as reported before [226] and similar to the experiments conducted previously for the 4-NBD radical in Section 4.3. The controlled formation of the monolayer has also been reported [239,246,364], where a small number of cycles (<5) gives the monolayer coverage. The second and subsequent scans did not show the reduction peak and this is attributed to the fact that the formed PEA monolayer blocks the surface rendering it inactive. In this study, five scans were used for the formation of PEA monolayer (Au-PEA) and the observed changes in the cyclic voltammograms clearly show that the monolayer formation is achieved during the first scan.

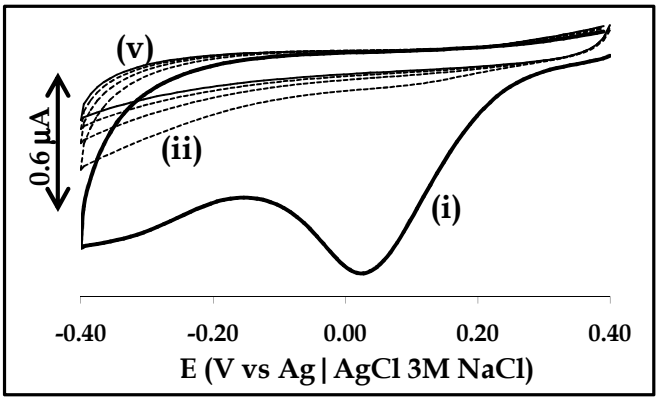

Figure 6.4: Cyclic voltammograms for the electrochemical grafting of 1 mM AEBD salt in ACN solution containing 0.1 M $TBABF_4$. Scan rate = 50 $mV.s^{-1}$.

The electrode was further modified with measles-antigen, by first activating the PEA monolayer with glutaraldehyde (Au-PEA-GA), to afford Schiff-base reactions between the amino group of PEA and the aldehyde group of GA. The other aldehyde group was exposed for further reaction with amine groups from biomolecules [375]. The immobilization of measles-antigen, in this study, was accomplished by

immersing the glutaraldehyde activated electrode into the measles-antigen solution (20 μg.ml^{-1}) and incubating overnight at 4^{o}C. The longer incubation time (12 hours) for the covalent immobilization of the measles-antigen was required thus giving measles-antigen enough time to structurally conform itself after covalent attachment. The electrode after covalent immobilization of measles-antigen is represented as Au-PEA-GA-antigen. The concentration used for measles-antigen immobilization solution is obtained on the ELISA experiment in Figure 6.3 which showed that the plateau was reached at 20 μg.ml^{-1} of antigen concentration. The non-specific binding sites on the bare and Au-PEA-GA modified gold electrodes were blocked using BSA (forming Au-PEA-GA-antigen/BSA). The BSA does not bind to the measles-specific antibodies (1°PAb) and the ELISA negative control (NC) wells blocked with BSA confirmed this by less or no colour changes in the negative control wells, Table 6.1.

6.2.1 Electrochemical characterization of bare and modified electrodes

The cyclic voltammetry and electrochemical impedance spectroscopy (EIS) were used to compare the electron transfer properties of the bare and modified gold electrodes in the presence of the redox probe ($[Fe(CN)_6]^{-3/-4}$) in solution, Figure 6.5.

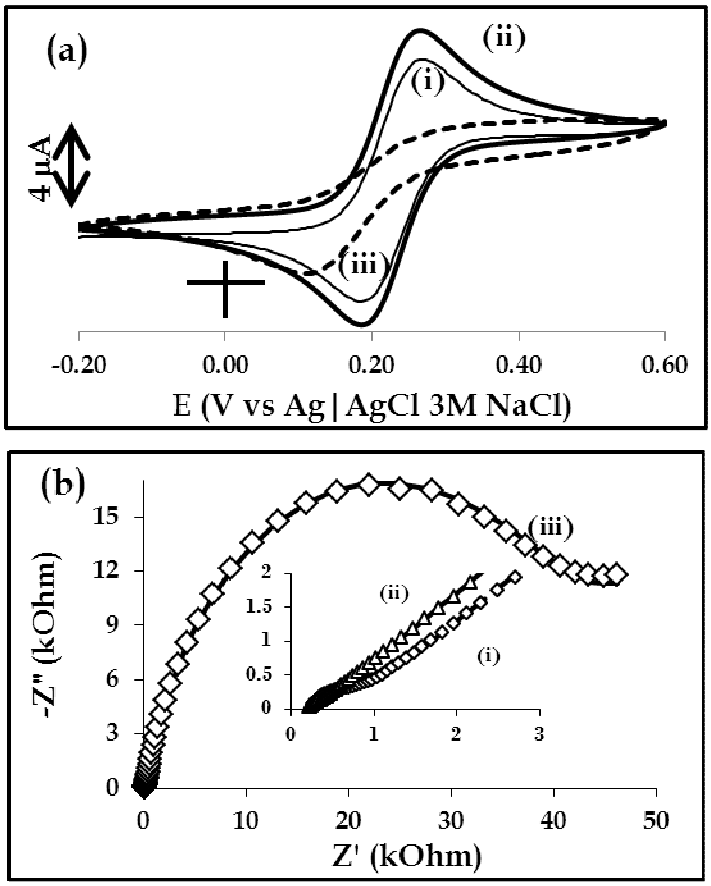

Figure 6.5: (a) Cyclic voltammograms and (b) Nyquist plots for (i) Au, (ii) Au-PEA and (iii) Au-PEA-GA-antigen/BSA electrodes in (1:1) $K_3/K_4Fe(CN)_6$ containing 0.1 M KCl. Scan rate: 25 $mV.s^{-1}$.

The cyclic voltammograms of bare and Au-PEA monolayer exhibited a reversible redox peaks due to $[Fe(CN)_6]^{3-/4-}$ with peak-to-peak separation (ΔE) = 0.073 V (typical one-electron transfer kinetics) for both electrodes. Upon modifying the electrode with the PEA monolayer; the increase in voltammetric peak current densities was observed. This increase in current densities may be attributed to the PEA monolayer being a good conductor of electrons and the protonation ($-NH_3^+$) of the grafted amino group at pH 7.4 allows the negatively charged $[Fe(CN)_6]^{3-/4-}$ to reach the underlying gold surface.

The antigen/BSA modified gold electrode (Au-PEA-GA-antigen/BSA) showed blocking properties towards $[Fe(CN)_6]^{3-/4-}$ redox probe, Figure 6.5(a)(iii). The oxidation peak disappeared and the reduction peak shifted to less positive peak, leading to an increase in ΔE. The increase in ΔE with the decreasing voltammetric peak current densities shows slow rate of electron transfer. The blocking behavior of antigen/BSA modified electrodes towards $[Fe(CN)_6]^{3-/4-}$ confirms the successful immobilization of the measles-antigen and the blocking of non-specific binding sites by BSA. The blocking and non-blocking behavior of the modified electrodes is related to the thickness and conducting properties of the immobilized film. The PEA monolayer is very thin and is a good conductor of electrons compared to the insulating non-conducting antigen/BSA film.

EIS measurements (Nyquist plot representation) in Figure 6.5(b) measured at the equilibrium potential for the bare electrode ($E_{1/2}$ = 0.227 V) showed the decrease in the semi-circle diameter (R_{CT}) from the bare (R_{CT} = 628 Ω) to the Au-PEA monolayer (R_{CT} = 124 Ω) modified gold electrodes, inset in Figure 6.5(b). The decrease in R_{CT} value for Au-PEA monolayer electrode indicates that the monolayer is conducting and hence increase in voltammetric peak current densities due to $[Fe(CN)_6]^{3-/4-}$ obtained from the cyclic voltammetry in Figure 6.5(a). Upon modifying the electrode with the antigen/BSA, the R_{CT} value increased to 42.2 kΩ clearly indicating the slowing of the rate of electron transfer between the underlying electrode and the redox probe in solution. The EIS results corroborate those that were obtained with the cyclic voltammetry. The observed results clearly confirm successful electrode modification. Furthermore, the characterization of the modification of gold electrode surfaces was investigated using atomic force microscope (AFM) and the obtained results are discussed in the next section.

6.2.2 AFM characterization of bare and modified gold electrode surfaces

The bare and modified gold coated quartz crystal (AuCQC) surfaces were employed to study the immobilization of the PEA monolayer and measles-antigen/BSA in air. The choice of AuCQC surfaces as compared to normal gold electrodes is due to the ease of mounting these surfaces for sample measurements on the AFM equipment. Figure 6.6 shows 2D and 3D AFM micrographs for (a) PEA monolayer (AuCQC-PEA), (b) measles-antigen/BSA (AuCQC-PEA-GA-antigen/BSA) and (c) measles-specific antibody (AuCQC-PEA-GA-antigen/BSA-1°PAb).

The AFM image of bare AuCQC surface is similar to that observed in Figure 4.16(a) above with roughness factor of 1.693 nm. The gold surface was modified with PEA monolayer (AuCQC-PEA) the AFM micrograph of the PEA modified electrodes is shown in Figure 6.6(a). The roughness factor value for the AuCQC-PEA was 2.626 nm. The increase in roughness factor at AuCQC-PEA confirms the modification of AuCQC surface with PEA monolayer. The image and the roughness factor values were similar to those obtained for the AuCQC-PA surface in Figure 4.16(b) which gave the roughness factor of 2.584 nm, but slightly higher for AuCQC-PEA (2.626 nm). The surface was further modified with measles-antigen/BSA and Figure 6.6(b) shows the AFM micrograph of AuCQC-PEA-GA-antigen/BSA. The images when compared to AuCQC-PEA were clearly different and this could be attributed to further modification of the surface with measles-antigen and BSA. The roughness factor of the antigen/BSA modified surface increased to 3.477 nm from 2.626 nm for the AuCQC-PEA and this increase is attributed to the immobilization of measles-antigen and blocking with BSA. The measles-antigen modified electrode was exposed to the solution containing 1 $\mu g.ml^{-1}$ 1°PAb and the AFM image was acquired to confirm the antigen-antibody immune complex formation.

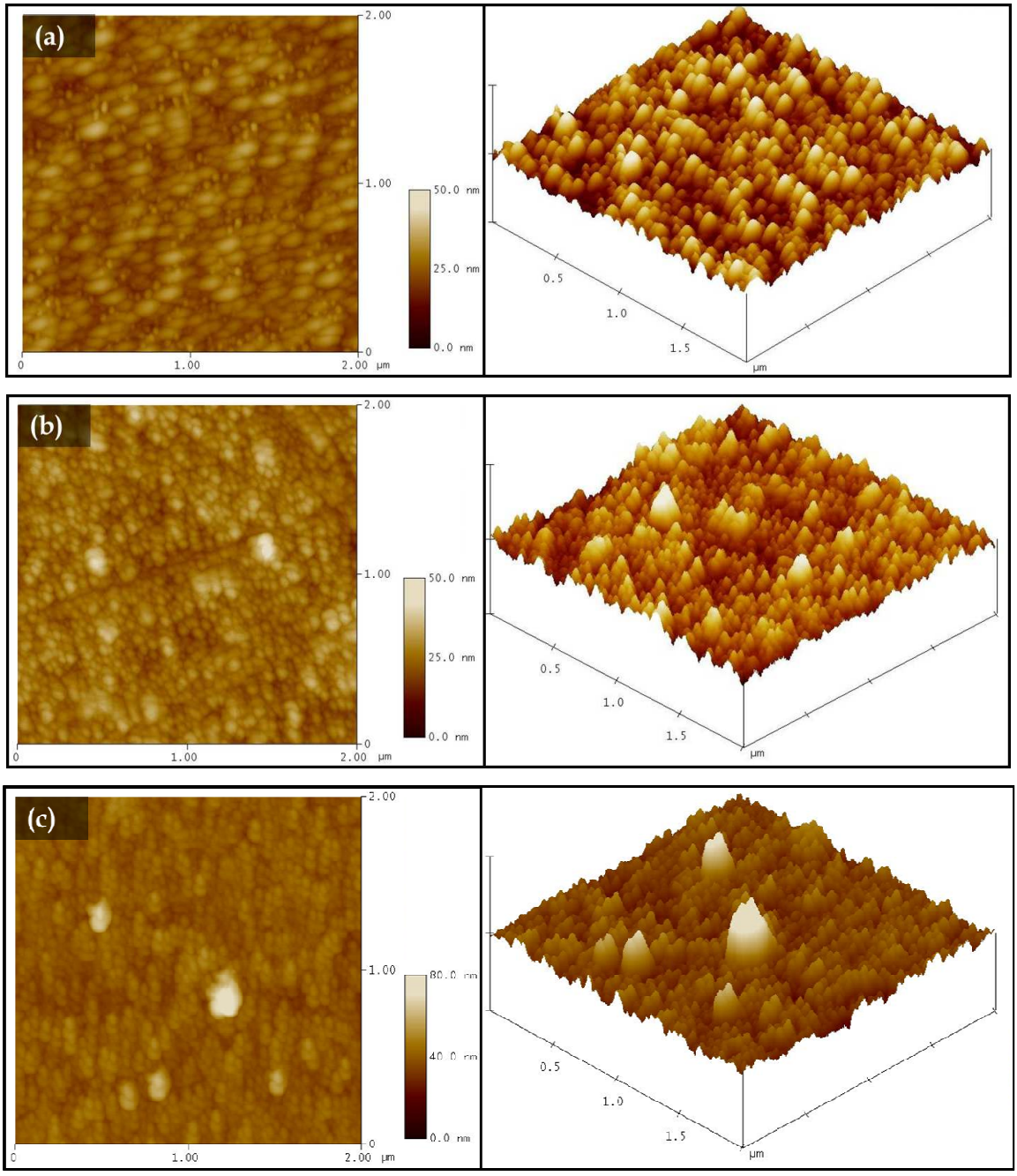

Figure 6.6: 2D and 3D AFM micrographs for (a) PEA monolayer (AuCQC-PEA), (b) measles-antigen/BSA (AuCQC-PEA-GA-antigen/BSA) and (c) antibody (AuCQC-PEA-GA-antigen/BSA-1°PAb).

The AFM image after the antigen-antibody recognition step is shown in Figure 6.6(c) and was different from that with only the antigen/BSA in Figure 6.6(b). The

observed changes confirm the recognition between the surface bound measles-antigen with the antibody (1°PAb). The surface roughness analysis showed an increase in the roughness factor value from 3.477 (for antigen/BSA) to 4.388 nm for an antibody modified surface. The increase in roughness factor at the antibody modified surfaces confirms the interaction and binding of antibody onto measles-antigen on the surface. The section analysis was also conducted and vertical distances measured from the images obtained taking the highest peak in the line analysis. The section analysis also showed an increase in peak height with each surface modification. The vertical distance (VD) values were 8.523 nm for AuCQC-PEA (slightly higher than the AuCQC-PA, 7.916 nm), 19.622 nm for AuCQC-PEA-GA-antigen/BSA and 37.851 nm for AuCQC-PEA-GA-antigen/BSA-antibody surfaces. The increase in vertical distance values clearly confirm the surface modifications as proposed in Scheme 6.1. The AFM and the electrochemical techniques employed for the characterization of the electrode modifications clearly showed changes in surface properties due to the films deposited and the recognition between measles-antigen and the primary antibody (1°PAb).

6.2.3 QCM-D studies for the immobilization of measles-antigen/BSA and antibody

The QCM-D studies conducted are important in monitoring *in situ* and in real-time the immobilization of measles-antigen and the formation antigen-antibody immune complex. The immune complex forms after the surface bound measles-antigen recognizes antibodies (1°PAb) in solution. The cysteamine self-assembled monolayer (CA SAM) modified gold surface was employed for the QCM-D studies, Scheme 6.2. The gold coated crystals (QSX-301) for QCM-D studies could not be modified using electrochemical grafting and hence the CA SAM modified gold crystals were used.

The formation of cysteamine SAMs and their uses for the immobilization of biomolecules using QCM-D technique has been reported before [221]. Similar method was employed in this work for the immobilization of measles-antigen using glutaraldehyde as a cross-linker. The AuCQC-CA SAMs immobilization and their activation using glutaraldehyde were conducted prior to mounting the quartz crystals onto the reaction chamber for QCM-D measurements. The covalent attachment of measles-antigen onto a glurataldehyde activated cysteamine gold surface (AuCQC-CA-GA) was studied. The method in Scheme 6.2 shows the protocol followed for the immobilization of measles-antigen and interaction of the surface bound measles-antigen with the primary antibody (1°PAb).

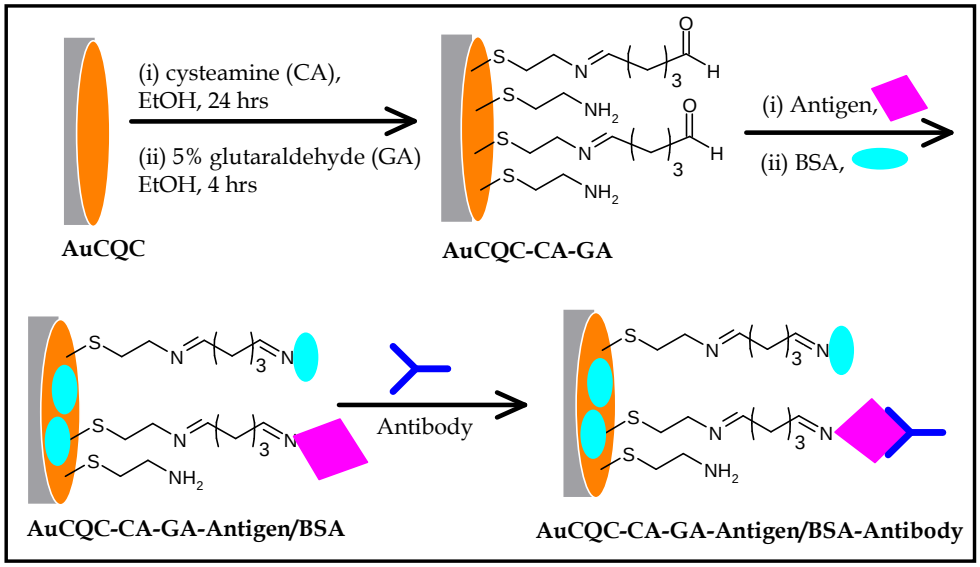

Scheme 6.2: QCM-D protocol followed for monitoring measles-antigen immobilization and their interaction with the primary antibody (1°PAb).

Figure 6.7 shows the change in (a) frequency, (b) dissipation and (c) the mass uptake as (i) the measles-antigen, (ii) BSA and (iii) the primary antibody (1°PAb). The electrode used was AuCQC-CA-GA.

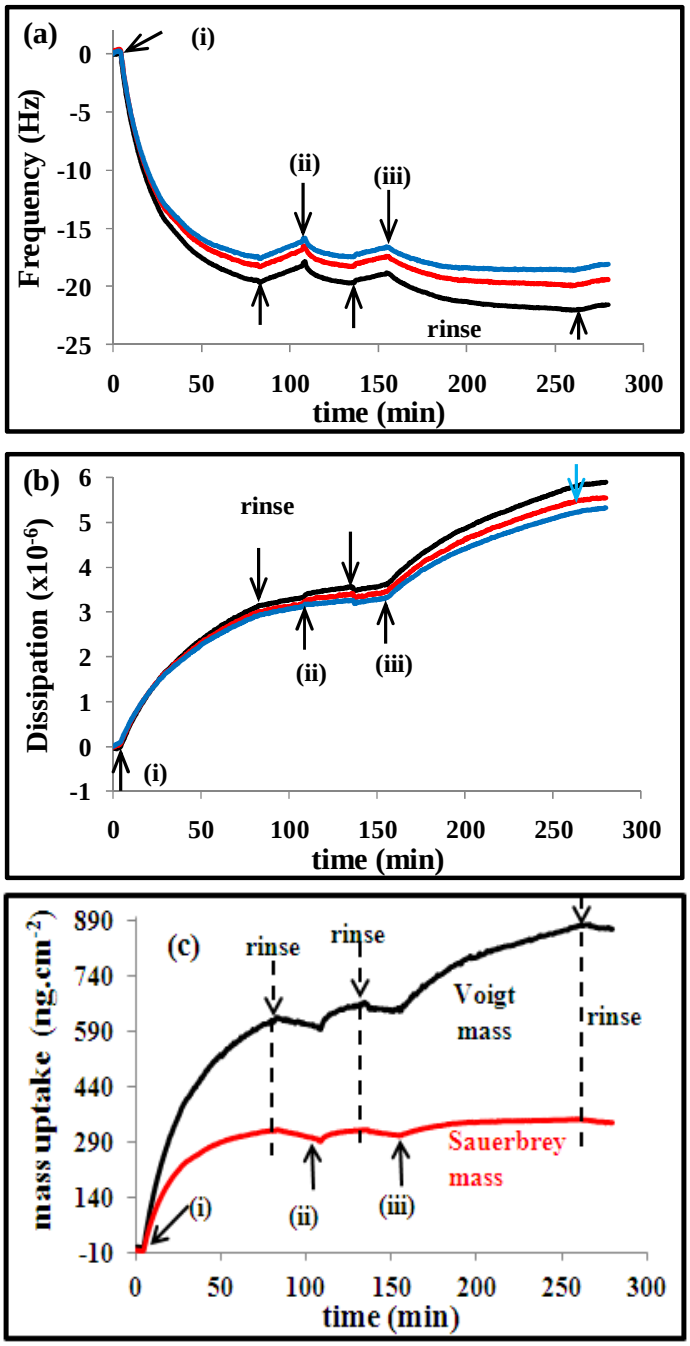

Figure 6.7: Changes in (a) frequency, (b) dissipation and (c) the calculated mass uptake during the immobilization of the (i) antigen, (ii) BSA blocker and (iii) 1° antibody. The electrode used is AuCQC-CA-GA. The unlabeled arrows are due to rinsing. Overtone numbers showed in (a) and (b) are n = 7 (blue), 9 (red) and 11 (black).

In-between the immobilization steps the physically adsorbed biomolecules were removed by rinsing with PBS (pH 7.4). The change in frequency (Δf) in Figure 6.7(a), and dissipation in Figure 6.7(b) (ΔD, in brackets) gave the values of about -16.90 Hz (3.20×10^{-6}), -0.30 Hz (2.00×10^{-7}) and -1.90 Hz (1.10×10^{-6}) obtained for measles-antigen, BSA and primary antibody (1°PAb) reactions, respectively and are summarized in Table 6.2. The high frequency change (-16.90 Hz) was observed for the measles-antigen immobilization and this could be attributed to the covalent attachment method used. An increase in frequency of about -0.3 Hz was observed for the BSA immobilization and also -1.90 Hz was observed for the antibody (1°PAb) binding to measles-antigen. The small changes observed for the 1°PAb was attributed to the small concentrations (1.0 $\mu g.ml^{-1}$) used. However, the observed changes were enough to confirm that recognition between the measles-antigen and primary antibody (1°PAb), thus confirming the formation of the immune complex.

Figure 6.7(c) shows the mass uptake for the layering of (i) measles-antigen, (ii) BSA and (iii) 1°PAb. The amount of mass attached was obtained using Kevin-Voigt model and Sauerbrey (in brackets) and gave the values of about 602 (297) $ng.cm^{-2}$, 43 (11) $ng.cm^{-2}$ and 224 (33) $ng.cm^{-2}$ for measles-antigen, BSA and 1°PAb immobilization, respectively, Table 6.2. It was interesting to note that the Sauerbrey mass was less than that obtained using Kevin-Voigt fitting model. The reason for the differences in mass is that Sauerbrey assumes a rigid film, whereas the Voigt mass takes into account the visco-elasticity of the materials adsorbed. In this instance, Voigt mass is the more realistic as the data, especially the dissipation clearly showing an increase confirming the visco-elasticity of the immobilized films. Sauerbrey mass calculations underestimate the mass and do not take into account the mass of the water molecules within the film.

Table 6.2: Kevin-Voigt parameters (viscosity, elasticity, thickness and mass per unit area) and the Sauerbrey parameters (mass per unit area, thickness and density) obtained using Q-tools modelling software from Q-Sense®. The electrode used is AuCQC-CA-GA.

Immobilized Layer	Kevin-Voigt				Sauerbrey		
	Viscosity ($kg.ms^{-1}$)	Elasticity (MPa)	Thickness (nm)	Mass/area ($ng.cm^{-2}$)	Mass/area ($ng.cm^{-2}$)	Thickness (nm)	Density ($kg.m^{-3}$)
Antigen :Δf_7= -16.9 Hz :$\Delta D_7 = 3.2 \times 10^{-6}$	0.0022	0.471	6.016	602	297	2.970	1970.24
BSA :Δf_7 = -0.30 Hz :$\Delta D_7 = 2.0 \times 10^{-7}$	0.0022	0.442	6.454	43	11	3.088	3087.54
Antibody :Δf_7 = -1.90 Hz :$\Delta D_7 = 1.1 \times 10^{-6}$	0.0018	0.344	8.689	224	33	3.414	3414.39
BSA[a] :Δf_7 = -9.09 Hz :$\Delta D_7 = 4.1 \times 10^{-7}$	0.0012	0.277	3.040	300	236	2.360	2359.60

[a] The parameters obtained for the control experiment with BSA immobilization onto AuCQC-CA-GA modified gold surface Figure 6.10.

The film thickness was also calculated using both Voigt and Sauerbrey (values in brackets) from the modeled data. The film thickness was found to be 6.016 (2.970) nm, 6.454 (3.088) nm and 8.689 (3.414) nm for the measles-antigen, BSA and 1°PAb surfaces, respectively, Table 6.2. An increase in film thickness was observed at each surface modification and this is due to the underlying layers contributing to the overall film thickness. The increase in the thickness clearly confirms the immobilization of various layers as proposed in Scheme 6.2. The QCM-D results clearly show the importance of modifying the gold surface before immobilizing the antigen and this experiement yielded good results. The QCM-D also showed that this

method can also be used for studying immunosensor design and the specificity of device depends on the sensing element bound onto the surface.

To relate the observed changes in dissipation (D) to the changes in frequency (*f*), the D and *f* plot was also studied and the time dependence of D and *f* is avoided. Figure 6.8 shows the ΔD vs Δ*f* plot which gives the change in damping for each layer immobilized on the AuCQC-CA-GA surface. The D versus *f* plot gives the effect of the attached layers and their structural confirmation during the immobilization. For a rigid layer, the slope (ratio of ΔD/Δf) value is low and the high ratio indicates that the film is soft or dissipative.

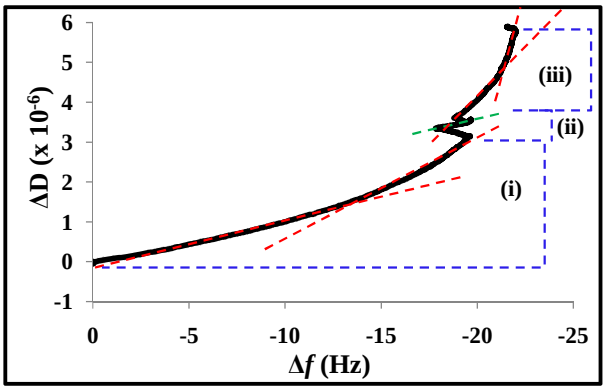

Figure 6.8: ΔD vs Δ*f* (n = 7) for the attachment of (i) measles-antigen, (ii) BSA and (iii) 1°PAb. Washing with PBS (pH 7.2) was performed between the binding steps. The electrode used was AuCQC-CA-GA.

For measles-antigen immobilization in Figure 6.8(i), the two slopes were observed indicating two different kinetic processes. The slope was low for the first phase and increased as the attachment of measles-antigen continued (second phase). The initial phase shows that the measles-antigen was binding freely to the underlying cysteamine-glutaraldehyde thin film. However as the reaction continued; the slope increased indicating changes in structural conformation of the measles-antigen

forming an open structure or dissipative film. The mass uptake in Figure 6.7(c) above showed high mass loading when comparing the Voigt mass and Sauerbrey indicating that the antigen film was highly dissipative due to the open structure it was forming. The BSA blocking in Figure 6.8(ii) showed low ratio of $\Delta D/\Delta f$ and this was attributed to very little of BSA binding onto the surface. The 1°PAb binding in Figure 6.8(iii) showed two phases as well and the slopes were higher than those observed for measles-antigen immobilization. The observed high slopes indicate the open structure and visco-elastic film forming also indicating the strong binding affinity between measles-antigen and measles-specific polyclonal antibody (1°PAb). The rinsing steps were clearly visible as they gave a negative slope in Figure 6.8. The various studies conducted clearly shows the immobilization of measles-antigen, BSA (very little) and 1°PAb onto activated surfaces.

The physical adsorption experiment of the measles-antigen was also investigated on bare gold surface (AuCQC), Figure 6.9. The frequency shift due to physical adsorption of meales-antigen was observed and stabilized quicker (50 minutes) compared to the measles-antigen layering which took 80 minutes, Figure 6.7(a), on the AuCQC-CA-GA functionalized gold surface. However, the physically adsorbed layer of measles-antigen was not stable as it washed off easily during the rinsing step with PBS (pH 7.4). This experiment shows the importance of electrode functionalization with CA SAM and activation with glutaraldehyde for a stable measles-antigen layer to form.

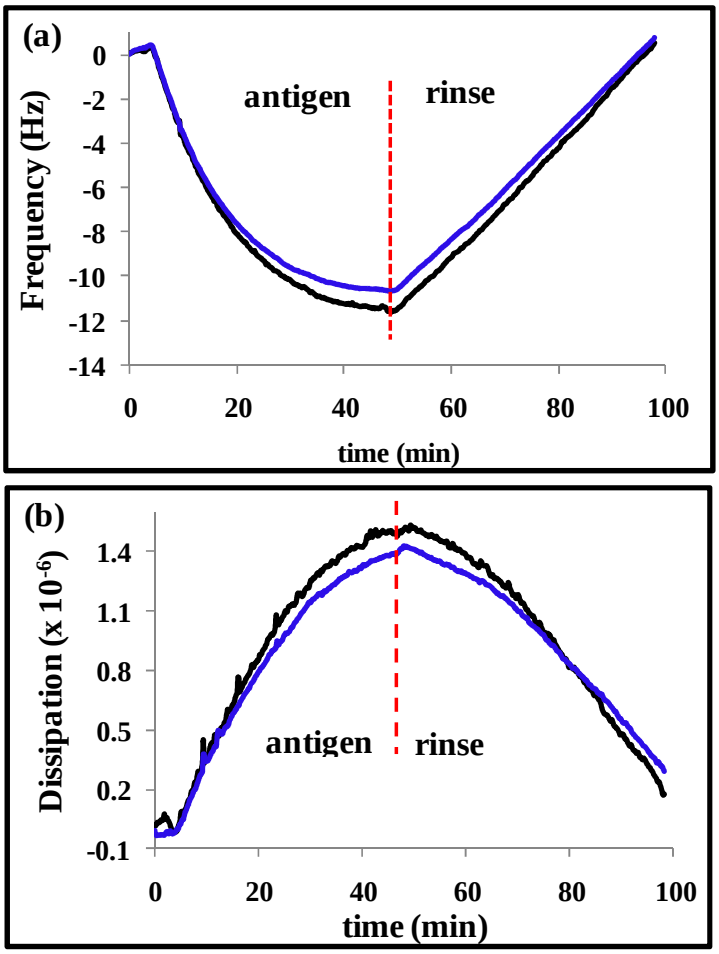

Figure 6.9: The immobilization of antigen using physical adsorption method onto bare AuCQC surface monitored using QCM-D: time dependence of (a) Δf and (b) ΔD for the 7th (blue) and 9th (black) overtones.

The control experiment (Figure 6.10) where the BSA was immobilized onto the cysteamine functionalized gold surface yielded a higher mass loading for BSA (Table 6.2) compared to the mass uptake after the surface is modified with the measles-antigen. This clearly showed that the measles-antigen film forms a compact layer on the gold surface and there were no sites for more BSA to bind. The immobilization of the primary antibody (1°PAb) did not occur on the BSA modified surface indicating that the binding observed at the measles-antigen modified surface was due to the immobilized measles-antigen forming an immune complex with 1°PAb.

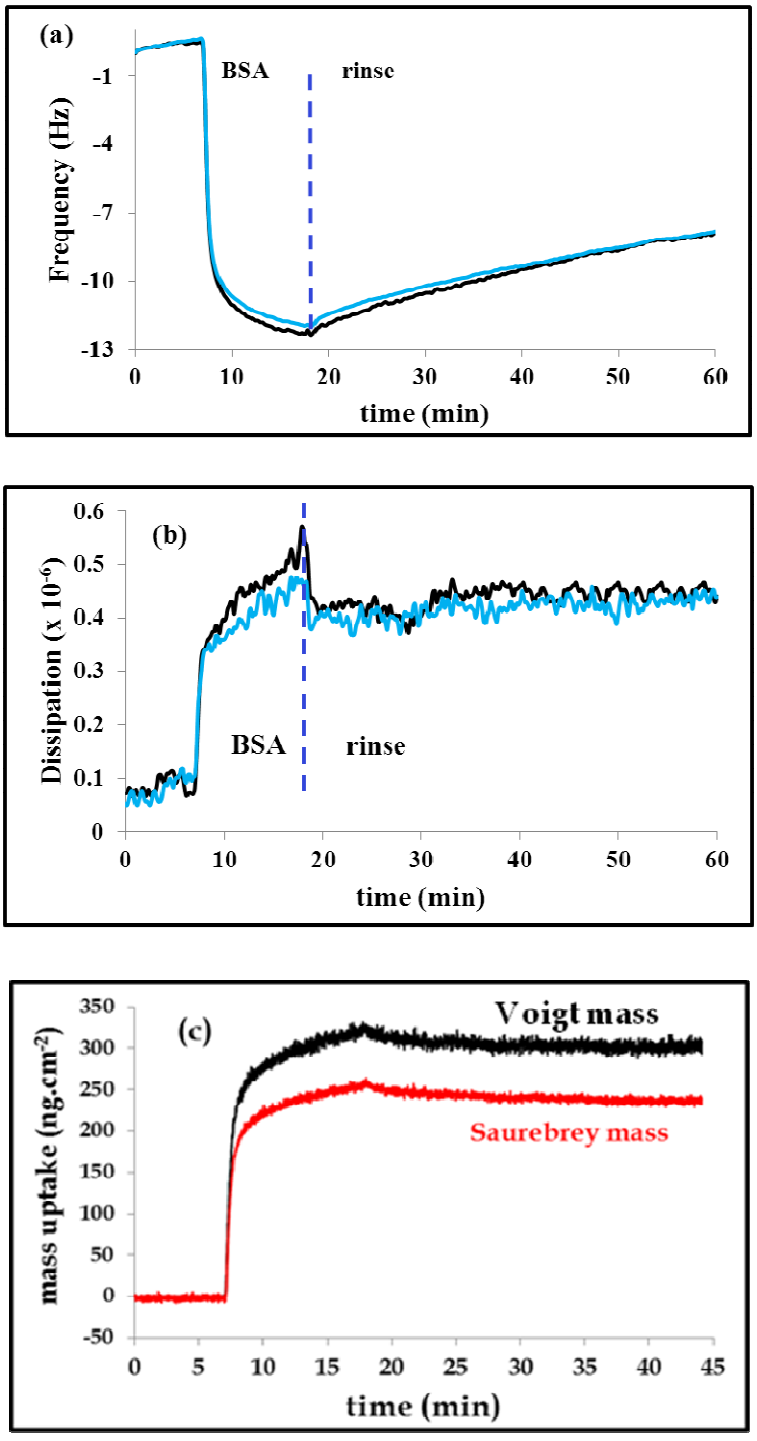

Figure 6.10: The immobilization of BSA (in the absence of antigen) onto AuCQC-CA-GA monitored using QCM-D (a) Δf, (b) ΔD at 7th (blue) and 9th (black) overtones and (c) mass uptake dependence on time.

The characterization of gold electrode surface modifications were confirmed for the immobilization of the measles-antigen using electrochemical methods, microscopic (AFM) method and quartz-crystal microbalance. The following section will utilize the measles-antigen functionalized gold electrode surfaces for the detection of measles-specific antibodies (1°PAb) using two electrochemical methods based on label-free (impedance) and HRP-labeled detection. The initial study involves label-free detection using electrochemical impedance spectroscopy.

6.3 Electrochemical detection of polyclonal primary antibodies

6.3.1 Label-free detection of measle-specific antibodies (1°PAb)

The initial experiments were conducted to find optimum conditions for the detection of measles-specific antibodies (1°PAb), i.e. the effect of incubation time of antibody (1°PAb) concentration in the formation of antigen-antibody immune complex. The experiments were conducted in $[Fe(CN_6)]^{-3/-4}$ solution where the degree of blocking the diffusion of the $[Fe(CN_6)]^{-3/-4}$ ions will indicate the interaction of antibodies in solution with the surface bound measles-antigen. An increase is semi-circle (R_{CT}) in the Nyquist plot will be an indication of the blocking of the ions due to $[Fe(CN)_6]^{-3/-4}$.

6.3.1.1 Effect of incubation time on the formation of antigen-antibody complex

The electrode used was modified with the measles-antigen and blocked with BSA (Au-PEA-GA-antigen/BSA) for the detection of measles-specific primary antibodies. Figure 6.11 shows a schematic representation of how the measles-antigen modified electrode reacts when exposed to the solution that contains antibodies specific to the sensing element (measles-antigen) attached onto the surface.

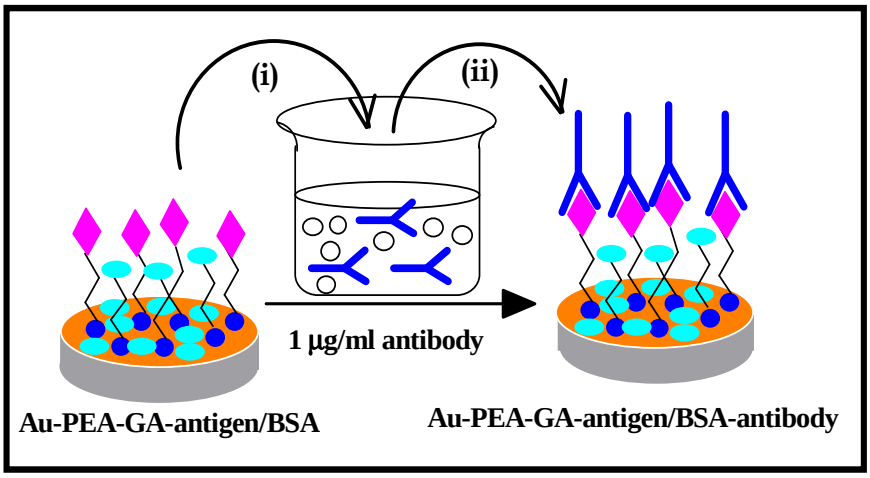

Figure 6.11: Schematic representation of measles-antigen/BSA modified gold electrodes and subsequent interaction with measles-specific antibodies in solution (i) immersion in antibody containing solution and (ii) antibody capture and rinsing of non-specific and physisorbed species.

The measles-antigen and measles-specific antibody interaction do not result in a cognizable electrical signal and therefore the use of electrochemical impedance spectroscopy and CV allowed for monitoring this reaction using a redox probing species, $[Fe(CN)_6]^{-3/-4}$.

Figure 6.12 shows the (a) cyclic voltammograms, (b) Nyquist plots and (c) R_{CT} (kΩ) vs incubation time (min), for (i) Au-PEA-GA-antigen/BSA and the fomation of antigen-antibody immune complex as a function of incubation time after (ii) 5, (iii) 10, (iv) 20, (v) 30, (vi) 40, 50 and 60 minutes of incubation, in (1:1) 1 mM $K_3/K_4Fe(CN)_6$ with 0.1 M KCl solution. The primary antibody (1°PAb) concentration used is 1 µg.ml^{-1}.

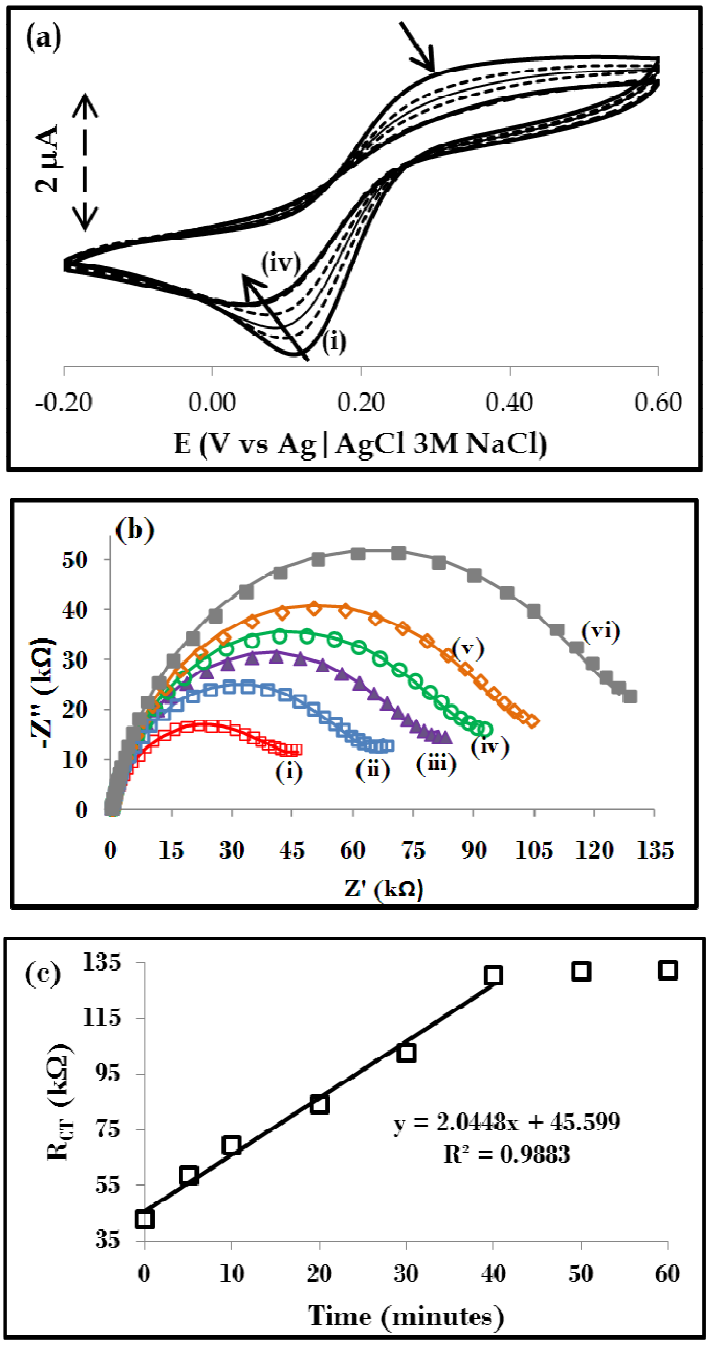

Figure 6.12: (a) Cyclic voltammograms, (b) Nyquist plots and (c) R_{CT} (kΩ) vs incubation time (min), for (i) Au-PEA-GA-antigen/BSA and the formation of antigen-antibody immune complex as a function of incubation time after (ii) 5, (iii) 10, (iv) 20, (v) 30, (vi) 40, 50 and 60 minutes of incubation, in (1:1) 1mM $K_3/K_4Fe(CN)_6$ with 0.1 M KCl solution. [1°PAb] = 1.0 µg.ml^{-1}. Scan rate = 25 mV.s^{-1}.

The cyclic voltammograms in Figure 6.12(a) shows the effect of electrode modification with antibody as a function of incubation time. As the incubation time increases, the redox process due to $[Fe(CN)_6]^{-3/-4}$ decreased in current densities and this was accompanied by the shift of the reduction peak to less positive values. This resulted in the increase in the peak-to-peak separation (ΔE). This decreasing in peak current densities and disappearance of the oxidation peak confirms the formation of antigen-antibody complex. This decreasing trend in cyclic voltammograms slowed or stopped after 40 minutes. This clearly indicates that the surface bound measles-antigens have completely reacted with the antibodies in solution and there are no free measles-antigens available for further reactions. The Nyquist plots in Figure 6.12(b) also exhibited similar trends in that the semi-circle (R_{CT}) increased linearly with the increasing incubation time up to 40 minutes and there was no further increase. The semi-circle (R_{CT}) stopped increasing after 40 minutes as the Nyquist plots were the same for 50 and 60 minutes. There was no measles-antigen available for reacting with antibodies and this clearly indicates the time dependence of the antibody-antigen immune reaction. The plot of R_{CT} versus incubation time in Figure 6.12(c) shows the observed trend on the Nyquist plots and after 40 minutes the R_{CT} stopped growing for the 1 $\mu g.ml^{-1}$ antibody concentration. According to the results obtained in Figure 6.12, the reaction or incubation time of 40 minutes was selected for the antigen-antibody immune complex formation in the following experiments. The antibody-antigen reaction is not only time dependant but also concentration dependant.

6.3.1.2 Effect of antibody concentration on the antigen-antibody complex formation

The effect of antibody concentration on the change in R_{CT} was also investigated, Figure 6.13. The increase in R_{CT} was observed with the increasing antibody

concentrations. The changes in the total charge transfer resistance ($\Delta R_{CT}/k\Omega$) for each concentration were calculated from equation (6.4) [35,36]:

$$\Delta R_{CT} = R_{Ag-Ab} - R_{Ag} \qquad (6.4)$$

where R_{Ag} is the electrode polarization (charge transfer) resistance of the Au-PEA-GA-antigen/BSA before incubation in the antibody solution and $R_{Ag\text{-}Ab}$ is the value of the electrode polarization (charge transfer) resistance after incubation of the Au-PEA-GA-antigen/BSA in the antibody solution with concentrations ranging from 10 $ng.ml^{-1}$ to 5 $\mu g.ml^{-1}$. The results are represented as bar chart in Figure 6.13(b) and show an increase in ΔR_{CT} with the increasing 1°PAb concentrations. The observed changes in ΔR_{CT} are affected by the antibody concentration and increases up to 5 $\mu g.ml^{-1}$ upon which it slows down. The varied concentration of antibody and its interaction with the surface bound measles-antigen is clearly observed.

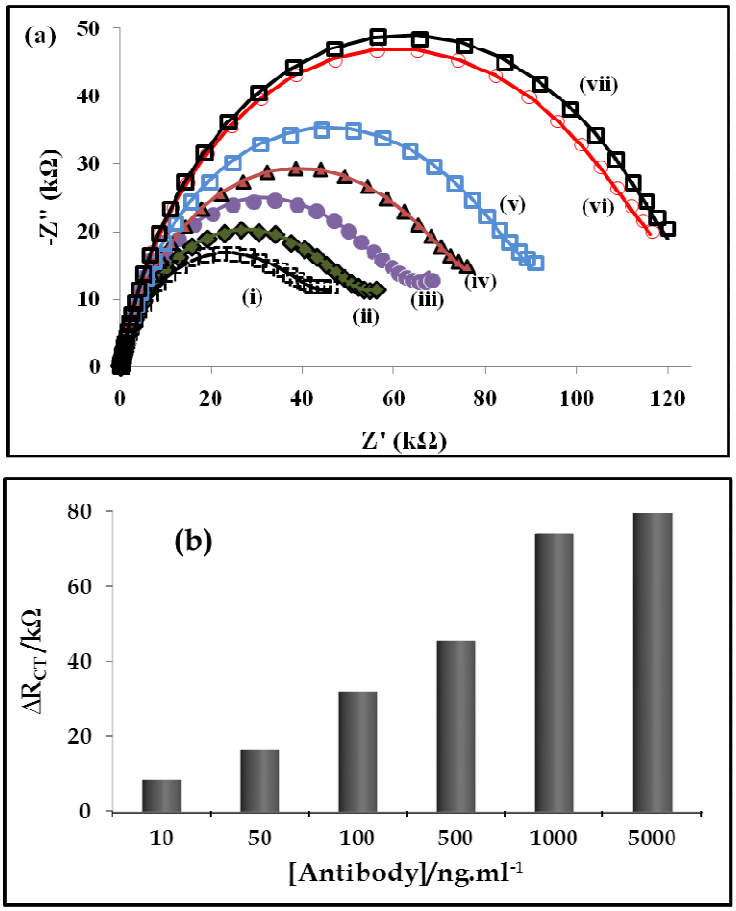

Figure 6.13: (a) Nyquist plots and (b) ΔR_{CT} versus [antibody] ranging from (10 ng.ml^{-1} – 5 µg.ml^{-1}) in (1:1) 1mM $K_3/K_4Fe(CN)_6$ solution containing 0.1 M KCl. Electrodes (i) Au-PEA-GA-antigen/BSA and varied [1°PAb] (ii) 10 ng.ml^{-1}, (iii) 50 ng.ml^{-1}, (iv) 0.1 µg.ml^{-1}, (v) 0.5 µg.ml^{-1}, (vi) 1.0 µg.ml^{-1}, and (vii) 5.0 µg.ml^{-1}.

6.3.1.3 Real sample analysis in human serum (HS) and newborn calf serum (NCS)

The measles-antigen modified (Au-PEA-GA-antigen/BSA) electrode was incubated for 40 minutes at 37°C into the human serum dilutions of (HS:buffer, µl:µl) of 1:100, 1:500, 1:1000, 1:2000 and 1:5000. Figure 6.14 shows Nyquist plots for the measles-antigen/BSA modified electrode before (i) and after incubating in (a) human serum for 40 minutes in (ii) 1:5000, (iii) 1:2000, (iv) 1:1000, (v) 1:500 and (vi) 1:100 dilutions,

(b) (i) measles-antigen modified electrode (Au-PEA-GA-antigen/BSA) and antibodies in NCS before (ii) and after (iii) antibody (5.0 $\mu g.ml^{-1}$, 1°PAb) injection and (c) the plot of ΔR_{CT} versus [serum dilution]. For the NCS, the negative serum (-ve NCS) refers to the serum without antibodies and positive serum (+ve NCS) referes to the serum which has been infected with antibody solution (5.0 $\mu g.ml^{-1}$).

Figure 6.14(a) exhibited an increase in R_{CT} with the increase in human serum (HS) concentration and this could be attributed to the HS antibodies binding to the measles-antigen. The World Health Organisation (WHO) together with the Department of Health (SA) through expanded programme of immunization (EPI-SA) stipulates that all the infants (>9 months) and children (<15 years) should be immunized against measles [376]. The antibodies due to measles are produced and increase in levels during immunization. Therefore, the human serum investigated in this work may contain measles-specific antibodies, especially IgG antibodies which are known to persist long after the infection and may still be present, hence giving the observed change in R_{CT} in Figure 6.14(a). The blocking of the antibodies in solution using measles-antigen, i.e. injecting measles-antigen (5 $\mu g.ml^{-1}$) into the HS solution, will deactivate the antibodies by blocking their measles-antigen binding site and therefore the antibodies will not bind to the surface immobilized measles-antigen. This resulted in a smaller R_{CT} value observed and clearly signifying that the species in the solution were not binding to the surface bound measles-antigen. The blocked HS or inhibited HS in Figure 6.14(c)(blue bar) showed negligible changes in R_{CT} values as compared to the human serum diluted as received, Figure 6.14(c)(red bar). This experimental observation led to a conclusion that the observed changes in the human serum were due to species that were binding to the antigen on the surface.

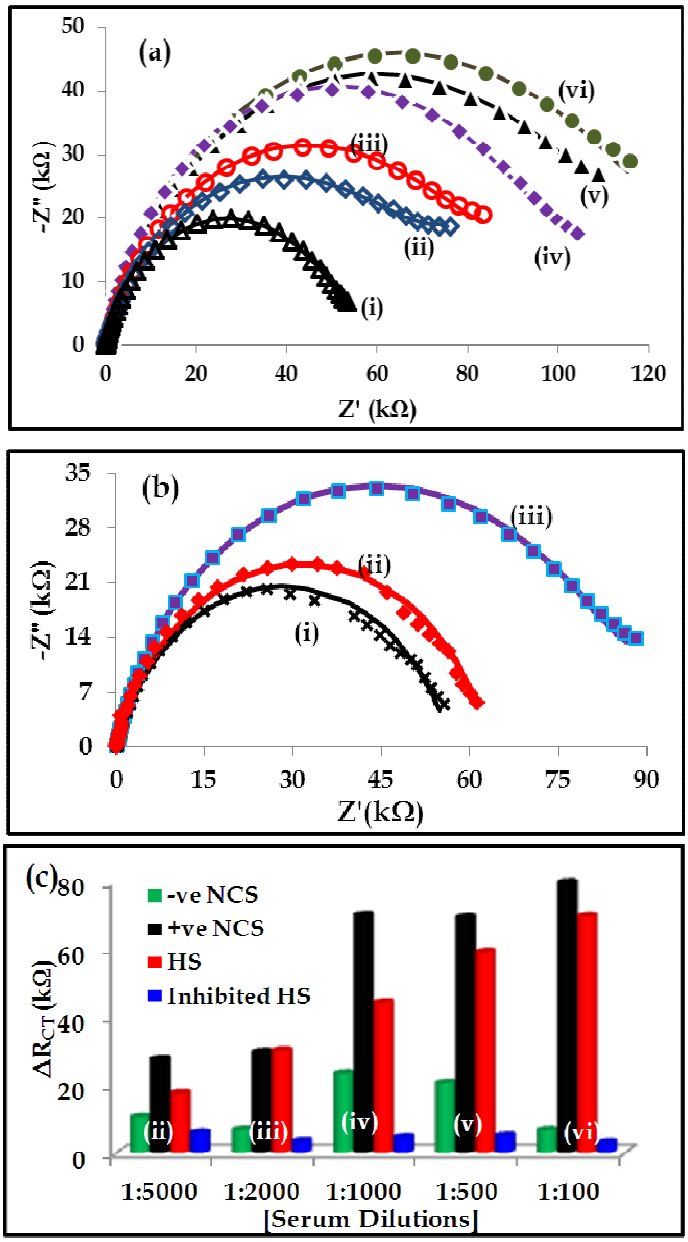

Figure 6.14: EIS showing interaction of the immobilized measles-antigen with antibodies in (a) HS (i) before and after (ii) 1:5000, (iii) 1:2000, (iv) 1:1000, (v) 1:500 and (vi) 1:100 dilutions, (b) (i) antigen\BSA and antibodies in NCS before (ii) and after (iii) spiking with antibody 1°PAb (5.0 µg.ml^{-1}) in (1:1) 1mM $K_3/K_4Fe(CN)_6$ solution containing 0.1 M KCl . (c) Bar chart showing the relationship between ΔR_{CT} vs [Serum Dilutions] labeled as (ii) – (vi) as in (a). Electrode: Au-PEA-GA-antigen/BSA.

The newborn calf serum (NCS) was also investigated. Figure 6.14(b)(ii) shows that in the negative serum, a slight increase of R_{CT} was observed and this may be attributed to physisorbed species from the serum. For positive (+ve) NCS at increasing [serial dilutions] an increase in R_{CT} was observed clearly confirmed the presence of the antibodies after antibody injection and binding to the surface immobilized measles-antigen. At the negative (-ve) NCS, the fluctuations in R_{CT} values were observed and much smaller than the values obtained at deliberately antibody infected solution, i.e. (+ve) NCS. These results highlight the important step towards the quest to find electrochemical based systems that can be used for the detection of immune-based reactions in a label-free manner.

6.3.2 Peroxidase labeled detection of measles-specific antibodies

The horse-radish peroxidase (HRP) enzyme is the most widely used enzyme for the conversion of H_2O_2 to water and this process result in the oxidation of an enzyme. The detection of H_2O_2 using HRP monitors the reduction of an enzyme to its native or stable oxidation state by losing electrons ($2e^-$), detectable electrochemically, equation 6.1. In this section, peroxidase enzymes are utilized as labels for the indirect detection of measles-specific antibodies (mimicking the ELISA) and using the method shown in Figure 1.3(a). Similar experimental setup to that of ELISA was used for the labeled detection of antibodies. However, instead of using ELISA microtitre plate, gold electrodes were modified as illustrated in Scheme 6.1 for the formation of the sensing layer. The detection mechanism studied will follow that of ELISA, i.e. looking at the (i) enzymatic reduction of H_2O_2 to H_2O (non-electrochemical), (ii) enzymatic oxidation of TMB (non-electrochemical) and (iii) monitoring the electron transfer during the electrochemical reduction of TMB (electrochemical step). The enzymatic steps (i) and (ii) are used for ELISA detection. The electrochemical

immunosensors utilizing TMB as a redox mediator for the detection of measles-specific antibody (1°PAb) will be employed and HRP conjugated secondary antibodies (HRP)2°PAb are used.

6.3.2.1 Enzymatic activity of HRP on the (HRP)2°PAb

The initial experiment conducted was to test the activity of the HRP bound to the secondary antibody (HRP-2°PAb). The secondary antibodies conjugated with HRP are used for the conversion and detection TMB to its oxidation products, this result in colour changes in ELISA and the products can also be monitored electrochemically. The use of (HRP)2°PAb in this section of work is due to the fact that they can bind to the primary antibodies (1°PAb) and allowing for its detection after binding to the measles-antigen as shown by the ELISA in Figure 6.2. The activity of the HRP to catalyse the oxidation of TMB was investigated using UV-vis spectroscopy where the oxidation of HRP on the (HRP)2°PAb was investigated. The HRP is known [34,272] to enzymatically catalyse the conversion of TMB into a blue coloured product (TMB) in the presence of H_2O_2 following the mechanism shown in equations 6.1 – 6.3 above. Since the antibodies are not electroactive, monitoring of the electroactive TMB will give an indication of the amount of the primary antibodies (1°PAb) bound onto the surface; as a result this method is an indirect detection of 1°PAb as compared to the direct detection method using impedance spectroscopy and CV as discussed above. The oxidation of TMB occur only in the presence of H_2O_2 which influences the enzymatic oxidation of antibody bound HRP from its native +3 oxidation state to the one with the oxidation state of +5. Figure 6.15 shows UV-vis spectral changes of (HRP)2°PAb (0.1 $mg.ml^{-1}$) (a) in the presence of H_2O_2 and (b) after introducing TMB.

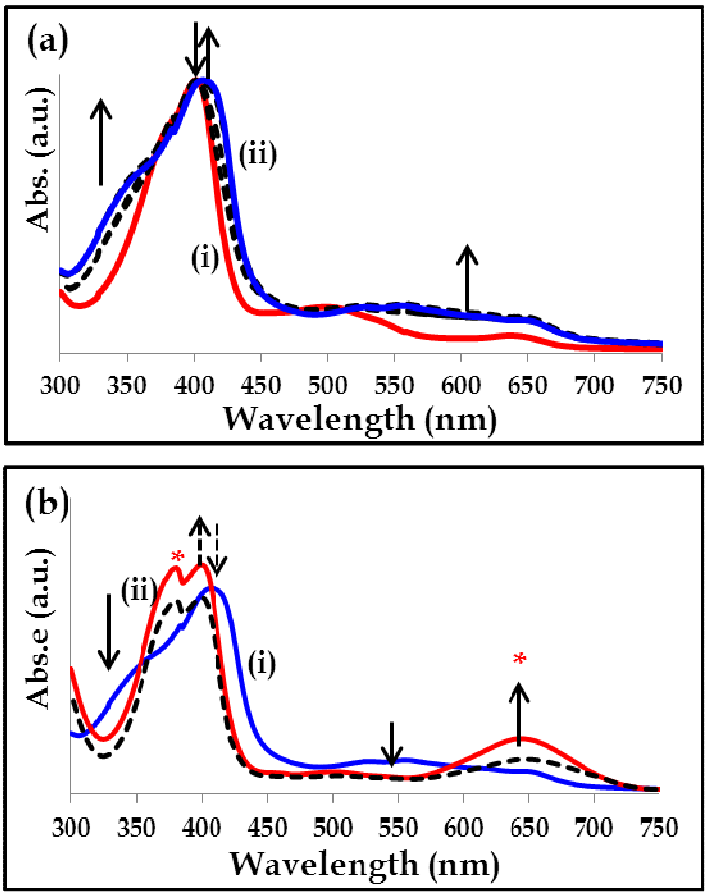

Figure 6.15: UV-vis spectral changes of (a) 0.1 mg.ml^{-1} (HRP)2°Ab (i) before and (ii) after 10 minutes in the presence of 20 µg.ml^{-1} H_2O_2 and (b) (i) before and (ii) after addition of 20 µg.ml^{-1} TMB. The spectrum (b)(i) is the same as (a)(ii). The dash line shows the spectrum during the experiment.

The spectrum in Figure 6.15(a)(i) shows an intense Soret band at 401 nm and this is typical of the HRP enzyme which consists of the redox active iron(III)pophyrin-like molecule [273,377]. In Figure 6.15(a), the 11 nm shift in the absorption peak for Soret band was observed from 401 nm for (HRP)2°PAb (+3) to 412 nm for (HRP)2°PAb (+5) and is attributed to the changes in oxidation states. Upon introducing TMB in the solution with +5 oxidised HRP in Figure 6.15(b), the Soret band absorption peak for the HRP (+5) at 412 nm shifted back to its original position 401 nm for HRP (+3) oxidation state. The movement of the Soret band to 401 nm was an indication of the

reduction of HRP (+5) back to its native oxidation state of +3. The TMB was consequently oxidized and the absorption peaks at 389 nm and 650 nm (marked by asterisk) are an indication of TMB oxidation products. The solution turned blue in colour indicating the oxidation of TMB to form TMB_{ox}. When the TMB was introduced to the HRP enzyme solution in the absence of H_2O_2, the spectrum observed was similar to that in Figure 6.15(a)(i) showing only the HRP absorption peak. TMB alone does not show any absorption peak when in solution [378]. Clearly this experiment confirms the activity of the HRP on the (HRP)2°PAb and also that the oxidation of TMB only takes place in the presence of H_2O_2 which initializes the enzymatic activity towards TMB. This experiment was used for the electrochemical detection of measles-specific antibodies using a immunoassay as illustrated in the design in Figure 6.16.

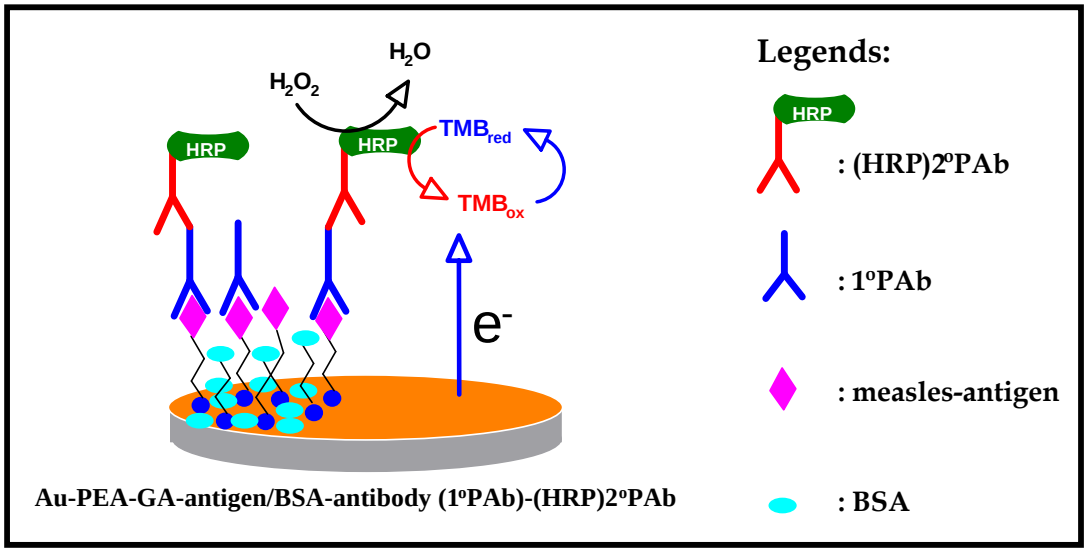

Figure 6.16: Electrochemical immunoassay detection of measles-specific antibodies using HRP-labeled secondary antibodies (HRP-2°PAb).

6.3.2.2 *Electrochemical detection of measles-specific antibodies using (HRP)2°PAb*

The electrode modified with measles-antigen was further exposed to the measles-specific antibody (1°PAb) solution (analyte solution) and followed by (HRP)2°PAb (detecting antibody), as shown in Figure 6.16. Figure 6.17 shows (a) cyclic voltammograms and (b) their corresponding bar chart showing the comparative current response during the electrochemical measurement in different solutions (i) pH 7.4, (ii) 20 µmol.l^{-1} H_2O_2, (iii) 20 µmol.l^{-1} TMB and (iv) 20 µmol.l^{-1} TMB + 20 µmol.l^{-1} H_2O_2.

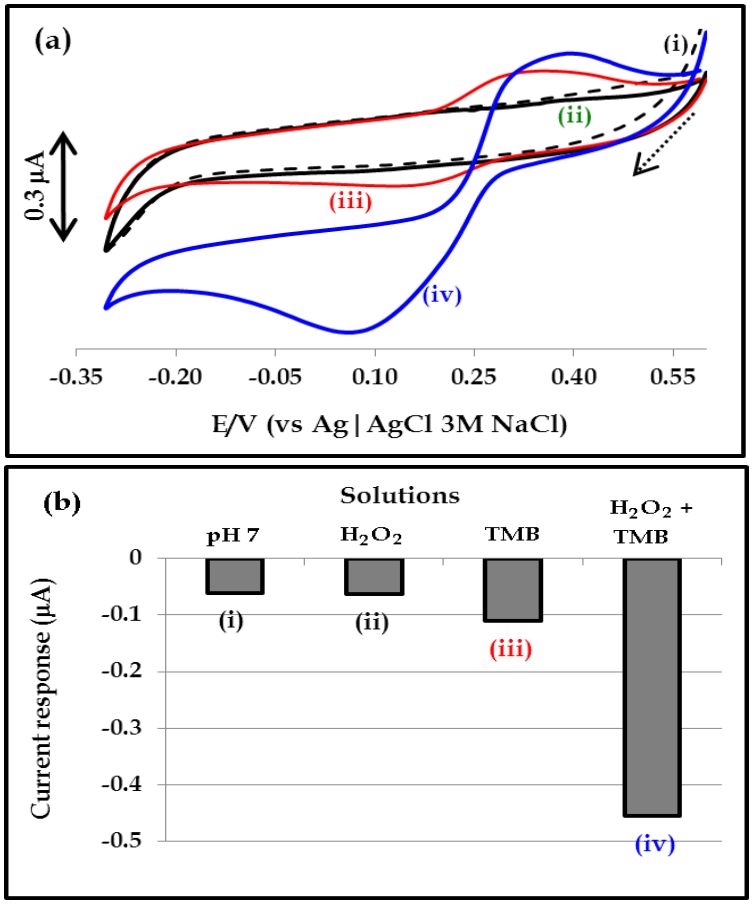

Figure 6.17: Cyclic voltammograms of (a) Au-PEA-GA-antigen/BSA-1°PAb-(HRP)2°PAb in (i) pH 7.4 (black dotted), (ii) 20 µM H_2O_2 (black solid), (iii) 20 µM TMB (red) and (iv) 20 µM TMB + 20 µM H_2O_2 (blue) and (b) bar chart showing the comparative current response at various detecting solutions. All potentials were obtained at 0.1 V. Scan rate 25 mV.s^{-1}.

From Figure 6.17(a)(i) in buffer alone and (ii) in 20 μM H_2O_2 there was no well defined peak observed. When TMB (20 μM) alone was introduced in Figure 6.17(a)(iii), a broad redox peak was observed at $E_{1/2}$ = 0.25 V, while the presence of 20 μM concentration for both H_2O_2 and TMB, Figure 6.17(a)(iv) resulted in a strong catalytic currents, with an increase in both the oxidation and reduction currents. The observed increase in the catalytic reduction peak currents has been shown before when HRP-labeled detection is utilized [228]. The increase in catalytic currents clearly demonstrates that an electrode prepared following the method as illustrated in Figure 6.16 is highly suitable for electrochemical immunoassay detection for the measles-specific antibodies. The respective catalytic currents are shown in Figure 6.17(b) in a bar chart. Clearly from the bar chart a strong catalytic currents were observed for the mixed H_2O_2 and TMB detecting solution. The importance of H_2O_2 for the initial enzymatic step is clearly demonstrated, as the catalytic current in the presence of TMB alone was very small when compared to when the both H_2O_2 and TMB were used. To demonstrate that the observed catalytic current was due to the (HRP)2°PAb, different electrodes, i.e. bare Au, Au-PEA, Au-PEA-GA-antigen/BSA, Au-PEA-GA-antigen/BSA-1°PAb and Au-PEA-GA-antigen/BSA-1°PAb-(HRP)2°PAb were studied. Figure 6.18 shows the (a) cyclic voltammograms and (b) bar chart (showing current responses) of 20 μM H_2O_2 + 20 μM TMB solution at various electrode surfaces, (i) bare Au, (ii) Au-PEA, (iii) Au-PEA-GA-antigen/BSA, (iv) Au-PEA-GA-antigen- 1°PAb and (v) Au-PEA-GA-antigen- 1°PAb-(HRP)2°PAb.

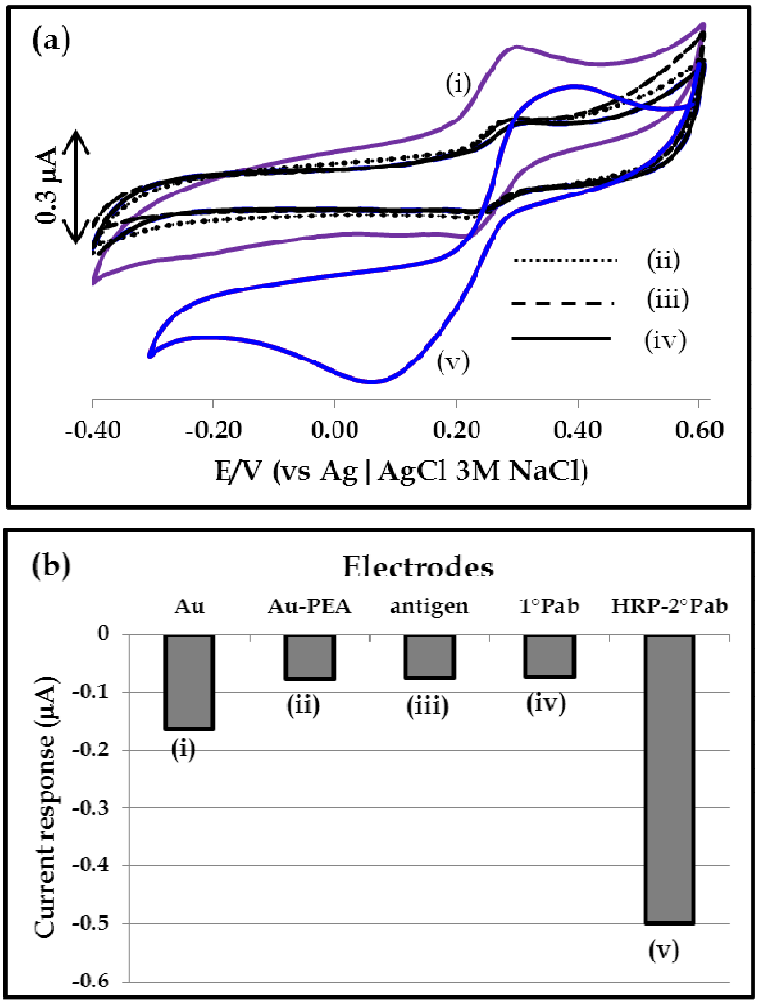

Figure 6.18: (a) Cyclic voltammograms and (b) catalytic current (bar chart) of (i) Au, (ii) Au-PEA, (iii) Au-PEA-GA-antigen/BSA, (iv) Au-PEA-GA-antigen/BSA-1°PAb and (v) Au-PEA-GA-antigen/BSA-1°PAb-(HRP)2°PAb in pH 7.4 + 20 µmol.l^{-1} TMB + 20 µmol.l^{-1} H_2O_2 solution. All potentials were obtained at 0.1 V. Scan rate 25 mV.s^{-1}.

At various electrodes a good increase in catalytic current was observed on the electrode modified with (HRP)2°PAb, in Figure 6.18(v). The bare gold electrode showed the redox peak at $E_{1/2}$ = 0.25 V due to TMB at the investigated concentrations. The observed redox peak due to TMB was suppressed at (ii) PEA, (iii) antigen/BSA and (iv) antibody (1°PAb) modified electrodes in Figure 6.18. This suppresion of the TMB peak was a confirmation of electrode modification and the

immobilization of PEA, antigen/BSA and 1°PAb. The cyclic voltammogram due to (HRP)2°PAb modified electrode was similar to the one observed in Figure 6.17(iv) as similar modified electrodes and solutions were used showing good catalytic currents. The perfomance of the designed immunosensor to varied antibody concentration follows.

6.3.2.3 Performance of the immunosensor at varied antibody (1°PAb) concentrations

All the electrodes contained (HRP)2°PAb. The performance of the immunosensor at varied antibody (1°PAb) concentrations ranging from 10 $ng.ml^{-1}$ to 10 $\mu g.ml^{-1}$ was studied. Figure 6.19 shows (a) the cyclic voltmmograms (forward scan only for clarity) recorded during the variation of antibody (1°PAb) concentrations ranging from (i) 10 $ng.ml^{-1}$ to (x) 10 $\mu g.ml^{-1}$; (b) shows the plot of catalytic current (I/nA) vs [1°PAb] $\mu g.ml^{-1}$; (c) is the linear calibration plotted on a semi log scale.

The increase in catalytic currents was observed as the antibody concentration increased, in Figure 6.19. The plot of catalytic currents gave a dose response curve shown in Figure 6.19(b). The dose response curve is similar to the one observed for the ELISA experiment measuring the increase in absorbance due to the increase in concentrations of measles-antigen. The catalytic currents exhibited a linear dependance on log[1°PAb] in Figure 6.19(c). The antigen modified electrode was sensitive for concentration as low as 10 $ng.ml^{-1}$. The sensitivity can be improved by incorporating nanomaterials as observed in literature [34]. The concentration of (HRP)2°PAb (= 50 $\mu g.ml^{-1}$) was kept constant for all the electrodes.

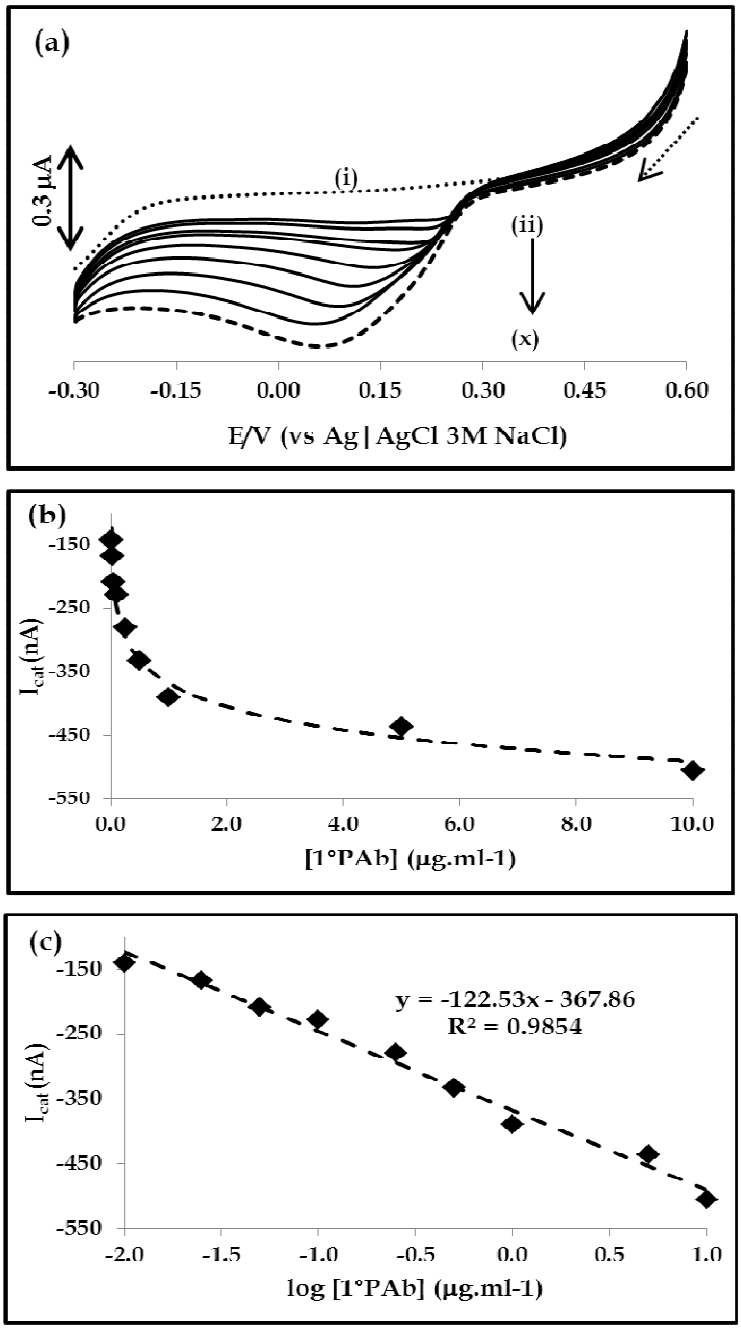

Figure 6.19: (a) Cyclic voltmmograms (forwad scan only for clarity) showing the variation of antibody(1°PAb) concentrations ranging from (i) 10 ng.ml^{-1} to (x) 10 µg.ml^{-1}; (b) plot of currents (I)/nA vs [1°PAb]/µg.ml^{-1} from the data obtained in (a); (c) is the linear calibration plotted on a semi log scale. Antibody(1°PAb) concentrations ranging from (i) 10 ng.ml^{-1} to (x) 10 µg.ml^{-1}. Electrode: Au-PEA-GA-antigen/BSA. [HRP-2°PAb] (= 50 µg.ml^{-1}) kept constant.

6.3.2.4 Real sample analysis (Human Serum and Newborn Calf Serum)

The newborn calf serum (NCS) and human serum (HS) were investigated for possible detection of antibodies present in the serum matrix with measles-antigen modified gold electrode surface. The measles-antigen modified gold electrode was immersed into either 0.1% HS or 0.1% NCS solutions followed by thorough rinsing with PBS (pH 7.4). The electrodes were further immersed in the (HRP)2°PAb solution with rinsing again. Scheme 6.3 shows the detection of antibodies (1°PAb) in 0.1% HS and NCS solution. After the experimental steps, the electrochemical measurements (cyclic voltammograms) were measured in pH 7.4 solution containing 20 µM TMB + 20 µM H_2O_2 and the electrochemical detection followed the mechanism in Figure 6.16.

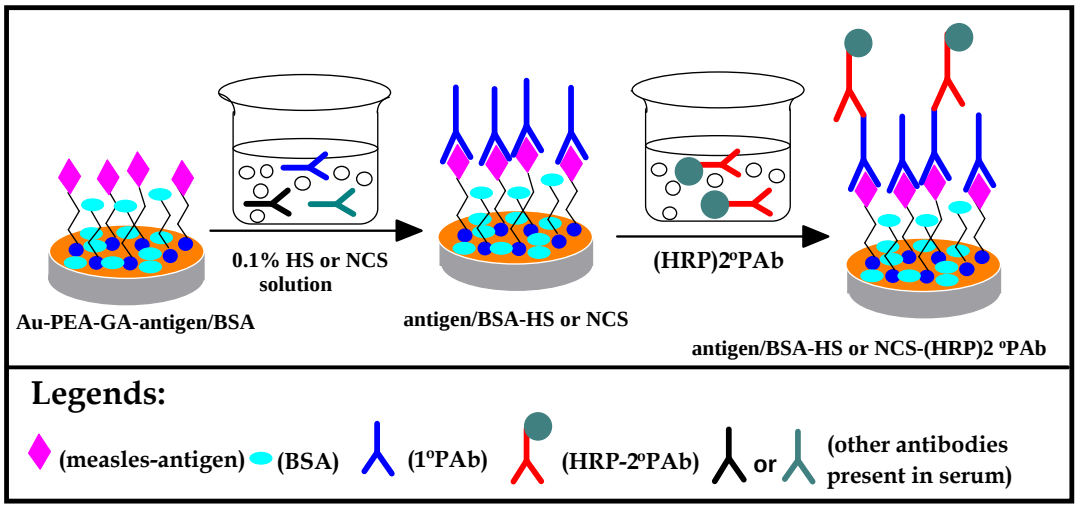

Scheme 6.3: Schematic representation of the detection of 1°PAb in 0.1% HS and 0.1% NCS sample matrix.

Figure 6.20 shows the (a) cyclic voltammograms and (b) bar chart (current response) of Au-PEA-GA-antigen/BSA electrode (i) before and after (ii) immersing in 0.1% HS

pH 7.4 buffer, (iii) 0.1% HS infected with 1°PAb (5 μg.ml^{-1}) and (iv) blocked 0.1% HS with 5 μg.ml^{-1} measles-antigen and all the electrodes were in the presence (HRP)2°PAb. The electrode (Au-PEA-GA-antigen/BSA) in Figure 6.20(a)(i) showed very small redox couple with small currents due to TMB. After the electrode was introduced into 0.1% HS, in Figure 6.20(a)(ii) an increase in the reduction current was observed. This increase in reduction current was attributed to the binding of antibodies available in solution onto the surface bound measles-antigen. When 0.1% HS was infected with 5.0 μg.ml^{-1} of 1°PAb, in Figure 6.20(a)(iii), higher reduction currents were observed due to an increasing concentrations of 1°PAb that are bound onto the electrode surface and more available binding sites on (HRP)2°PAb for electrochemical reduction of TMB. To confirm that the observed increase in current at 0.1% HS was due to antibodies in HS binding onto the measles-antigen, the blocking of the measles-antigen binding site on antibodies was conducted by injecting the 5.0 μg.ml^{-1} of measles-antigen in HS solution before immersing the electrode (Au-PEA-GA-antigen/BSA). Figure 6.20(a)(iv) shows the drastic decrease in catalytic currents (almost similar to the electrode with the antigen/BSA, i.e. Au-PEA-GA-antigen/BSA) for the blocked antibody solution. This clearly indicate that there are antibodies in the HS solution that binds to the measles-antigen on the surface and are blocked when 5.0 μg.ml^{-1} measles-antigen is introduced in HS solution. Figure 6.20(b) shows the relative catalytic peak currents obtained from the cyclic voltammograms in Figure 6.20(a) for the modified electrodes.

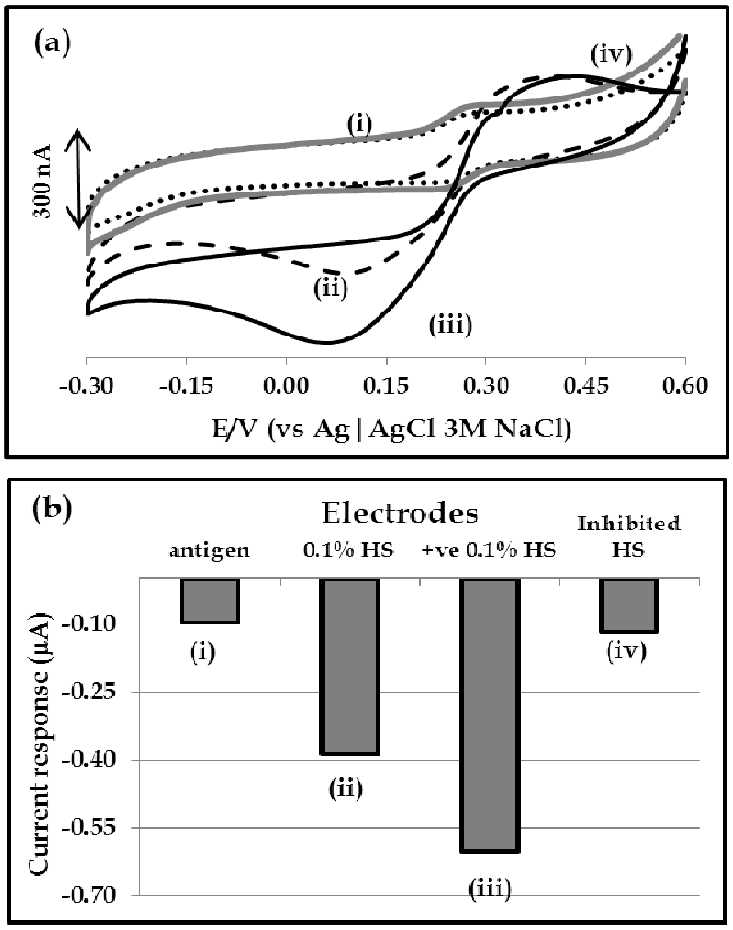

Figure 6.20: (a) Cyclic voltammograms and (b) bar chart (current response) of Au-PEA-GA-antigen/BSA electrode (i) as prepared and after immersing in (ii) 0.1% HS pH 7.4 buffer, (iii) 0.1% HS injected with 1°PAb (5 µg.ml^{-1}) and (iv) inhibited 0.1% HS with 5 µg.ml^{-1} antigen. All in the presence of (HRP)2°PAb and measured in pH 7.4 solution containing 20 µM TMB + 20 µM H_2O_2. +ve 0.1% HS = 0.1% HS + 5 µg.ml^{-1} 1°PAb. All potentials were obtained at 0.1 V. Scan rate 25 mV.s^{-1}.

The NCS was also investigated and Figure 6.21 shows the (a) cyclic voltammograms and (b) bar chart (comparative current response) of Au-PEA-GA-antigen/BSA electrode (i) before and after immersing in (ii) 0.1% NCS and (iii) 0.1% NCS infected with 1°PAb (5 µg.ml^{-1}). All the electrodes were in the presence of (HRP)2°PAb. The negative serum (-ve NCS) refers to NCS alone and positive serum (+ve NCS) refers to

the serum infected deliberately with 5 µg.ml^{-1} antibody (1°PAb) solution to mimic an infected sample.

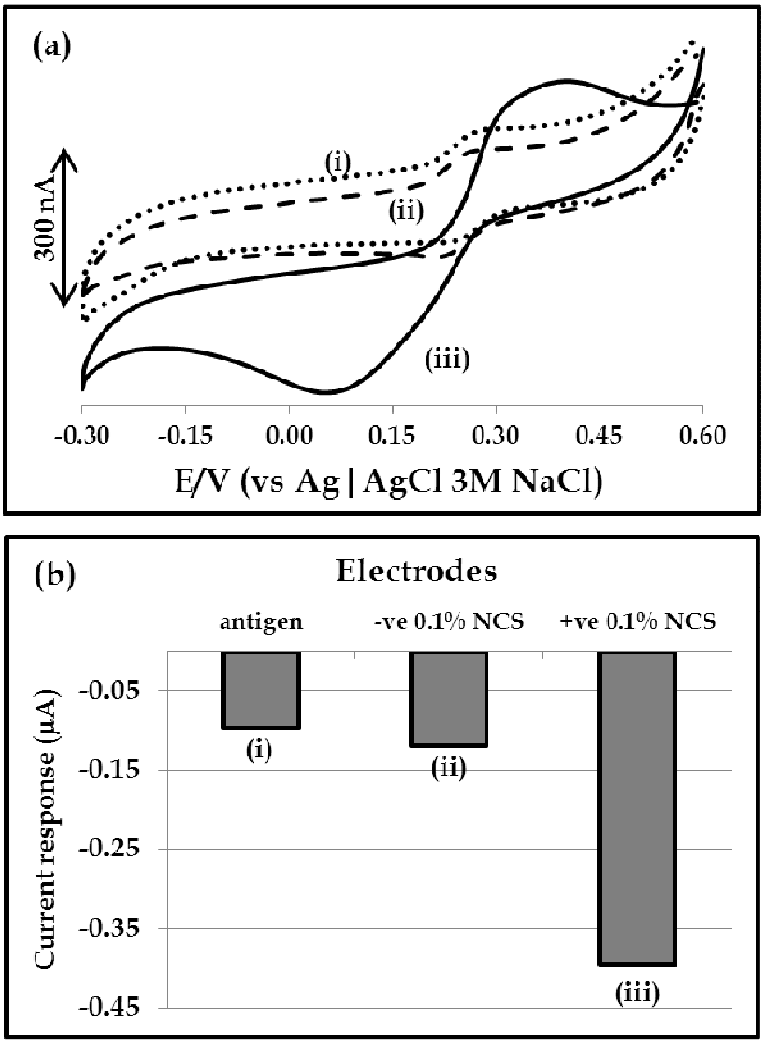

Figure 6.21: (a) cyclic voltammograms and (b) bar chart (comparative current response) of Au-PEA-GA-antigen/BSA electrode (i) before and after immersing in (ii) 0.1% NCS pH 7.4 buffer and (iii) 0.1% NCS injected with 1°PAb (5 µg.ml^{-1}). All in the presence of (HRP)2°PAb and measured in pH 7.4 solution containing 20 µM TMB + 20 µM H_2O_2. +ve 0.1% NCS = 0.1% NCS + 5 µg.ml^{-1} 1°PAb. All potentials were obtained at 0.1 V. Scan rate 25 mV.s^{-1}.

The electrodes with the antigen/BSA and 0.1% NCS alone, in Figure 6.21(a)(i and ii) gave almost similar cyclic voltammograms with no noticeable catalytic currents. The

lack of observable increase currents clearly shows that there is no interfering species with the measles-antigen in the negative serum (-ve NCS). However, when the serum 0.1% NCS was deliberately infected with the 5 $\mu g.ml^{-1}$ 1°PAb (+ve NCS), the increase in current was observed, Figure 6.21(a)(iii). All the electrodes studied were in the presence of (HRP)2°PAb. The increase in catalytic currents are an indication that the electrode can selectively detect the antibodies in the complex NCS sample matrix. The studies conducted here clearly show the potential use of these electrode systems for the detection of measles-specific IgG antibodies.

In conclusion, this chapter demonstrated the design of electrochemical immunosensor using the intimate and covalent immobilization of measles-antigen onto gold electrode surface. The detection of measles-specific (IgG) antibodies (1°PAb) was shown to be possible using two methods, i.e. label-free (impedance) and HRP-labeled detection methods. The use of measles-antigen modified gold surfaces was also possible in various samples representing or mimicking real samples, i.e. human serum and newborn calf serum. The modified surfaces could selectively detect antibodies in these solution as the increase in currents and charge-transfer resistane was observed.

CONCLUSIONS

CONCLUSIONS

The aim of this work was to study several electrode modification methods with electrocatalytic materials such as metallophthalocyanine (MPc) and investigate their potential use for the design of electrochemical sensors. The use of these electrochemical sensors was demonstrated towards the detection of H_2O_2, a very important biological and environmental molecule. Electrodes modified with MPc complexes were characterized using various surface techniques and these confirmed the modification of the electrode surfaces. The used surface characterization methods were in agreement with each other as these confirmed the presence of the thin films due to phthalocyanine molecules.

The synthesis and characterization of new thiol derivatised MPc complexes containing cobalt and manganese as metal ions centers and bearing octahexylthio groups on the phthalocyanine ring was accomplished. The characterization of these new complexes was achieved using spectroscopic and electrochemical methods which confirmed the succesful synthesis of these complexes. The use of these new complexes for the formation of thin films onto gold electrode surfaces using self-assembly method was studied. The self-assembled monolayers (SAMs) formation was confirmed using various electrochemical and microscopic methods. The electrochemical sensing using the SAMs modified gold electrodes were investigated for the detection of hydrogen peroxide (H_2O_2) and these systems gave good analytical properties.

The cobalt and manganese tetraamino phthalocyanine were also studied for their thin film forming capabilities on various electrode surfaces, i.e. glassy carbon, gold and indium tin oxide (ITO) surfaces. The polymer modified electrodes were further

used for the electrocatalytic detection of H_2O_2 with success. The tetraamino phthalocyanine complexes were further immobilized onto screen-printed gold electrode (SPAuE) using covalent immobilization method for monolayer thin films formation. The modified SPAuE surfaces were characterized using electrochemical (cyclic voltammetry and impedance spectroscopy), spectroscopic (Raman spectroscopy and X-ray photoelectron spectroscopy) and microscopic (atomic force microscopy and scanning electron microscopy) methods. The monolayer modified screen-printed gold electrodes gave good catalytic properties towards the detection of H_2O_2.

Furthermore, the metal tetraamino phthalocyanine (MTAPc) were studied their conjugation onto carbon nanotubes modified electrode following a Schiff-base surface reactions. The immobilized carbon nanotubes and MTAPc hybrid systems were also studied for their thin film forming properties with surfaces characterization techniques; based on electrochemical, spectroscopic and microscopic methods. All the studied surface characterization methods were in agreement with each other in confirming the modification of electrodes with carbon nanotube-MTAPc conjugates. The modified electrodes were then investigated for their electrocatalytic properties towards the detection of H_2O_2.

The electrocatalytic and electroanalysis studies towards H_2O_2 detection showed that this is a metal mediated reaction. The metal ions from the immobilized electrocatalysts were taking active role in the electrocatalytic step. At the CoPc modified electrode surface and in buffer alone or electrolyte solution, the metal redox processes were observed for Co^{II}/Co^{I} or Co^{III}/Co^{II}, depending on the potential range scanned. The MnPc modified electrode surface in buffer or electrolyte solution alone also showed the metal redox processes due to Mn^{III}/Mn^{II} and Mn^{IV}/Mn^{III} depending on the potential range scanned. The metal redox processes were observed at potential

between 0 to -0.6 V in pH 7.4 buffer solution. In the presence of analyte (H_2O_2) the increase in peak currents was observed clearly indicating the electrocatalysis of H_2O_2. The H_2O_2 electrocatalytic peak currents showed a well-resolved peak at potentials close to where the metal reduction peaks occurred indicating the involvement of the metal ions in the catalytic process. The modified electrode gave good electronalytical properties and the surfaces were reproducible with good stability.

Chronoamperometry was used to study the electroanalytical parameters of the modified electrodes. All the modified electrodes gave good limits of detection in the order of 10^{-7} M. The electrodes displayed good linearity in the concentration ranges studied; i.e. 9.90 – 74.07 µM for SAMs, 0.99 – 8.26 µM for the GCE-polyMTAPc, 0.50 – 4.46 µM for Au-polyMTAPc, 1.0 – 30.0 µM for SPAuE-PA-MTAPc and SPAuE-PA-SWCNT-MTAPc modified electrodes. The modified electrodes gave good sensitivity, i.e. 0.068 – 0.262 $mA.mM^{-1}.cm^{-2}$ for SAMs, 6.00 – 15.40 $mA.mM^{-1}.cm^{-2}$ for polyMTAPc, 0.15 – 0.19 $mA.mM^{-1}.cm^{-2}$ for PA-MTAPc and 2.79 – 5.16 $mA.mM^{-1}.cm^{-2}$ for PA-SWCNT-MTAPc modified electrodes. The sensitivity of the modified electrodes was increasing in this order (according to the method of modification): SAMs ≤ PA-MTAPc < PA-SWCNT-MTAPc < Au-polyMTAPc < GCE-polyMTAPc.

The electrochemical immunosensor design for the detection of measles-specific antibody (1°PAb) was studied. The studies showed that the covalent immobilization of the measles-antigen as asensing layer was accomplished. The characterization of modified surfaces using electrochemical and microscopic method confirmed the modification of PEA via grafting method and the immobilization measles-antigen on the PEA-glutaraldehyde activated electrode surface. The QCM-D characterization also showed the immobilization of measles-antigen as a visco-elastic layer. The covalent attachment method was preferred to the physical adsorption method which showed that the measles-antigen does not attach itself onto the gold electrode

surface. The mass loading of measles-antigen was found to be 602 ng.cm^{-2} and this interacted with the antibody which gave mass loading of about 224 ng.cm^{-2}. The use of QCM-D also confirmed the film thickness of the measles-antigen (6.016 nm) and 8.689 nm for an antibody. The detection of measles-specific antibodies was accomplished using impedance and voltammetric methods. Both these methods confirmed the binding of measles-antigen with an antibody (forming an immune complex) and the surface changes could be monitored impedometrically in a label-free manner and using horse-radish peroxidase conjugated secondary antibody as an electrochemical reporter. The immunosensor studies for the detection of measles-antibodies in human serum and newborn calf serum were successful.

Recommendation and future outlook

The systems studied here for the detection of H_2O_2 may further be used for the detection of any enzymatic reactions that produces H_2O_2 as a by-product; e.g. conversion and detection of glucose by glucose oxidase. Furthermore, nanomaterial conjugates with MPc is still an area that needs to be explored and the systems will give enhanced analytical properties for the detection of various other analytes of interest. The use of nanomaterials for the fabrication of immunosensor is still a growing field of research and the nanomaterial based systems may give very low limits of detection required for an early disease and virus detection.

REFERENCES

[1] X. Zhang, H. Ju, J. Wang, in *Electrochemical Sensors, Biosensors and Their Biomedical Applications*, First Edition, Academic Press, New York, 2008.

[2] S. Alegret, A. Merkoci, in *Electrochemical Sensor Analysis*, First Edition, Elsevier, Amsterdam, 2007, Volume 49.

[3] P. D'Orazio, *Clin. Chim. Acta* 2011 (**412**) 1749.

[4] P. D'Orazio, *Clin. Chim. Acta* 2003 (**334**) 41.

[5] S. Rodriguez-Mozaz, M.P. Marco, M. J. Lopez de Alda, D. Barcelo, *Anal. Bioanal. Chem*. 2004 (**378**) 588.

[6] S. Rodriguez-Mozaz, M. P. Marco, M. J. Lopez de Alda, D. Barcelo, *Talanta* 2005 (**65**) 219.

[7] S. Rodriguez-Mozaz, M. J. Lopez de Alda, *Anal. Bioanal. Chem*. 2006 (**386**) 1025.

[8] A. K. Wanekaya, W. Chen, A. Mulchandani, *J. Environ. Monit*. 2008 (**10**) 703.

[9] J. Wang, G. Rivas, X. Cai, E. Palecek, P. Nielsen, H. Shiraishi, N. Dontha, D. Luo, C. Parrado, M. Chohcarro, P. A. M. Farias, F. S. Valera, D. H. Grant, M. Ozsoz, M. N. Flair, *Anal. Chim. Acta* 1997 (**347**) 1.

[10] K. R. Rogers, *Biosens. Bioelectron.* 1995 (**10**) 533.

[11] K. R. Rogers, *Anal. Chim. Acta* 2006 (**568**) 222.

[12] M. L. Evenson, M. Ward Hinds, R. S. Bernstein, M. S. Bergdoll, *Int. J. Food Microbiol*. 1988 (**7**) 311.

[13] B. Pejcic, R. DeMarco, G. Parkinson, *Analyst* 2008 (**131**) 1079.

[14] L. R. Goulart, C. U. Vieira, A. P. P. Freschi, F. E. Capparelli, P. T. Fujimura, J. F. Almeida, L. F. Ferreira, I. M. B. Goulart, A. G. Brito-Madurro, J. M. Madurro *Crit. Rev. Immun*. 2010 (**30**) 201.

[15] E. Palecek, E. Scheller, J. Wang in *Electrochemistry of Nucleic Acids and Proteins*, First Edition Perspectives in Bioanalysis, Volume 1, Elsevier, 2005.

[16] A. Nezich, *Microbiol. Mol. Gen.* 2007 (**3**) 80.

[17] N. J. Rankainen, H. B. Halsall, W. R. Heineman, *Chem. Soc. Rev.* 2010 (**39**) 1747.

[18] A. Heller, B. Feldman, *Acc. Chem. Res*. 2010 (**43**) 963.

[19] J. Wang, *Electroanal.* 2001 (**13**) 983.

[20] A. Voller, A. Bartlett, D. E. Bidwell, *J. Clin.Path.* 1978 (**31**) 507.

[21] J. R. North, *Trends Biotechnol.* 1985 (**3**) 180.

[22] A. Sobarzo, J. T. Paweska, S. Herrmann, T. Amir, R. S. Marks, L. Lobel, *J. Virol. Methods,* 2007 (**146**) 327.

[23] J. Wang, *Biosens. Bioelectron.* 2006 (**21**) 1887.

[24] F.R.R. Teles, L.P. Fonseca, *Talanta* 2008 (**77**) 606.

[25] A. L. Ghindilis, P. Atanosov, M. Wilkins, E. Wilkins, *Biosens. Bioelectron.* 1998 (**13**) 113.

[26] P. Currie, J. C. Currie, *Comput. Rend. Acad. Sci. Paris* 1880 (**91**) 294.

[27] M. Rodahl, F. Hook, A. Krozer, P. Brzezinski, B. Kasemo, *Rev. Sci. Instrum.* 1995 (**66**) 3294.

[28] M. Rodahl, B. Kasemo, *Rev. Sci. Instrum*. 1996 (**67**) 3238.

[29] M. Rodahl, *On the frequency and Q-factor response of the quartz crystal microbalance to liquid overlayers*, PhD Thesis, Chalmers (1995).

[30] U. Jonsson, L. Fagerstam, B. Ivarsson, B. Jonsson, R. Karlsson, K. Lundh, S. Lofas, B. Persson, H. Ross, I. Ronnberg, S. Sjolander, E. Stenberg, R. Stahlberg, C. Urbaniczky, H. Ostlin, M. Malmqvist, *Biotechnologies* 1991 (**11**) 620.

[31] M. Piliarik, H. Vaisocherová, J. Homola, *Surface Plasmon Resonance Biosensing* in *Biosensors and Biodetection Methods in Molecular Biology*, 2009, Volume 503, I, 65-88.

[32] J. M. Fowler, D. K. Y. Wong, H. B. Halsall, W. R. Heinemann, in *Electrochemical Sensors, Biosensors and their Biomedical Applications*, Eds. X. Xhang, H. Ju, J. Wang, First Edition, Academic Press (2008) Chapter 5, pp 115-143.

[33] S. Piermarini, L. Micheli, N.H.S. Ammida, G. Palleschi, D. Moscone, *Biosens. Bioelectron.* 2007 (**22**) 1434.

[34] G. K. Ahirwal, C. K. Mitra, *Biosens. Bioelectron.* 2010 (**25**) 2160.

[35] N. S. Mathebula, J. Pillay, G. Toschi, J. A. Verschoor, K. I. Ozoemena, *Chem. Commun*. 2009, 3345.

[36] R. Maalouf, C. Fournier-Wirth, J. Coste, H. Chebib, Y. Saikali, O. Vittori, A. Errachid, J.-P. Cloarec, C. Martelet, N. Jaffrezic-Renault, *Anal. Chem.* 2007 (**79**) 4879.

[37] O. A. Sadik, A. O. Alouch, A. Zhou, *Biosens. Bioelectron*. 2009 (**24**) 2749.

[38] P.U. Abel, T. van Woedtke, *Biosens. Bioelectron*. 2002 (**17**) 1059.

[39] R. I. Stefan, H. Y. Aboul-Eneim, J. F. van Staden, *Sens. Update* 2002 (**10**) 123.

[40] S. Subrahymanyann, S. A. Piletsky, A. P. F. Turner, *Anal. Chem*. 2002 (**74**) 3942.

[41] M. Cardoso, S. Birch, J. Talbot, A. Phhillips, *J. Electroanal*. 1991 (**3**) 169.

[42] J. L. Brooks, M. B. Mirhabibollahy, R. G. Kroll, *J. Appl. Bacteriol*. 1992 (**73**) 189.

[43] D. Trau, T. Theueler, M. Wilmer, M. Meusel, F. Spener, *Biosens. Bioelectron*. 1997 (**12**) 499.

[44] P. Skladal, *Electroanal.* 1997 (**9**) 737.

[45] F. Ricci, G. Vople, L. Micheli, G. Palleschi, *Anal. Chim. Acta* 2007 (**605**) 111.

[46] N. J. Ronkainen, H. B. Halsall, W. R. Heineman, *Chem. Soc. Rev*. 2010 (**39**) 1747.

[47] R.M. Carter, M. A. Poli, M. Pesavento, D. E. T. Sibley, G. J. Lubrano, G. G. Guilbault, *Immunomethods* 1993 (**3**) 128.

[48] R. Krishnan, A. L. Ghindilis, P. Atanasov, E. Wilkins, *Anal. Lett*. 1998 (**123**) 1303.

[49] T. Kalab, P. Skladal, *Anal. Chim. Acta* 1995 (**304**) 361.

[50] M. Del Carl, M. Mascini, *Anal. Chim. Acta* 1996 (**336**) 167.

[51] G. Volpe, D. Compagnone, R Draisci, G. Palleschi, *Analyst* 1998 (**123**) 1303.

[52] P. Gregory, *J. Porphyrins Phthalocyanines* 2000 (**4**) 432.

[53] N. B. McKeown, *Chem. Ind.* 1999, 92.

[54] E. A. Luckyanets, *J. Porphyrins Phthalocyanines* 1999 (**3**) 424.

[55] J. D. Spikes *J. Photochem. Photobiol.* 1986 (**43**) 691.

[56] I. Rosenthal, E. Ben-Hur in *Phthalocyanine: Properties and Applications,* eds. C. C. Leznof, A. B. P. Lever, VCH Publishers, New York, 1989, Volume 1.

[57] R. Bonnett *In Chemical Aspects of Photodynamic Therapy*, Gordon and Breach Science, Canada, (2000).

[58] A. W. Snow, W. R. Barger in *Phthalocyanine: Properties and Applications,* eds. eds. C. C. Leznoff, A. B. P. Lever, VCH Publishers, New York, 1989, Volume 1.

[59] J. H. Zagal, F. Bedioui, J.-P. Dodelet, in *N4-Macrocylic Metal Complexes,* Springer, 2006.

[60] M. J. Stillman, T. Nyokong, *In Phthalocyanines: Properties and Applications,* eds. Leznoff. C.C. and Lever, A. B. P., VCH Publishers: New York, Volume 3, (1993).

[61] D. Wöhrle and V. Schmidt, *J. Chem. Soc., Dalton Trans.*1988, 549.

[62] M. Hanack, P. Haisch and H. Lehman, *Synthesis*, 1993, 387.

[63] D. Wöhrle, M. Eskes, K. Shigehara and A. Yamada, *Synthesis*, 1993, 194.

[64] A. G. Gürek and Ö. Bekaroğlu, J. *Chem. Soc., Dalton Trans*., 1994, 1419.

[65] G. Mbambisa, P. Tau, E. Antunes, T. Nyokong, *Polyhedron* 2007 (**26**) 5355.

[66] T. B. Ogunbayo, T. Nyokong, *Polyhedron* 2009 (**28**) 2710.

[67] K. Ozoemena, P. Westbroek, T. Nyokong *Electrochem. Comm.* 2001 (**3**) 529.

[68] K. I. Ozoemena, T. Nyokong, P. Westbroek *Electroanal.* 2003 (**15**) 1762.

[69] K. Ozoemena, P. Westbroek, T. Nyokong *J. Porphyrins Phthalocyanines* 2002 (**6**) 98.

[70] K. Ozoemena, P. Westbroek, T. Nyokong, *Electrochim. Acta* 2002 (**47**) 4035.

[71] O. A. Osmanbas, A. Koca, I. Ozcesmeci, A. I. Akur, A. Gul *Electrochim. Acta* 2008 (**53**) 4969.

[72] T. Ceyhan, A. Altindal, M. K. Erbil, O. Bekaroglu *Polyhedron* 2006 (**25**) 737.

[73] T. Ceyhan, A. Altindal, A. R. Ozkaya, M. K. Erbil, O. Bekaroglu *Polyhedron* 2007 (**26**) 73.

[74] T. V. Basova, A. G. Gurek, D. Atilla, A. K. Hassan, V. Ahsen *Polyhedron* 2007 (**26**) 5045.

[75] G. Mbambisa, N. Nombona, T. Nyokong *Microchem. J.* 2009 (**93**) 60.

[76] I. A. Akinbulu, S. Khene, T. Nyokong *Electrochim. Acta* 2010 (**55**) 7085.

[77] S. Khene, D. A. Geraldo, C. A. Togo, J. Limson, T. Nyokong *Electrochim. Acta* 2008 (**54**) 183.

[78] B. Agboola, T. Nyokong *Electrochim. Acta* 2007 (**52**) 5039.

[79] B. Agboola, P. Westbroek, K. I. Ozoemena, T. Nyokong *Electrochem. Comm.* 2007 (**9**) 310.

[80] Z. Li, M. Lieberman, W. Hill *Langmuir* 2001 (**17**) 4887.

[81] D. J. Revell, I. Chambrier, M. J. Cook, D. A. Russell *J. Mater. Chem.* 2000 (**10**) 31.

[82] B. Agboola, K. I. Ozoemena, T. Nyokong *Electrochim. Acta* 2006 (**51**) 6470.

[83] B. Agboola, T. Nyokong *Talanta* 2007 (**72**) 691.

[84] B. Agboola, T. Nyokong *Anal. Chim. Acta* 2007 (**587**) 116.

[85] B. Agboola, K. I. Ozoemena, P. Westbroek, T. Nyokong *Electrochim. Acta* 2007 (**52**) 2520.

[86] M. Nicolau, B. del Rey, T. Torres, C. Mingotaud, P. Delhaes, M. J. Cook, S. C. Thorpe, *Synth. Met*. 1999 (**102**) 1462.

[87] T. R. E. Simpson, D. A. Russell, I. Chambrier, M. J. Cook, A. B. Horn, S. C. Thorpe *Sens. Actuat. B* 1995 (**29**) 353.

[88] M. A. Gulppi, M. A. Paez J. A. Costamagna, G. Cardenas-Jiron, F. Bedioui, J. H. Zagal *J. Electroanal. Chem.* 2005 (**580**) 50.

[89] S. Griveau, M. Gulppi, J. Paez, J. H. Zagal, F. Bedioui *Electroanal.* 2003 (**15**) 779.

[90] S. Griveau, M. Gulppi, F. Bedioui, J. H. Zagal *Solid State Ionics* 2004 (**169**) 59.

[91] S. Griveau, J. Pavez, J. H. Zagal, F. Bedioui *J. Electroanal. Chem*. 2001 (**497**) 75.

[92] A. Goux, F. Bedioui, L. Robbiola, M. Paez *Electroanal.* 2003 (**15**) 969.

[93] J. S. Cortes, S. G. Granados, A. A. Ordaz, J. A. L. Jimenez, S. Griveau, F. Bedioui *Electroanal.* 2007 (**19**) 61.

[94] Y.-H. Tse, P. Janda, H. Lam, A. B. P. Lever *Anal. Chem.* 1995 (**67**) 9981.

[95] M. P. Somashekarrapa, S. Sampath *Chem. Comm.* 2002, 1262.

[96] J. Zhu, Y. Shen, F. Gu, J. Tao, J. Zhang *Mater. Lett.* 2007 (**61**) 1296.

[97] J. Pillay, K. I. Ozoemena *Chem. Phys. Lett.* 2007 (**441**) 72.

[98] S. Zhang, W.-L. Sun, Y.-Z. Xian, W. Zhang, L.-T. Jin, K. Yamamoto, S. Tao, J. Jin *Anal. Chim. Acta* 1999 (**399**) 213.

[99] P. Ardiles, E. Trollund, M. Isaacs, F. Armijo, J. C. Canales, M. J. Aguirre, M. J. Canales *J. Mol. Cat. A: Chem* 2001 (**165**) 169.

[100] E. Trollund, P. Ardiles, M. Aguirre, S. R. Biaggio, R. C. Rocha-Fihlo *Polyhedron* 2000 (**19**) 2303.

[101] Q.-Y. Peng, T. F. Guarr, *Electrochim. Acta* 1994 (**39**) 2629.

[102] K. L. Brown, J. Shaw, M. Ambrose, H. A. Mattola *Microchem. J.* 2002 (**72**) 285.

[103] F. Matemadombo, P. Westbroek, T. Nyokong, K. Ozoemena, K. de Clerk, P. Kiekens *Electrochim. Acta* 2007 (**52**) 2024.

[104] O. El Mouahid, C. Coutanceau, E. M. Belgsir, P. Crouigneau, J. M. Leger, C. Lamy *J. Electroanal. Chem.* 1997 (**426**) 117.

[105] J. Obirai, T. Nyokong *Electrochim. Acta* 2004 (**49**) 1417.

[106] J. Obirai, T. Nyokong, *J. Electroanal. Chem.* 2004 (**573**) 77.

[107] N. Nombona, P. Tau, N. Sehlotho, T. Nyokong *Electrochim. Acta* 2008 (**53**) 3139.

[108] C. Barrera, I. Zhukov, E. Villagra, F. Bedioui, M. A. Paez, J. Costamagna, J. H. Zagal *J. Electroanal. Chem.* 2006 (**589**) 212.

[109] J. H. Zagal, M. A. Gulppi, C. A. Caro, G. I. Cardenas-Jiron *Electrochem. Comm.* 1999 (**1**) 389.

[110] J. H. Zagal, M. A. Gulppi, G. Cardenas-Jiron *Polyhedron* 2000 (**19**) 2255.

[111] M. Gulppi, S. Griveau, F. Bedioui, J. H. Zagal *Electrochim. Acta* 2001 (**46**) 3397.

[112] K. L. Brown, H. A. Mottola *Langmuir* 1998 (**14**) 3411.

[113] M. P. Somashekarrapa, J. Keshavayya, S. Sampath *Pure Appl. Chem.* 2002 (**74**) 1609.

[114] K. I. Ozoemena, T. Nyokong, D. Nkosi, I. Chambrier, M. J. Cook *Electrochim. Acta* 2007 (**52**) 4132.

[115] K. I. Ozoemena, J. Pillay, T. Nyokong *Electrochem. Comm.* 2006 (**8**) 1391.

[116] M. P. Siswana, K. I. Ozoemena, T. Nyokong *Electrochim. Acta* 2006 (**52**) 114.

[117] Z. Zhao, A. Ogunsipe, M. D. Maree, T. Nyokong, *J. Porphyrins Phthalocyanines* 2005 (**9**) 186.

[118] M. D. Maree, N. Kuznetsova, T. Nyokong, *J. Photochem. Photobiol. A: Chem*. 2001 (**140**) 117.

[119] M. J. Cook, *Chem. Rev*. 2002 (**4**) 225.

[120] N. Nombona, T. Nyokong, *Dyes and Pigments* 2009 (**80**) 130.

[121] T. Nyokong, H. Isago, *J. Porphyrins Phthalocyanines* 2004 (**8**) 1083.

[122] F. R. Fronczek, R. J. Johnson, R. M. Strongin, *Acta Cryst.* 2001 (**E57**) 447.

[123] A. B. P. Lever, E. R. Milaeva, G. Speier, *In Phthalocyanines: Properties and applications,* eds. C.C. Leznoff, A. B. P. Lever, VCH Publishers: New York, 1993, Volume 3.

[124] J. F. Myer, R. G. W. Canham, A. B. P. Lever, *Inorg. Chem.* 1975 (**14**) 461.

[125] A. B. P. Lever, M.R. Hempstead, C. C. Leznoff, W. Liu, M. Melnik, W. A. Nevin, P. Seymour, *Pure Appl. Chem*. 1989 (**58**) 1467.

[126] M. L'Her, A. Pondaven, in *The Porphyrin Handbook,* eds. K. M. Kadish, K. M. Smith, R. Guilard, Academic Press (San Diego), 2003, Volume 16.

[127] A. B. P. Lever, S. Licoccia, K. Magnell, R. C. Minor, B. S. Ramaswamy, *ACS Symp. Ser.* 1982 (**201**) 237.

[128] M. N. Golovin, P. Seymour, K. Jayaraj, Y. S. Fu, A. B. P. Lever, *Inorg. Chem.* 1990 (**29**) 1719.

[129] T. Nyokong, *Polyhedron* 1993 (**12**) 375.

[130] T. Kuwana, R. K. Darlington, D. W. Leedy, *Anal. Chem.* 1964 (**36**) 2023.

[131] J. Obirai, T. Nyokong, *J. Electroanal. Chem.* 2004 (**573**) 77.

[132] M. J. Stillman, in *Phthalocyanines: Properties and applications*, eds. C. C. Leznoff, A. B. Lever, VCH Publishers, New York, 1993 Volume 3.

[133] L. D. Rollman, R. T. Iwamoto, *J. Am. Chem. Soc.* 1968 (**90**) 1455.

[134] J. W. Dodd, N. S. Hush, *J. Chem. Soc.* 1964, 4607.

[135] E. A. Ough, Z. Gasyna, M. J. Stillmann, *Inorg. Chem*. 1991 (**30**) 2301.

[136] D. W. Clack, J. R. Yandle, *Inorg. Chem.* 1972 (**11**) 1738.

[137] T. Nyokong, in *N4-Macrocyclic Metal Complexes*, eds. J. H. Zagal, F. Bedioui, J.-P. Dodelet, Springer, New York, 2006, Chapter 8, pp. 363 - 438.

[138] D. Nkosi, K. I. Ozoemena, *J. Electroanal. Chem.* 2008 (**621**) 304.

[139] M. A. Gilmartin, R. J. Ewen, J. P. Hart, *J. Electroanal. Chem.* 1996 (**401**) 127.

[140] K. I. Ozoemena, Z. Zhao, T. Nyokong, *Electrochem. Comm.* 2005 (**7**) 679.

[141] J. H. Zagal, M. A. Paez, J. F. Silva, in *N4-Macrocylcic Metal Complexes,* eds. J. H. Zagal, F. Bedioui, J.-P. Dodelet, Springer Science + Business Media, Inc. New York, 2006.

[142] J. H. Zagal, R. K. Sen, E. yeager, *J. Electroanal. Chem.* 1977 (**83**) 207.

[143] J. Pillay, K. I. Ozoemena *Electrochim. Acta* 2009 (54) 5053.

[144] M. Gulppi, F. Bedioui, J. H. Zagal, *Electroanal.* 2001 (**13**) 1136.

[145] J. Oni, T. Nyokong, *Anal. Chim. Acta* 2001 (**434**) 9.

[146] S. Maree, T. Nyokong, *J. Electroanal. Chem*. 2000 (**492**) 120.

[147] M. Sekota, T. Nyokong, *Electroanal.* 1997 (**9**) 1257.

[148] J. Wang, B. Tian, V. B. Nascimento, L. Angnes, *Electrochim. Acta* 1998 (**43**) 3459.

[149] S. Ledru, N. Ruillé, M. Boujtita, *Biosens. Bioelectron.* 2006 (**21**) 1591.

[150] S. Laschi, I. Palchetti, M. Mascini, *Sens. Actuat.B* 2006 (**114**) 460.

[151] A. Cagnini, I. Palchetti, I. Lionti, M. Mascini, A. P. F. Turner, *Sens. Actuat. B* 1995 (**24**) 85.

[152] A. Cagnini, I. Palchetti, M. Mascini, A. P. F. Turner, *Mikrochim. Acta* 1995 (**121**) 155.

[153] G. Marrazza I. Chianella, M. Mascini, *Biosens. Bioelectron.* 1999 (**14**) 43.

[154] F. Ricci, A. Amine, G. Palleschi, D. Moscone, *Biosens. Bioelectron.* 2003 (**18**) 165.

[155] G. Carpini, F. Lucarelli, G. Marrazza, M. Mascini, *Biosens. Bioelectron.* 2004 (**20**) 167.

[156] S. D. Sprules, J. P. Hart, S. A. Wring, R. Pittson, *Anal. Chim. Acta* 1995 (**304**) 17.

[157] C. D. Kuhnline, M. G. Gangel, M. K. Hulvey, R. S. Martin, *Analyst* 2006 (**131**) 202.

[158] A. Napier, J. P. Hart, *Electroanal*. 1996 (**8**) 1006.

[159] M. J. Cook, *J. Mater. Chem.* 1996 (**6**) 677.

[160] M . Iwamoto, *J. Mater. Chem.* 2000 (**10**) 99.

[161] M. J. Cook, *Pure Appl. Chem.* 1999 (**71**) 2145.

[162] D. Crouch, S. C. Thorpe, M.J . Cook, I. Chambrier, A.K. Ray, *Sens. Actuators B*, 1994 (**18-19**) 411.

[163] J. Obirai, N. Periera-Rodriguez, F. Bedioui, T. Nyokong, *J. Porhyrins Phthalocyanines* 2003 (**7**) 508.

[164] A. Pailleret, F. Bedioui, in *N4-Macrocyclic Metal Complexes*, eds. J. H. Zagal, F. Bedioui, J.-P. Dodelet, Springer, New York, 2006, Chapter 8, pp. 363 - 438.

[165] C. A. Caro, F. Bedioui, J. H. Zagal, *Electrochim. Acta* 2002 (**47**) 1489.

[166] N. Sehlotho, T. Nyokong, J. H. Zagal, F. Bedioui, *Electrochim. Acta* 2006 (**51**) 5125.

[167] F. Matemadombo, P. Westbroek, T. Nyokong, *Electrochim. Acta* 2007 (**53**) 480.

[168] R.W. Murray, A. G. Ewing, R. A. Durst, *Anal. Chem.* 1987 (**59**) 379A.

[169] M.-C. Pham, P.-C. Lacaze, J.-E. Dubois, *J. Electroanal. Chem. Inter. Electrochem.* 1979 (**99)** 331.

[170] A. Volkov, G. Tourillon, P.C. Lacaze, J.-E. Dubois, *J. Electroanal. Chem*. 1980 (**115**) 279.

[171] A. F. Diaz, J. A. Logan, *J. Electroanal. Chem.*, 1980 (**111**) 111.

[172] A. F. Diaz, J. I. Castillo, J. A. Logan, W.-Y. Lee, *J. Electroanal. Chem.* 1981 (**129**) 115.

[173] E. M. Genies, G. Bidan, A. F. Diaz, *J. Electroanal. Chem*., 1983 (**149**) 101.

[174] R. M. Penner, C. R. Martin, *J. Electrochem. Soc*., 1986 (**133**) 300.

[175] K. K. Kanazawa, A. F. Diaz, R. H. Geiss, W. D. Gill, J. F. Kwak, J. A. Logan, J. F. Rabolt, G. B. Street, *J. Chem. Soc.* 1979, 854.

[176] R. John and G.G. Wallace, *J. Electroanal. Chem*., 1991 (**306**) 157.

[177] A. E. Kaifer, M. Gomez-Kaifer, *Supramolecular Electrochemistry*, Wiley-VCH, Germany, 1999.

[178] J. J. Gooding, F. Mearns, W. Yang, J. Liu, *Electroanal.* 2003 (**15**) 81.

[179] R. K. Smith, P. A. Lewis, P. S. Weiss, *Prog. Surf. Sci.* 2004 (**75**) 1.

[180] H. O. Finklea in *Electroanalytical Chemistry*, eds. A. J. Bard, I. Rubinstein, Marcel Dekker, New York, 1996 Volume 19.

[181] H. O. Finklea in *Encyclopedia of Analytical Chemistry: Applications, Theory and Instrumentations*, eds. R. A. Meyer, Wiley & Sons, Chichester, 2000, Volume 11.

[182] R. G. Nuzzo, D. L. Allara, *J. Am. Chem. Soc.* 1983 (**105**) 4481.

[183] R. G. Nuzzo, F. A. Fusco, D. L. Allara, *J. Am. Chem. Soc*. 1987 (**109**) 2358.

[184] M.D. Porter, T. B. Bright, D. L. Allara, C. E. D. Chidsey, *J. Am. Chem. Soc.* 1987 (**109**) 3559.

[185] H. O. Finklea, S. Avery, M. Lynch, T. Furtsch, *Langmuir* 1987 (**3**) 409.

[186] E. B. Troughton, C. D. Bain, G. M. Whiresides,R. G. Nuzzo, D. L. Allara, M. D. Porter, *Langmuir* 1988 (**4**) 365.

[187] L. Strong, G. M. Whitesides, *Langmuir* 1988 (**4**) 546.

[188] C. D. Bain, G. M. Whitesides, *J. Am. Chem. Soc.* 1988 (**110**) 3665.

[189] C. D. Bain, G. M. Whitesides, *J. Am. Chem. Soc.* 1988 (**110**) 5897.

[190] C. D. Bain, G. M. Whitesides, *J. Am. Chem. Soc.* 1988 (**110**) 6560.

[191] C. D. Bain, G. M. Whitesides, *Science* 1988 (**240**) 62.

[192] A.J. Bard, *J. Chem. Educ*., 1983 (**60**) 302.

[193] C.R. Martin and C.A. Foss Jr, in *Laboratory Techniques in Electroanalytical Chemistry*, 2nd ed., P.T. Kissinger and W.R. Heineman (Eds), Marcel Dekker Inc., New York, 1996.

[194] C.M. Elliot, R.W. Murray, *Anal. Chem.* 1976 (**48**) 1247.

[195] R.F. Lane, A.T. Hubbard, *J. Phys. Chem.* 1973 (**77**) 1401.

[196] T. Nyokong, F. Bedioui, *J. Porphyrins Phthalocyanines* 2006 (**10**) 1101.

[197] M.J. Cook, *Pure Appl. Chem*. 2002 (**71**) 2145.

[198] T.R.E. Simpson. M.J. Cook, M.C. Petty, S.C. Thorpe, D.A. Russell, *Analyst* 1996 (**121**) 1501.

[199] T.R.E. Simpson, D. J. Revell, M.J. Cook, D.A. Russell, *Langmuir* 1997 (**13**) 461.

[200] H.O. Finklea, D.D. Hansheu, *J. Am. Chem. Soc*. 1992 (**114**) 3173.

[201] A.M. Becka, C.J. Miller, *J. Phys. Chem*. 1992 (**96**) 2657.

[202] C. C. Leznoff, A. B. P. Lever (eds), *Phthalocyanines: Properties and Applications*, VCH Publishers, New York, 1989 – 1996, Volumes 1 – 4.

[203] M. J. Cook, I. Chambrier, *Porphyrin Handbook*, (eds.) K. M. Kadish, K.M. Smith, R. Guilard, Academic Press, San Diego, 2003, Volume 17.

[204] G. Che, Z. Li, H. Zhang, C.R. Cabrera, *J. Electroanal. Chem.* 1998 (**453**) 9.

[205] J. J. Gooding, V. Praig, E. A. H. Hall, *Anal. Chim. Acta* 1998 (**70**) 2396.

[206] J. J. Gooding, D. B. Hibbert, *TrAC* 1999 (**18**) 525.

[207] J. J. Gooding, P. Erokhin, D. B. Hibbert, *Biosens. Bioelectron*. 2000 (**15**) 229.

[208] J. J. Gooding, L Pugliano, D. B. Hibbert, P. Erohkin, *Electrochem. Comm*. 2000 (**2**) 217.

[209] M. Mrksich, G.M. Whitesides, *Annu. Rev. Biomol. Struct.* 1996 (**25**) 55.

[210] I. Willner, R. Blonder, A. Dagan, *J. Am. Chem. Soc*. 1994 (**115**) 4935.

[211] V.W. Jones, J.R. Kenseth, M.D. Porter, C.L. Mosher, E. Henderson, *Anal. Chem.* 1998 (**70**) 1233.

[212] Y. Okahata, Y. Matsunobu, K. Ijiro, M. Mukae, A. Murakami, K. Makino, *J. Am. Chem. Soc*. 1992 (**114**) 8299.

[213] I. Willner, M. Lion-Dagan, S. Marx-Tibbon, E. Katz, *J. Am. Chem. Soc*. 1995 (**117**) 6581.

[214] W. Yang, J.J. Gooding, D.B. Hibbert, *J. Electroanal. Chem*. 2001 (**516**) 10.

[215] A. G. Kanaras, F. S. Kamounah, K. Schaumburg, C. J. Kiely, M. Brust, *Chem. Comm*. 2002, 2294.

[216] T. R. Tshikhudo, Z. Wang, M. Brust, *Mater. Sci. & Technol*. 2004 (**20**) 980.

[217] R. C. Doty, T. R. Tshikhudo, M. Brust, D. G. Fernig, *Chem. Mater*. 2005 (**17**) 4630.

[218] R. T. Tshikhudo, D. Demuru, Z. Wang, M. Brust, A. Secci, A. Arduini, A. Pochini, *Angew. Chem. Int. Ed*. 2005 (**44**) 2913.

[219] K. I. Ozoemena, T. Nyokong, *Electrochim. Acta* 2006 (**51**) 2669.

[220] D. Nkosi, K. I. Ozoemena, *Electrochim. Acta* 2008 (**53**) 2782.

[221] R. Fogel, P. Mashazi, T. Nyokong, J. Limson, *Biosens. Bioelectron*. 2007 (**23**) 95.

[222] C. C. Leznoff, L. S. Black, A. Heibert, P. W. Causey, D. Christendat, A. B. P. Lever *Inorg. Chim. Acta* 2006 (**359**) 2690.

[223] M Delamar, R. Hitmi, J. Pinson, J.-M. Savéant, *J. Am. Chem. Soc*. 1992 (**114**) 5883.

[224] O. Ghodbane, G. Chamoulaud, D. Belanger, *Electrochem. Comm*. 2004 (**6**).

[225 G. Liu, J. Liu, T. Bocking, P. K. Eggers, J. J. Gooding, *Chem. Phys*. 2005 (**319**) 136.

[226] S. Griveau, D. Mercier V. Vautrin-UI, A. Chause, *Electrochem. Comm*. 2007 (**9**) 2768.

[227] R. Polsky, J. C. Harper, S. M. Dirk, D. C. Arango, D. R. Wheeler, S. M. Brozik, *Langmuir* 2007 (**23**) 364.

[228] R. Polsky, J. C. Harper, D. R. Wheeler, S. M. Dirk, D. C. Arango, S. M. Brozik, *Biosens. Bioelectron*. 2008 (**23**) 757.

[229] C. Bourgillon, M. Delamar, C. Demaille, R. Hitmi, J. Moiroux, J. Pinson, *J. Electroanal. Chem*. 1992 (**336**) 113.

[230] G. Liu, M. N. Paddon-Row, J. J. Gooding, *Electrochem. Comm.* 2007 (**9**) 2218.

[231] A.-E. Radi, J. M. Montornes, C. K. O'Sullivan, J. *Electroanal. Chem*. 2006 (**587**) 140.

[232] M. F. W. Dunker, E. B. Starkey, G. L. Jenkins, *J. Am. Chem. Soc.* 1936 (**58**) 2308.

[233] N. Kornblum, D. C. Ifflan, *J. Am. Chem. Soc.* 1949 (**71**) 2137.

[234] J. L. Bahr, J. M. Tour, *Chem. Mater*. 2001 (**13**) 3823.

[235] J. L. Bahr, J. M. Tour, *J. Mater. Chem*. 2002 (**12**) 1952.

[236] C. A. Dyke, J. M. Tour, *J. Am. Chem. Soc*. 2003 (**125**) 1156.

[237] C. A. Dyke, J. M. Tour, *Nano Lett*. 2003 (**3**) 1215.

[238] J. L. Bahr, J. Yang, D. V. Kosynkin, M. J. Bronikowski, R. E. Smalley, J. M. Tour, *J. Am. Chem. Soc*. 2001 (**123**) 6536.

[239] J. K. Kariuki, M. T. McDermott, *Langmuir* 1999 (**15**) 6534.

[240] A. Laforgue, T. Addou, D. Belanger, *Langmuir* 2005 (**21**) 6855.

[241] G. Liu, T. Bocking, J. J. Gooding, *J. Electroanal. Chem*. 2007 (**600**) 335.

[242] P. A. Brooksby, A. J. Downard, *J. Phys. Chem. B*. 2005 (**109**) 8791.

[243] B. Ortiz, C. Saby, G. Y. Champagne, D. Belanger, *J. Electroanal.Chem.* 1998 (**455**) 75.

[244] P. Allongue, M. Delamar, B. Desbat, O. Fagebaume, R. Hitmi, J. Pinson, J.-M. Saveant, *J. Am. Chem. Soc.* 1997 (**119**) 201.

[245] M. Kullapere, G. Jurmann, T. T. Tenno, J. J. Paprotny, F. Mirkhalaf, K. Tammeveski, *J. Electroanal. Chem.* 2007 (**599**) 183.

[246] J. K. Kariuki, M. T. McDermott, *Langmuir* 2001 (**17**) 5947.

[247] M.-C. Bernard, A. Chausse, E. Cabet-Deliry, M. C. Chehimi, J. Pinson, F. Podvorica, C. Vautrin-UI, *Chem. Mater*. 2003 (**15**) 3450.

[248] J. L. Lyskawa, D. Belanger, *Chem. Mater.* 2006 (**18**) 4755.

[249] G. Chamoulaud, D. Belanger, *J. Phys. Chem. C* 2007 (**111**) 7501.

[250] A. Benedetto, M. Balog, P. Viel, F. Le Derf, M. Salle, S. Palacin, *Electrochim. Acta* 2008 (**53**) 7117.

[251] J. Haccoun, C. Vautrin-UI, A. Chausse, A. Adenier, *Prog. Org. Coat.* 2008 (**63**) 18.

[252] A. Adenier, M.-C. Bernard, M. M. Chehimi, E. Cabet-Deliry, B. Desbat, O. Fagebaume, J. Pinson, F. Podvorica, *J. Am. Chem. Soc*. 2001 (**123**) 4541.

[253] K. Boukerma, M. M. Chehimi, J. Pinson, C. Blomfield *Langmuir* 2003 (**19**) 6333.

[254] M. Ebadi, S. K. Srinivasan, M. D. Baxi, *Prog. Neurobiol.* 1996 (**48**) 1.

[255] B. R. Eggins, *Chemical Sensors and Biosensors,* John Wiley & Sons, Chichester, 2003.

[256] P. Westbroek, B. van Hayte, E. Temmerman, *Fres. J. Anal. Chem.* 1996 (**354**) 405.

[257] P. A. Tanner, A. Y. S. Wong, *Anal. Chim. Acta* 1998 (**370**) 279.

[258] W. Sun, H. Jiang, K. Jiao *J. Chem. Sci.* 2005 (**117**) 317.

[259] P. Westbroek, E. Temmerman, *J. Electroanal. Chem.* 2000 (**482**) 40.

[260] B. Halliwell, M. V. Clement, L. H. Long, *FEBS Letters* 2000 (**486**) 10.

[261] G. G. Guildibault, *Enzymatic Methods of Analyst*, Pergamon, Oxford 1970.

[262] P. Westbroek, E. Temmerman, F. Govaert, B. van Houte, *Bull. Soc. Chim. B* 1997(**106**) 755.

[263] E. Ferapontova, L.Gorton, *Bioelectrochem.* 2002 (**55**) 83.

[264] E. E. Ferapontova, V. G. Grigorenko, A. M. Egorov, T. Bırchers, T. Ruzgas, L. Gorton, *Biosens. Bioelectron.* 2001 (**16**) 147.

[265] E. Ferapontova, K. Schmengler, T. Bırchers, T. Ruzgas, L. Gorton, *Biosens. Bioelectron*. 2002 (**17**) 953.

[266] D. F. Laine, I. F. Cheng, *Microchem. J.* 2009 (**91**) 78.

[267] X. Ji, J. Huang-Xian, C. Hong-Yuan, *Anal. Biochem*. 2000 (**278**) 22.

[268] N. Kiba, T. Tokizawa, S. Kato, M. Tachibana, K. Tani, H. Koizuma, M. Edo, E. Yonezawa, *Anal. Sci*. 2003 (**19**) 823.

[269] C. Matsubara, N. Kawamoto, K. Takamura, *Analyst* 1992 (**117**) 1781.

[270] G. Shi, J. Liu, F. Xu, H. Zhou, L. Jin, J. Jin, *Anal. Chim. Acta* 2000 (**314**) 131.

[271] E. C. Hurdis, H. Romeyn Jr. *Anal. Chem.* 1954 (**26**) 320.

[272] T. Ruzgas, E. Csoregi, J. Emneus, L. Gorton, G. M. Varga, *Anal. Chim. Acta* 1996 (**330**) 123.

[273] S.-I. Adachi, S. Nagano, K. Ishimori, Y. Wanatabe, I. Morishima, T. Egawa, T. Kitagawa, R. Mukino, *Biochem.* 1993 (**32**) 241.

[274] M. S. M. Quintino, H. Wimischofer, K. Araki, H. E. Toma, L. Agnes, *Analyst* 2005 (**130**) 221.

[275] K. I. Ozoemena, Z. Zhao, T. Nyokong, *Inorg. Chim. Comm.* 2006 (**9**) 223.

[276] J. Wang, P. V. A. Pamidi, C. Parrado, D. S. Park, J. Pingarron *Electroanal*. 1997 (**9**) 908.

[277] M. A. T. Gilmartin, R. J. Ewen, J. P. Hart, C. L. Honeybourne *Electroanal.* 1995 (**7**) 547.

[278] C. Coutanceau, A. El Hourch, P. Crouigneau, J. M. Leger, C. Lamy *Electrochim. Acta* 1995 (**40**) 2739.

[279] F. J. Rawson, W. M. Purcell, J. Xu, D. C. Cowell, P. R. Fielden, N. Biddle, J. P. Hart *Electrochim. Acta* 2007 (**52**) 7248.

[280] K. Wang, J.-J. Xu, H.-Y. Chen *Biosens. Bioelectron*. 2005 (**20**) 1388.

[281] R. Feynman, *Caltech Engineering and Science*, 1960 (**23**) 22.

[282] R. Feynmann, *J. Microelectromechanical Systems*, 1992 (**1**) 60.

[283] P. G. Wiles, J. Abrahamson, *Carbon* 1978 (**6**) 341.

[284] S. Iijima, *Nature* 1991 (**354**) 56.

[285] S. C. Lyu, T. J. Lee, C. W. Yang, J. C. Lee, *Chem. Comm.* 2003 (**12**) 1404.

[286] M. Endo, T. Hayashi, Y.-A. Kim, *Pure Appl. Chem.* 2006 (**78**) 1703.

[287] S. Iijima, C. Brabec, A. Maiti, J. Bernholc, *J. Chem. Phys. 1996 (***104**) 2089.

[288] B. I. Yakobson, C. J. Brabec, J. Bernholc, *Phys. Rev. Lett.* 1996 (**76**) 2511.

[289] J. Hone, M. Whitney, A. Zettle, *Synth. Met.* 1999 (**103**) 2498.

[290] A. Thess, R. Lee, P. Nikolaev, H. Dai, P. Petit, J. Robert, C. Xu, Y. H. Lee, S. G. Kim, A. G. Rinzler, D. T. Colbert, G. E. Scuseria, D. Tomane'k, J. E. Fischer, R. E. Smalley, *Science* 1996 (**273**) 483.

[291] P.L. McEuen, M. Fuhrer, H. Park, *IEEE Trans. Nanotech*. 2002 (**1**) 78.

[292] J. W. G. Wilder, L. C. Venema, A. G. Rinzler, R.E. Smalley, C. Dekker, *Nature* 1998 (**391**) 59.

[293] K. Kataura, Y. Kumazawa, Y. Maniwa, I. Umezu, S. Suzuki, Y. Ohtsuka, Y. Achiba, *Synth. Met.* 1999 (**103**) 2555.

[294] F. Cordella, M. Nardi, E. Menna, C. Hebert, M. A. Loi, *Carbon* 2009 (**47**) 1264.

[295] P. J. Britto, K. S. Santhanam, P. M. Ajayan, *Bioelectron. Bioenerg*. 1996 (**41**) 121.

[296] J. Liu, A. G. Rinzler, H. Dai, J. H. Hafner, R. K. Bradley, P. J. Boul, A. Lu, T. Iverson, K. Shelimov, C. B. Huffman, F. J. Rodriguez-Macias, Y.-S. Shon, T. R. Lee, D. T. Colbert, R. E. Smalley, *Science* 1998 (**280**) 1253.

[297] Y.-P. Sun, K. Fu, Y. Lin, W.Huang, *Acc. Chem. Res.* 2002 (**35**) 1096.

[298] M. V. Naseh, A. A. Khodadadi, Y. Mortazavi, O. A. Sahraei, F. Pourfayaz, S. M. Sedghi, *World Acad. Sci. Eng. Tech*. 2009 (**49**) 177.

[299] Y. Wang, Z. Iqbal and S. Mitra, *J. Am. Chem. Soc*. 2006 (**128**) 95.

[300] G.-W. Lee and S. Kumar, *J. Phys. Chem. B* 2005 (**109**) 17128.

[301] M. S. Strano, C. A. Dyke, M. L. Usrey, P. W. Barone, M. J. Allen, H. Shan, C. Kittrell, R. H. Hauge, J. M. Tour, R. E. Smalley, *Science* 2003 (**301**) 1591.

[302] M. D. Ellison, P. J. Gasda, *J. Phys. Chem. C* 2008 (**112**) 738.

[303] T. Mugadza, T. Nyokong, *Synth. Met.* 2010 (**160**) 2089.

[304] T. Muganda, T. Nyokong, *Electrochim. Acta* 2010 (**55**) 2606.

[305] T. Mugadza, T. Nyokong, *Electrochim. Acta* 2010 (**55**) 6049.

[306] K. I. Ozoemena, D. Nkosi, J. Pillay, *Electrochim. Acta 2008* (**53**) 2844.

[307] M. C. A. Brett, A. M. O. Brett, *Electrochemistry Principles, Methods and Applications*, Oxford University Press, New York, 1993.

[308] A. J. Bard, L.R. Faulkner, *Electrochemical Methods: Fundamentals and Applications,* John Wiley & Sons, New York, 1980.

[309] S. Krause, *Instrumentation and Electroanalytical Chemistry*, eds. A. J. Bard, M. Stratmann, P. R. Irwin, Wiley-VCH GmbH & Co. KGaA, 2003, Volume 3.

[310] P. Westbroek, G. Priniotakis, P. Kiekens, *Analytical Electrochemistry in Textiles*, Woodhead Publishing LTD and CRC Press LLC, Cambridge England, 2005.

[311] J. R. MacDonald, W. B. Johnson, in *Impedance Spectroscopy*, (eds) E. Barsoukov, J. R. MacDonald, Second Edition, John Wiley & Sons Inc. New Jersey, 2005.

[312] J. B. Hudson, *Surface Science: An Introduction*, John Wiley & Sons, New York, 1998.

[313] M. H. Kibel, *Surface Analysis Methods in Material Science*, (eds) D. J. O'Connor, B. A. Sexton, R. St. C. Smart, Springer-Verlag, Berlin Heidelberg, Germany, 1993.

[314] M. J. Pelletier, *Analytical Applications of Raman Spectroscopy*, Michigan, USA, 1999.

[315] J. Popp, W. Keifer, *Encyclopedia of Analytical Chemistry: Applications, Theory and Instrumentation*, (eds) R. A. Meyer, John Wiley & Sons, New York, 2000, Volume 15.

[316] J. Goldstein, D. Newbury, D. Joy, C. Lyman, P. Echlin, E. Lifshin, L. Sawyer, J. Michael, *Scanning Electron Microscopy and X-Ray Microanalysis,* Kluwer Academic/Plenum Publishers, New York, 2003.

[317] S. Cengiz, A. C. Karaca, I. Cakir, H. B. Uner, A. Sevindik, *Forensic Sci. Int.* 2004 (**141**) 33.

[318] A. R. Hillman, *Instrumentation and Electroanalytical Chemistry*, eds. A. J. Bard, M. Stratmann, P. R. Unwin, Wiley-VCH GmbH & Co. KGaA, 2003, Volume 3.

[319] G. Sauerbrey, *Z. Phys.* 1959 (155) 206.

[320] F. Hook, B. Kasemo, T. Nylander, C. Fant, K. Sott, and H. Elwing, *Anal. Chem.* 2001 (**73**) 5796.

[321] R. Saber, S. Mutlu, E. Piskin, *Biosens. Bioelectron.* 2002 (**17**) 727.

[322] C. A. Keller, B. Kasemo, *Biophys. J.* 1998 (**75**) 1397.

[323] M. Liebau, A. Hilderbrand, R.H. H. Neubert, *Eur. Biophys. J.* 2001 (**30**) 42.

[324] L. Tedeschi, L. Citti, C. Domenici, *Biosens. Bioelectron.* 2005 (**20**) 2376.

[325] F. Hook, M. Rodahl, P. Brzezinski, B. Kasemo, *Langmuir* 1998 (**14**) 729.

[326] E. J. Calvo, R. Etchenique, L. Pietrasanta, A. Wolosiuk, *Anal. Chem.* 2001 (**73**) 1161.

[327] B. N. Achar, K. S. Lokesh, *J. Organometal. Chem.* 2004 (**689**) 3357.

[328] J. Obirai, T. Nyokong, *Electrochim. Acta* 2005 (**50**) 5427.

[329] T. Mugadza, T.Nyokong, *J. Colloid Interface Sci.* 2011 (**354**) 437.

[330] M. D. Ellison, P. J. Gasda, *J. Organometal. Chem.* 2004 (**689**) 3357.

[331] A. G. Gurek,O. Bekaroglu, *J. Chem. Soc. Dalton Trans.* 1994, 1419.

[332] F. Hook, A. Ray, B. Norden, B. Kasemo, *Langmuir* 2001 (**17**) 8305.

[333] D. L. Pilloid, X. Chen, P. L. Dutton, C. C. Mosser, *J. Phys. Chem.* 2001 (**17**) 2868.

[334] D. Losic, J. G. Shipter, J. J. Gooding, *Langmuir* 2001 (**17**) 8305.

[335] M. J. Stillman, T. Nyokong, in *Phthalocyanine: Properties and Applications*, eds. A. B. P. Lever, C. C. Leznoff, VCH-Publishers, New York, 1989.

[336] A. B. P. Lever, S. R. Pickens, P. C. Minor, L. Liccoccia, B. S. Ramaswamy, K. Magnel, *J. Am. Chem. Soc.* 1981 (**103**) 6800.

[337] F. D. Cong, B. Ning, X. G. Du, D. J. Chen, B. Chen, *J. Mol. Sci.* 2001 (**20**) 27.

[338] H. Li, T. F. Guarr, *J. Chem. Soc. Chem. Comm.* 1989, 832.

[339] A. Yu. Tolbin, V. E. Pushkarev, G. F. Nikiti, L. G. Tomilova, *Tetrahedron Lett.* 2009 (**50**) 4848–4850

[340] P. Tau, T. Nyokong, *Dalton. Trans.* 2006, 4482.

[341] N. Kobayashi, H. Ogata, N. Nonaka, E. A. Luk'yanets, *Chem.-Eur. J.* 2003 (**9**) 5123.

[342] N. Kobayashi, H. Konami, in *Phthalocyanines: Properties and Applications*, eds. C. C. Leznoff, A. B. P. Lever, VCH-Publishers, New York, 1996.

[343] G. Mbambisa, T. Nyokong, *Polyhedron* 2008 (**27**) 2799.

[344] K. Takahashi, M. Kawashima, Y. Tomita, M. Itoh, *Inorg. Chim. Acta* 1995 (**232**)69.

[345] B. Yu, A. B. P. Lever, Y. W. Swaddle, *Inorg. Chem.* 2004 (**34**) 4496.

[346] J. Obirai, T. Nyokong, *Electrochim. Acta* 2005 (**50**) 3296.

[347] G. Kalyuzhny, A. Vaskevich, G. Ashkenasy, A. Shanzer, I. Rubinstein, *J. Phys. Chem. B* 2000 (**104**) 8238.

[348] A. B. P. Lever, P. C. Minor, J. P. Wilshire, *Inorg. Chem.* 1981 (**20**) 2550.

[349] F. Matemadombo, M. Durmus, C. A. Togo, J. Limson, T. Nyokog, Electrochim. Acta 2009 (**54**) 5557.

[350] K. H. Schweikart, V. L. Malinovskii, A. A. Yasseri, J. Li, A. B. Lysenko, D. F. Bocian, J./ S. Lindsey, *Inorg. Chem.* 2003 (**42**) 7341.

[351] D. Gryko, J. Li, J. R. Diers, K. M. Roth, D. F. Bocian, W. G. Kuhr, J. S. Lindsey, *J. Mater. Chem*. 2001 (**11**) 1162.

[352] K. V. Gothelf, *J. Electroanal. Chem.* 2000 (**494**) 147.

[353] A. Nion, P. Jiang, A. Popoff, D. Fichou, *J. Am. Chem. Soc.* 2007 (**129**) 2450.

[354] H. S. Nalwa, *in Handbook of Conductive Molecules and Polymers*, John Wiley & Sons Ltd. 1997, Volume 2.

[355] P. S. Kumar, V. Lakshminarayanan, *Langmuir* 2007 (**23**) 1548.

[356] L. Yang, Y. Li, *Biosens. Bioelectron.* 2005 (**20**) 1407.

[357] J. Pillay, K. I. Ozoemena, *Electrochem. Comm*. 2007 (**9**) 1816.

[358] E. Sabatani, I. Rubinstein, *J. Phys. Chem.* 1987 (**91**) 6663.

[359] V. Lakshminarayanan, U. K. Sur, *Pramana J. Phys.* 2003 (**9**) 361.

[360] A.-E. Radi, X. Munoz-Berbel, M. Cortina-Piug, J.-L. Marty, *Electrochim. Acta* 2009 (**54**) 2180.

[361] S.-N. Song, D.-M. Li, C.-F. Zhuang, H. Ding, W.-B. Song, L.-F. Ciu, G.-Z. Cao, G.-F. Liu, *Eur. J. Inorg. Chem.* 2007, 1844.

[362] H. L. Anderson, *Chem. Comm*. 1999, 2323.

[363] C. Saby, B. Ortiz, G. Y. Champagne, D. Belanger, *Langmuir* 1997 (**13**) 6805.

[364] F. Anariba, S. H. DuVall, R. L. McCreery, *Anal. Chem.* 2003 (**17**) 3837.

[365] E. Smith, G. Dent, in *Modern Raman Spectroscopy: A Practical Approach,* John Wiley & Sons Ltd, Chichester, England, 2005.

[366] B. Simic-Glavaski, S. Zecevic, E. Yeager, *J. Am. Chem. Soc*. 1985 (**107**) 5625.

[367] B. Simic-Glavaski, S. Zecevic, E. Yeager, *J. Electroanal. Chem*. 1983 (**150**) 469.

[368] K. De Wael, P. Westbroek, P. Bultinck, D. Depla, P. Vandenabeele, A. Andriens, E. Temmerman, *Electrochem. Comm*. 2005 (**7**) 87.

[369] D. R. Tackley, G. Dent, W. E. Smith, *Phys. Chem. Chem. Phys*. 2000 (**2**) 3949.

[370] D. R. Tackley, G. Dent, W. E. Smith, *Phys. Chem. Chem. Phys*. 2001 (**3**) 1419.

[371] M. S. Dresselhaus, G. Dresselhaus, A. Jorio, A. G. S. Saito, *Carbon* 2002 (**40**) 2043.

[372] R. Saito, T. Takeya, T. Kimura, G. Dresselhaus, M. S. Dresselhaus, *Phys. Rev. B* 1998 (**57**) 4145.

[373] N. Sehlotho, T. Nyokong, *J. Electroanal. Chem*. 2006 (**595**) 161.

[374] R. I. Stefan, J. F. van Staden, H. Y. Aboul-Enein, in *Electrochemical Sensors in Bioanalysis*, Marcel Dekker: New York, 2001.

[375] E. A. de Vasconcelos, N. G. Peres, C. O. Pereira, V. L. da Silva, E. F. da Silva, R. F. Dutra, *Biosens. Bioelectron.* 2009 (**25**) 870.

[376] Department of Health (South Africa), *Annual Report*, 2001 – 2002.

[377] X. Chen, C. Ruan, J. Kong, J. Deng, *Fresenius J. Anal. Chem*. 2000 (**367**) 172.

[378] S. Liu, J. Tian, L. Wang, G. Chang, X. Sun, *Analyst* 2011 (**136**) **DOI:** 10.1039/ C1AN15654C.